Rotordynamic Tests in Cavitation of the SEP Inducer

Michael P. Karyeaclis

R. Scott Miskovish

Christopher E. Brennen

Division of Engineering and Applied Science

1989

CALIFORNIA INSTITUTE OF TECHNOLOGY

PASADENA, CALIFORNIA

Rotordynamic Tests in Cavitation of the SEP Inducer

Michael P. Karyeaclis

R. Scott Miskovish

Christopher E. Brennen

Division of Engineering and Applied Science

1989

Report E200.27

ROTORDYNAMIC TESTS IN CAVITATION OF THE SEP INDUCER

Michael P. Karyeaclis

R. Scott Miskovish

Christopher E. Brennen

Report E200.27

on contract with

Société Européenne de Propulsion,

Division à Liquides et Espace,

Vernon, France

Division of Engineering and Applied Science

California Institute of Technology

Pasadena, California

1989

Acknowledgements

The authors would like to thank Professors Alan Acosta and Thomas Caughey for their valuable suggestions and assistance throughout this investigation. We would especially like to thank Ron Franz, whose help was instrumental in performing the tests.

In addition, we would like to thank Sophie Verzat of SEP for her help during the preliminary stages of the tests, Vianney Duthoit and Adiel Guinzburg for their help in taking the data, and Joe Fontana for helping with the installation of the auxiliary pump.

Finally, we appreciate the generous donation of the auxiliary pump by the Byron-Jackson Co.

Contents

List of Figures

List of Tables

List of Symbols

$R,\ D$	Largest inducer radius, diameter
$Cr_1,\ Cr_2$	Mean radial tip clearances, phase 1, phase 2
ν_1	Hub/tip ratio of diameters at inlet section A_1
A_1	Area of inlet section, $R^2(1-\nu_1^2)$
l	Axial length of blades measured at the hub
Ω	Rotating speed of the inducer
Δp_t	Total pressure rise between inlet section and outlet
Q_v	Flow rate
C_{m1}	Mean axial velocity at the inlet, Q_v/A_1
U_1	Relative velocity of the tip at inlet, $R^2\Omega^2 + C_{m1}^2$
T	Shaft torque
ρ	Density
ψ	Head coefficient, $\frac{\Delta p_t}{\frac{1}{2}\rho R^2\Omega^2}$
ϕ	Flow coefficient, $\frac{C_{m1}}{R\Omega}$
τ	Torque coefficient, $\frac{T}{\rho R^5\Omega^2}$
p_1	Static pressure at the inlet section A_1
p_{v1}	Vapor pressure at the inlet section
NPSP	Net positive suction pressure, $p_1 + \frac{1}{2}\rho C_{m1}^2 - p_{v1}$
k	Cavitation factor, $\frac{\text{NPSP}}{\frac{1}{2}\rho C_{m1}^2}$
σ	Cavitation number, $\frac{p_1 - p_{v1}}{\frac{1}{2}\rho U_1^2}$
t	Time
(X, Y)	Fixed laboratory reference frame

$x(t),\ y(t)$	Instantaneous radial coordinates of the inducer center in the fixed reference frame, nondimensionalized by R
$\dot{x},\ \dot{y}$	Time derivatives of x and y, nondimensionalized by $R\Omega$
$\ddot{x},\ \ddot{y}$	Acceleration, nondimensionalized by $R\Omega^2$
ε	Radius of whirl orbit, nondimensionalized by R
α	Angular polar coordinate of impeller on the whirl orbit
ω	Circular frequency of whirl motion
$\frac{\omega}{\Omega} = \frac{I}{J}$	Whirl speed ratio, I, J integers
$F_x,\ F_y$	Components of the instantaneous lateral forces in the reference frame (X, Y), nondimensionalized by $\pi\rho\Omega^2 R^3 l$
$M_x,\ M_y$	Components of the instantaneous moments in the reference frame (X, Y), nondimensionalized by $\pi\rho\Omega^2 R^3 l^2$
$F_1,\ F_2$	Components of the instantaneous lateral forces in the rotating frame of the balance, nondimensionalized by $\pi\rho\Omega^2 R^3 l$
$M_1,\ M_2$	Components of the instantaneous moments in the rotating frame of the balance, nondimensionalized by $\pi\rho\Omega^2 R^3 l^2$
$F_{0x}, F_{0y}, M_{0x}, M_{0y}$	Steady lateral forces and moments
$[A] = \begin{bmatrix} A_{xx} & A_{xy} \\ A_{yx} & A_{yy} \end{bmatrix}$	Hydrodynamic force matrix, nondimensionalized by $\pi\rho\Omega^2 R^2 l$
$[B] = \begin{bmatrix} B_{xx} & B_{xy} \\ B_{yx} & B_{yy} \end{bmatrix}$	Hydrodynamic moment matrix, nondimensionalized by $\pi\rho\Omega^2 R^2 l^2$
$F_n,\ F_t$	Components of the unsteady force along directions normal and tangential to the whirl motion, nondimensionalized by $\pi\rho\Omega^2 l$
$M_n,\ M_t$	Components of the unsteady moment about axes normal and tangential to the whirl motion, nondimensionalized by $\pi\rho\Omega^2 l^2$

$[K]$	Generalized stiffness matrix, nondimensionalzed by $\pi\rho\Omega^2R^2l$
$[C]$	Generalized damping matrix, nondimensionalized by $\pi\rho\Omega R^2l$
$[M]$	Generalized inertia matrix, nondimensionalized by $\pi\rho R^2l$
SF_{xx}, SF_{yy}	Spectral densities of F_x and F_y respectively
SF_{xy}	Cross-spectral density of F_x and F_y
SM_{xx}, SM_{yy}	Spectral densities of M_x and M_y respectively
SM_{xy}	Cross-spectral density of M_x and M_y
SF_{11}, SF_{22}	Spectral densities of F_1 and F_1 respectively
SF_{12}	Cross-spectral density of F_1 and F_2
SM_{11}, SM_{22}	Spectral densities of M_1 and M_2 respectively
SM_{12}	Cross-spectral density of M_1 and M_2
Δt	Sampling interval
N	Total number of samples
T	Total signal duration, $N\Delta t$
f	Frequency in Hz
f_r	Reference cycle frequency in Hz
f_0	Shaft frequency, $\frac{\Omega}{2\pi}$
$w_j(t)$	Bridge signal, $j = 1,\ldots,6$
$\hat{W}_j(f)$	Fourier transform of $w_j(t)$, $j = 1,\ldots,6$
$W_j(f)$	Fourier transform of shifted bridge signals, $j = 1,\ldots,6$
$\tilde{F}_k(f)$, $\tilde{M}_k(f)$	FFT's of forces and moments, $k = 1,2$

1

Introduction

The problem of rotordynamic instability has had a long history and a significant impact on the design and operation of rotating machinery. As the search for higher power density and sophistication intensified, so have efforts to understand better and solve the instability problem and the difficulties often associated with it, such as noise and vibration, excessive bearing loads, loss of performance and catastrophic failure.

The Rotor Force Test Facility at the California Institute of Technology is a unique facility which was constructed under NASA contracts to examine the forces and rotordynamic coefficients which limit the design and performance of the high-speed turbopumps in the Space Shuttle Main Engine and other modern rocket engines. The central feature of the facility is the combination of a rotating dynamometer and an eccentric drive mechanism. The latter prescribes a circular whirling orbit to the tested impeller, while the rotating dynamometer measures the resulting steady and unsteady hydrodynamic forces and moments. This approach is essentially an experimental perturbation technique, which allows the correlation of the force measurements with the position of the impeller on its orbit as well as its speed. This information is sufficient to determine the hydrodynamic force matrix for the particular pump and flow conditions, and, therefore, the effect of these forces on the stability of the rotor.

The work discussed here concerns tests carried out for the Société Européenne de Propulsion (SEP), Division à Liquides et Espace, Vernon, France, on a half-scale model of inducer TPLH2. The tests were conducted in order to obtain measurements of the performance, radial forces and rotordynamic coefficients for this particular inducer design under cavitating and noncavitating flow conditions. Because the inducer has been designed to operate with very small impeller tip clearance ($\sim$ 0.01 mm), the presence of destabilizing hydrodynamic forces could result in relatively excessive shaft deflection with catastrophic consequences. Therefore, the determination of such forces is essential in the evaluation of the current design. To this end, the following measurements were taken:

1. Steady state noncavitating and cavitating performance data (head coefficient as a function of the flow coefficient, ϕ, and as a function of the cavitation number σ) at a speed of 3000 RPM and cavitation numbers as low as possible.

2. Radial forces and bending moments for a range of flow conditions (ϕ and σ).

3. Rotordynamic coefficients of radial forces and bending moments for an eccentricity of 0.254mm (0.010 in.) over a range of whirl/shaft speed ratios.

4. Spectral analysis of the radial forces and moments induced by the flow at zero whirl frequency.

In order to install and test the SEP inducer, a number of modifications were made to the RFTF. The facility as well as the modifications are decribed in section 2. Section 3 consists of a description of the test procedures and a discussion on the choice of actual test parameters. Data acquisition and reduction are discussed in section 4, while the results are presented in section 5. Finally, section 6 contains a summary and the conclusions drawn from the tests.

2

Test Facility

Force and moment measurements were performed at the Rotor Force Test Facility (RFTF) of the California Institute of Technology. The facility has been described and documented extensively by Ng (1976), Braisted (1979), Jery (1987) and Franz (1989). As a result, we present a brief description of the main components pertinent to this series of tests, and emphasize only the modifications required by the testing of the SEP inducer.

2.1 Description of the Test Facility

Figure 2.1 shows a view of the RFTF. Force and moment measurements are made by the rotating dynamometer, located between the eccentric drive mechanism and the impeller. Flow is clockwise and is monitored by the turbine flowmeter. The output of the turbine meter is used by the servo-controlled "silent" throttle valve to control the flow. The pressure or vacuum in the system is regulated by the amount of air in the submerged air bag. The heat exchanger utilizes chilled water and, therefore, can only be used to remove heat from the system water. In addition to dial gauges and a Heise gauge used for visual readings, upstream and downstream pressure transducers were used to monitor these pressures.

The impeller is driven by a 20hp d.c. "main" motor at maximum speed of 3500 RPM. The eccentric drive mechanism induces a whirling motion on the impeller.

All previous tests at the RFTF were performed with a whirl orbit radius of 1.27mm (0.050 in.) in order to ensure that the forces induced during testing were sufficiently large to provide meaningful results. This, however, was considered too high for the present tests, since it would result in mean impeller tip clearance of at least 1.3mm, while the tests required clearances of the order of 0.5mm. Consequently, for the SEP tests the radius of whirl orbit was set at 0.254mm (0.010 in.) in a compromise between small tip clearance and sufficiently large orbit radius. The maximum allowable speed of the whirl motor is 1800 RPM in either direction. The two motors are controlled using both velocity and phase feedback in order to monitor precisely the position of the impeller during data acquisition, as well as to maintain steady test conditions. This is described and documented in detail by Franz (1989).

2.2 SEP Impeller Description and Installation

The impeller tested was a half-scale model of an inducer pump manufactured by SEP, consisting of three parts: (i) inducer nose, (ii) central part consisting of 4 blades with sweep leading edge and (iii) rear-hub, corresponding to the hub of the second row of blades, not tested here. The complete assembly, including the second stage is shown in figure 2.2, while the model tested is shown in figures 2.3, 2.4 and 2.5.

In order to install and test the SEP model, the test section had to be adapted appropriately. A new inlet plexiglass duct was manufactured to accomodate the large diameter of the model. In addition, a new impeller housing was made with a nominal diameter of 5 in, and was fitted to the front plate of the test section as shown in figure 2.6. With the position of the inducer fixed, the inducer tip clearance was adjusted using 4 set-screws distributed evenly around the perimeter of the housing. Because of the eccentric position of the inducer inside the housing, during adjustment, the eccentric drive mechanism was locked to the shaft in such

a way that rotation of the main shaft caused synchronous whirling motion of the spindle. With a dial-indicator attached to the spindle, the housing was adjusted so as to be concentric with the indicator orbit. The final position of the housing was secured by means of a retaining ring bolted onto the front plate.

In an attempt to guide the flow past the inducer, a stator-deflector was manufactured and attached to the back plate of the test section as shown in figure 2.6. This arrangement created a cavity immediately behind the inducer and bounded by the stator and the impeller rear-hub. Fluid trapped in this cavity would rotate at mean fluid rotation speed proportional to half the shaft speed. Three pressure taps were also drilled on the impeller housing in order to measure the static pressure just downstream of the inducer. These were used in conjunction with three mercury manometers, and pressures were recorded during some of the tests. One of the pressure taps was located at the top of the housing while the other two were evenly distributed along the circumference.

2.3 Modifications Required by the Test Conditions

Some changes in the RFTF were required in order to

1. achieve and maintain the chosen test conditions

2. accomodate the SEP inducer's hydraulic performance.

Early tests indicated that in order to achieve the desired operating points, i.e., low cavitation number σ (~ 0.04) and high flow coefficient ϕ (~ 0.085), the water in the facility would have to be heated to at least 49°C (120°F) and the system be subjected to vacuum of the order of 20 in.Hg. Air leaks into the system, caused by the high vacuum applied, would result in unacceptable levels of air content in the water. To minimize the amount of air leakage, all drain and bleed valves were replaced with new ones. The O-ring used to seal the test section was also replaced. Moreover, since the back seal of the test section was originally designed to perform

under pressure, the cavity behind it, as well as the entire eccentric drive mechanism were flooded with high viscosity oil. This proved effective in blocking air passage through the back seal while at the same time providing lubrication for the eccentric drive mechanism.

The facility was also thermally insulated wherever possible using glass fibre insulation blankets. To heat the water to the desired temperature, three electrical heating tapes were wrapped around the outside of the loop pipes at the locations marked H1, H2 and H3 in figure 2.1. The maximum power delivered by the tapes was 2 kW. The temperature of the water was recorded regularly by visual inspection of the heat exchanger thermometer. Water temperature was regulated by adjusting both the flowrate of chilled water through the heat exchanger and the power delivery of the heating tapes. During the heating process, the inducer was run at maximum speed. After the addition of the auxiliary pump, the latter was used to speed up the process while the the inducer was held stationary.

With the inducer delivering a maximum of 235 GPM ($\phi \approx 0.072$) at 3000 RPM, and in view of the anticipated deterioration of performance under cavitation conditions, an additional "boost" pump was installed to increase the maximum flowrate possible. This was a Byron Jackson TXR centrifugal pump (donated by the company) with a 6in-diameter (152.4 mm) impeller, driven by a 10hp motor at 3600 RPM. The pump characteristics are shown in figure 2.7. In installing the pump, care was taken to minimize pressure losses at the inlet. Thus, the pump was positioned in such a way as to replace the 90° bend dowmstream of the test section, with its inlet and outlet axes coinsident with the axes of the loop pipes. This arrangement allowed for a straight inlet pipe.

With the boost pump installed and the inducer running at the nominal test speed of 3000 RPM, the maximum attainable flowrate increased to 310 GPM ($\phi \approx 0.094$). Nevertheless, this combination of the SEP inducer and the auxiliary pump in cascade proved inadequate for the cavitation tests at the higher flow rates due to the

fact that the head rise across the inducer at the high flow rates was inadequate to produce sufficient NPSH for the boost pump. For example, the measured head coefficient at design flowrate ($\phi = 0.085$) for the inducer was $\psi \approx 0.1$ (figure 5.1). Thus, with the upstream pressure low and $\psi \approx 0$ during cavitation tests, the estimated NPSH for the boost pump was 4-5 ft of water.

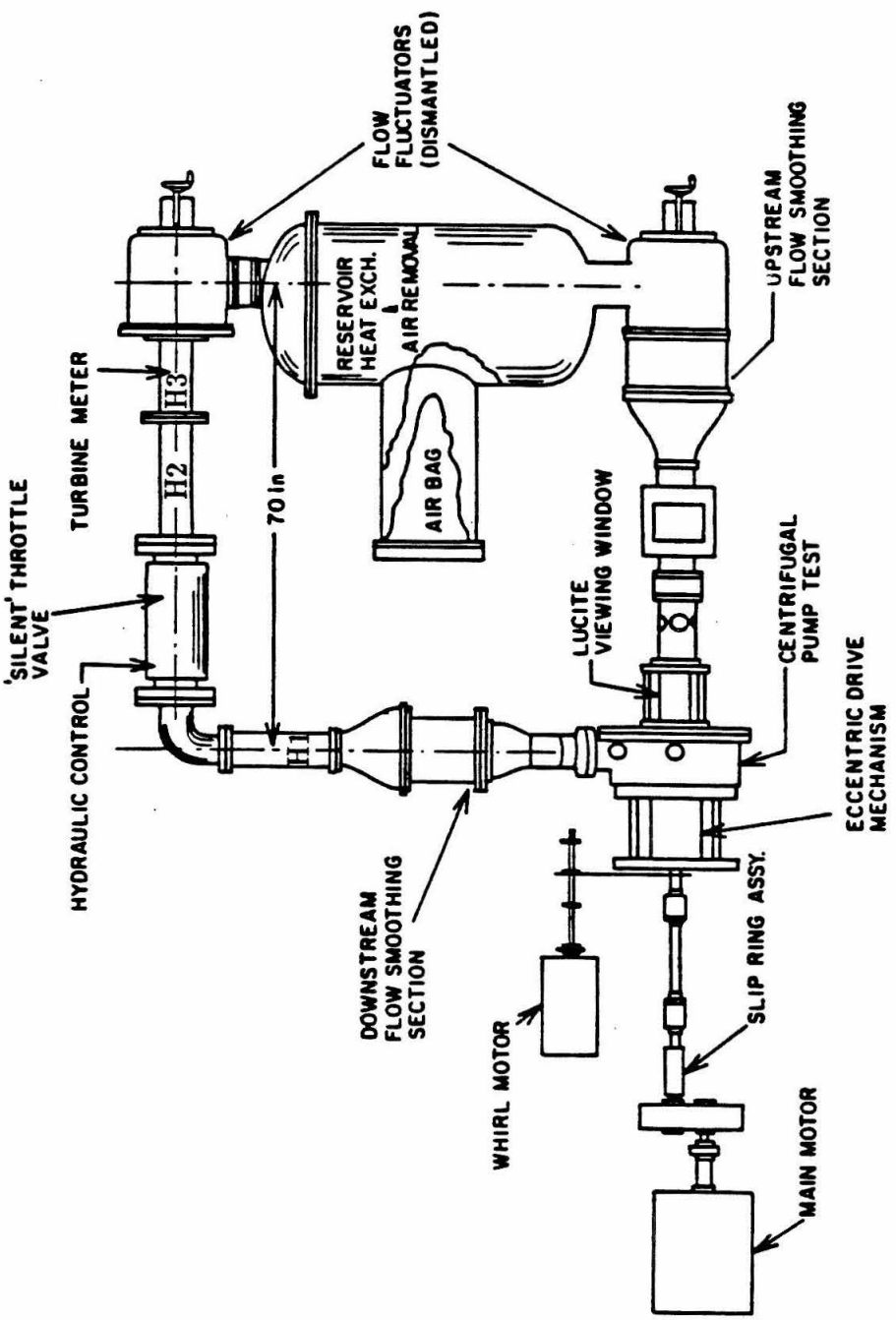

Figure 2.1: Top view of the Rotor Force Test Facility.

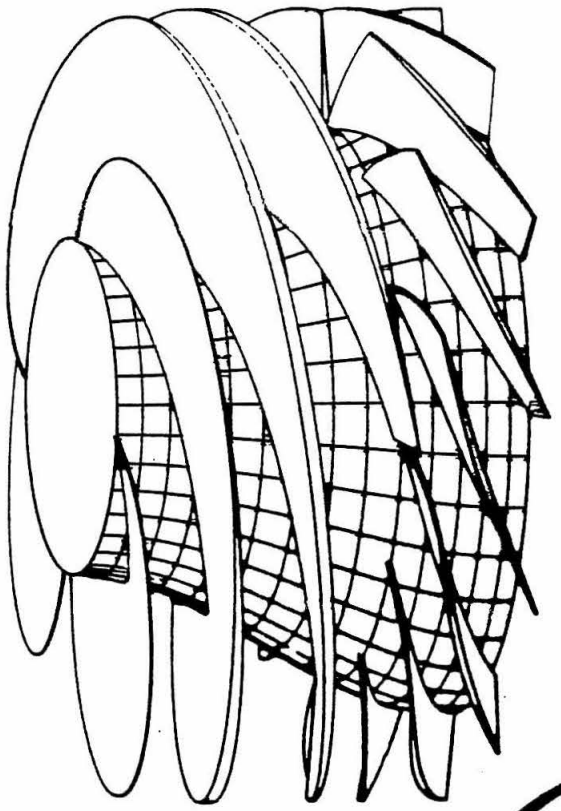

	1st row	2nd row
Number of blades	6	12
Tip radius (mm)	91	91
Tip solidity	1.8	1.4
Inlet blade angle (°) (mean tip-value)	6.5	11.9

Hub/tip ratio . inlet .625
outlet . 78

(a)

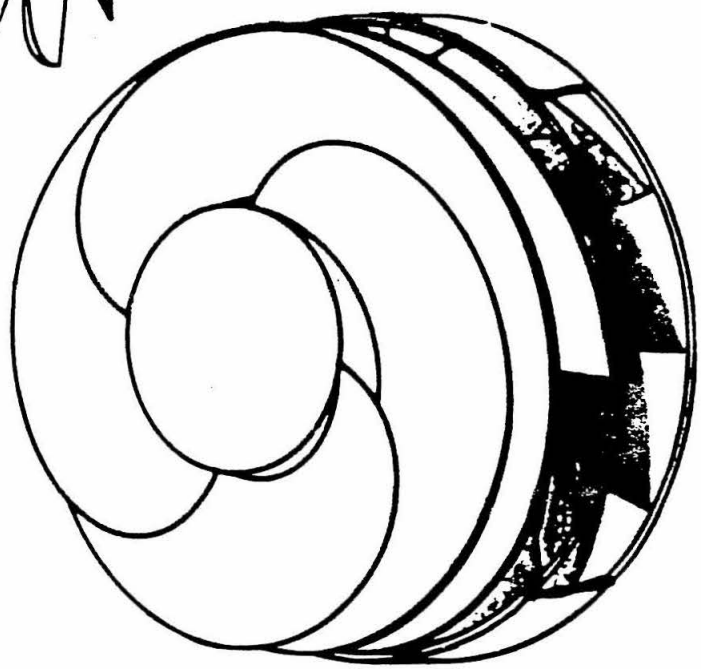

(b)

Figure 2.2: (a) SEP inducer without shroud. (b) SEP inducer with second stage shrouded.

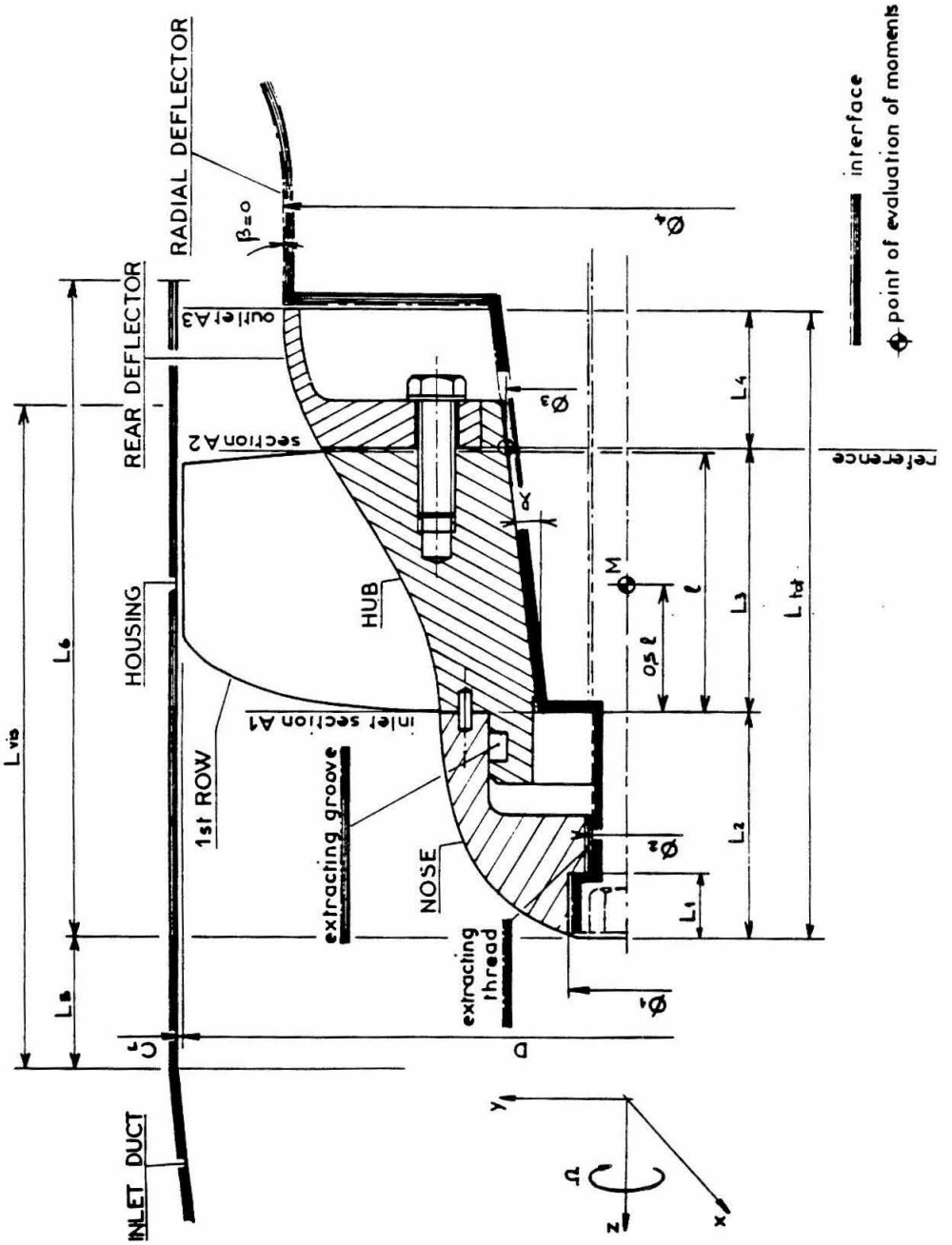

Figure 2.3: Model assembly with rear-hub.

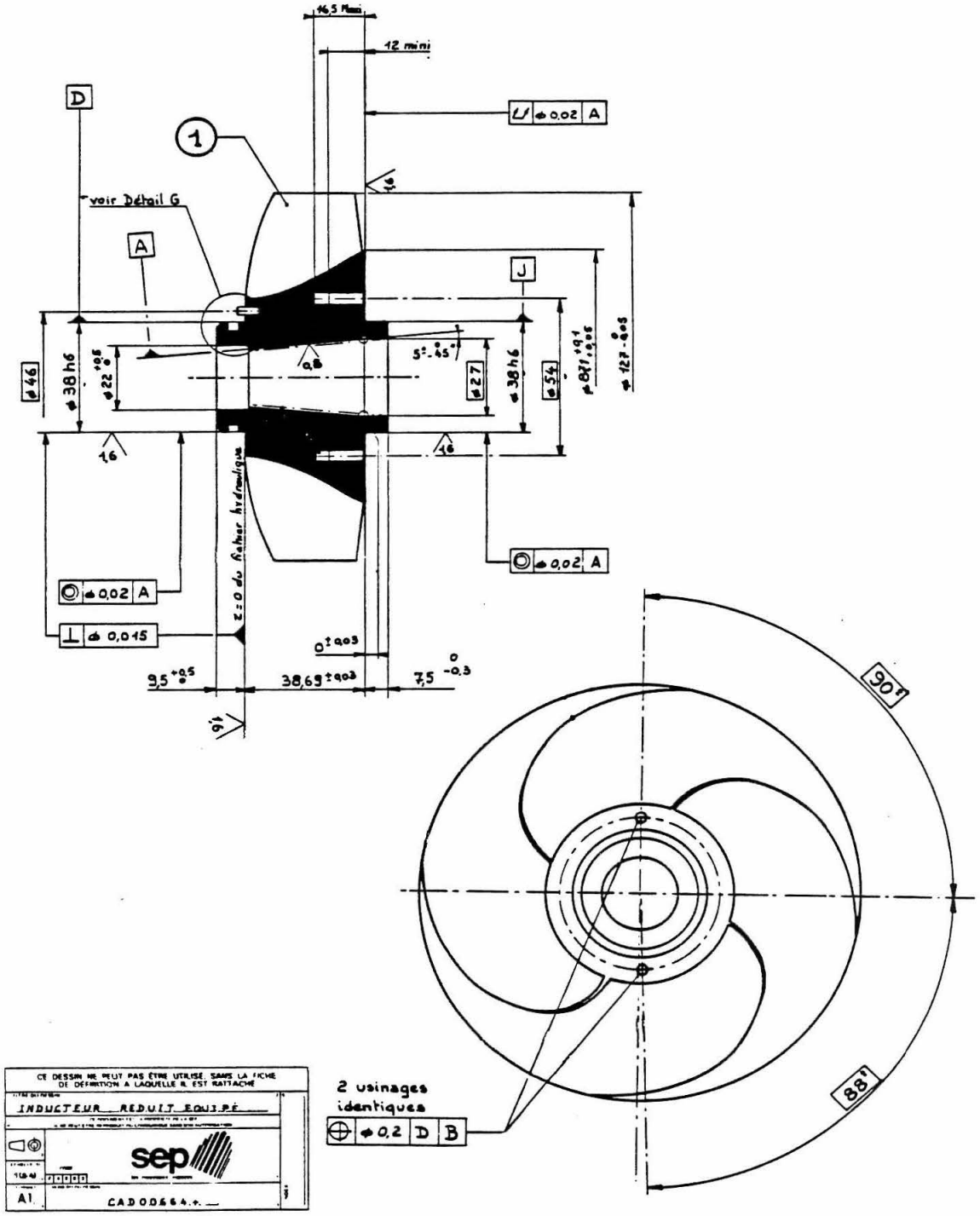

Figure 2.4: Schematic of half-scale inducer model.

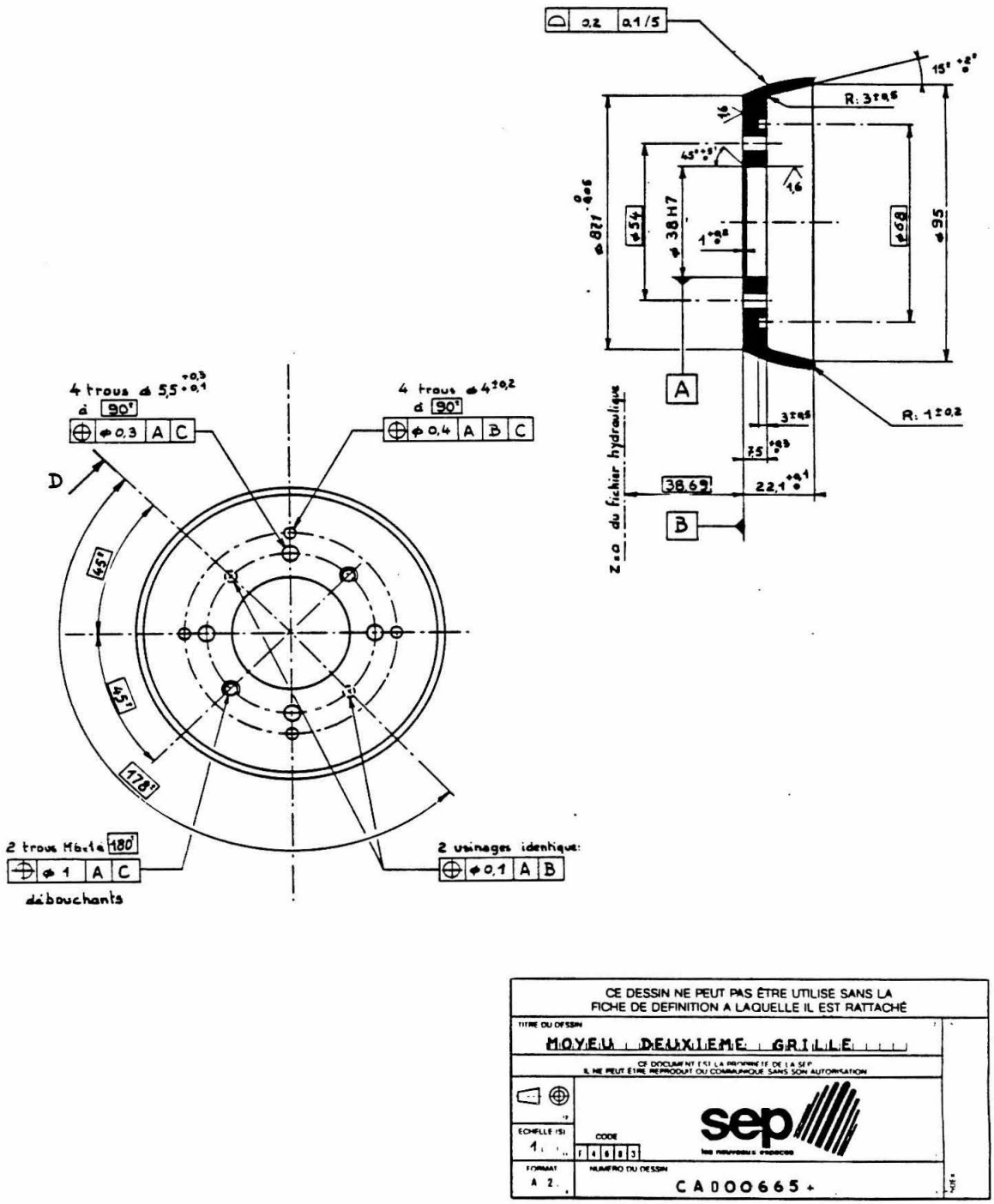

Figure 2.5: Schematic of inducer rear-hub.

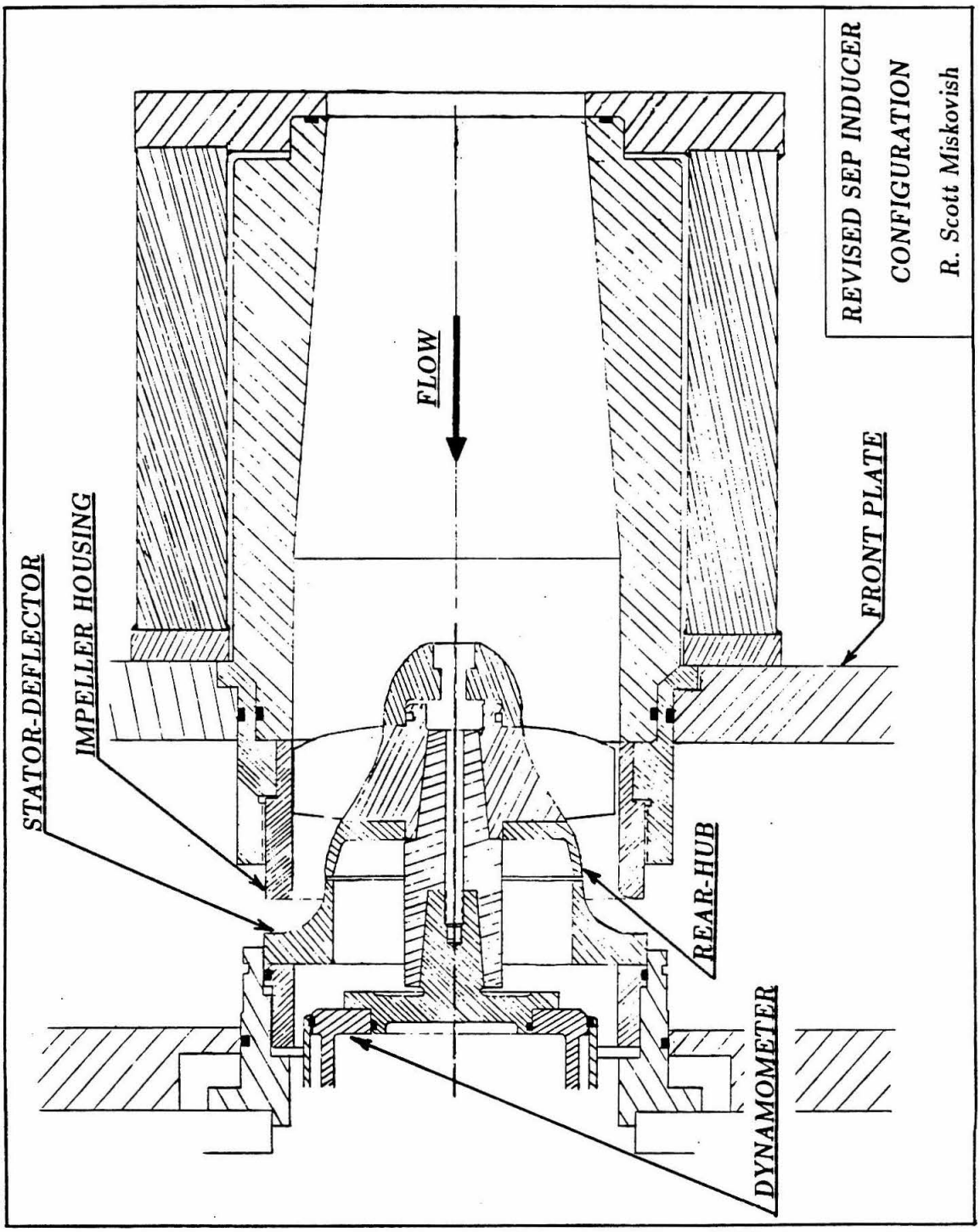

Figure 2.6: Schematic assembly drawing of the test section with inducer model and stator-deflector installed.

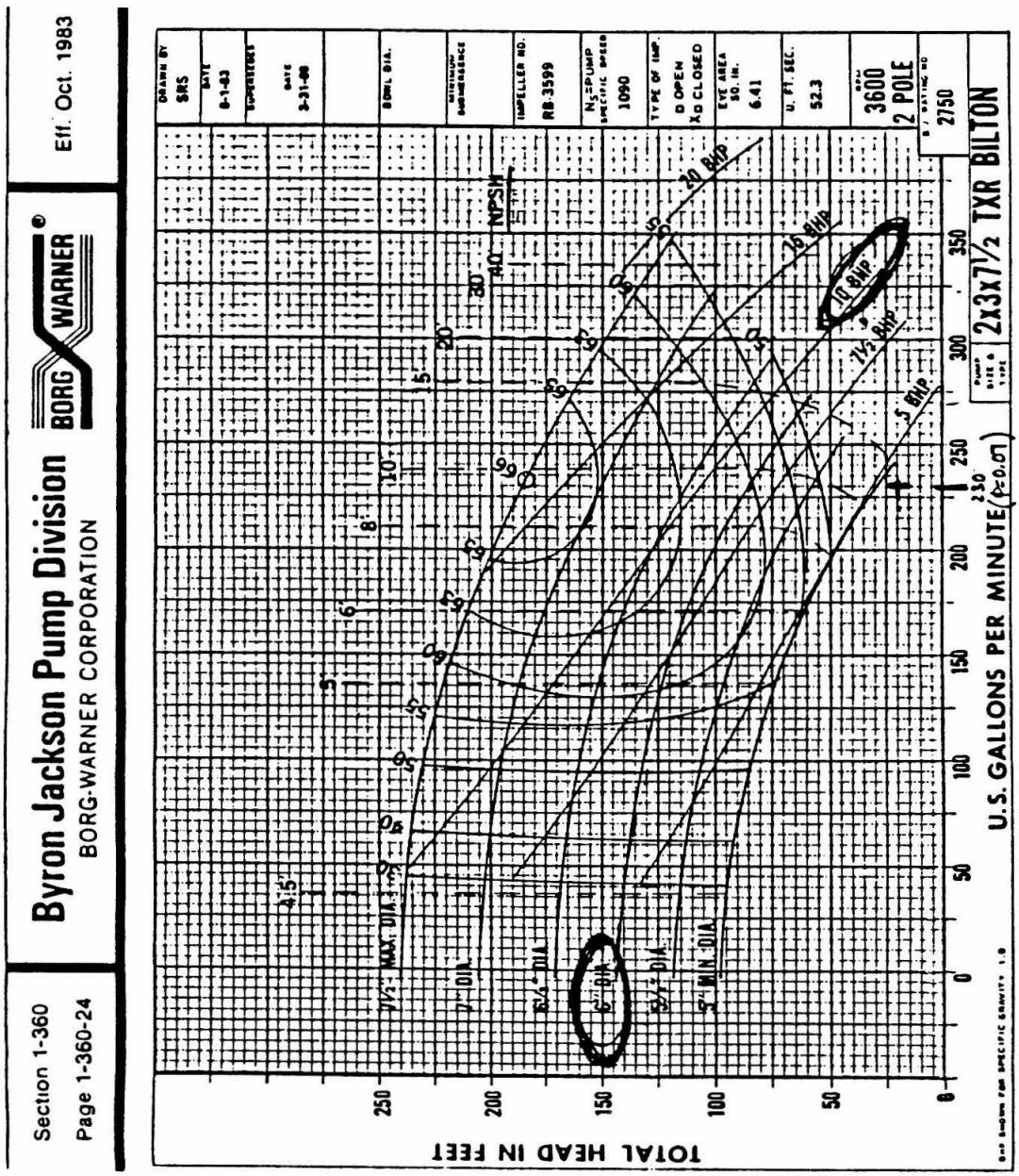

Figure 2.7: Performance characteristics of Byron-Jackson TXR auxiliary pump.

3

Test Conditions

3.1 Choice of Parameters

A number of trial runs were performed in order to determine the final test conditions, operating parameters, procedures and modifications to be used during the testing. Carefull consideration of these early results lead to the parameters and conditions described below.

It is typical of inducers to cavitate only under severe conditions. This, together with the unusually high choice of the design coefficient ($\phi = 0.085$) suggested that the pump speed would have to be as high as possible. Given that the whirl motor had a maximum speed of 1800 RPM, the final choice of speed was a compromise between high main motor speed and the range of whirl ratios over which tests would be carried out. The final choice of 3000 RPM allowed whirl ratios up to $\frac{\omega}{\Omega} = \pm 0.6$ while at the same time being close to the top speed of the main motor. Nevertheless, this was not sufficient to induce cavitation at room temperature, and it was necessary to heat up the water during the cavitation tests to 49°C – 52°C (120°F – 126°F). At this temperature, the vapour pressure of water is 11 kPa (up from 2.5 kPa at room temperature). Moreover, by subjecting the system to vacuum (~560 mm Hg upstream), the cavitation number σ was reduced to levels favorable for the tests. Noncavitating tests were performed at room temperature

(20°C – 26°C) and with the upstream pressure set at 62-70 kPa (9-10 psi) and 55 kPa (8 psi) for phases 1 and 2 respectively.

Phase 1 and phase 2 refer to series of tests conducted at two different impeller tip clearances. Initially set at 0.1mm, the minimum clearance was subsequently increased to 0.19±0.01mm (0.0075±0.0005in.) in order to avoid any possible contact between the impeller and its housing. Thus, during phase 1, the measured maximum clearance was 0.71±0.01mm (0.028±0.0005 in.) and the mean clearance was $Cr_1 = 0.45 \pm 0.02$mm (0.0175±0.001 in.). Impeller housing diameter was 127.89mm (5.035 in.). During phase 2, the mean clearance was increased to $Cr_2 = 0.71 \pm 0.02$mm (0.028±0.001 in.).

During the noncavitating tests, the water was not deaerated and, therefore, presumed saturated with air. Cavitation tests however, were preceeded by the deaeration procedure which is described in detail by Ng (1983). The only deviation from that method involved using the system loop as part of the water reservoir. It was found that air removal at elevated temperatures was also more efficient. Air content of 3.5 ppm or less, as measured by the Van Slyke apparatus, was deemed adequate. Water quality was also visually inspected during the tests.

The performance curves obtained for the inducer under the conditions described above are shown in figures 5.2 and 5.3. The test matrices were decided on the basis of these curves and are presented in tables 3.1 and 3.2. Two flow coefficients, 0.07 and 0.08 are below the design point and one flow coefficient, 0.090, is above. design. As was mentioned and explained in section 2.2, some of the tests could not be performed. As a result, for the two higher flow coefficients, data is available for noncavitating flow conditions only. It was suggested that tests be performed with $\sigma = 0.13$ and $\sigma = 0.07$ in order to compensate for this. However, the performance curves obtained and the fact that the only pump cavitating under these conditions was the boost pump, indicated that such tests would provide little information concerning the inducer itself.

3.2 Test procedures

The experimental procedure during noncavitating tests was as follows: for fixed ϕ and whirl speed ratio $I/J = \omega/\Omega$, the only other control variable was the upstream pressure, regulated automatically by means of the pressure regulator. Water temperature was maintained within bounds using the heat exchanger. Data were recorded once steady state conditions were reached. Actual data acquisition times varied from 20.4 to 51.2 sec depending on the whirl speed. All data concerning the hydraulic characteristics of the inducer were taken with the impeller whirling at 300 RPM ($\frac{\omega}{\Omega} = 0.1$) in the positive direction. Due to the eccentric position of the impeller, four non-whirling runs were taken, each with the impeller positioned at 0°, 90°, 180° and 270° around the whirl orbit. Results were averaged over the four positions.

Cavitation tests were preceeded by the lengthy deaeration process. Typically, the water would be deaerated for a minimum of 24 hours and often up to 72 hours in order to achieve acceptable air content. The heating process involving the tapes and inducer only was also lengthy. After the addition of the auxiliary pump, heating time was reduced to 2 hours. The actual experimental procedure was similar to that for noncavitating runs except that the upstream pressure (vacuum) was controlled manually. With the pressure regulator disengaged, the amount of vacuum applied was controlled through the vacuum and air bleed valves. Due to the high vacuum demanded for most of the tests, the vacuum valve would be opened fully, while the bleed valve would be adjusted so as to reach and maintain the proper cavitation number. Having the vacuum valve fully open, resulted in flow conditions which were very sensitive to variations in the bleed valve position. Between tests, the system was pressurized in order to minimize the amount of air leakage into it, as well as to bleed any air which collected at the top of the heat exchanger.

ϕ (GPM)	Cavitation number, σ					
	NC σ, P_{up}	0.070	0.050	0.040	0.035	0.026
0.070 (230)	⊗ 0.77, 65kPa		⊗	⊗	⊗	⊗
0.080 (263)	⊗ 0.85, 69kPa		⊗	⊗		
0.085 (279)	⊗ 0.78, 69kPa					
0.090 (295)	⊗ 0.83, 69kPa					

Table 3.1: Test Matrix, Cr_1.

ϕ (GPM)	Cavitation number, σ					
	NC σ, P_{up}	0.070	0.050	0.040	0.035	0.026
0.070 (230)	⊗ 0.77, 55kPa		⊗	⊗		
0.080 (263)	⊗ 0.77, 55kPa	⊗				
0.085 (279)	⊗ 0.76, 55kPa					
0.090 (295)	⊗ 0.76, 55kPa					

Table 3.2: Test Matrix, Cr_2.

4

Data Acquisition and Reduction

4.1 Data Acquisition

The data acquisition system was essentially the same used by Jery (1987) and Franz (1989). As a result we only present here the information pertinent to the SEP inducer tests. Two data acquisition systems were used utilizing two Zenith Z-120 personal computers. Some additional data were recorded manually.

The data taker scans 16 channels in a sequence controlled by a clock signal whose frequency is coherently derived from that of the reference wave signal. In this series of tests, the reference signal frequency used was equal to Ω/J[1]. For the no-whirl experiments, J was initially set to 2. This was later changed to 5. Channels 1-6 and 9-14 were used to receive signals from bridges 1,3,4,6,8 and 9 of the rotating dynamometer. Channels 7,8,15 and 16 were used to record upstream and downstream pressure transducer signals, flowrate and torque respectively. During the reference cycle, 64 samples from each data channel were recorded (sampling frequency 640Hz-3200Hz). Each "run" consisted of 256 reference cycles. For each channel, samples were averaged over the 256 cycles. Thus, the end result of each experiment was in the form of 1024 (64 data points $\times$ 16 channels) digital values stored in the internal memory of the data taker. For purposes of computing the

[1]Note that $\frac{\omega}{\Omega} = \frac{I}{J}, I, J$ integers.

spectral densities of forces and moments at zero whirl speed, the instantaneous data of 128 cycles were also recorded and stored in floppy disks during phase 2.

The second data acquisition system displayed on screen instantaneous and time-averaged upstream and downstream pressure transducer readings, cavitation number and head coefficient for the particular flow conditions of the test. The final averaged values for each run were recorded.

In addition to the above, pressure gauge readings and manometer readings, as well as the water temperature were recorded for each run.

4.2 Data Reduction

Data reduction techniques were identical to those described by Jery (1986). Here we present a brief overview of the form in which data are presented, and a more extensive discussion on spectral density computations.

4.2.1 Forces and Bending Moments

A diagram showing reference frames and the sign convention is shown in figure 4.1. Unless otherwise stated, all forces are normalized by $\frac{1}{2}\rho C_{m1}^2 A_1$ and all moments by $\frac{1}{2}\rho C_{m1}^2 A_1 R$.

The raw output from the 6 Wheatstone bridge signals are first processed and combined to yield the six components of forces and moments in the rotating frame of the balance. These are denoted by F_1, F_2, F_3, M_1, M_2 and M_3. Moments were computed about the point shown in figure 2.3.

At a given pump operating condition and a given whirl ratio, the instantaneous normalized radial force components (F_x, F_y in the laboratory frame) are decomposed into

$$\begin{bmatrix} F_x \\ F_y \end{bmatrix} = \begin{bmatrix} F_{0x} \\ F_{0y} \end{bmatrix} + \frac{\varepsilon}{R} \begin{bmatrix} A_{xx} & A_{xy} \\ A_{yx} & A_{yy} \end{bmatrix} \begin{bmatrix} \cos \omega t \\ \sin \omega t \end{bmatrix} \tag{4.1}$$

where F_{0x}, F_{0y} are the steady forces and $[A]$ is the rotordynamic force matrix. It is found experimentally that for circular whirl orbit the matrices are very close to the form in which $A_{xx} = A_{yy}$ and $A_{xy} = -A_{yx}$. It follows that if F_n and F_t are mean values (over an integer number of whirl periods) of the forces normal (positive outward) and tangential (positive in the direction of shaft rotation) to the whirl orbit, then[2]

$$F_n = \frac{1}{2}(A_{xx} + A_{yy}) = A_{xx} = A_{yy} \tag{4.2}$$

$$F_t = \frac{1}{2}(A_{yx} - A_{xy}) = -A_{xy} = A_{yx} \tag{4.3}$$

Hence, the rotordynamic force matrix $[A]$ is fully described by presenting the values of F_n and F_t as functions of the operating conditions and the whirl speed ratio I/J.

It should be noted that both the steady forces and the matrix $[A]$ are obtained from the experimental data by appropriate but different integration over many cycles of rotation and whirl. This integration process eliminates any uncorrelated fluctuations in the data.

Furthermore, the actual data which is processed, is the result of two experiments. An experiment in air is first run to determine the tare forces due to slight imbalance, etc. These tare forces are then subtracted from the measurements in water to extract the purely hydrodynamic forces on the impeller.

An analogous procedure was used to determine the bending moments M_{0x} and M_{0y} and the rotordynamic moment matrix $[B]$, which are related to the instantaneous bending moments M_x and M_y by

$$\begin{bmatrix} M_x \\ M_y \end{bmatrix} = \begin{bmatrix} M_{0x} \\ M_{0y} \end{bmatrix} + \frac{\varepsilon}{R} \begin{bmatrix} B_{xx} & B_{xy} \\ B_{yx} & B_{yy} \end{bmatrix} \begin{bmatrix} \cos\omega t \\ \sin\omega t \end{bmatrix} \tag{4.4}$$

The mean moments about the normal and tangential directions to the whirl orbit,

[2]This is the standard expression. All computations in this report were made using $F_n = \frac{1}{2}\frac{\varepsilon}{R}(A_{xx} + A_{yy})$ and $F_t = \frac{1}{2}\frac{\varepsilon}{R}(A_{yx} - A_{xy})$.

M_n and M_t are given by

$$M_n = \frac{1}{2}(B_{xx} + B_{yy}) \tag{4.5}$$

$$M_t = \frac{1}{2}(B_{yx} - B_{xy}) \tag{4.6}$$

The stability of rotor motion depends solely on the characteristics of the matrix $[A]$. An alternative way of expressing the forces $F_x(t)$ and $F_y(t)$, which is often more suitable for stability analysis is

$$\begin{bmatrix} F_x \\ F_y \end{bmatrix} = \begin{bmatrix} F_{0x} \\ F_{0y} \end{bmatrix} - [K] \begin{bmatrix} x \\ y \end{bmatrix} - [C] \begin{bmatrix} \dot{x} \\ \dot{y} \end{bmatrix} - [M] \begin{bmatrix} \ddot{x} \\ \ddot{y} \end{bmatrix} + \text{higher order terms} \tag{4.7}$$

The matrices $[K]$, $[C]$ and $[M]$ are called stiffness, damping and inertia matrices respectively. Clearly, there is no compelling reason why the forces should follow this simple model. Note that $[A]$ is a function of ω/Ω as well as the flow coefficient. Expanding $[A]$ in powers of ω/Ω we obtain

$$A_{xx} = M_{xx}\left(\frac{\omega}{\Omega}\right)^2 - C_{xy}\left(\frac{\omega}{\Omega}\right) - K_{xx} \tag{4.8}$$

$$A_{xy} = M_{xy}\left(\frac{\omega}{\Omega}\right)^2 + C_{xx}\left(\frac{\omega}{\Omega}\right) - K_{xy} \tag{4.9}$$

$$A_{yx} = M_{yx}\left(\frac{\omega}{\Omega}\right)^2 - C_{yy}\left(\frac{\omega}{\Omega}\right) - K_{yx} \tag{4.10}$$

$$A_{xx} = M_{yy}\left(\frac{\omega}{\Omega}\right)^2 + C_{yx}\left(\frac{\omega}{\Omega}\right) - K_{yy} \tag{4.11}$$

The validity of expression (4.7) is not universal, and is justified only after experimental verification.

4.2.2 Spectral Densities

Let $F_1(n\Delta t)$, $F_2(n\Delta t), n = 1, \ldots, N$ be two sequences of sampled data, Δt being the sampling interval. Let $T = N\Delta t$ be the total time for which records are available. Let $\tilde{F}_{1k} = \tilde{F}_1(k\Delta f)$, $\tilde{F}_{2k} = \tilde{F}_2(k\Delta f)$ be the FFT's[3] of the two records, where

[3] N must be a power of 2.

$\Delta f = 1/T$. Then, following Bendat and Piersol (1971), the spectral density of F_1 is defined by

$$SF_{11}^k = SF_1(f_k) = \frac{2\Delta t}{N}\left|\tilde{F}_{1k}\right|^2, \quad k = 0, \ldots, \frac{N}{2} \tag{4.12}$$

where $f_k = k\Delta f$. The cross spectral desnsity of the two records is defined by

$$SF_{12}^k = SF_{12}(f_k) = \frac{2\Delta t}{N}\left|\tilde{F}_{1k}^* \tilde{F}_{2k}\right|^2, \quad k = 0, \ldots, \frac{N}{2} \tag{4.13}$$

where $\tilde{F}_{1k}^*$ is the complex conjugate of $\tilde{F}_{1k}$. All density computations were based on the above definitions. However, some signal processing was needed in order to arrive at the final results from the instantaneous data.

Let $w_j(t_j)$, $j = 1, \ldots, 6$ be the six bridge signals. Since the data taker samples the channels sequentially, these signals are shifted in time by an amount $s = (1024 f_r)^{-1}$, $f_r = \Omega/2\pi J$ being the reference cycle frequency. Thus, $t_j = t - (j-1)s$, and $w_j(t_j) = w_j(t-(j-1)s)$. Let $W_j(f)$ be the Fourier transform of the jth signal and $\hat{W}_j(f) = \mathcal{F}\{w_j(t)\}$. Then

$$\begin{aligned} W_j(f) &= \mathcal{F}\{w_j(t-(j-1)s\} \\ &= \hat{W}_j(f) e^{-2\pi f(j-1)si} \\ &= \hat{W}_j(f)\left[\cos\left(2\pi f(j-1)s\right) - i\sin\left(2\pi f(j-1)s\right)\right] \end{aligned} \tag{4.14}$$

Now, let $D = [d_{jk}]$ be the calibration matrix. Then, the forces and moments in the rotating frame are given by

$$\tilde{F}_1(f) = \sum_{j=1}^{6} d_{1j}\hat{W}_j(f) e^{-2\pi f(j-1)si} \tag{4.15}$$

$$\tilde{F}_2(f) = \sum_{j=1}^{6} d_{2j}\hat{W}_j(f) e^{-2\pi f(j-1)si} \tag{4.16}$$

$$\tilde{M}_1(f) = \sum_{j=1}^{6} d_{4j}\hat{W}_j(f) e^{-2\pi f(j-1)si} \tag{4.17}$$

$$\tilde{M}_2(f) = \sum_{j=1}^{6} d_{5j}\hat{W}_j(f) e^{-2\pi f(j-1)si} \tag{4.18}$$

Since the forces in the laboratory frame are given by

$$\begin{aligned} F_x &= F_1(t)\cos(2\pi f_0) - F_2(t)\sin(2\pi f_0) \\ F_y &= F_1(t)\sin(2\pi f_0) + F_2(t)\cos(2\pi f_0) \end{aligned}$$

then

$$\tilde{F}_x(f) = \frac{1}{2}\left[\tilde{F}_1(f-f_0) + \tilde{F}_1(f+f_0)\right] - \frac{1}{2i}\left[\tilde{F}_2(f-f_0) - \tilde{F}_2(f+f_0)\right] \quad (4.19)$$

$$\tilde{F}_y(f) = \frac{1}{2i}\left[\tilde{F}_1(f-f_0) - \tilde{F}_1(f+f_0)\right] + \frac{1}{2}\left[\tilde{F}_2(f-f_0) + \tilde{F}_2(f+f_0)\right] \quad (4.20)$$

The final result for the forces may be obtained by substitution from (4.15)-(4.18) into (4.19) and (4.20). Similar expressions hold for the moments in the laboratory frame.

The effect of (4.19) and (4.20) is not only to shift the spectra of the force components by the shaft frequency f_0, but also to combine these in one expression for the force components in the laboratory frame. The net result of this "mixing" of the signals is clearly a wider and more uniformly distributed spectrum. Such loss of information is clearly to be avoided unless there is a need to correlate the forces to other signals measured in the laboratory frame. In most cases, however, the spectral densities of the forces in the rotating frame provide more information, and are, therefore, more desirable.

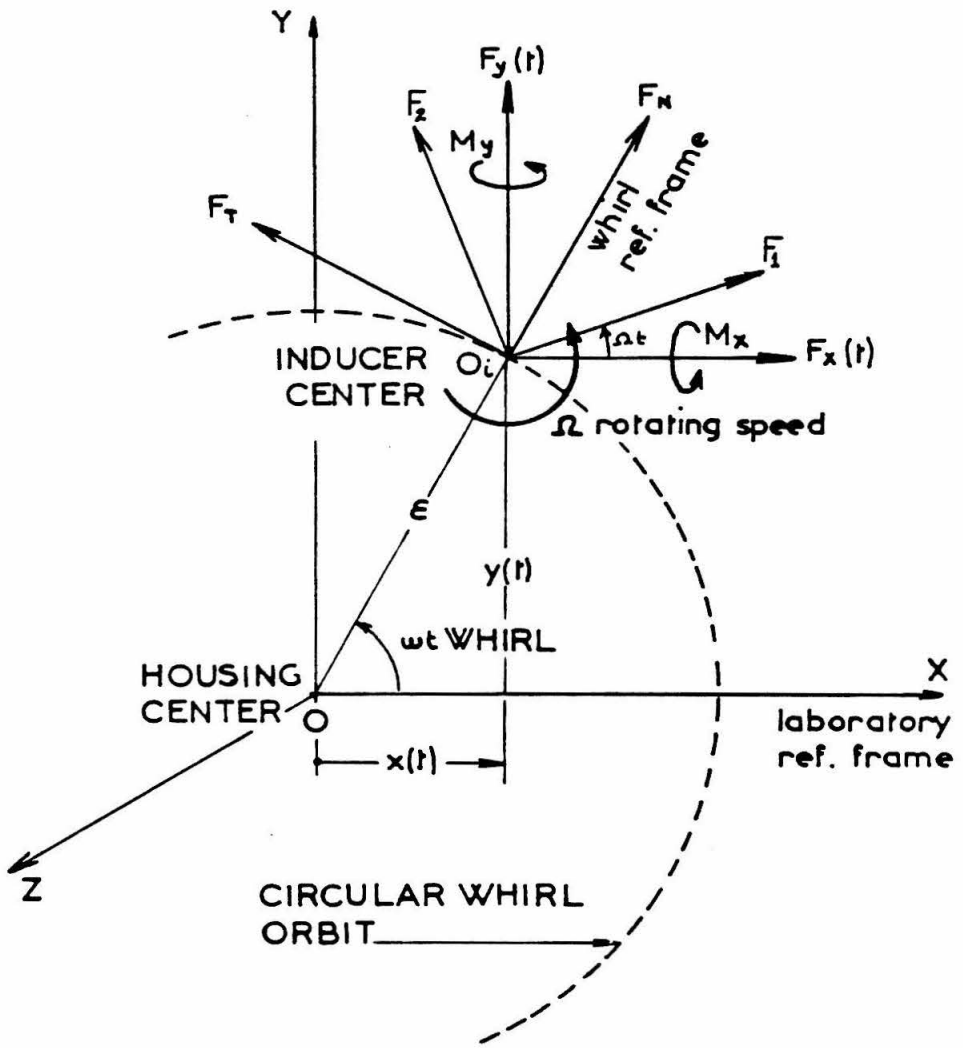

Figure 4.1: Schematic showing laboratory and rotating reference frames as well as lateral forces.

5

Results

Results are grouped in three categories: (a) hydraulic performance characteristics, (b) hydrodynamic forces and moments and (c) spectral densities of forces and moments. Emphasis is placed on the hydrodynamic force matrix $[A]$ (indirectly, through F_n and F_t), and the effects of flow coefficient, impeller tip clearance and cavitation number on it.

The reliability of force measurements taken at the RFTF has been repeatedly demonstrated by earlier investigators. It is further strengthened here by the comparison of measurements taken prior to and after the addition of the auxiliary pump in figure 5.5 in which the normal and tangential forces and moments on the inducer for noncavitating flow at design ($\phi = 0.085$) are shown.

5.1 Hydraulic Performance Curves

Plots of the head coefficient, ψ, versus flow coefficient, ϕ, for the two different impeller tip clearances are shown in fig 5.1. The effect of the larger clearance is small but consistent and predictable; as expected, the increase in clearance degrades the performance. The curve obtained by SEP for the inducer is also shown in the same figure. The difference in the head coefficient measured by SEP and Caltech is attributed to the different ways in which the discharge is treated in the actual pump and in the RFTF. As expected, the use of the stator-deflector causes losses which

are not present in the prototype and which tend to increase somewhat with flow rate. The main conclusion of the $\psi - \phi$ plots is that the design point of $\phi = 0.085$ is unusually high ($\psi = 0.14$), especially since even a small reduction in the design flow rate would result in significant increase in the head rise across the inducer.

The cavitation performance curves, ψ vs. σ, are shown in figures 5.2 and 5.3 for Cr_1 and Cr_2 respectively. Performance breakdown starts anywhere between $\sigma = 0.04$ and $\sigma = 0.08$ for low flow rates. The curves for higher flow rates are incomplete for the reasons discussed in section 3.1. The effect of the clearance, at least for the low flow rates, is to raise the minimum cavitation number at which acceptable performance is observed, as shown in figure 5.4. Note that since the inducer has been designed to operate with very tight impeller tip clearance, the closer this is to the design value, the better the expected performance. Thus, the performance curves obtained strengthen the case for small clearance, even though there might be other drawbacks associated with it.

5.2 Hydrodynamic Forces and Moments

Before discussing the effects of the various parameters on the unsteady forces and moments, a number of facts and observations concerning the representation (4.1) and (4.2) are needed.

The "steady" forces F_{0x} and F_{0y} are temporal and spatial averages of the lateral forces sensed by the dynamometer. As a result, they are independent of the whirl speed ratio. This is demonstrated in figure 5.6 for the cases $\phi = 0.070$, $\sigma = 0.04$ and $\phi = 0.085$, noncavitating (Cr_2). Moreover, their magnitude is small compared to the unsteady forces, because the steady forces only occur due to slight asymmetries in positioning and geometry and in the volute far downstream of the inducer. In the idealized case where the impeller is perfectly symmetric, centered, and is fitted to a matching volute and flow conditions, steady forces should be zero. Steady forces, averaged over all whirl ratios for each flow coefficient are plotted versus ϕ

ϕ	0.070	0.080	0.085	0.090
Cr_1	0.314×10^{-3}	0.0318×10^{-3}	0.0432×10^{-3}	0.0672×10^{-3}
Cr_2	0.255×10^{-3}	0.0206×10^{-3}	0.0342×10^{-3}	0.0307×10^{-3}

Table 5.1: Magnitude of the steady force in noncavitating flow.

in fig. 5.7. The effect of impeller tip clearance is also shown in these plots. The magnitudes of the forces for noncavitating flows are listed in table 5.1. The effect of larger clearance is to reduce slightly the magnitude of the steady force as well as the moment. Cavitation on the other hand has a more drastic effect as seen in figure 5.8. Note that the changes in the steady forces due to cavitation are much larger than that due to the change in clearance.

From the point of view of rotordynamics, it is the unsteady tangential force F_t which is of importance. A tangential force in the direction of whirl motion serves as to drive the motion, and is, therefore, destabilizing. Thus, the sign of F_t is essential in determining the behavior of the rotor under the action of the hydrodynamic forces. Note that the assumption that $A_{xx} = A_{yy}$, $A_{xy} = -A_{yx}$ is validated by the data. Moreover, this property of the coefficient matrix implies that it is independent of the particular orientation of the axes (X, Y). Plots of these coefficients for each flow condition are given in the appendix.

Moment analysis, however, is not as simple. Associated with the steady forces F_{0x}, F_{0y} are steady bending moments M_{0x}, M_{0y} which in principle help to define the axial position of the line of action of the steady forces. The measurements made by the rotating dynamometer give the *net* moment acting on the rotor, and, therefore, include contributions from the forces F_1, F_2 and the thrust F_3 in addition to any purely hydrodynamic moments which may be acting on the impeller. Thus, in order to identify the latter and estimate the axial position of the line of action of the steady forces, additional information, such as the location of the center of

pressure on the impeller, is needed. Data for M_{0x}, M_{0y} are presented in figures 5.9–5.10.

5.2.1 Rotordynamic forces: influence of the flow coefficient

Since the flow around the impeller depends heavily on the flow coefficient, it is natural to expect a significant dependence of all forces on ϕ. The data obtained on rotordynamic forces for noncavitating flows are shown in figures 5.11 and 5.12.

A pronounced feature in all plots is the presence of a sharp peak between $\frac{\omega}{\Omega} = +0.5$ and $\frac{\omega}{\Omega} = +0.6$. In this region, there are large variations in the force magnitude and abrupt changes in their sign. Specifically, the tangential force F_t becomes positive and relatively large, and, therefore, has a destabilizing effect on the rotor motion. Such behavior has not been observed among the limited number of available data on other impellers. Note, however, that the fact that this phenomenon occurs at a whirl speed near $\frac{1}{2}\Omega$ suggests that perhaps fluid motion in the cavity behind the inducer plays a role in this. Recall that the mean fluid rotation speed in the cavity is about $\frac{1}{2}\Omega$. Therefore, a sympathetic interaction between fluid motion and whirling motion could result in the resonance peak observed and the associated rotor instability. Fortunately, this "resonance" is so narrowly confined to a frequency ratio band of about 0.02 that it does not affect the bulk of the rest of the data outside of this narrow band of frequencies.

The effect of the flow coefficient on the forces is significant in the region between $\frac{\omega}{\Omega} = 0$ and $\frac{\omega}{\Omega} = 0.3$. Here the tangential force is positive indicating destabilizing fluid forces. As the flow rate increases, the region of destabilization diminishes. For example, for $\phi = 0.090$, F_t is stabilizing above a whirl ratio of 0.15 (and below 0.5) while for $\phi = 0.070$ it is stabilizing above $\frac{\omega}{\Omega} = 0.3$. Note that for the low flow rate, the F_t curve is complicated and changes sign more than once. Similar behavior has been observed by Jery (1986) on centrifugal pumps. For negative whirl ratios, the effect of the higher ϕ is simply to lower the magnitude of the tangential force. The

force is always positive and, therefore, stabilizing for all $\frac{w}{\Omega} < 0$.

Data for cavitating runs is available only for the low flow rates. Figures 5.13 and 5.14 show the effect of ϕ on the forces for cavitation numbers 0.05 and 0.04 respectively. In both cases we note that the influence of the flow coefficient is more drastic than in noncavitating flows. It also has the opposite effect that it has on noncavitating flows, at least as judged from the limited number of cases: *generally, the region of destabilization is larger as ϕ increases.* For moderate cavitation ($\sigma = 0.05$) and $\phi = 0.070$, F_t is destabilizing only between 0.2 and 0.35, while for $\phi = 0.080$ *all* positive whirl ratios are unstable. For $\sigma = 0.04$ the effect of higher ϕ is even more pronounced, rendering *all whirling motions destabilizing in the case of $\phi = 0.08$.* The fact that for a given cavitation number the higher flow rate influences the forces more is expected, in the sense that such flows are also closer to the performance breakdown point.

5.2.2 Rotordynamic forces: influence of the clearance

The influence of impeller tip clearance on the forces can be seen in figures 5.15 through 5.20. Again we distinguish between noncavitating and cavitating flows.

In the first case, clearance has an effect only for flow rates below the design point. In these cases, the smaller the clearance, the larger the instability region. For example, for $\phi = 0.070$ and Cr_2, F_t is destabilizing for whirl speed ratios between 0 and 0.05 as well as in small neighborhoods around 0.3 and 0.55. For Cr_1 though, F_t is destabilizing for $\frac{w}{\Omega}$ between 0 and 0.07 as well as between 0.17 and 0.33. This is in addition to the instability region around $\frac{w}{\Omega} = 0.55$. The effect of the clearance is less pronounced for $\phi = 0.080$ and is negligible in the higher flow rates. In all cases F_t changes sign a number of times. Negative whirl speed ratios are always stable, but the magnitude of the force is smaller in the case of larger clearance.

Data under cavitating conditions for both clearances is available for $\phi = 0.070$ only. In this case, the effect of the clearance is the opposite of that in noncavitating

flows, namely, the destabilizing region *is larger* for larger clearance. For moderate cavitation ($\sigma = 0.05$) there is a significant decrease in $|F_t|$ ($\frac{\omega}{\Omega} < 0$), even though this region remains stable. For $\sigma = 0.04$, the larger clearance affects even this region, rendering all whirl speed ratios above -0.45 and below 0.55 destabilizing. Note that $\sigma = 0.04$ represents flow past the point of performance breakdown.

5.2.3 Rotordynamic forces: influence of cavitation

That cavitation would have the most significant effect on the forces is expected, since its main result is to disturb the flow around the impeller. Moreover, the phenomenon itself is temporal, resulting in local pressure fluctuations felt by the impeller. We distinguish between two different regimes of cavitation: namely those associated with and without significant head loss across the inducer.

The general shape of the F_t vs. $\frac{\omega}{\Omega}$ curve has the following features: (a) relatively flat and smooth portion for negative whirl ratios, (b) two relative maxima at $\frac{\omega}{\Omega} = 0.3$ and $\frac{\omega}{\Omega} = 0.55$, and (c) two relative minima at $\frac{\omega}{\Omega} = 0.1$ and $\frac{\omega}{\Omega} = 0.5$. For moderate cavitation with small head loss, cavitation essentially preserves these features and only affects the size of the force at these stationary points. The net effect is a noticable enlargement of the instability region associated with larger forces for forward whirl. This is observed in figures 5.20–5.28.

Associated with significant head loss is the creation of a minimum at some negative whirl ratio. With the exception of a small region near the origin, all forward whirling motions are destabilizing. Further cavitation results in destabilization in reverse whirl as the minimum drops below the axis, as well as in forward whirl. Generally, with the exception of the neighborhood of the origin, *all* whirl ratios eventually become destabilizing. This is most evident in the case of $\phi = 0.080$, $\sigma = 0.04$ with small clearance (fig. 5.26).

Regardless of the flow conditions, the presence of the peak around $\frac{\omega}{\Omega} = 0.55$ and

the complicated nature of the F_t vs. $\frac{\omega}{\Omega}$ curve, mean that a quadratic fit of the data is not possible. A higher order polynomial is needed in order to approximate the forces. Thus, the representation (4.7)–(4.11) is not valid for this inducer. Similar results on other inducers investigated by Arndt and Franz (1986) corroborate this finding. Therefore, it is not possible to estimate the generalized stiffness, damping and inertia matrices for the SEP inducer and the model is not valid.

5.3 Spectral Densities

One bank of instantaneous data (4096 points) was used in the computation of spectral densities. The reference cycle frequency was 10Hz (J=5). This resulted in frequency resolution of 0.3125Hz.

As was mentioned in section 4.2.2, the effect of computing spectral densities of forces and moments in the laboratory frame is to mix and shift practically all the signals, resulting in loss of information. This is evident in figures 5.29–5.34 and is even more significant in the case of moments. Recall that moments are computed about a point outside the calibration plane of the balance. Thus M_x and M_y include contributions from F_x and F_y. Essentially all bridge signals have been used to compute the moments in the laboratory frame. In order to minimize this loss of information, the spectral densities of forces (and moments) in the rotating frame of the balance are presented (fig. 5.35–5.52). In all cases, whirl speed is zero with the impeller positioned at the top of the whirl orbit ($\alpha = 0°$). The frequency range shown is five times the shaft frequency, i.e., 250Hz. Note that the position of the impeller on the whirl orbit does not affect the qualitative features of these results. For example, the spectral densities of forces for $\phi = 0.070$ (noncavitating flow), obtained with the impeller at $\alpha = 90°$ (figures 5.53–5.56) show the same features as those obtained with the impeller at the top of the orbit.

Due to the symmetry in the construction of the dynamometer as well as the fact that the frame axes continuously rotate at the shaft speed, the signals measured in

any direction would have similar frequency content. This is verified by inspection of all the plots shown, as expected. Moreover, the cross-spectral density SF_{12} (or SM_{12}) is a measure of how similar the signals are with respect to their energy distribution. Therefore, the cross-spectral density of the forces (and moments) in the rotating frame would be very much like the individual signal densities. And, indeed, this is the case.

Whereas in computing the average forces, dry runs are subtracted to yield the hydrodynamic forces, this cannot be done with the instantaneous data, because the two signals (dry and wet) represent two different time-histories. Thus, the forces (and moments) plotted are the *net forces* acting on the impeller. The spectral densities obtained for the dry runs are shown for comparison purposes. The presence of the peak at 50Hz is expected since it represents the weight of the impeller as felt by the rotating dynamometer.

In the frequency range 0–100Hz, the dominant peak for noncavitating flows (other than shaft frequency) is located between 20Hz and 25Hz, depending on the flow rate. The fact that it is also present in the force spectra of the dry runs (at $\sim$ 21 Hz), eliminates the possibility that it is solely due to hydrodynamic forces. Note that the size of this peak increases drastically as a result of fluid interaction. Moreover, not only does the location of the peak shift slightly to a higher frequency as the flow rate increases, but also its width increases significantly. The fact that it is located near half the shaft speed indicates that there is a resonance associated with the motion of the fluid in the cavity behind the inducer. An additional effect of the flow coefficient is that the average force level at all frequencies decreases as ϕ increases. The resonance peak at half shaft speed disappears completely in the presence of cavitation and no explanation is available at this point.

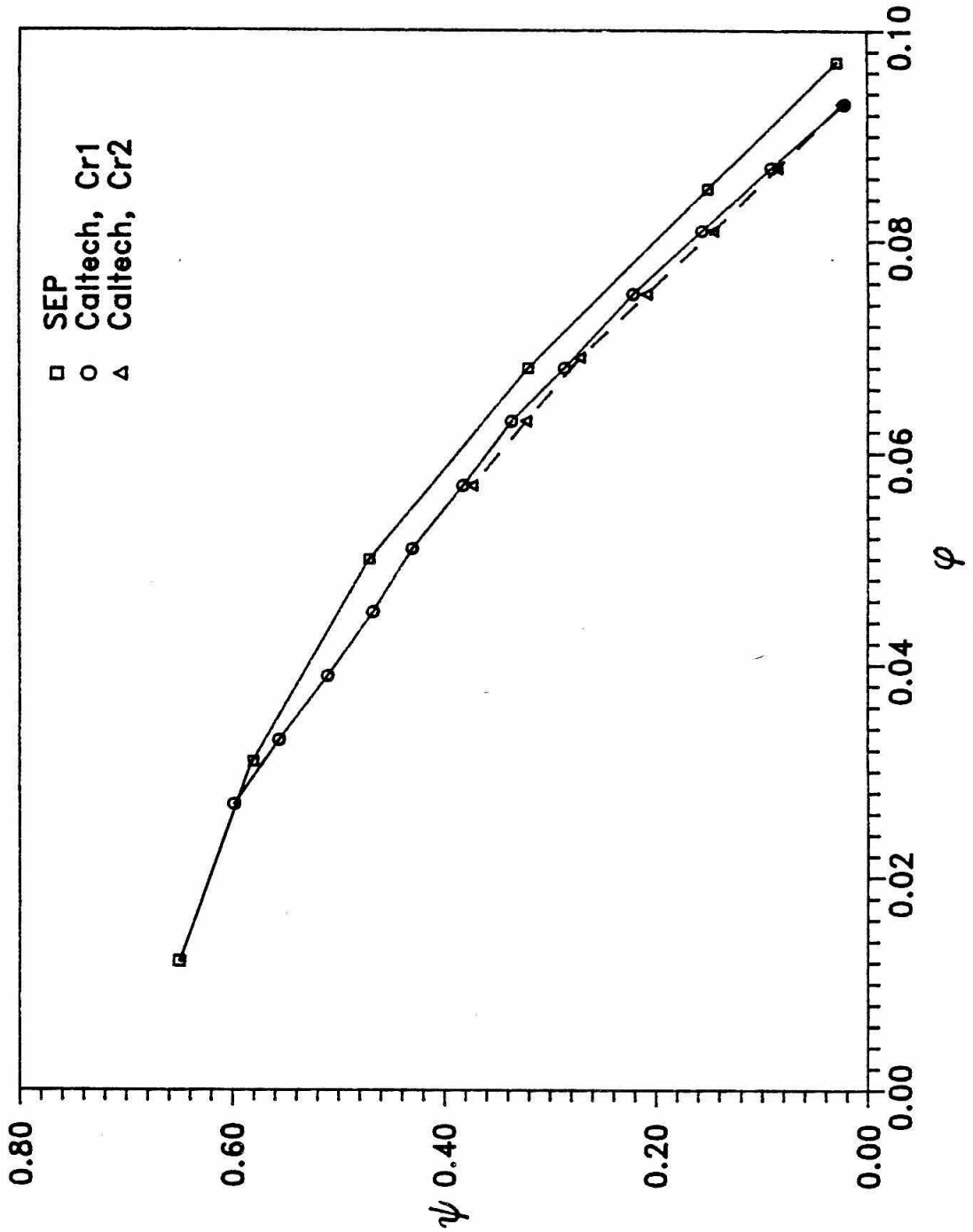

Figure 5.1: Head rise across the inducer versus flow rate, as measured by SEP and at RFTF.

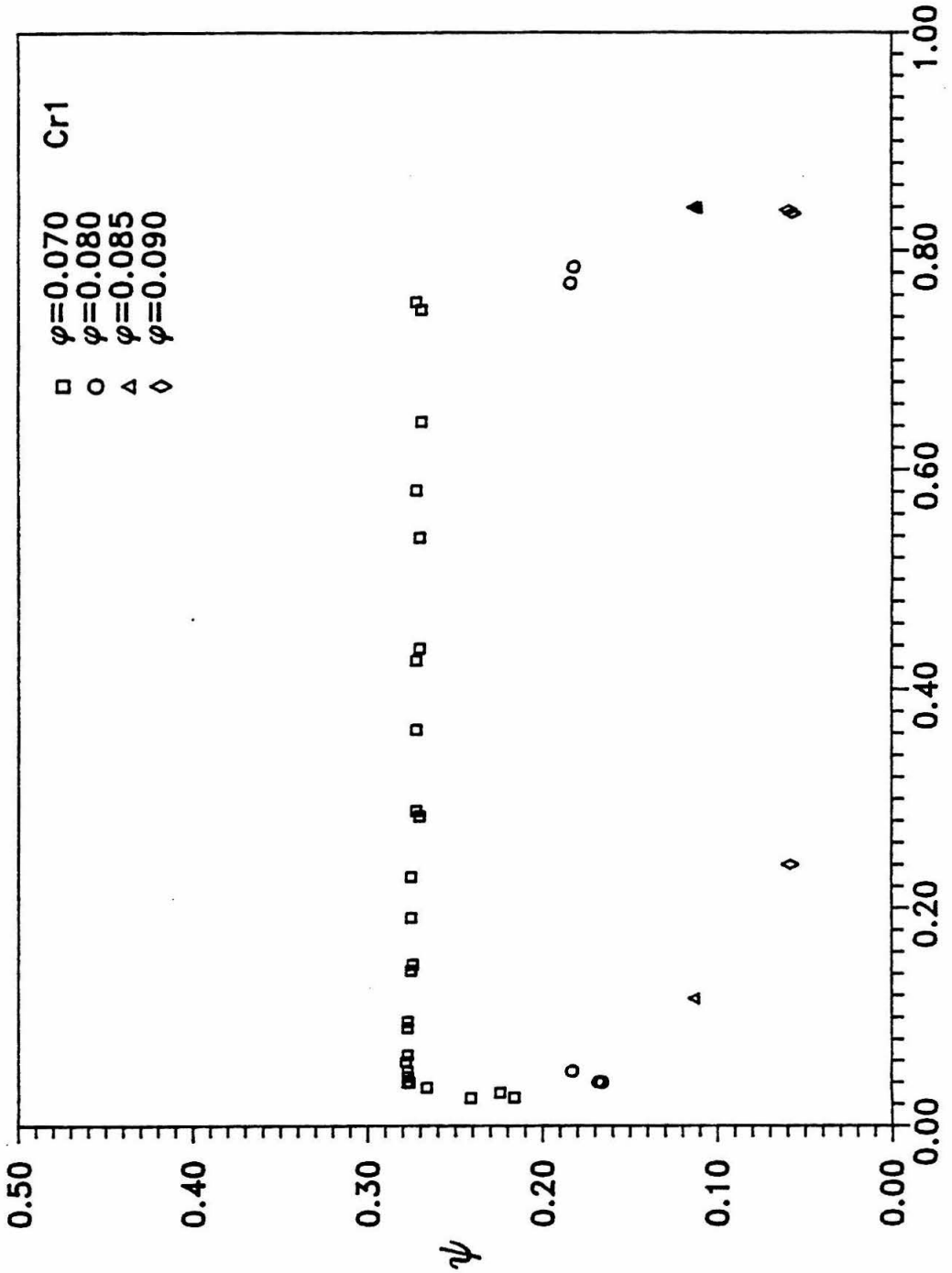

Figure 5.2: Cavitation performance curves obtained during phase 1.

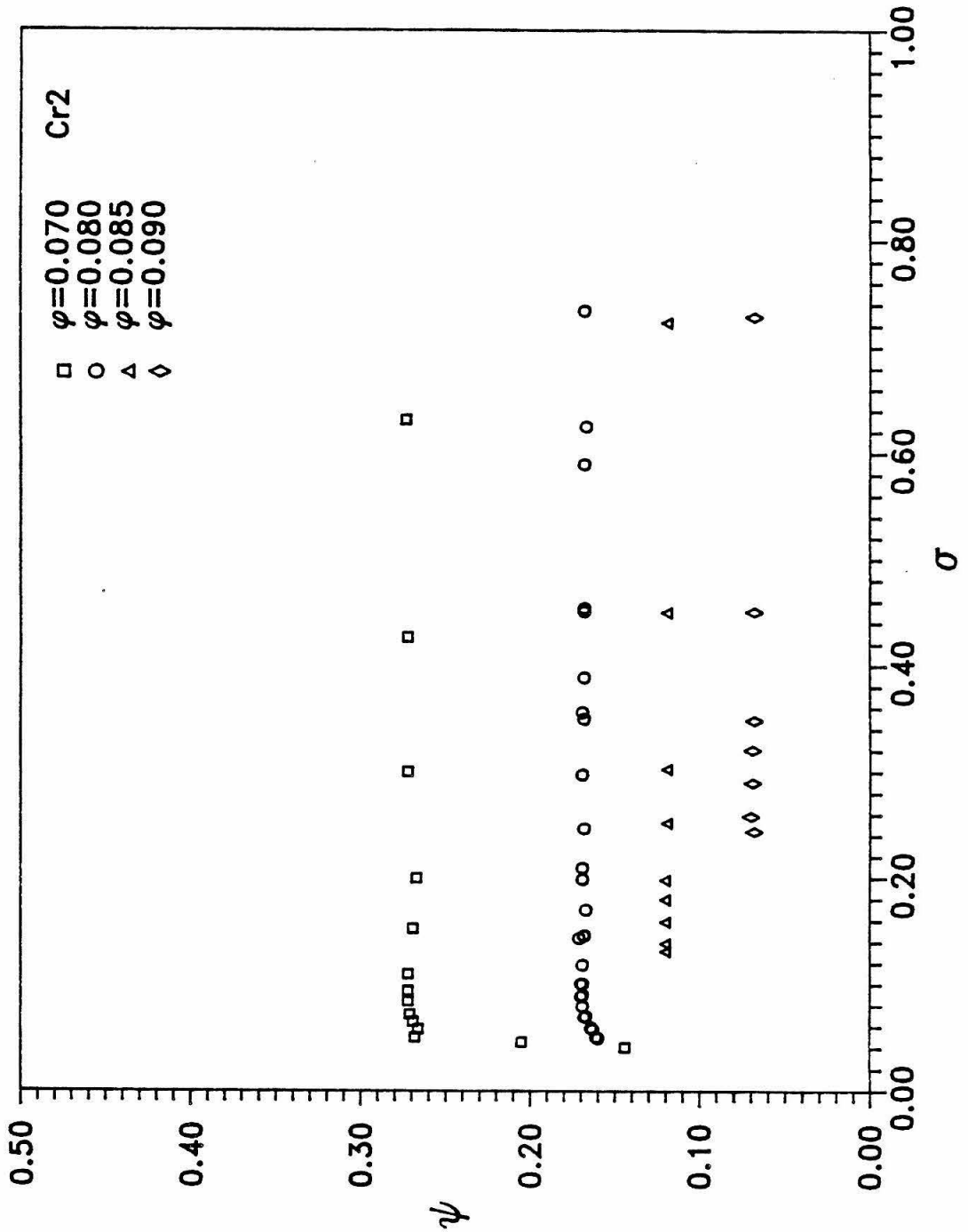

Figure 5.3: Cavitation performance curves obtained during phase 2.

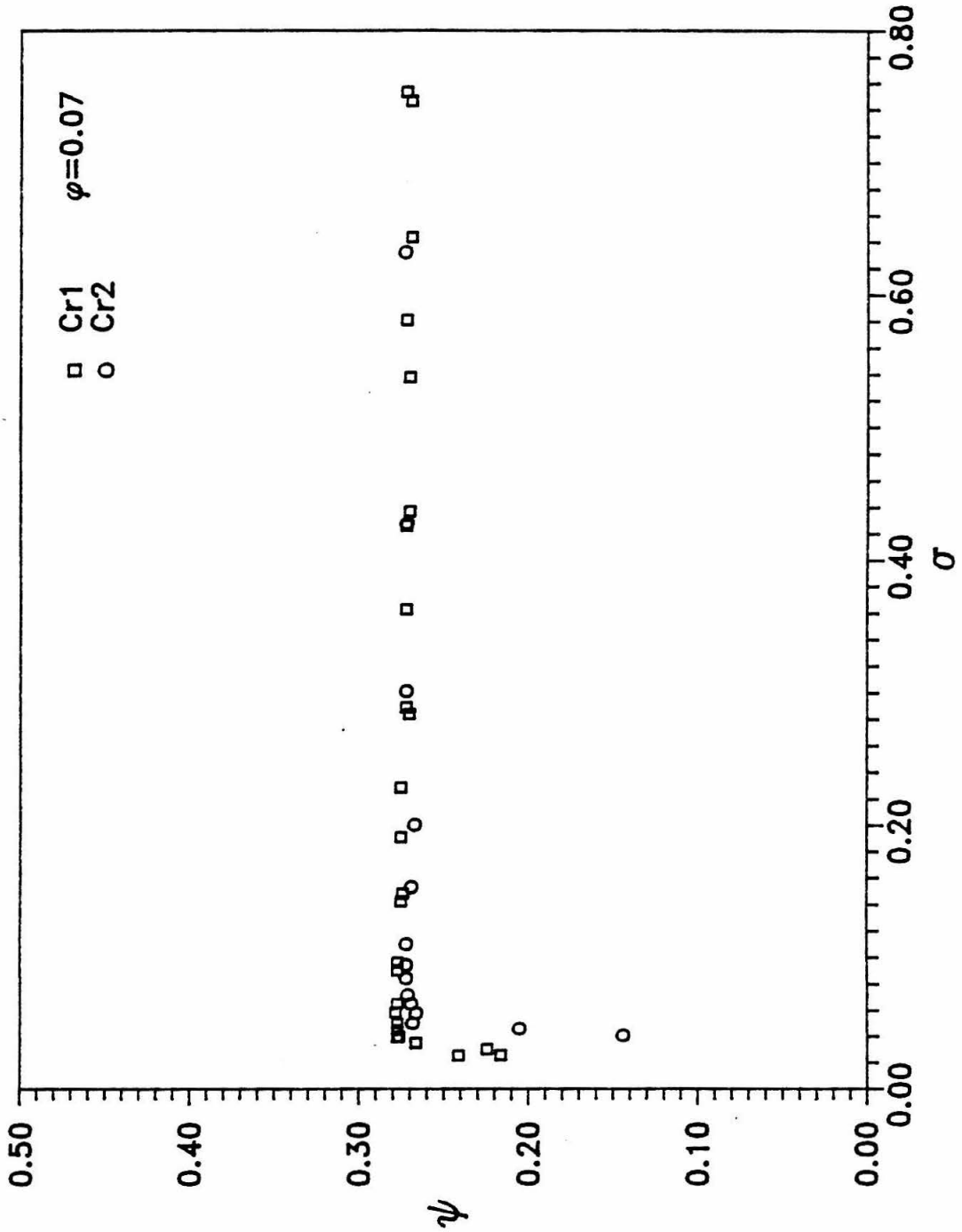

Figure 5.4: Effect of the impeller tip clearance on the cavitation performance curves, $\phi = 0.070$.

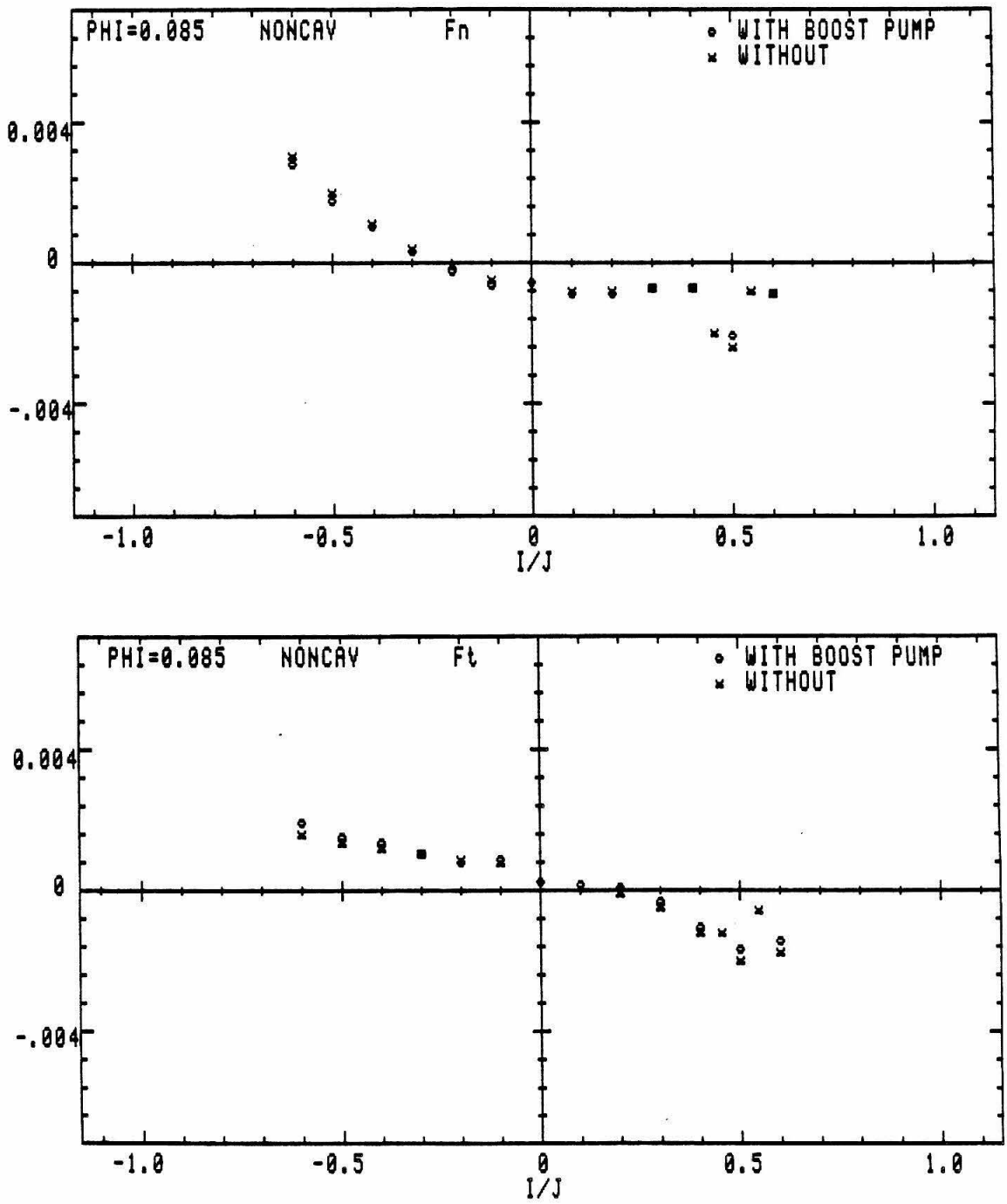

Figure 5.5: Comparison of force measurements obtained prior to and after the addition of the auxiliary pump ($\phi = 0.085$, noncavitating).

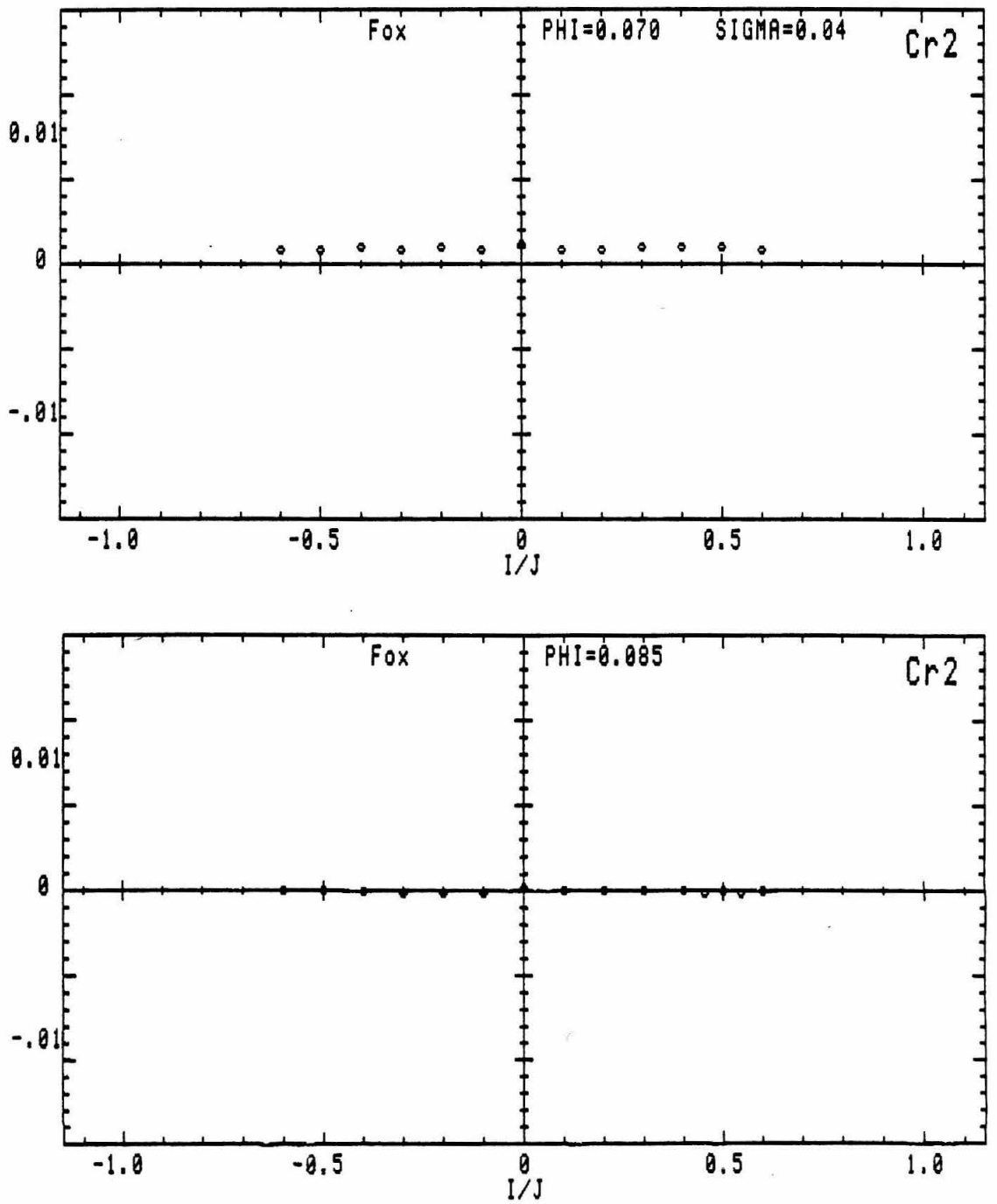

Figure 5.6: Steady lateral forces as a function of whirl/shaft speed ratio for $\phi = 0.070$, $\sigma = 0.040$ (top) and $\phi = 0.085$, noncavitating (bottom).

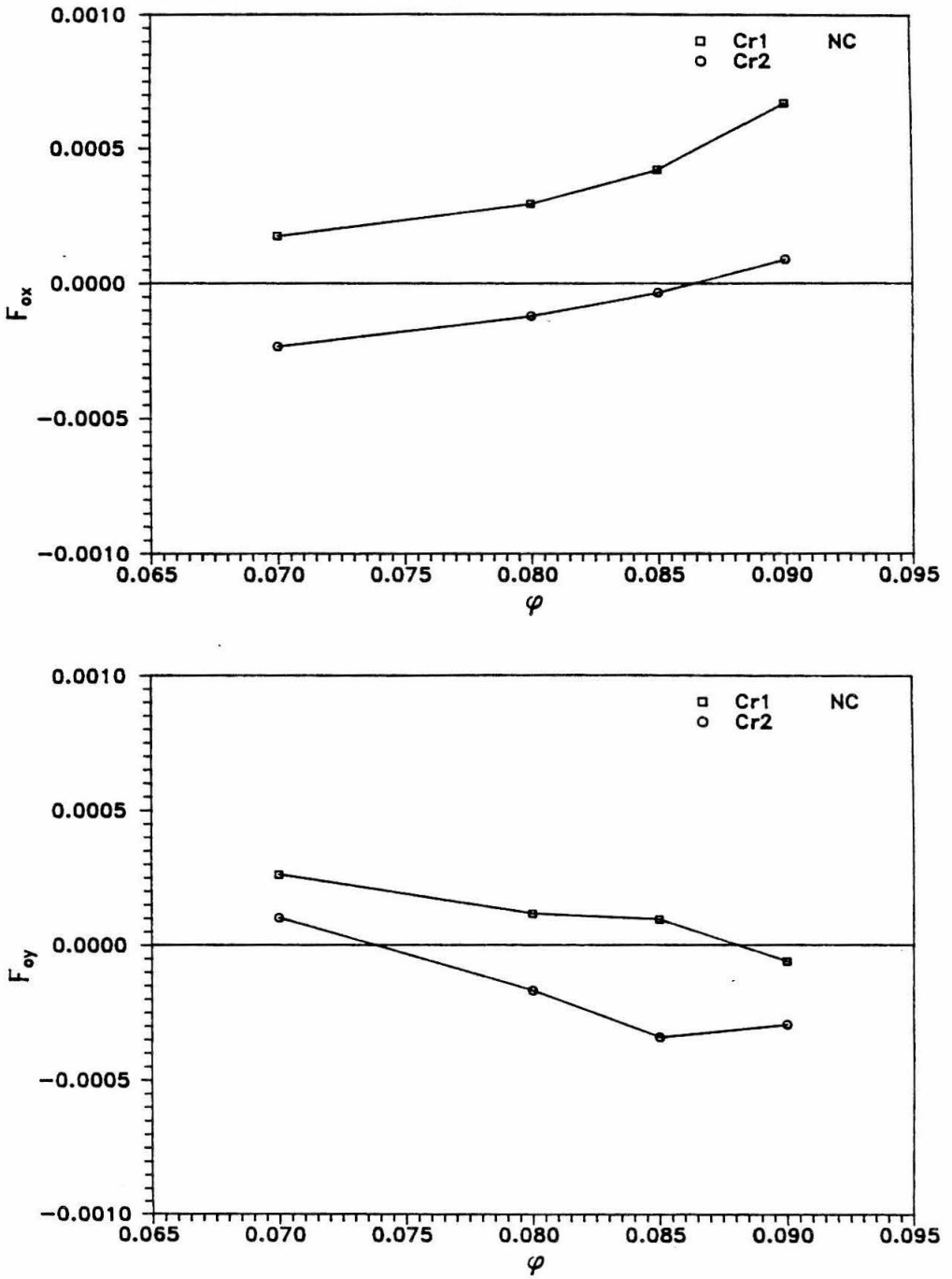

Figure 5.7: Effect of the flow rate on the steady lateral forces (noncavitating flow, both clearances).

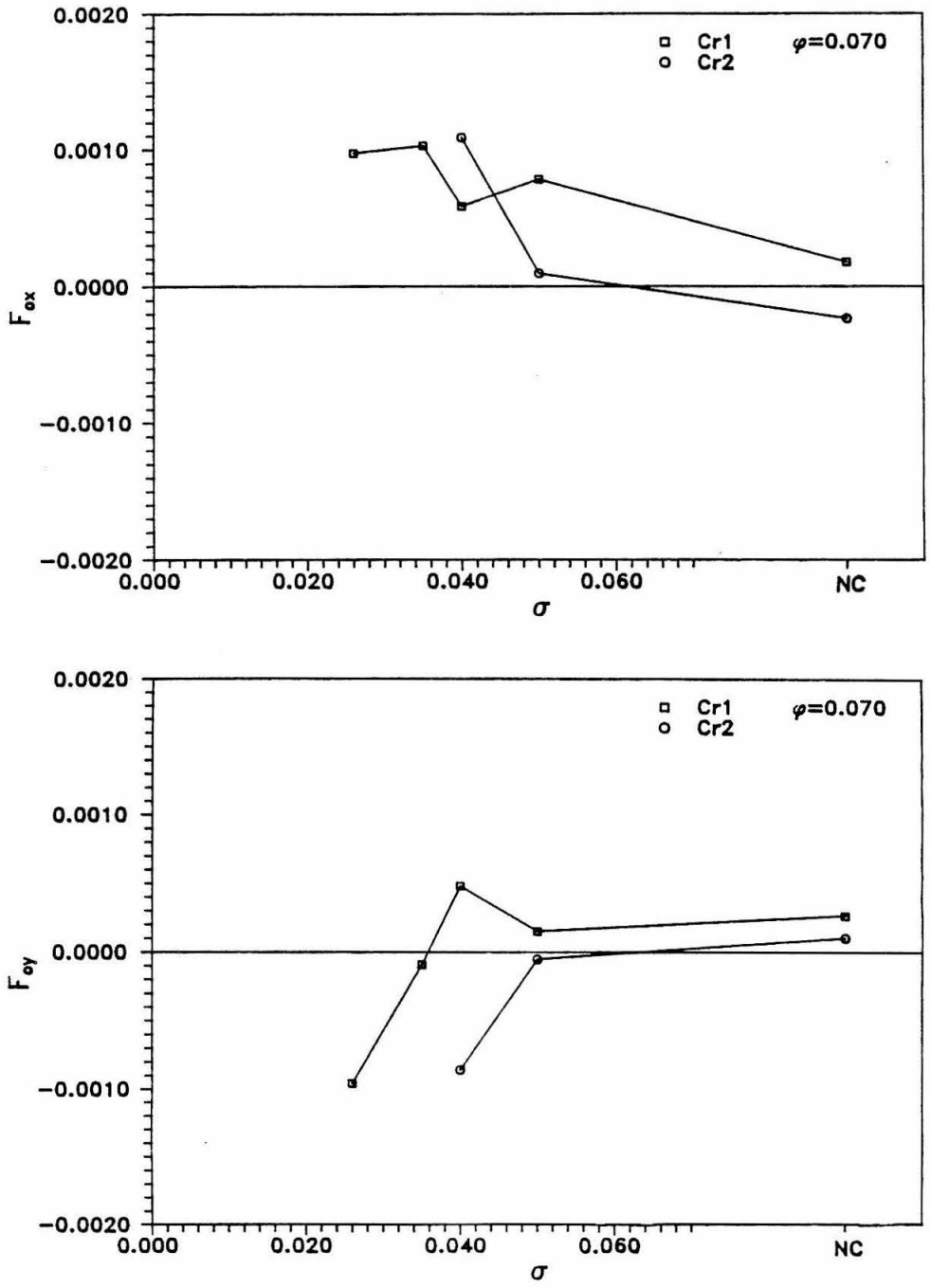

Figure 5.8: Effect of cavitation on the steady lateral forces, both clearances ($\phi = 0.070$).

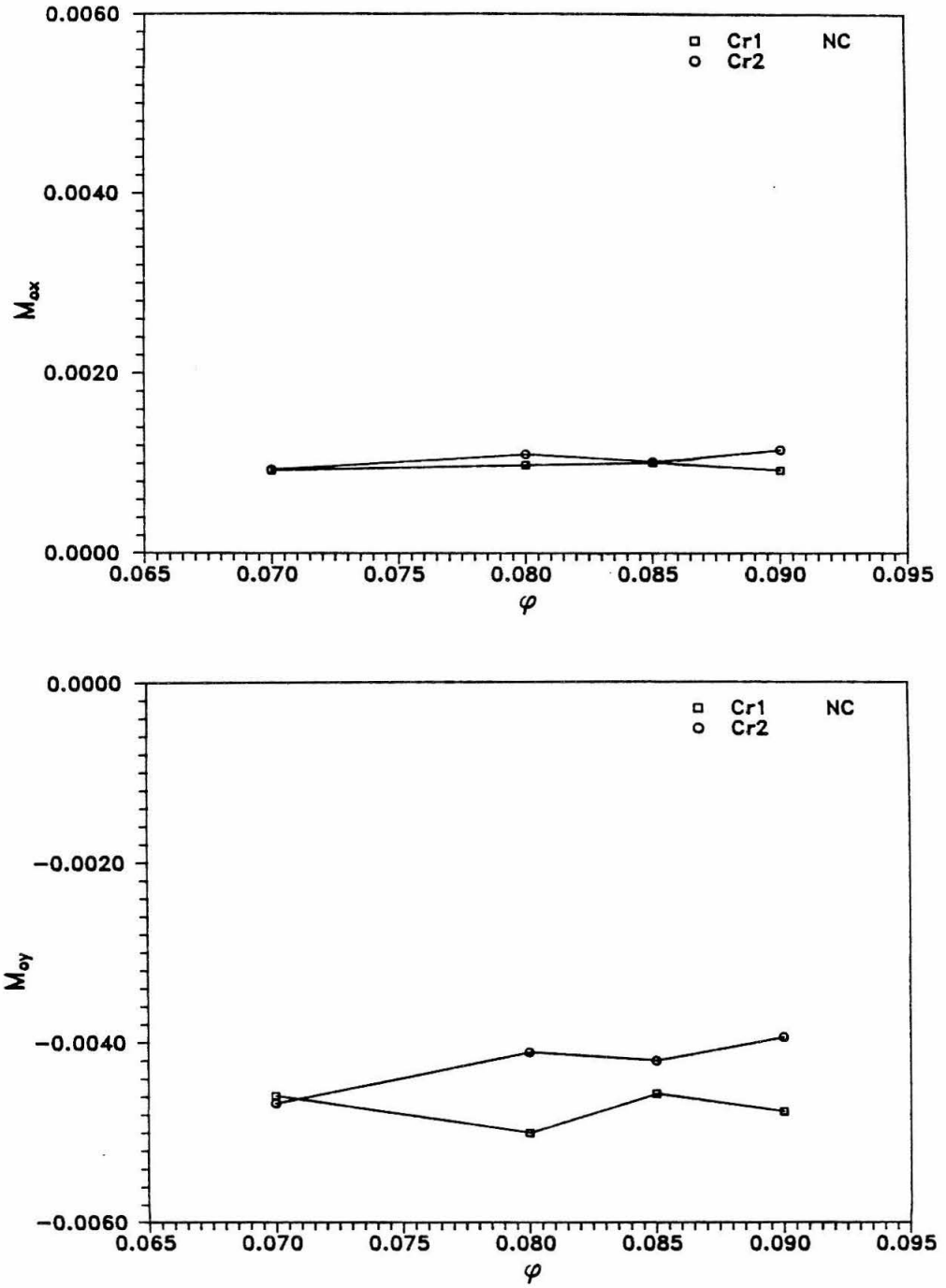

Figure 5.9: Effect of the flow rate on the steady moments (both clearances, non-cavitating flow).

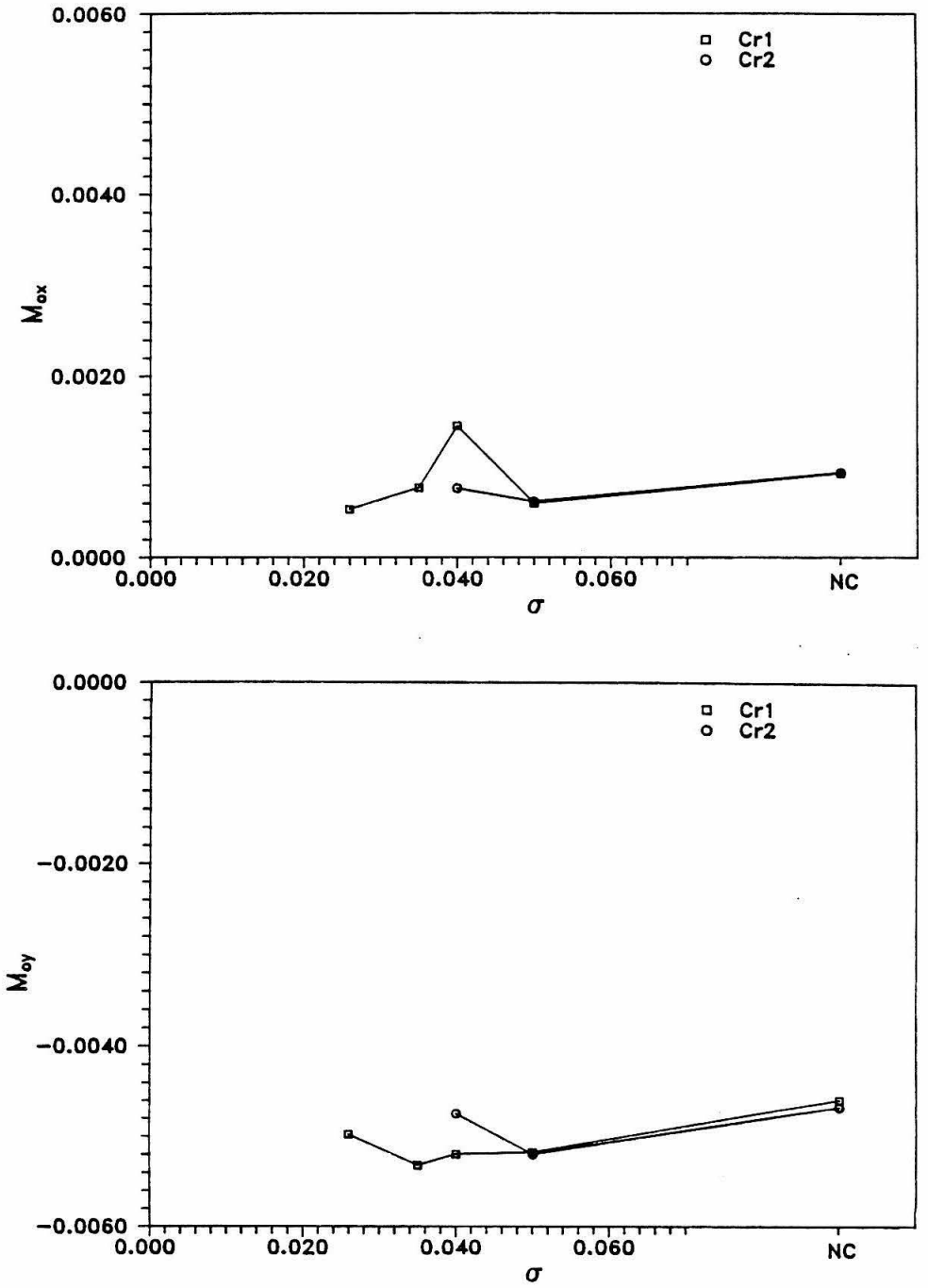

Figure 5.10: Effect of cavitation on the steady moments, $\phi = 0.070$.

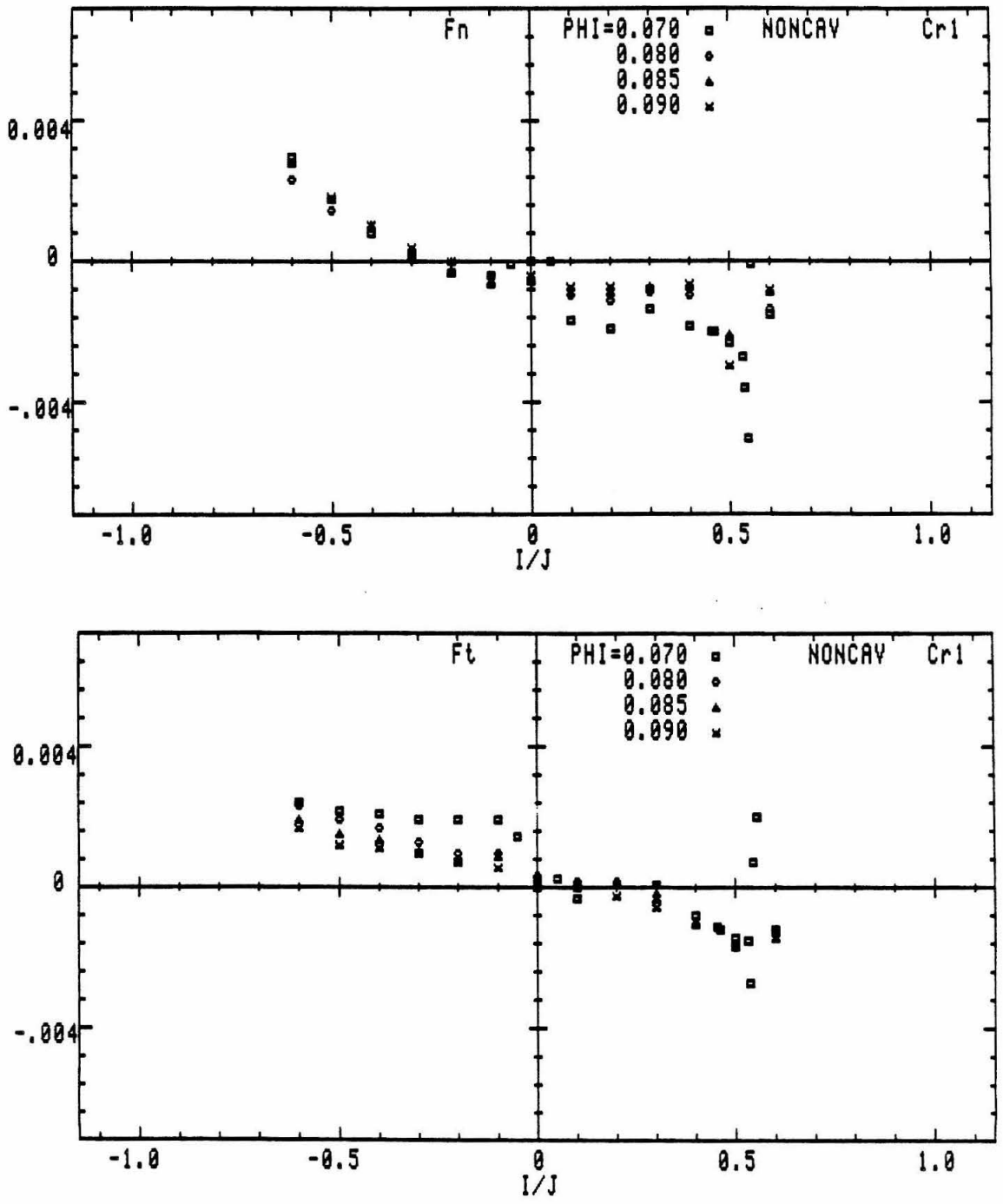

Figure 5.11: Effect of the flow coefficient on normal and tangential forces in non-cavitating flow (Cr_1).

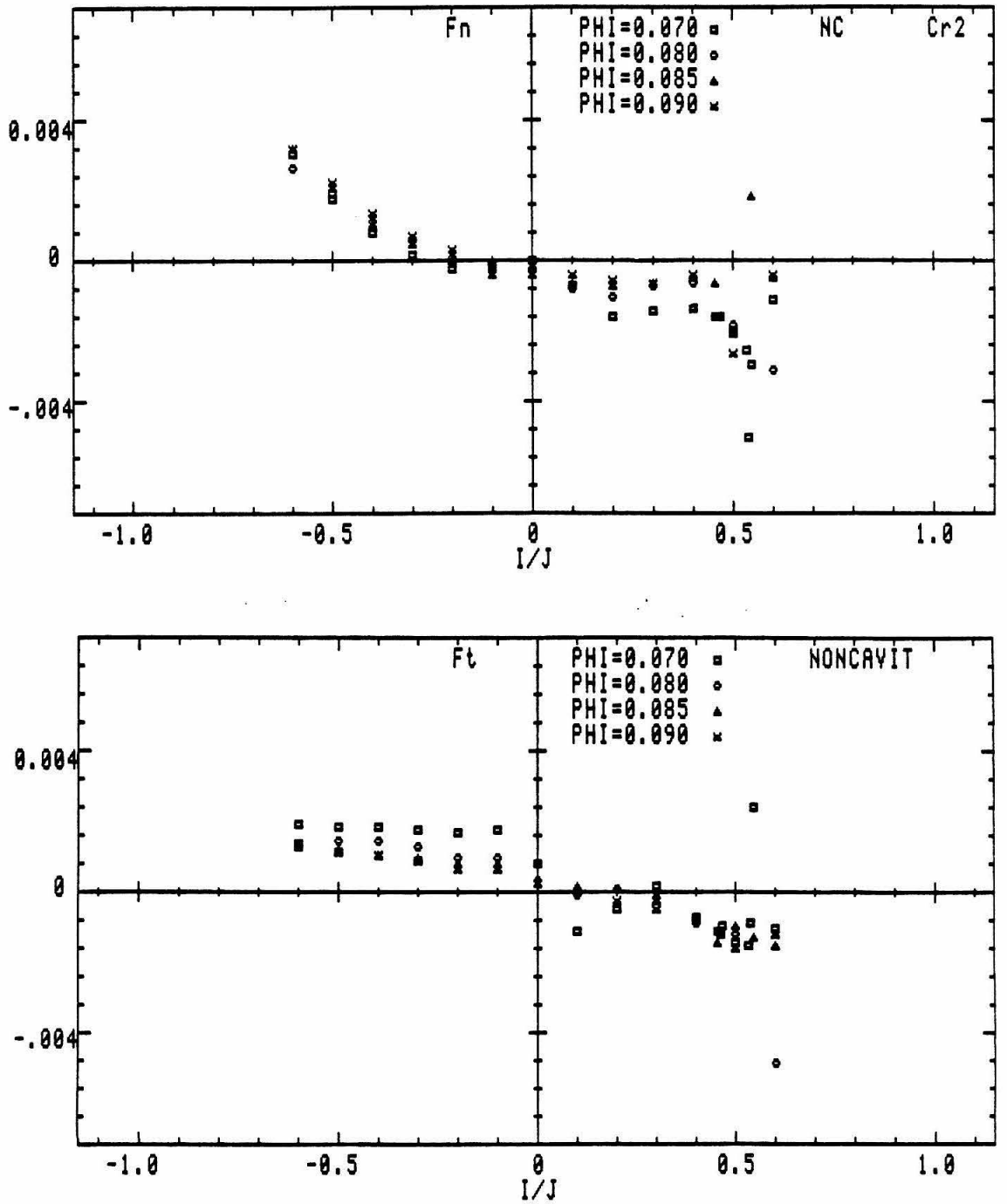

Figure 5.12: Effect of the flow coefficient on normal and tangential forces in non-cavitating flow (Cr_2).

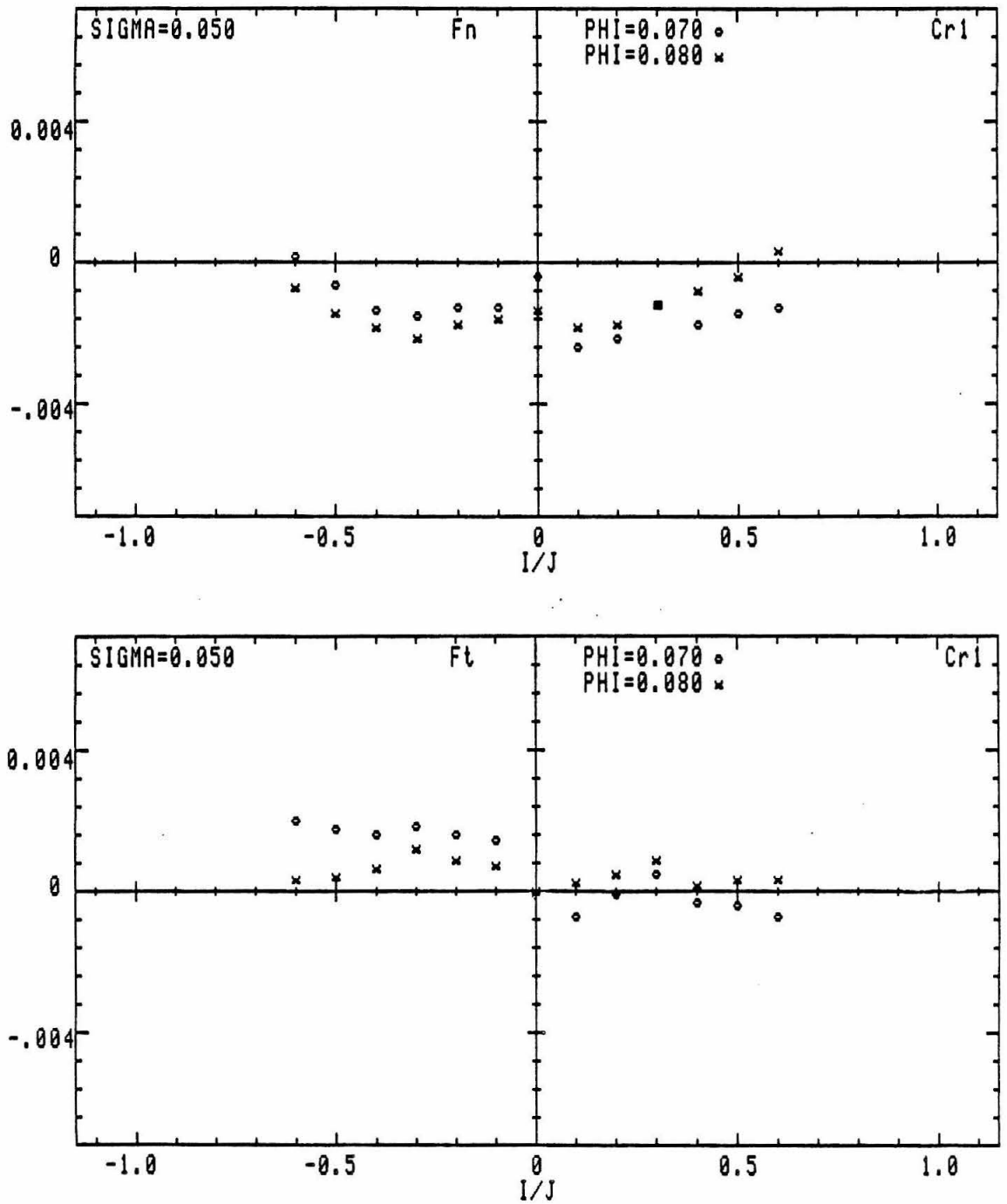

Figure 5.13: Effect of the flow coefficient on normal and tangential forces in cavitating flow with $\sigma = 0.050$ (Cr_1).

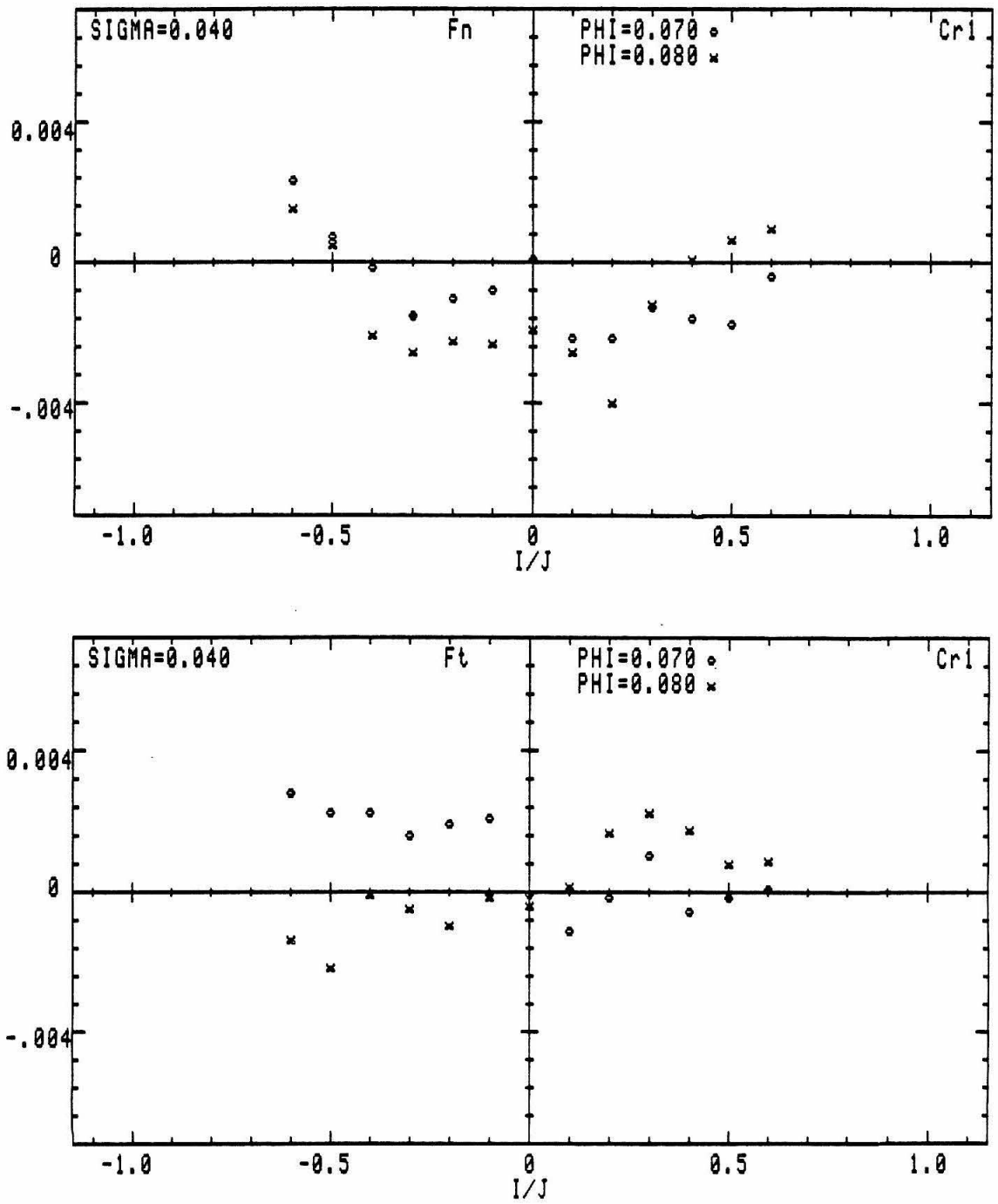

Figure 5.14: Effect of the flow coefficient on normal and tangential forces in cavitating flow with $\sigma = 0.040$ (Cr_1).

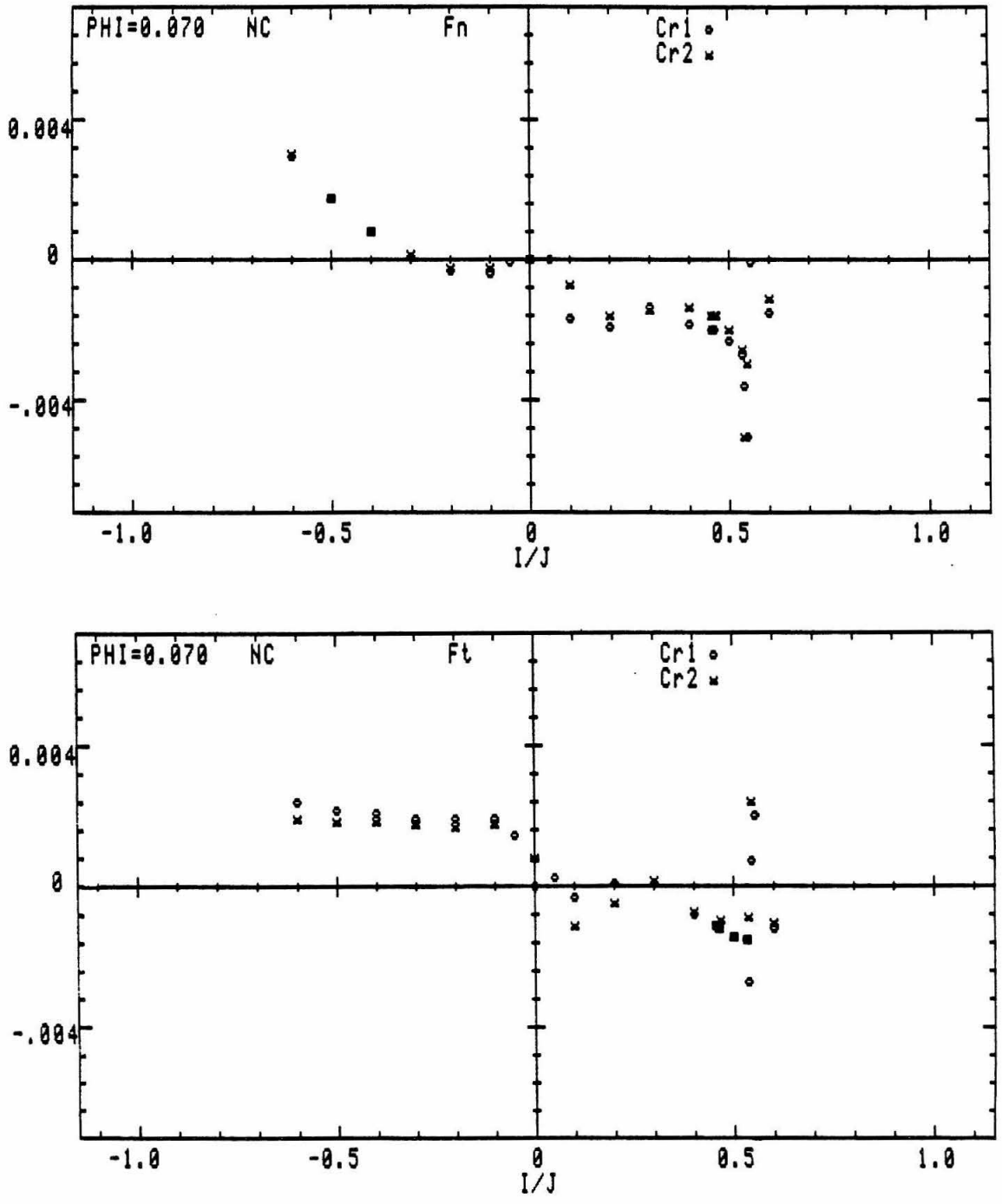

Figure 5.15: Effect of the impeller tip clearance on normal and tangential forces in noncavitating flow ($\phi = 0.070$).

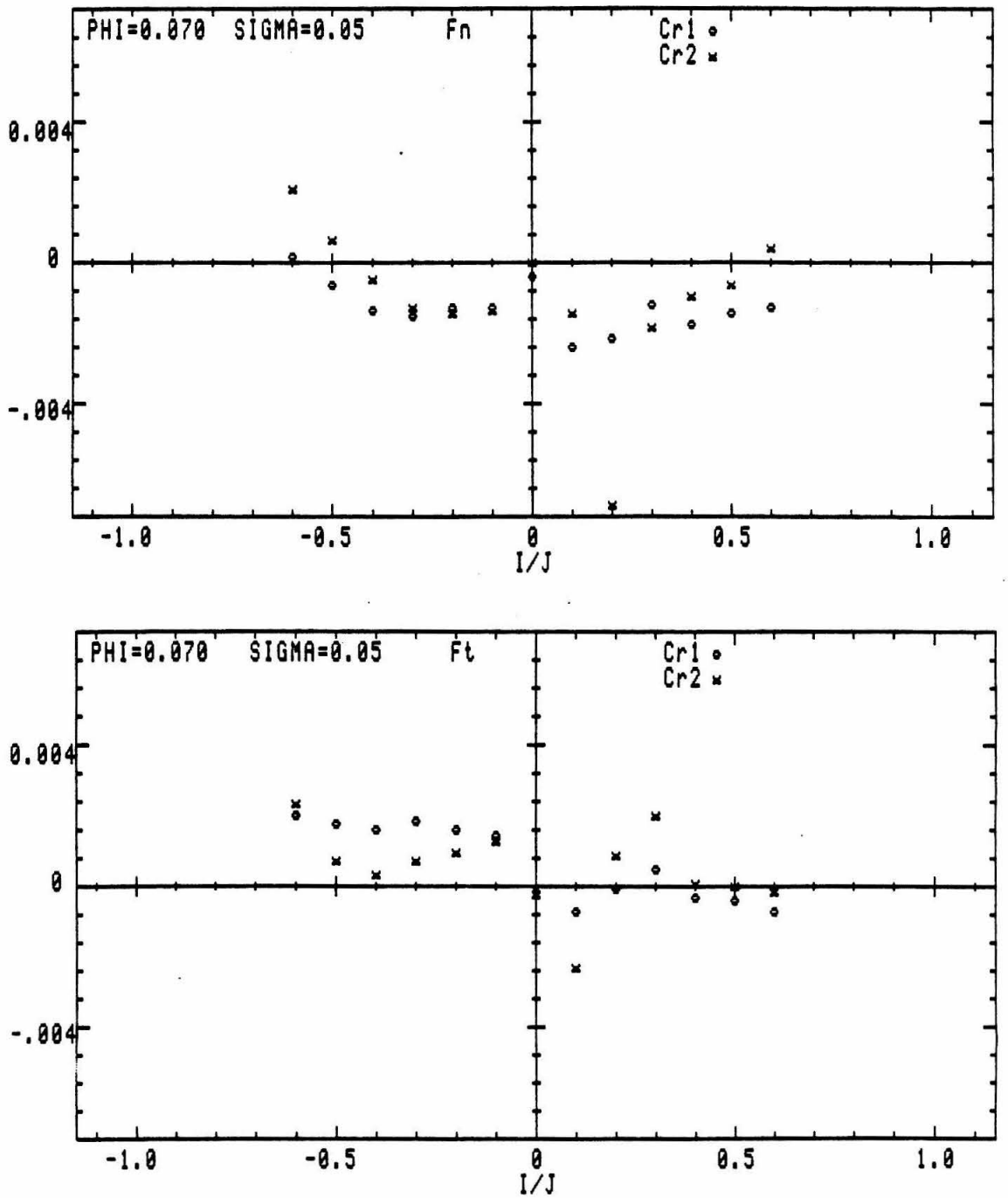

Figure 5.16: Effect of the impeller tip clearance on normal and tangential forces in cavitating flow with $\sigma = 0.050$ ($\phi = 0.070$).

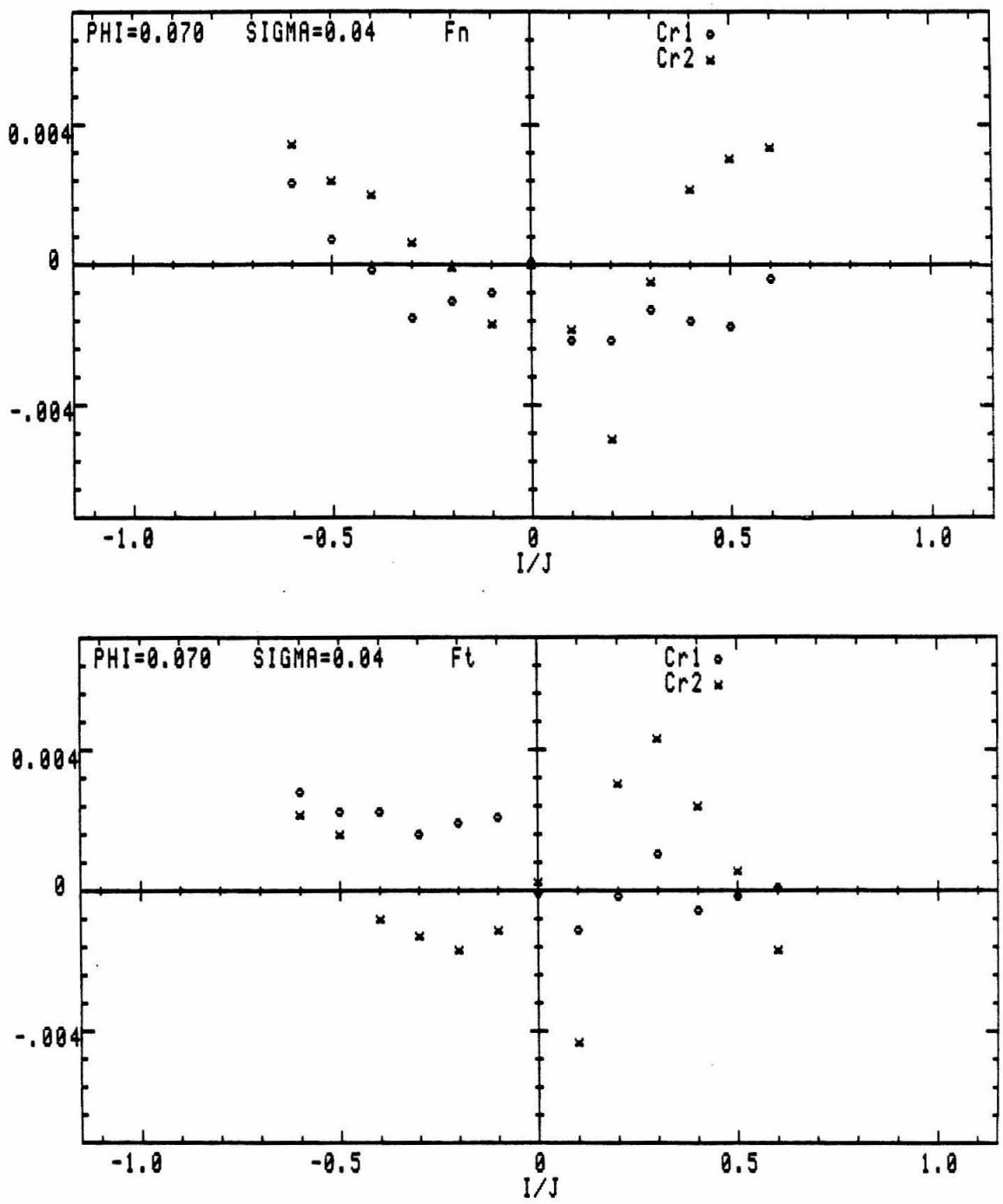

Figure 5.17: Effect of the impeller tip clearance on normal and tangential forces in cavitating flow with $\sigma = 0.040$ ($\phi = 0.070$).

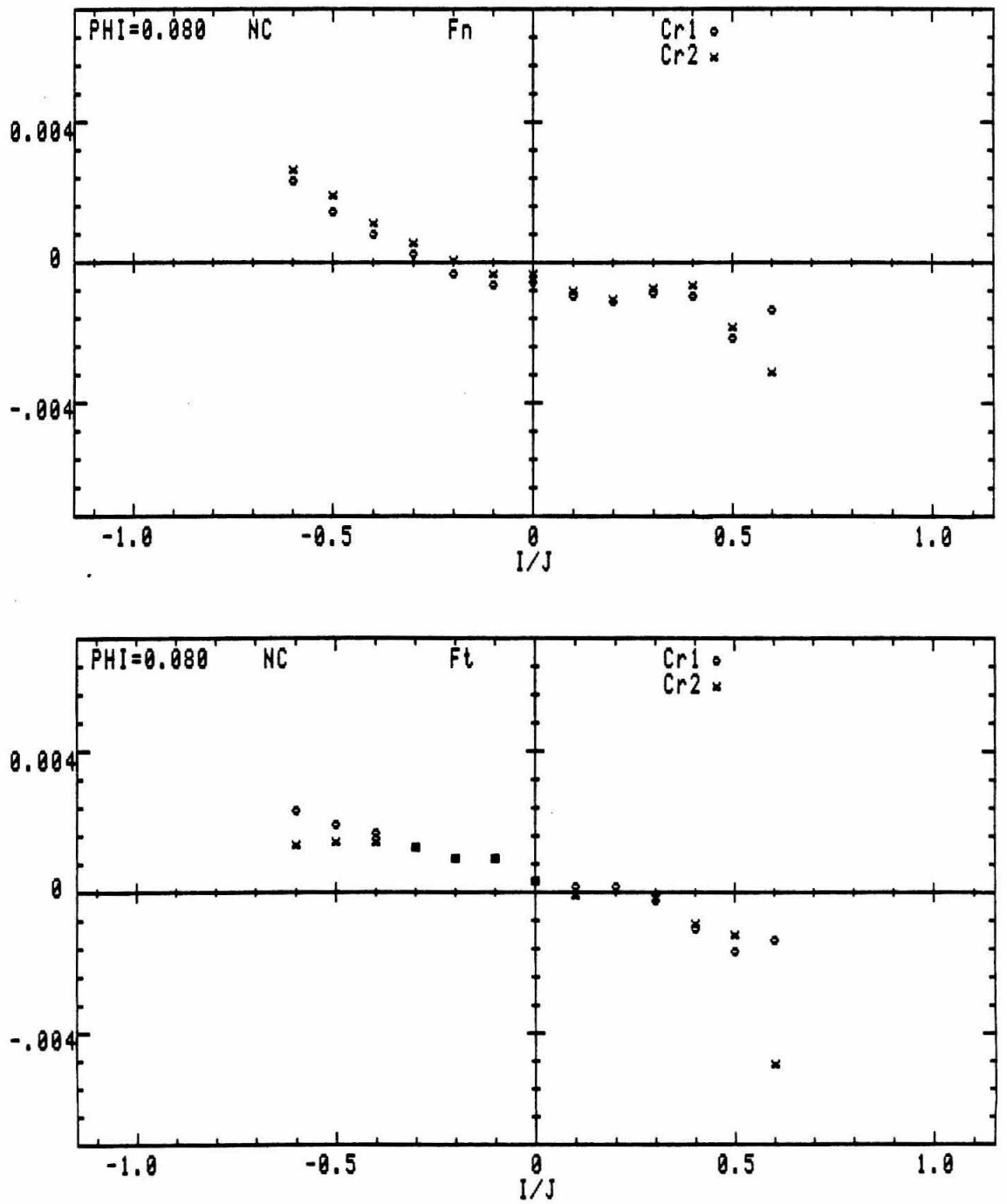

Figure 5.18: Effect of the impeller tip clearance on normal and tangential forces in noncavitating flow ($\phi = 0.080$).

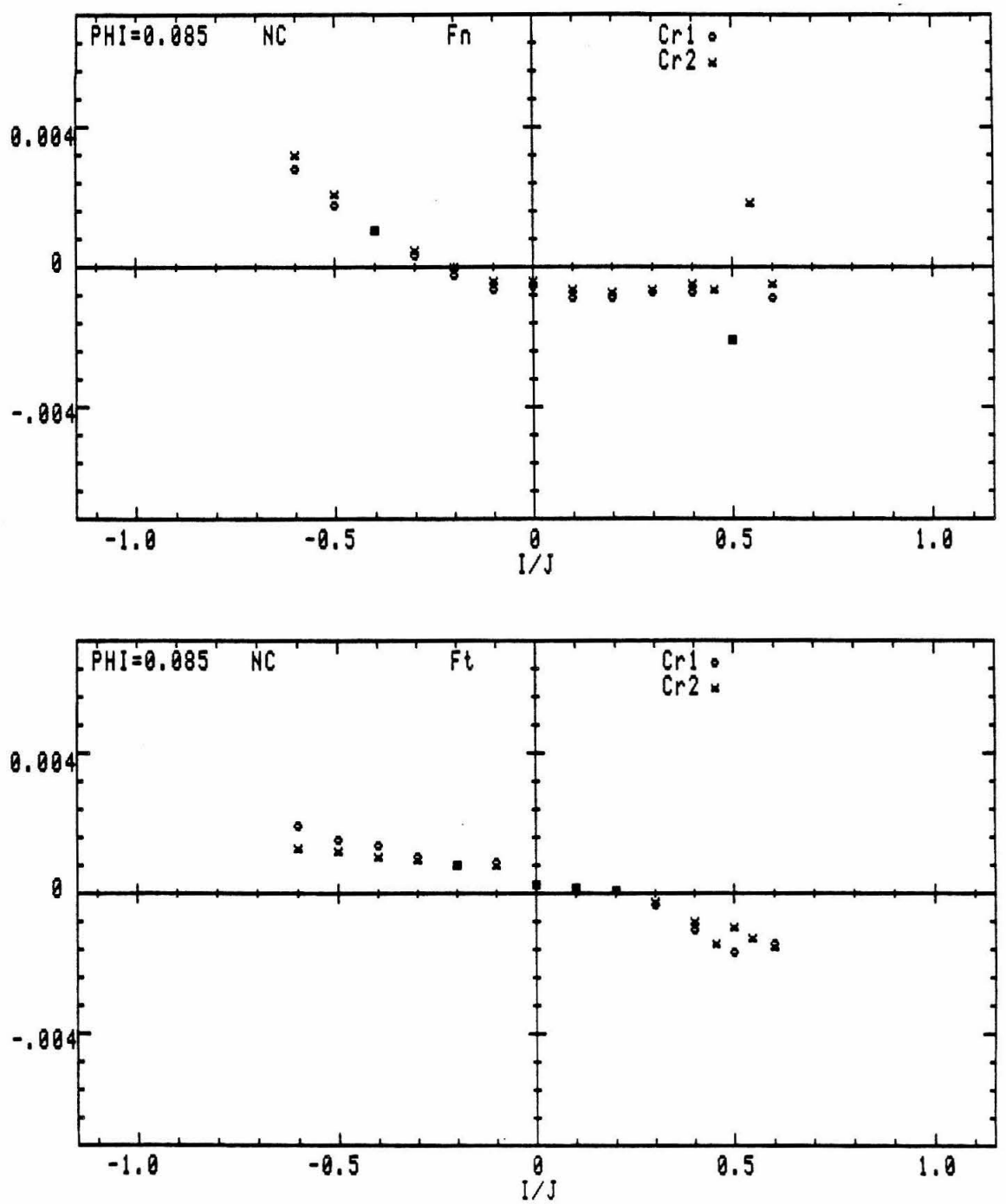

Figure 5.19: Effect of the impeller tip clearance on normal and tangential forces in noncavitating flow (at design, $\phi = 0.085$).

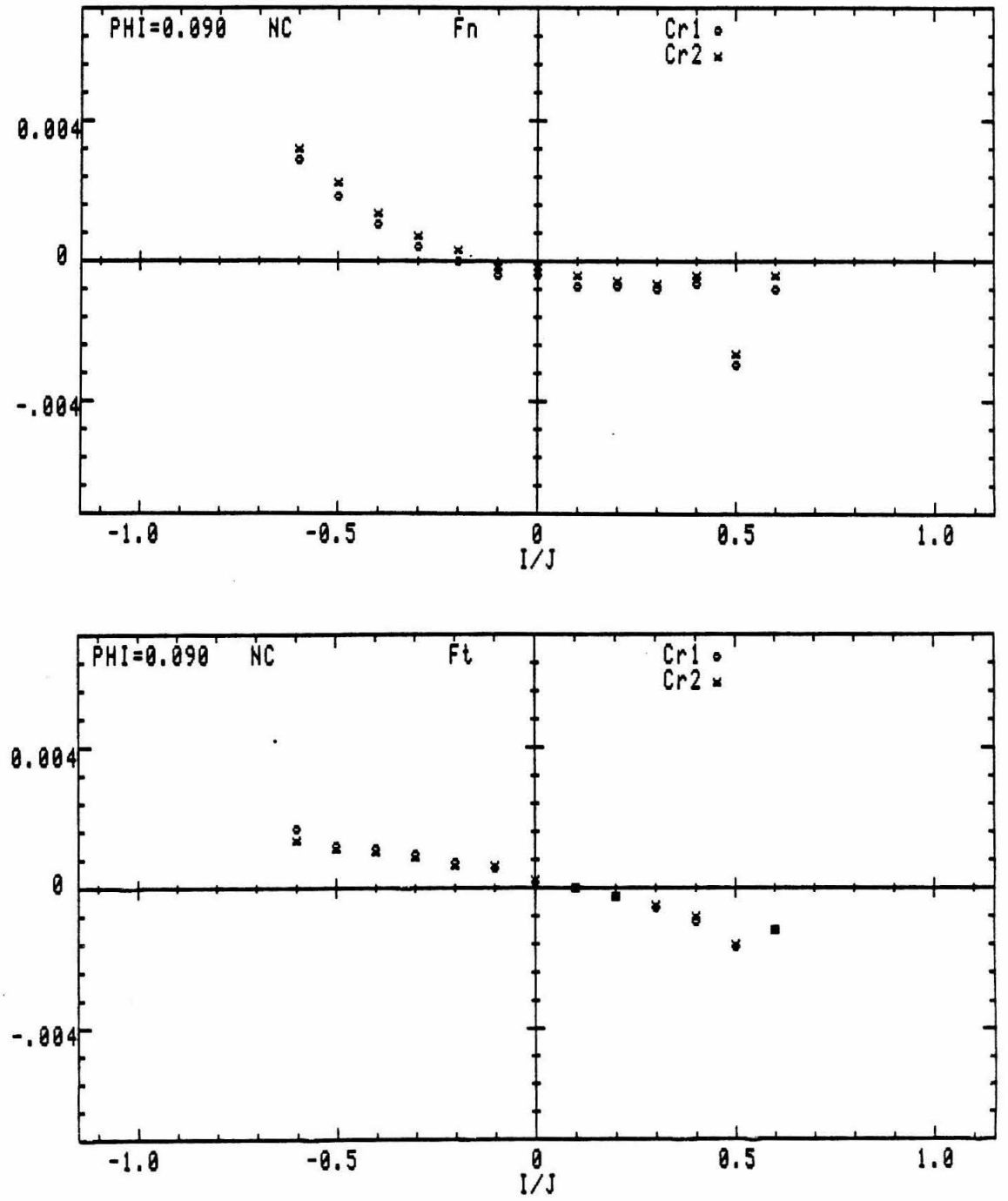

Figure 5.20: Effect of the impeller tip clearance on normal and tangential forces in noncavitating flow ($\phi = 0.090$).

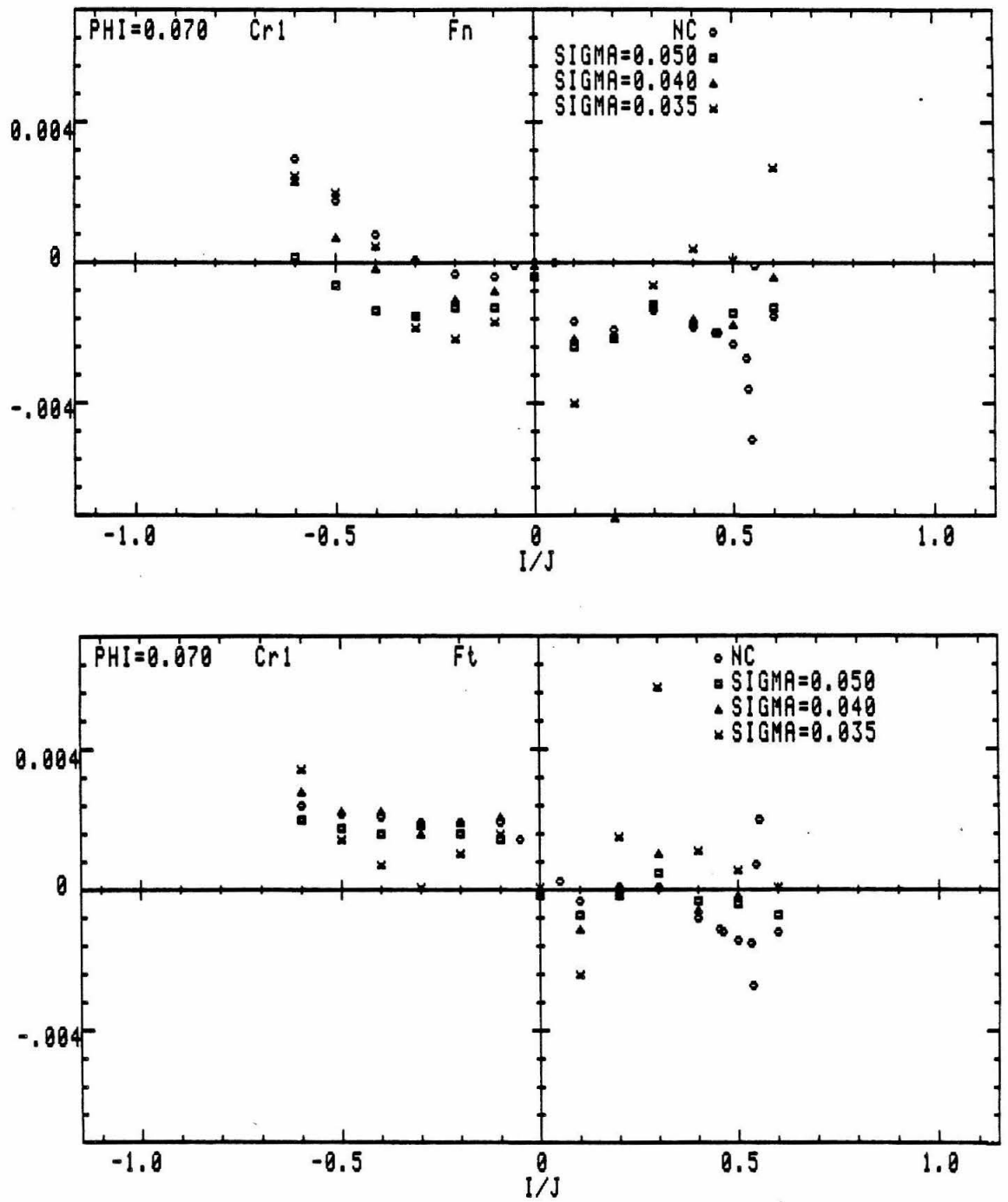

Figure 5.21: Effect of cavitation on the normal and tangential forces for $\phi = 0.070$ (Cr_1).

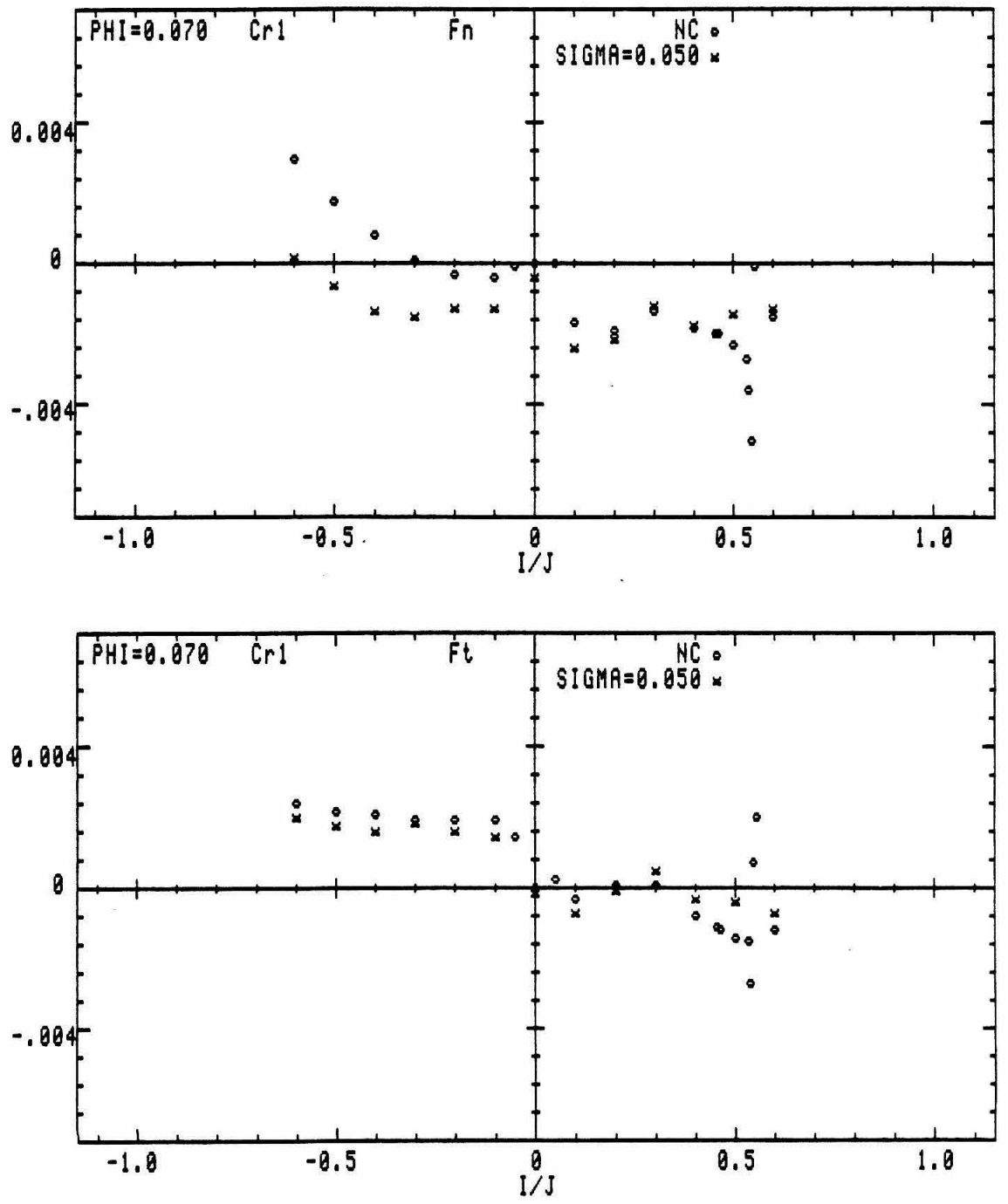

Figure 5.22: Comparison of unsteady forces in noncavitating flow and in the presence of moderate cavitation, $\sigma = 0.050$ ($\phi = 0.070$, Cr_1).

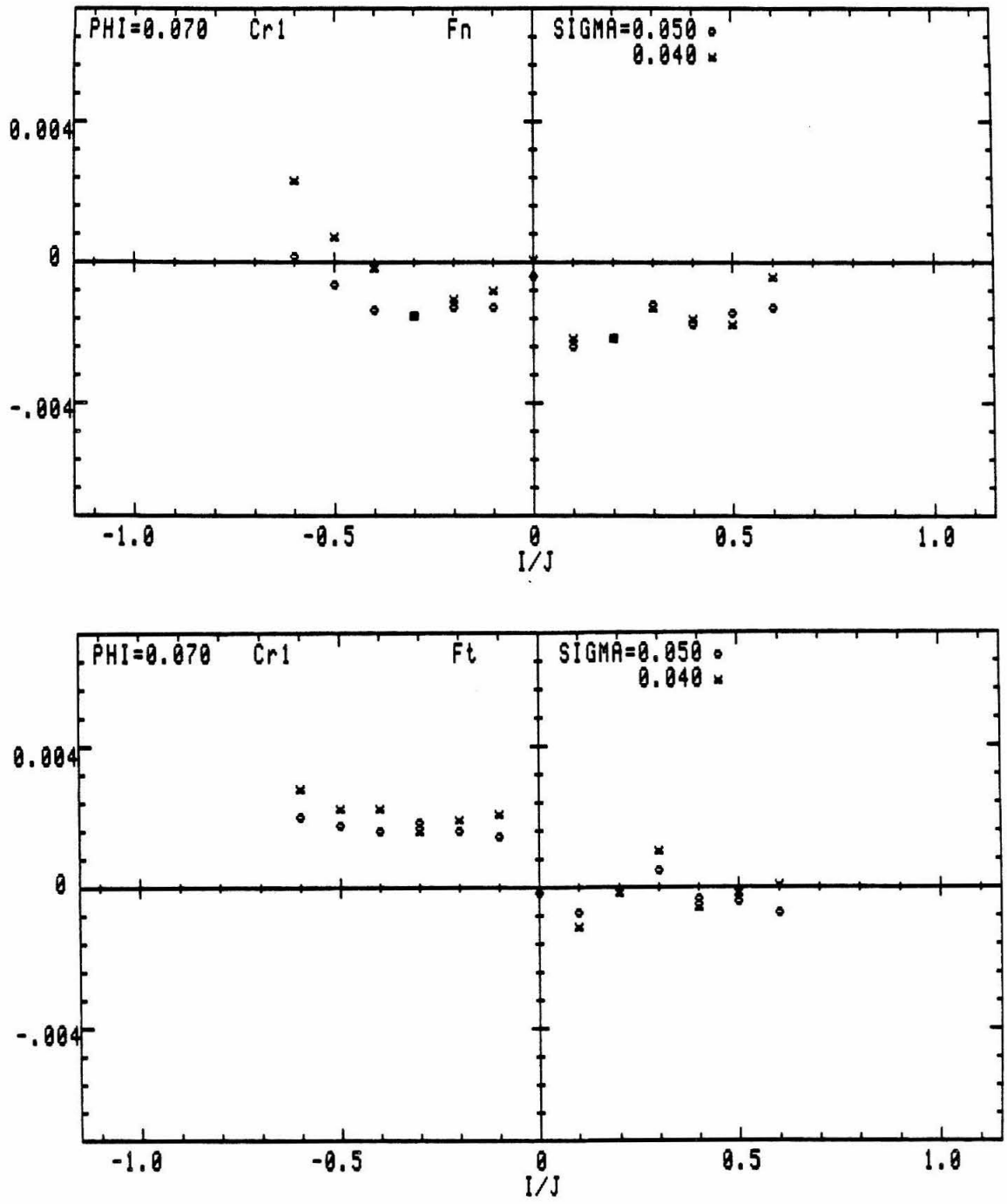

Figure 5.23: Effect of cavitation ($\sigma = 0.050$ and $\sigma = 0.040$) on the normal and tangential forces for $\phi = 0.070$ (Cr_1).

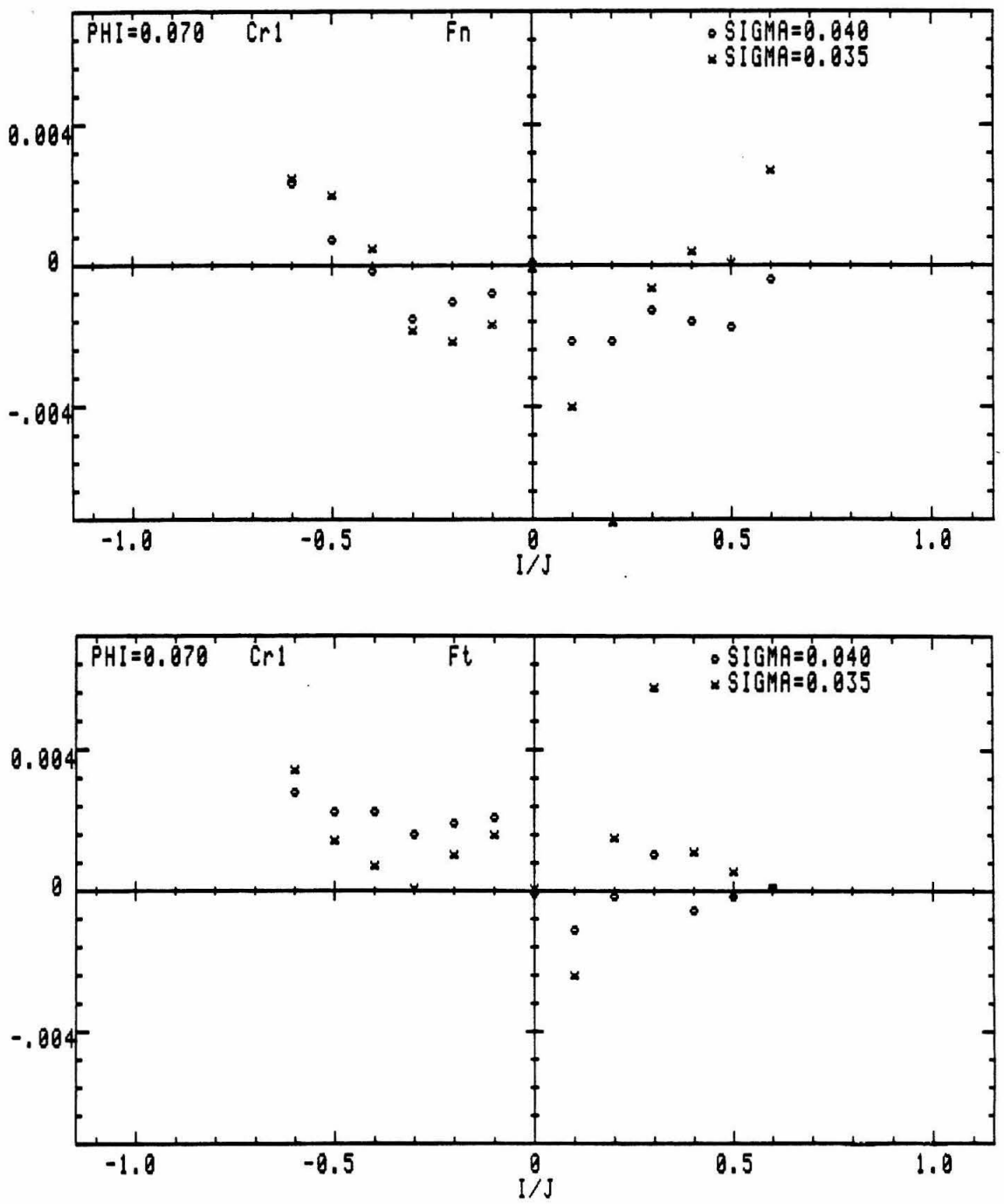

Figure 5.24: Effect of cavitation ($\sigma = 0.040$ and $\sigma = 0.035$) on the normal and tangential forces for $\phi = 0.070$ (Cr_1).

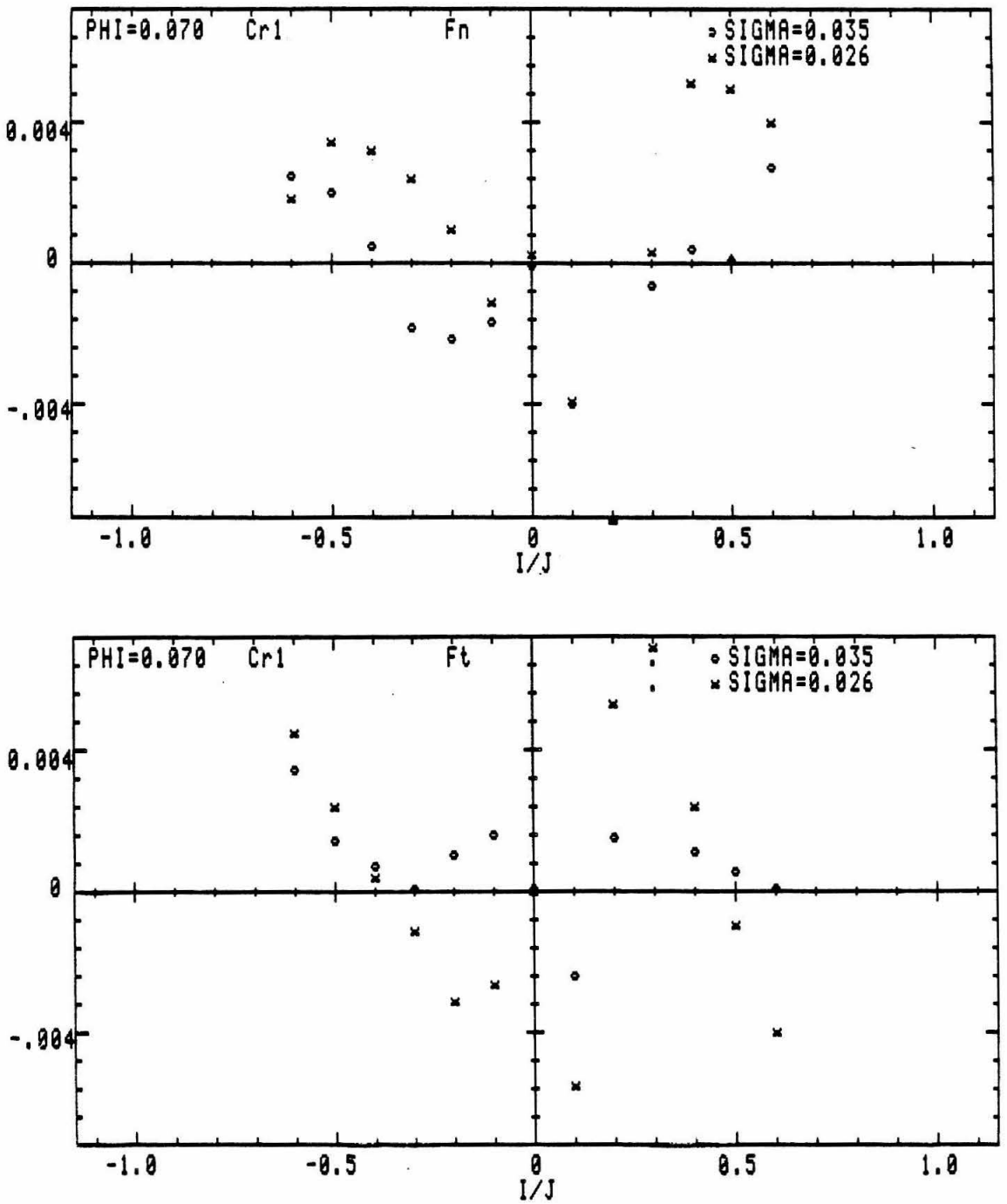

Figure 5.25: Effect of cavitation ($\sigma = 0.035$ and $\sigma = 0.026$) on the normal and tangential forces for $\phi = 0.070$ (Cr_1).

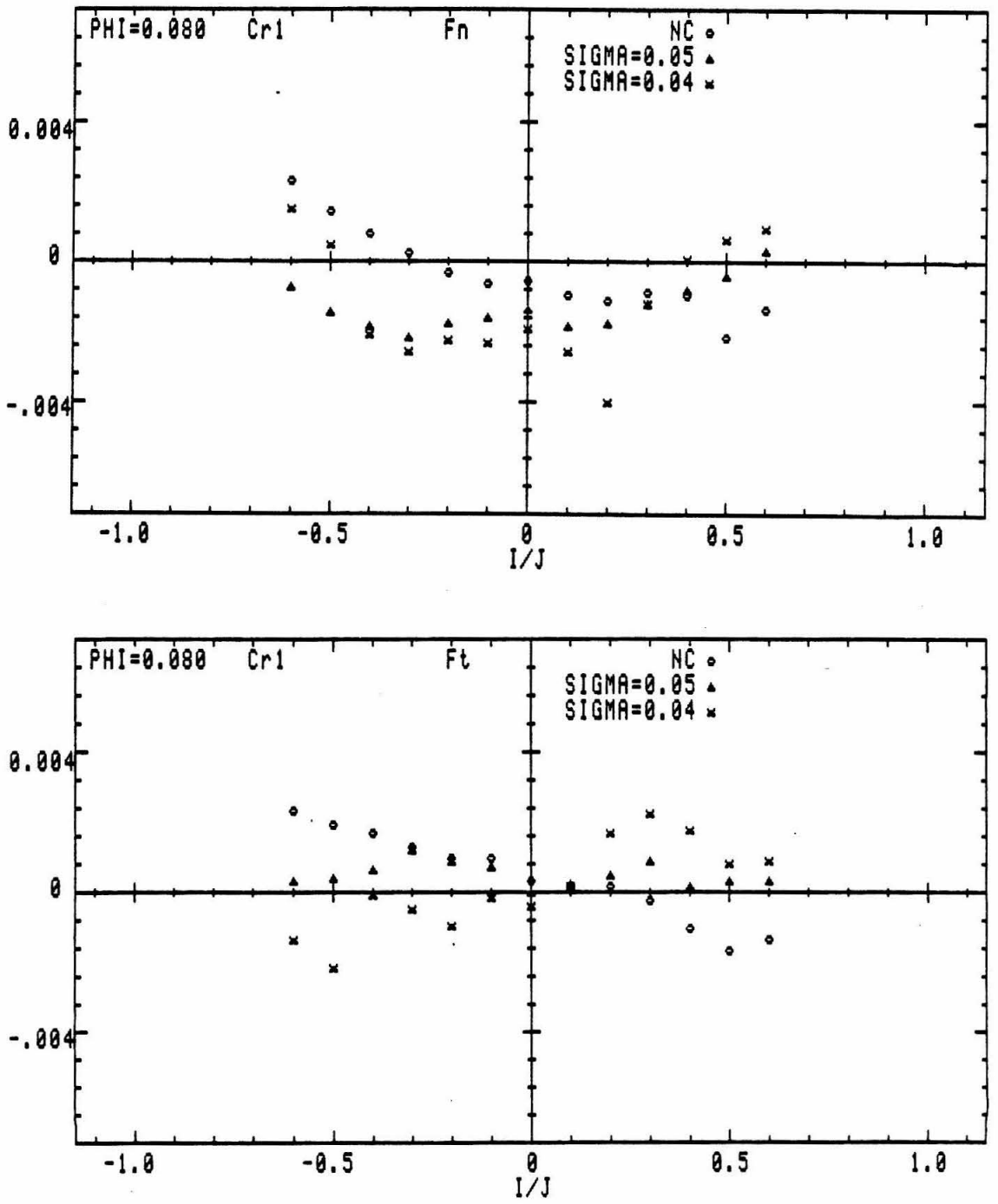

Figure 5.26: Effect of cavitation on the normal and tangential forces for $\phi = 0.080$ (Cr_1).

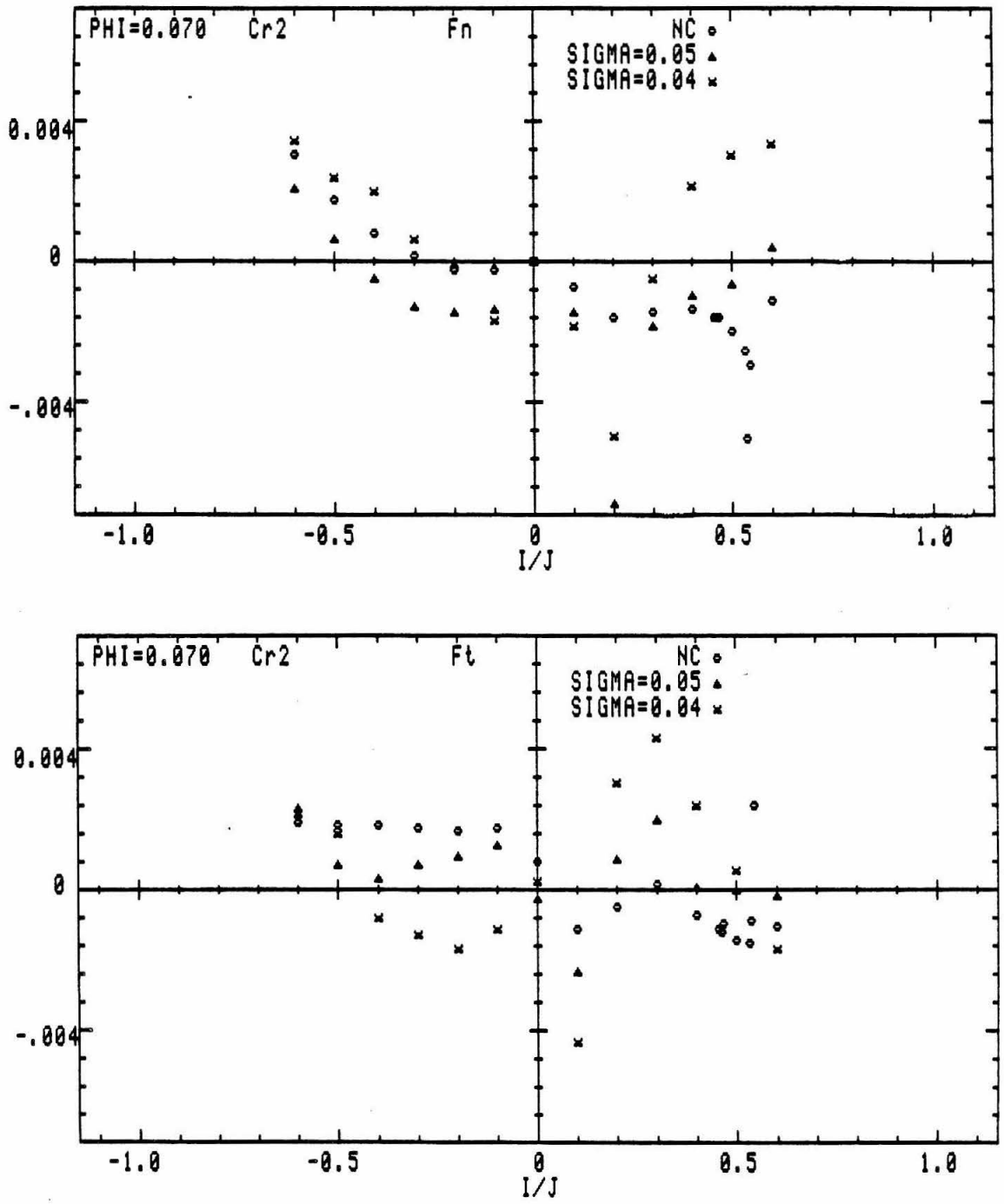

Figure 5.27: Effect of cavitation on the normal and tangential forces for $\phi = 0.070$ (Cr_2).

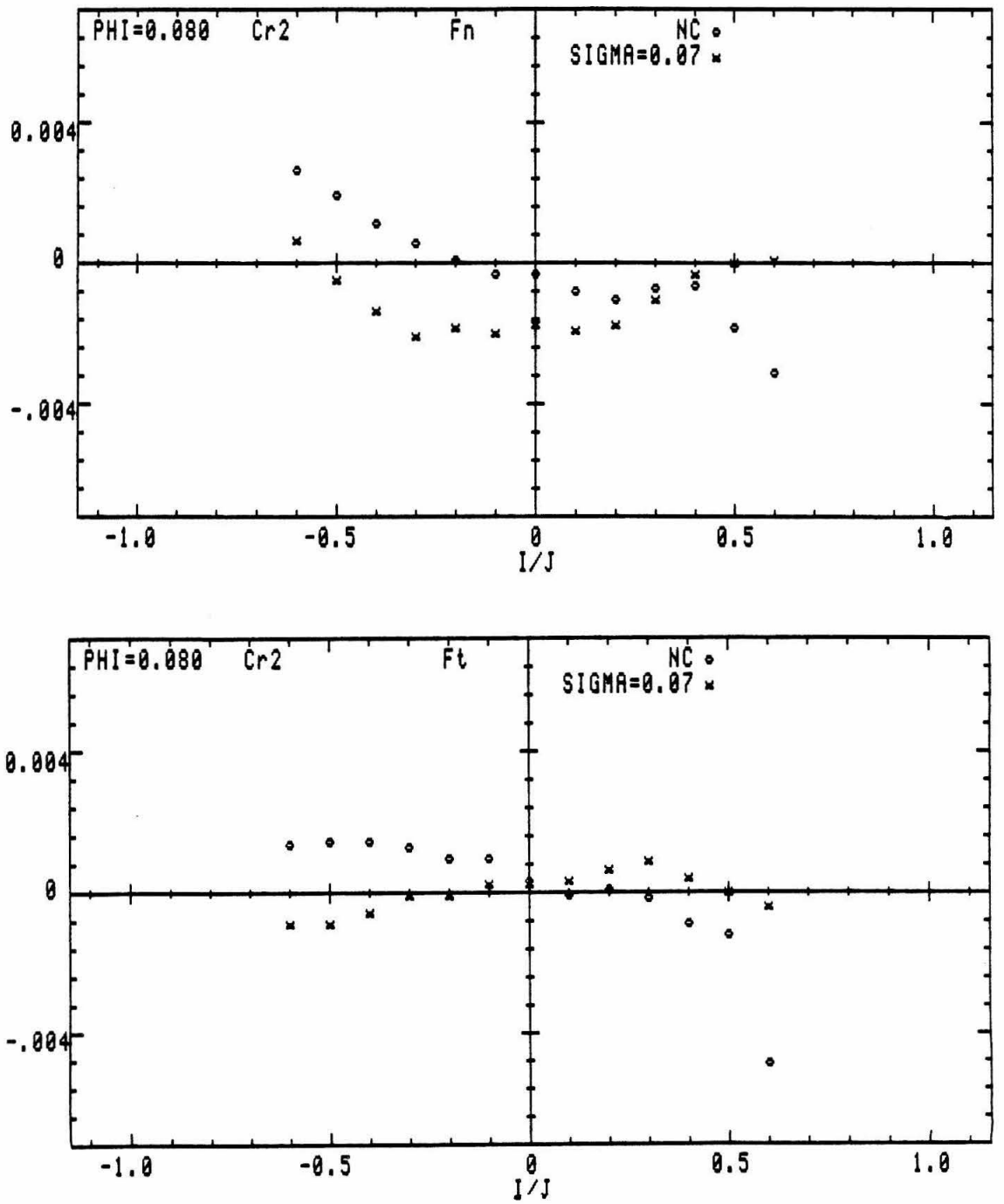

Figure 5.28: Comparison of unsteady forces in noncavitating flow and in the presence of moderate cavitation with $\sigma = 0.070$ ($\phi = 0.080$, Cr_2).

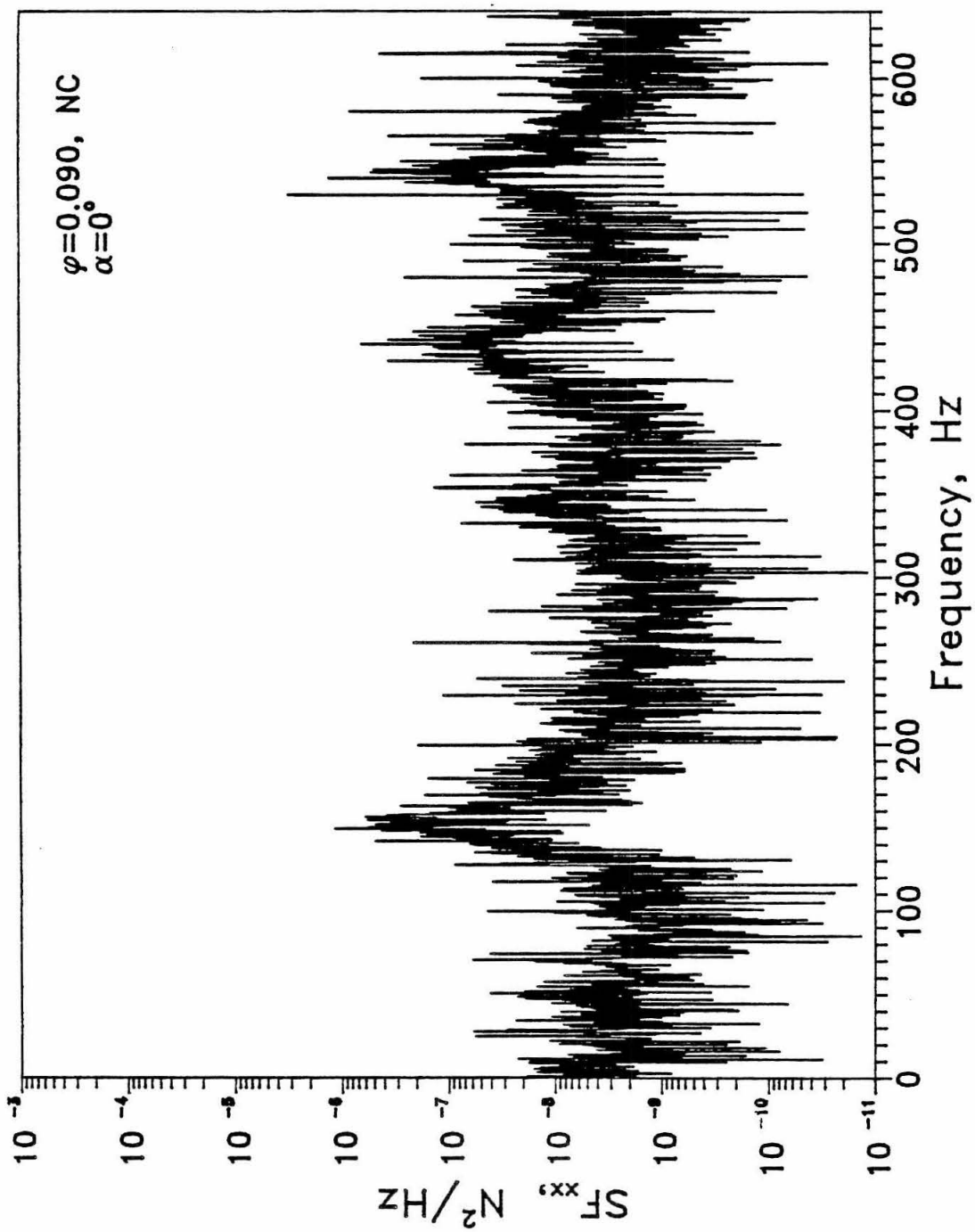

Figure 5.29: Spectral density of the X-component of the lateral force measured in the laboratory frame with the impeller at the top of the whirl orbit ($\phi = 0.90$, noncavitating flow).

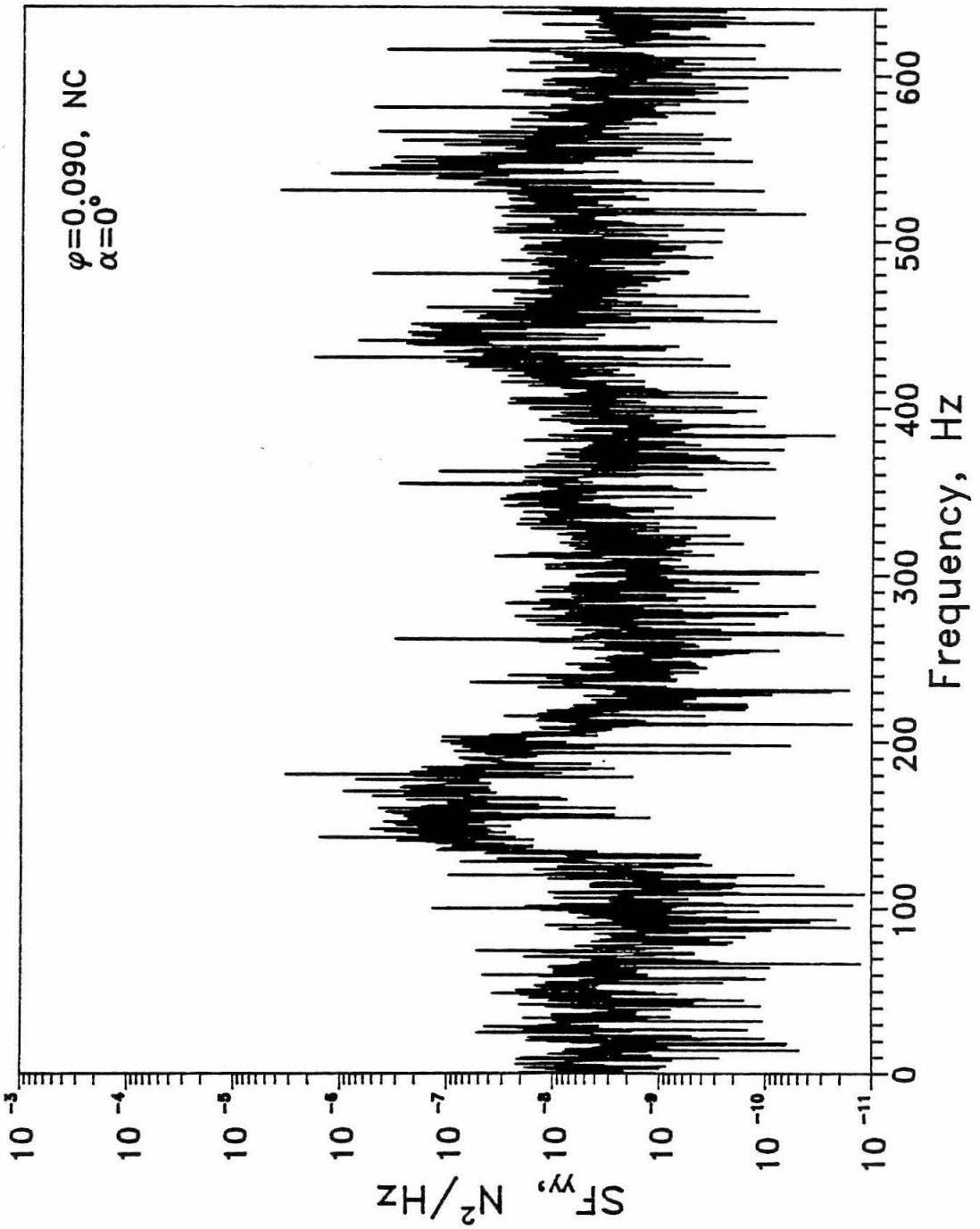

Figure 5.30: Spectral density of the Y-component of the lateral force measured in the laboratory frame with the impeller at the top of the whirl orbit ($\phi = 0.90$, noncavitating flow).

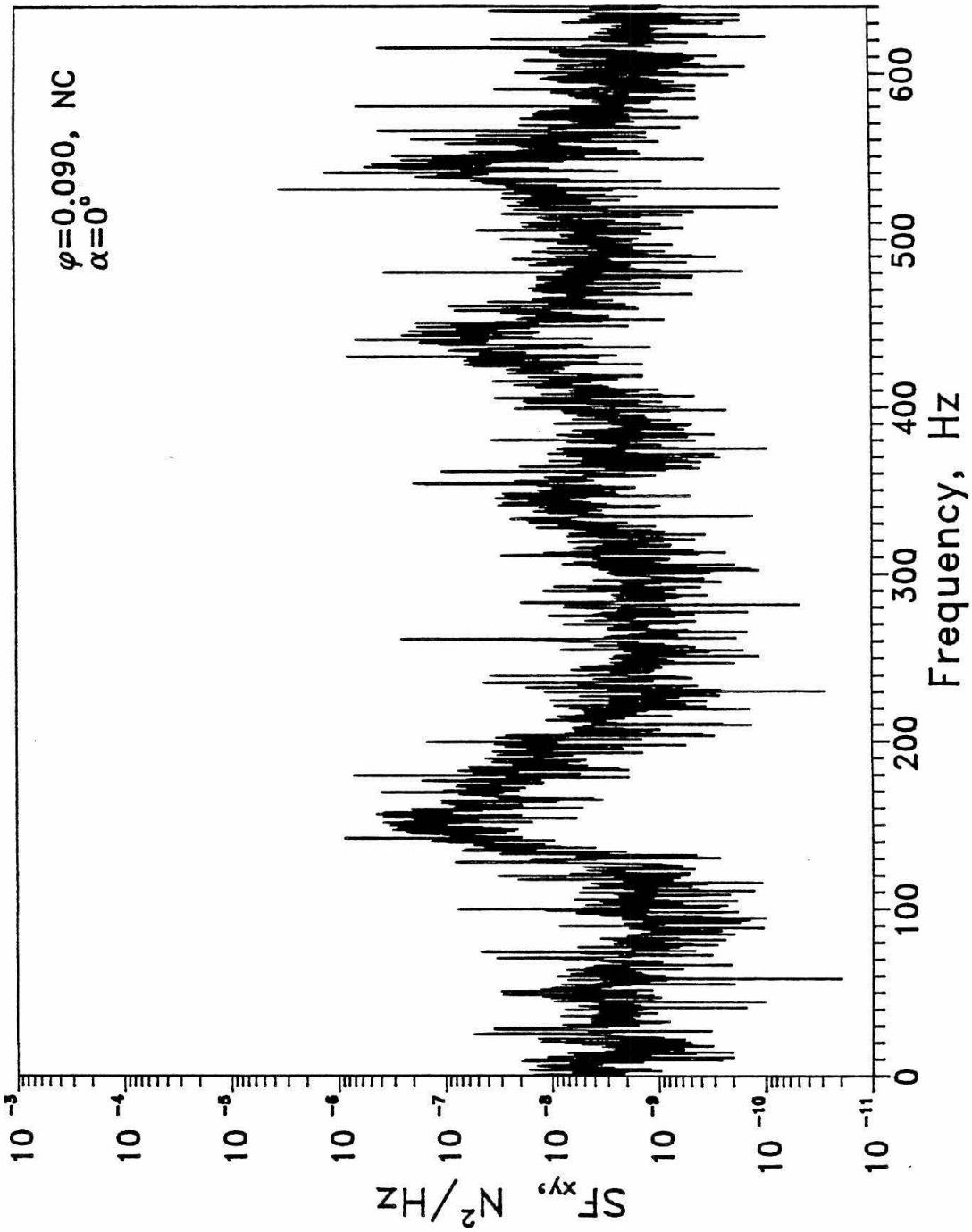

Figure 5.31: Cross-spectral density of the lateral force components measured in the laboratory frame with the impeller at the top of the whirl orbit ($\phi = 0.090$, noncavitating flow).

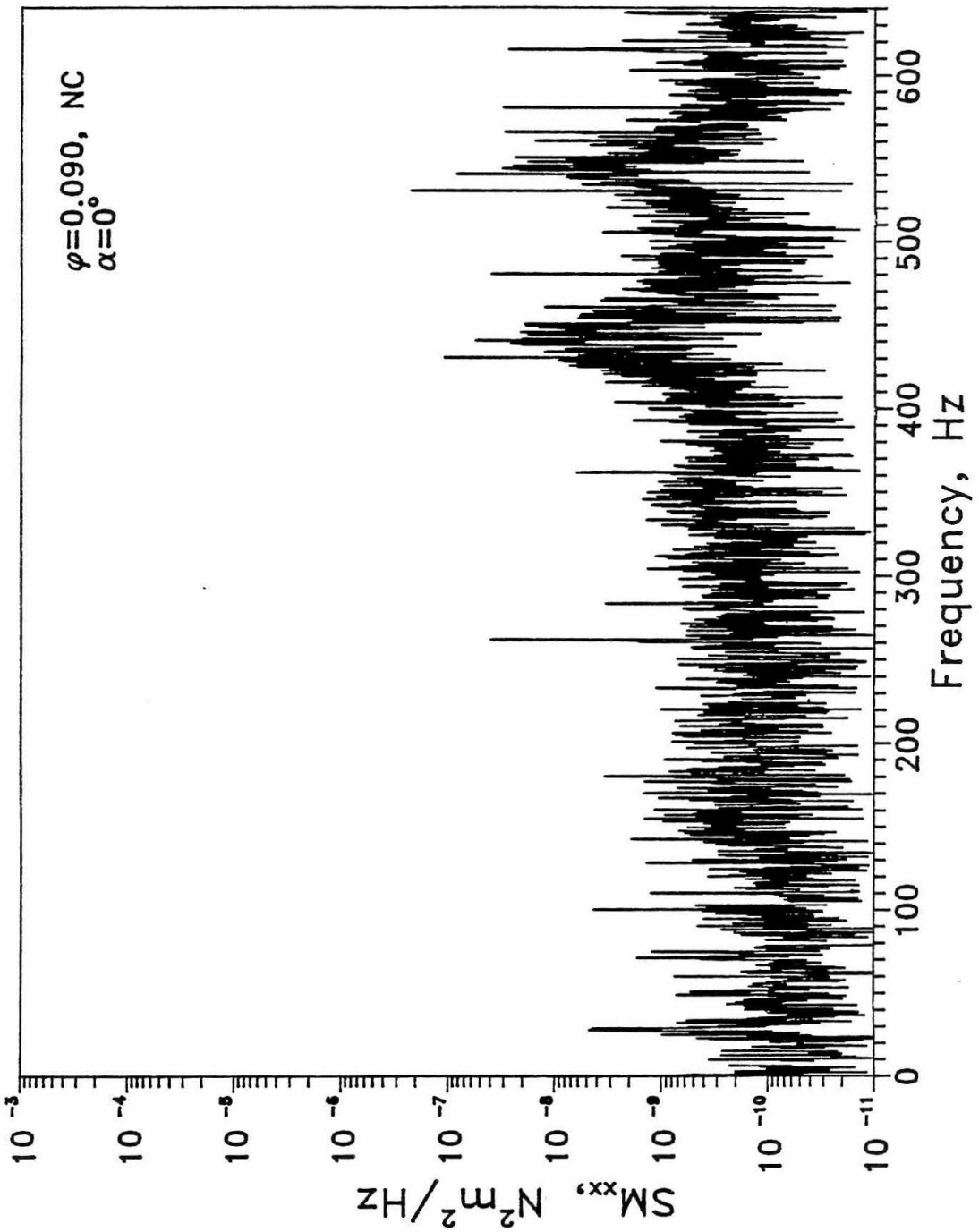

Figure 5.32: Spectral density of the X-component of the moment measured in the laboratory frame with the impeller at the top of the whirl orbit ($\phi = 0.90$, noncavitating flow).

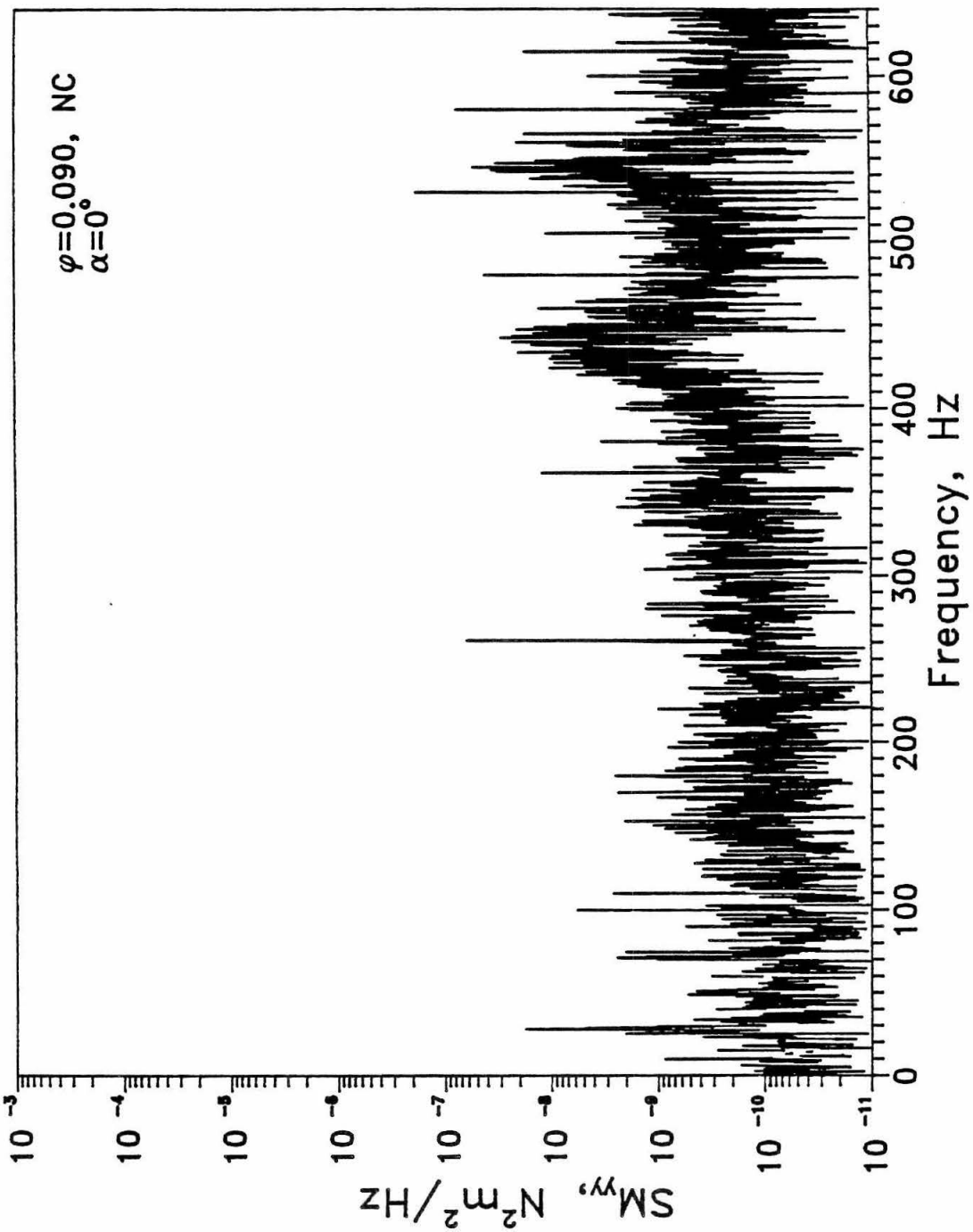

Figure 5.33: Spectral density of the Y-component of the moment measured in the laboratory frame with the impeller at the top of the whirl orbit ($\phi = 0.90$, noncavitating flow).

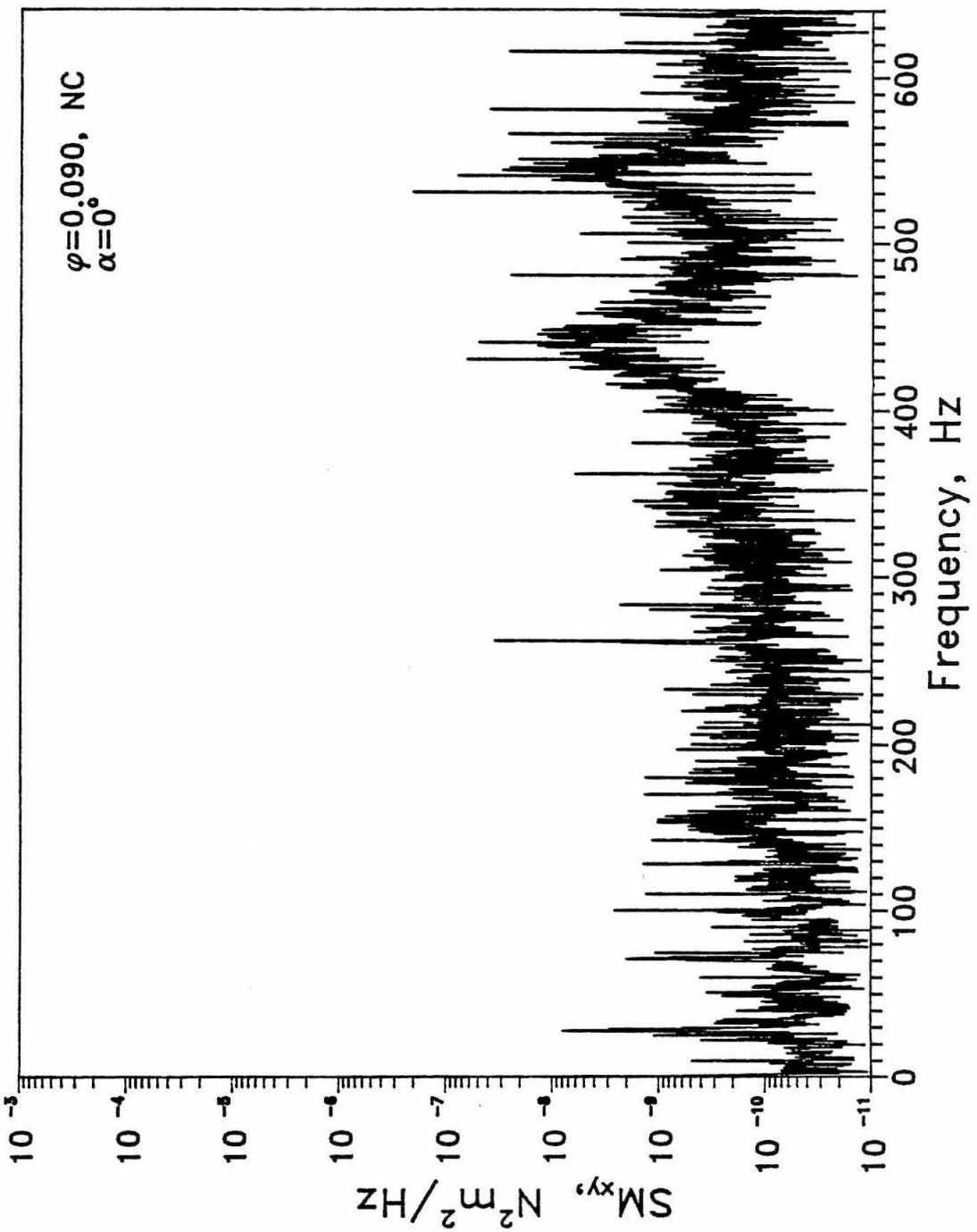

Figure 5.34: Cross-spectral density of the moment components measured in the laboratory frame with the impeller at the top of the whirl orbit ($\phi = 0.090$, non-cavitating flow).

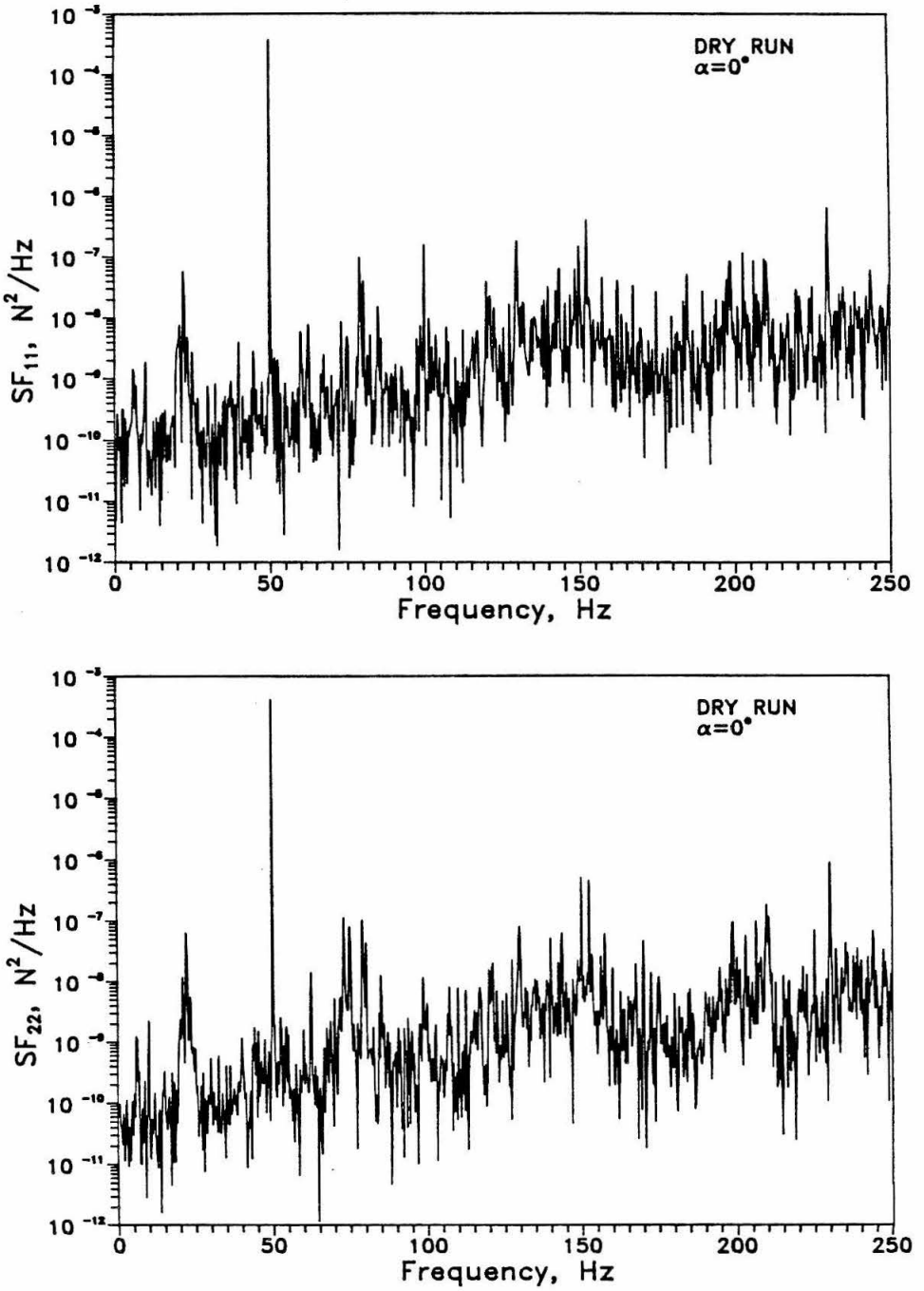

Figure 5.35: Spectral densities of the lateral force components measured in the rotating frame with the impeller at the top of the whirl orbit running in air.

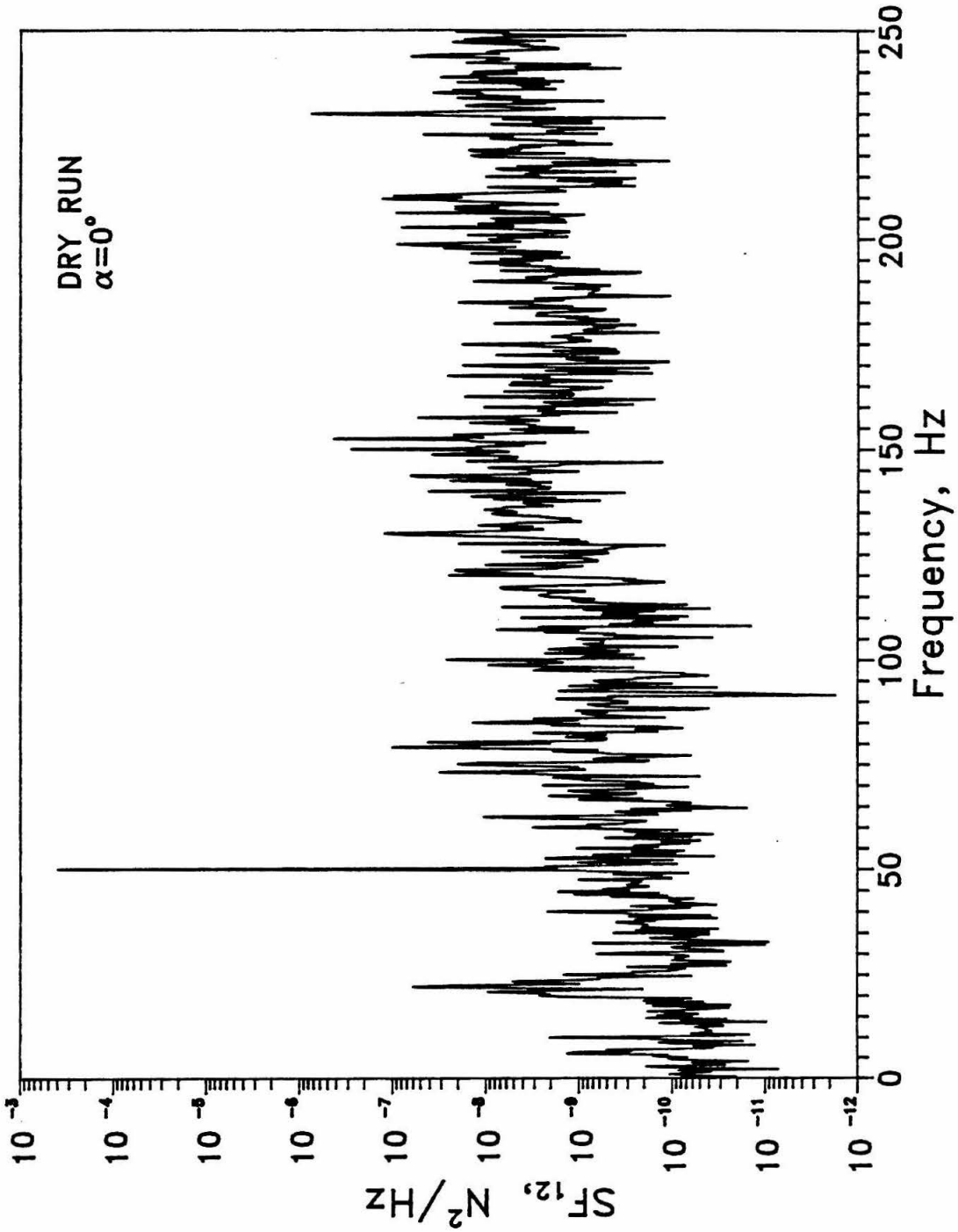

Figure 5.36: Cross-spectral density of the lateral force components measured in the rotating frame with the impeller at the top of the whirl orbit running in air.

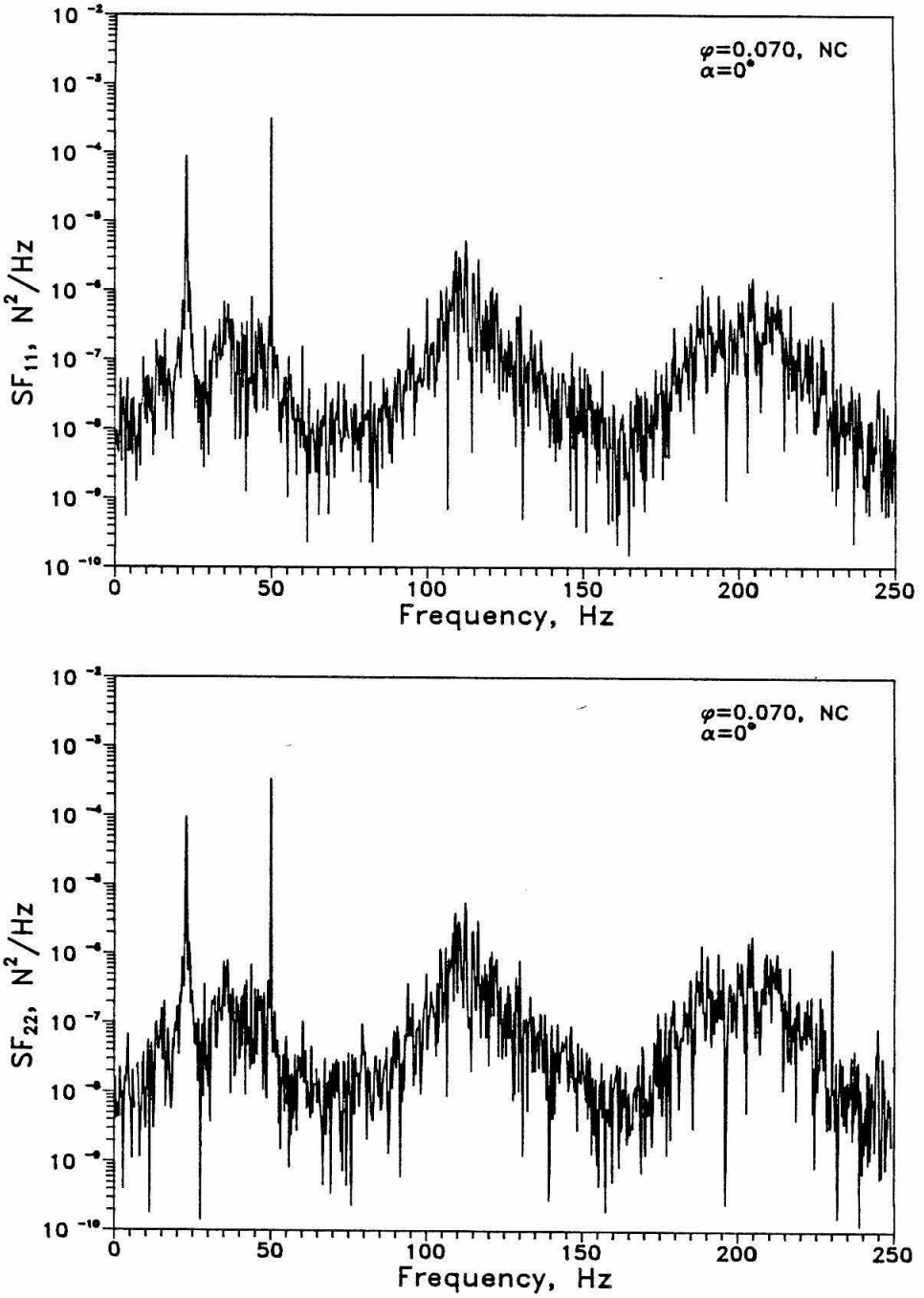

Figure 5.37: Spectral densities of the lateral force components measured in the rotating frame ($\alpha = 0°$), in noncavitating flow ($\phi = 0.070$).

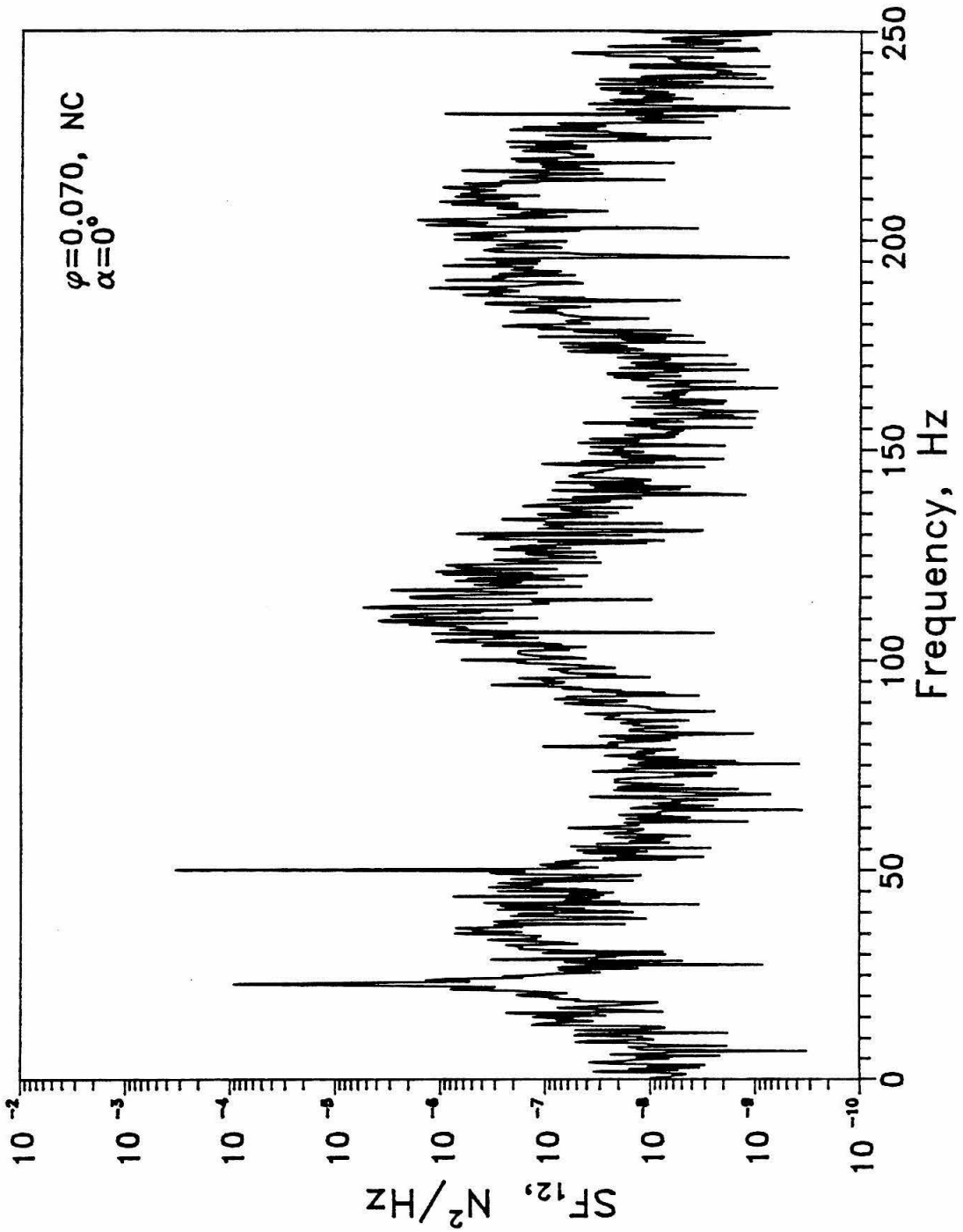

Figure 5.38: Cross-spectral density of the lateral force components measured in the rotating frame ($\alpha = 0°$), in noncavitating flow ($\phi = 0.070$).

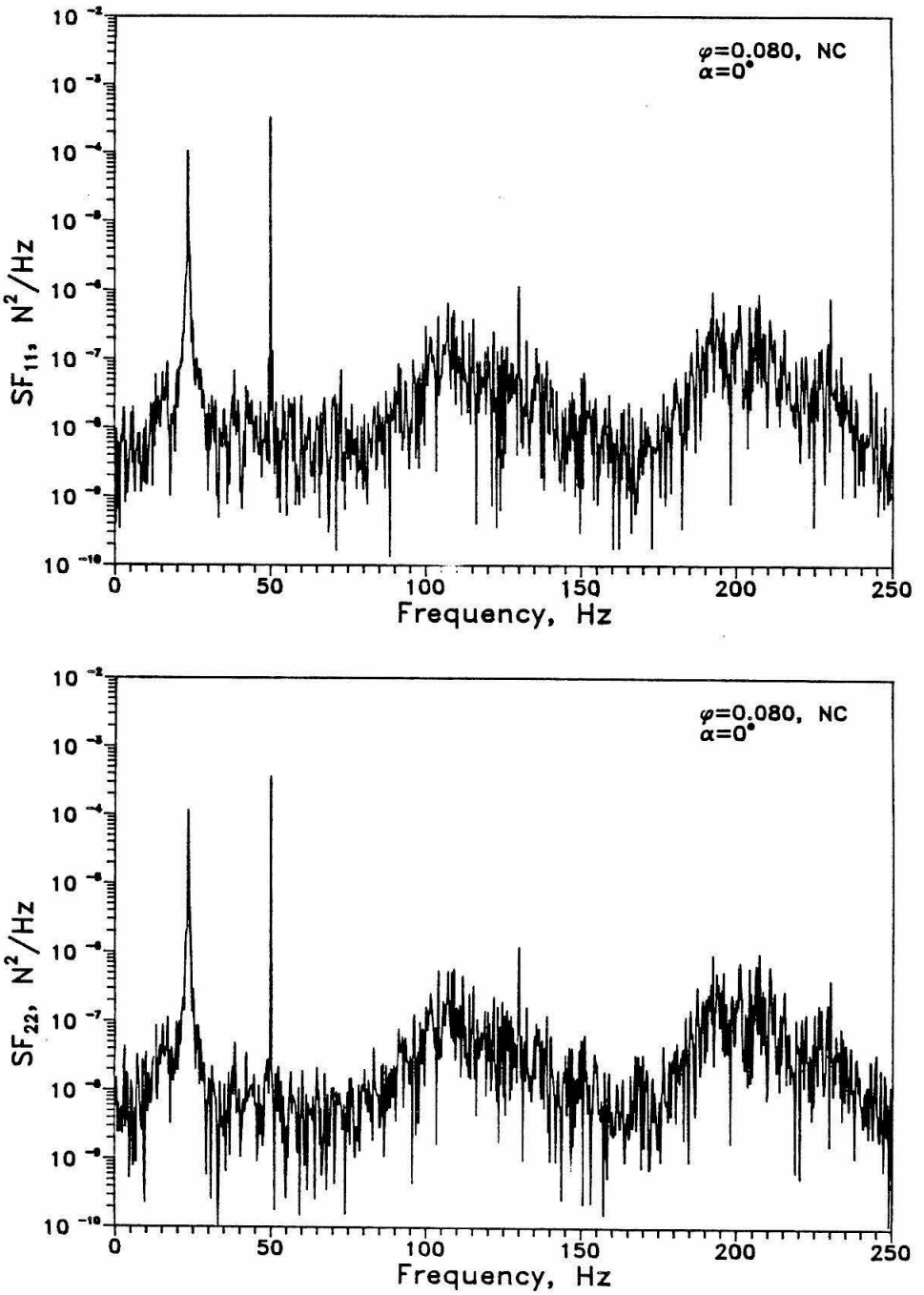

Figure 5.39: Spectral densities of the lateral force components measured in the rotating frame ($\alpha = 0°$), in noncavitating flow ($\phi = 0.080$).

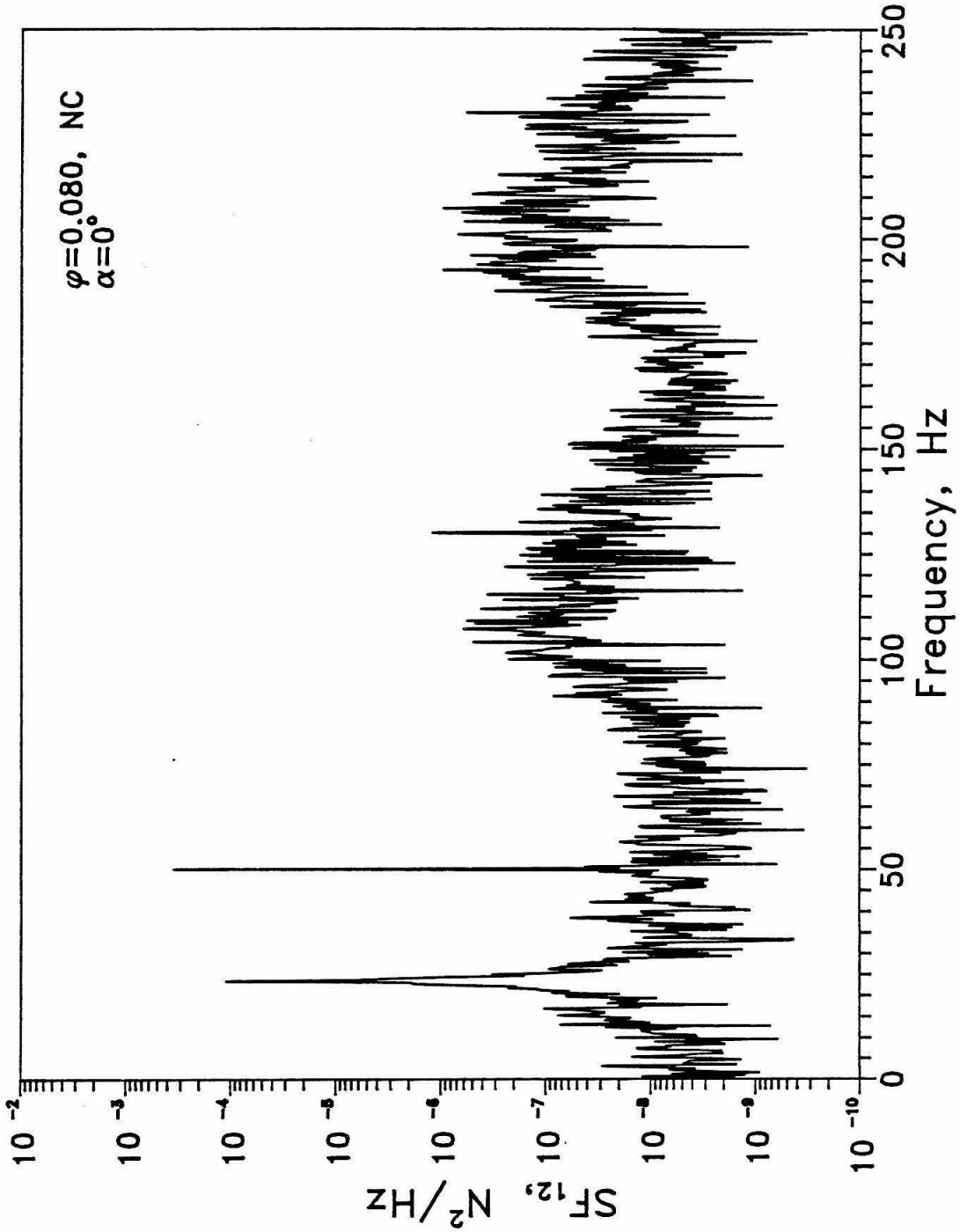

Figure 5.40: Cross-spectral density of the lateral force components measured in the rotating frame ($\alpha = 0°$), in noncavitating flow ($\phi = 0.080$).

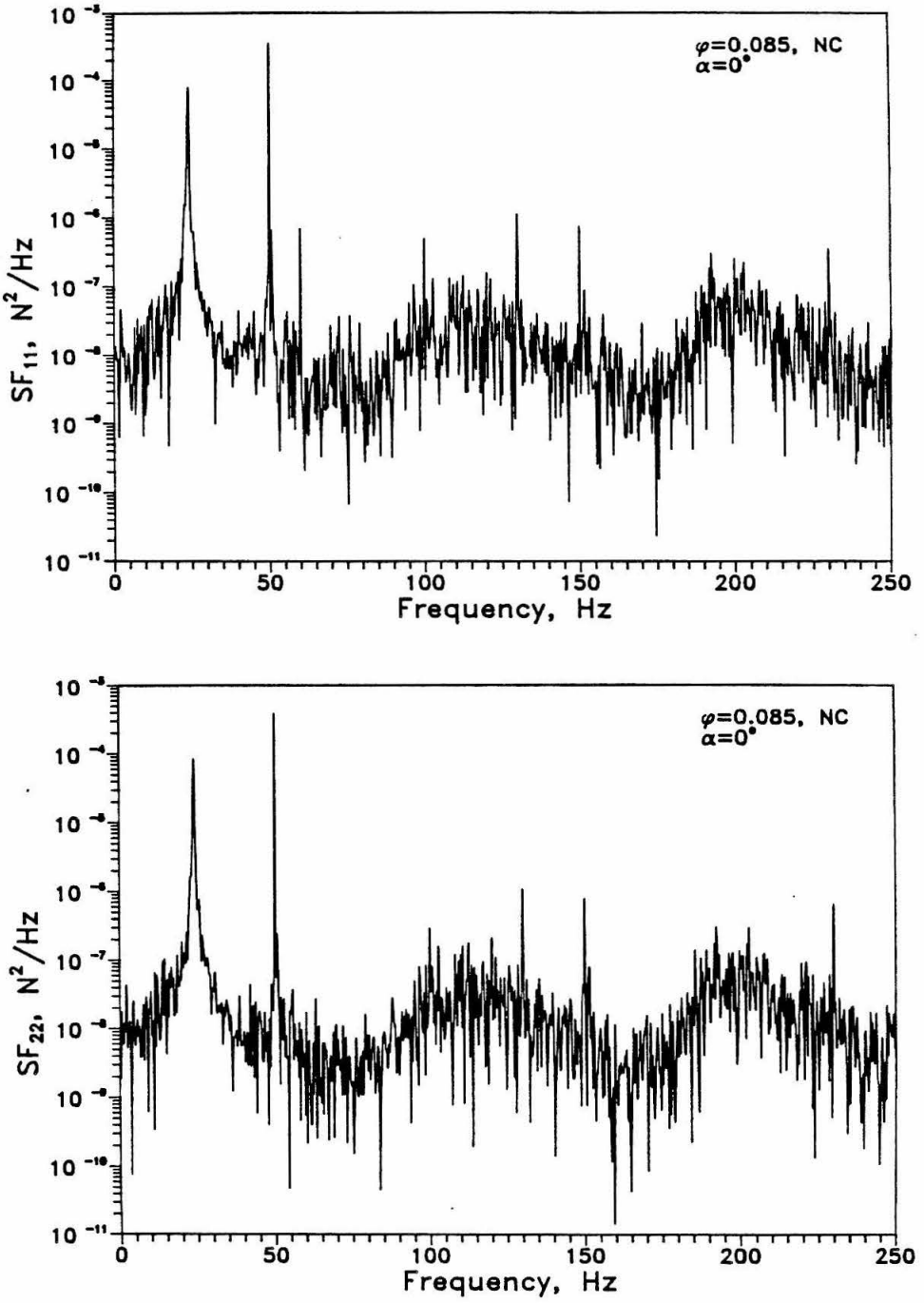

Figure 5.41: Spectral densities of the lateral force components measured in the rotating frame ($\alpha = 0°$), in noncavitating flow (at design, $\phi = 0.085$).

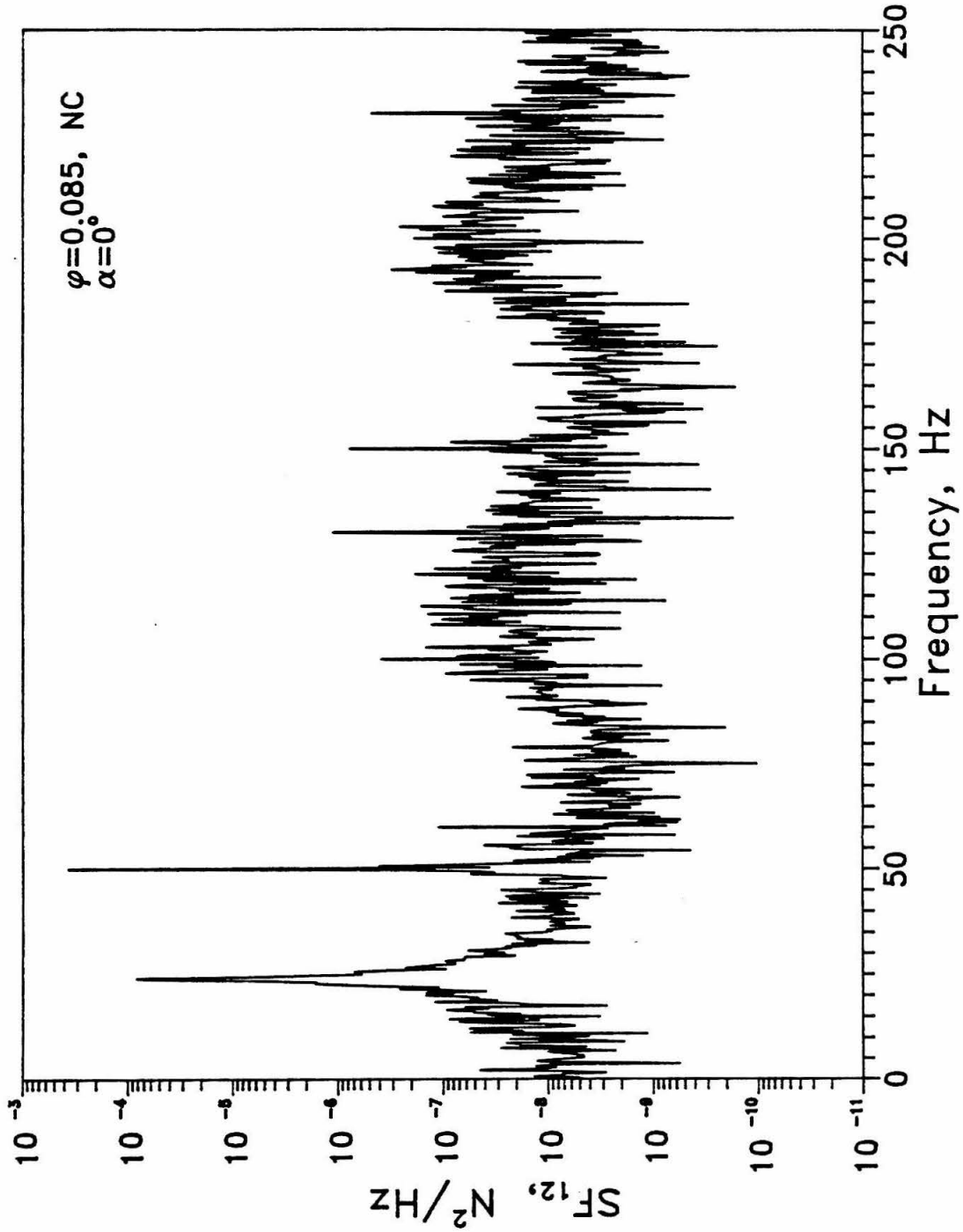

Figure 5.42: Cross-spectral density of the lateral force components measured in the rotating frame ($\alpha = 0°$), in noncavitating flow (at design, $\phi = 0.085$).

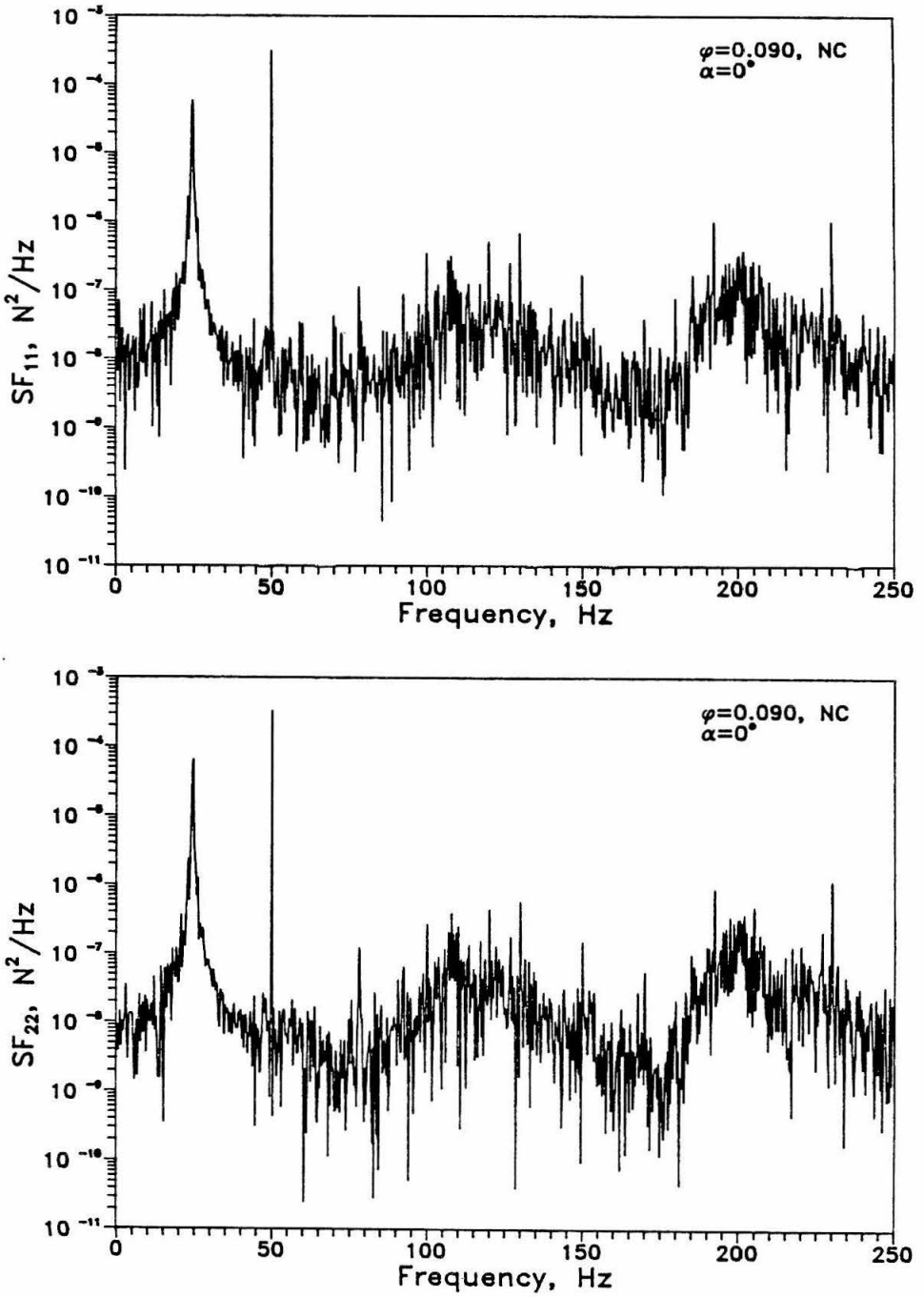

Figure 5.43: Spectral densities of the lateral force components measured in the rotating frame ($\alpha = 0°$), in noncavitating flow ($\phi = 0.090$).

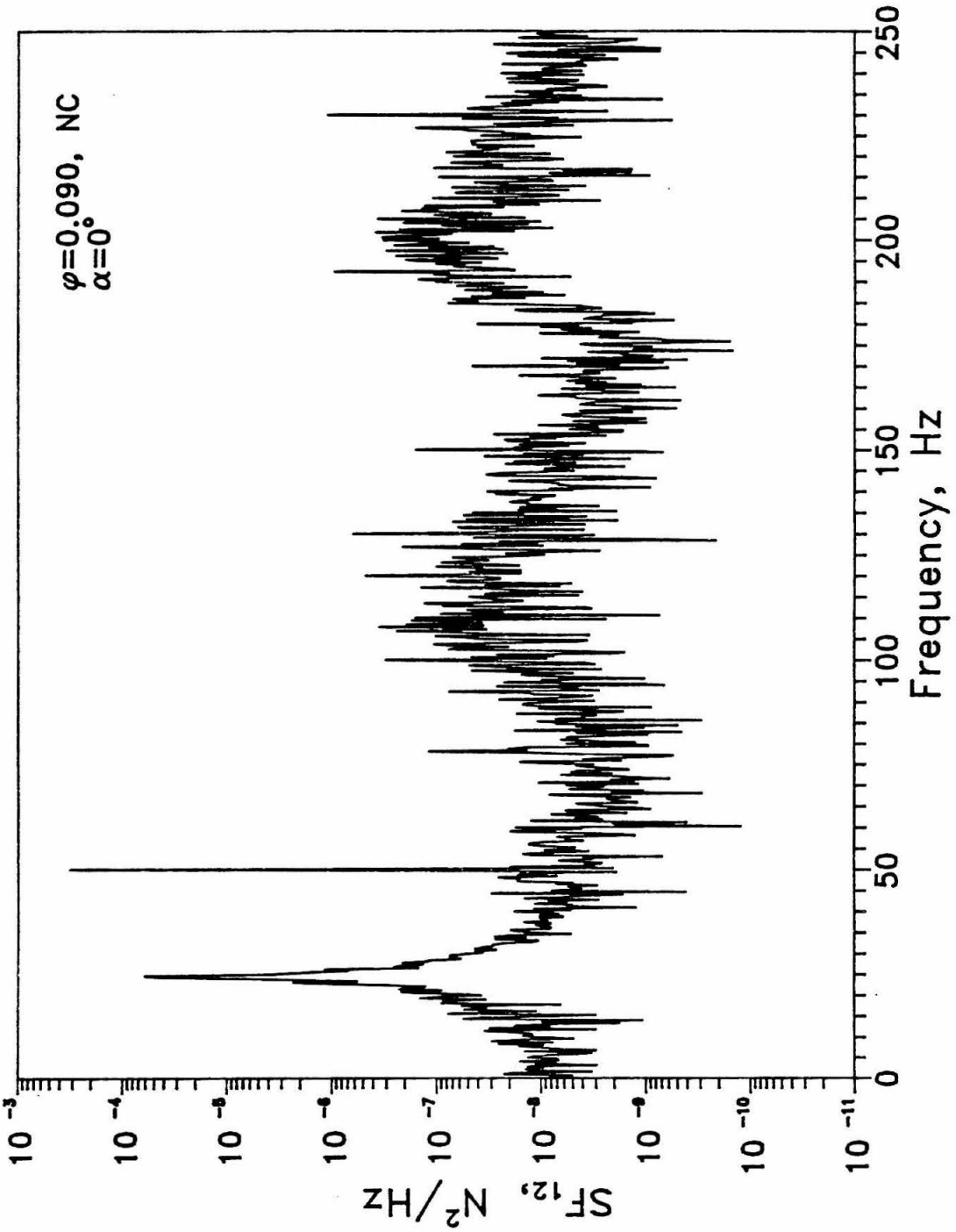

Figure 5.44: Cross-spectral density of the lateral force components measured in the rotating frame ($\alpha = 0°$), in noncavitating flow ($\phi = 0.090$).

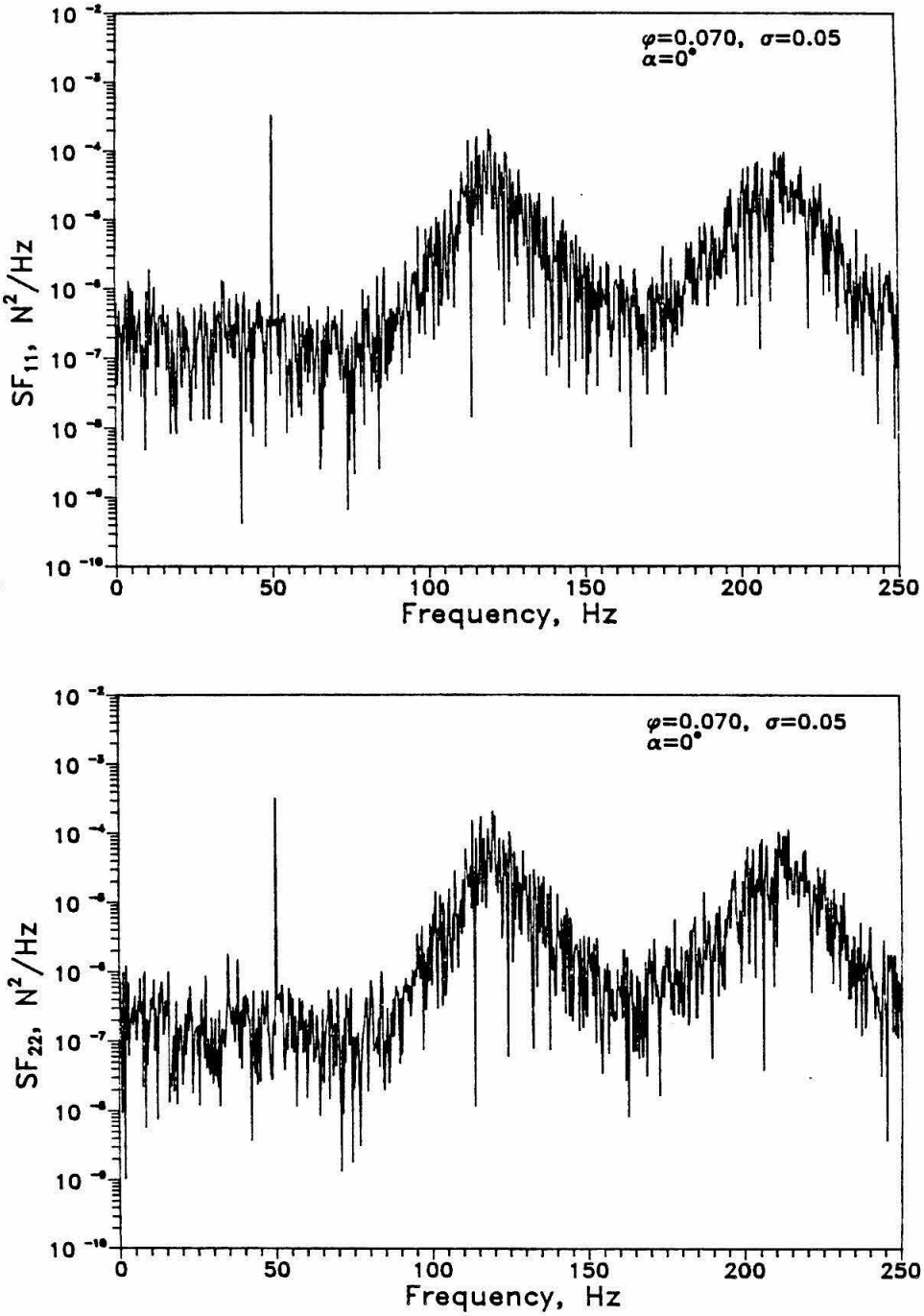

Figure 5.45: Spectral densities of the lateral force components measured in the rotating frame ($\alpha = 0°$), in cavitating flow ($\sigma = 0.05$, $\phi = 0.070$).

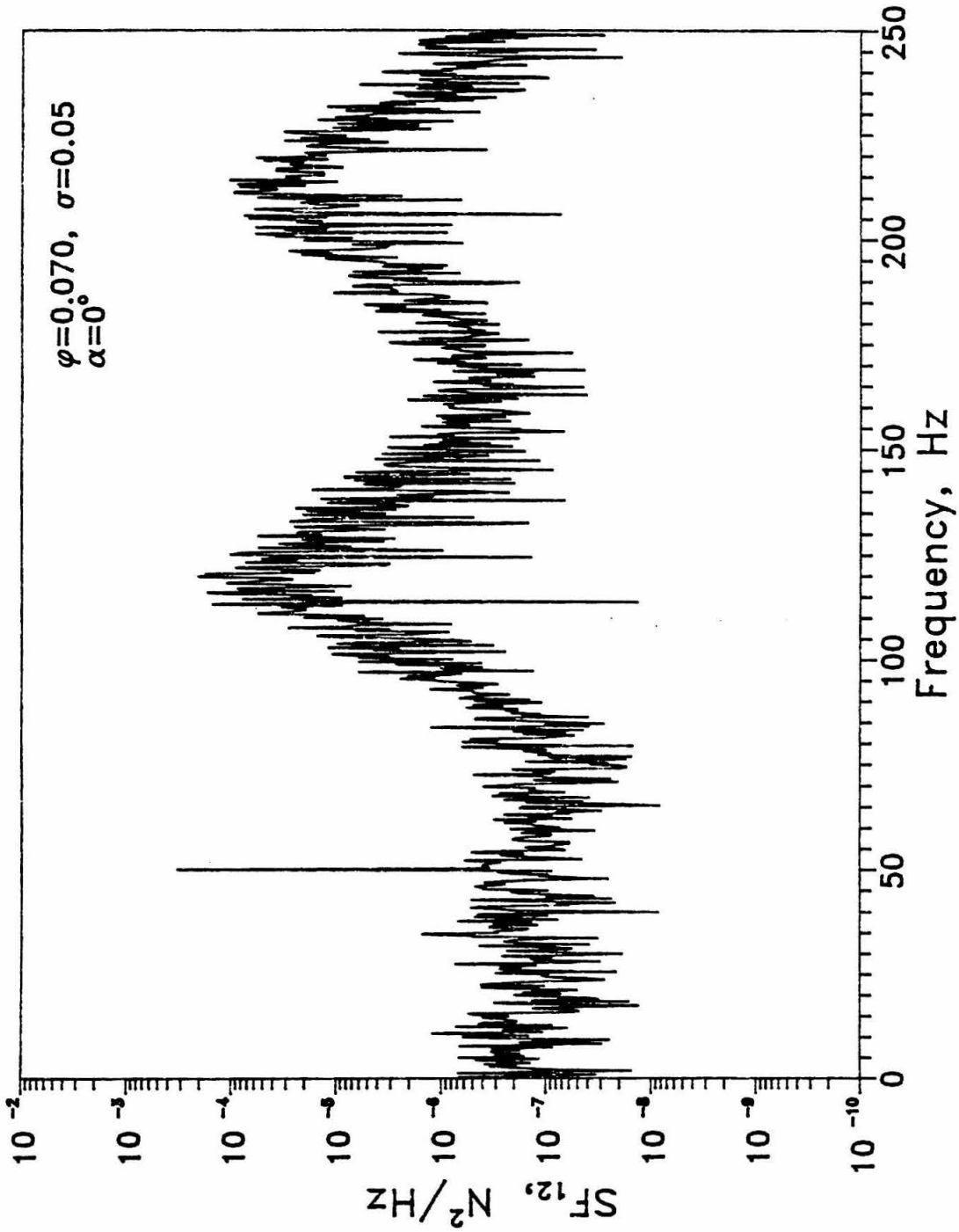

Figure 5.46: Cross-spectral density of the lateral force components measured in the rotating frame ($\alpha = 0°$), in cavitating flow ($\sigma = 0.05$, $\phi = 0.070$).

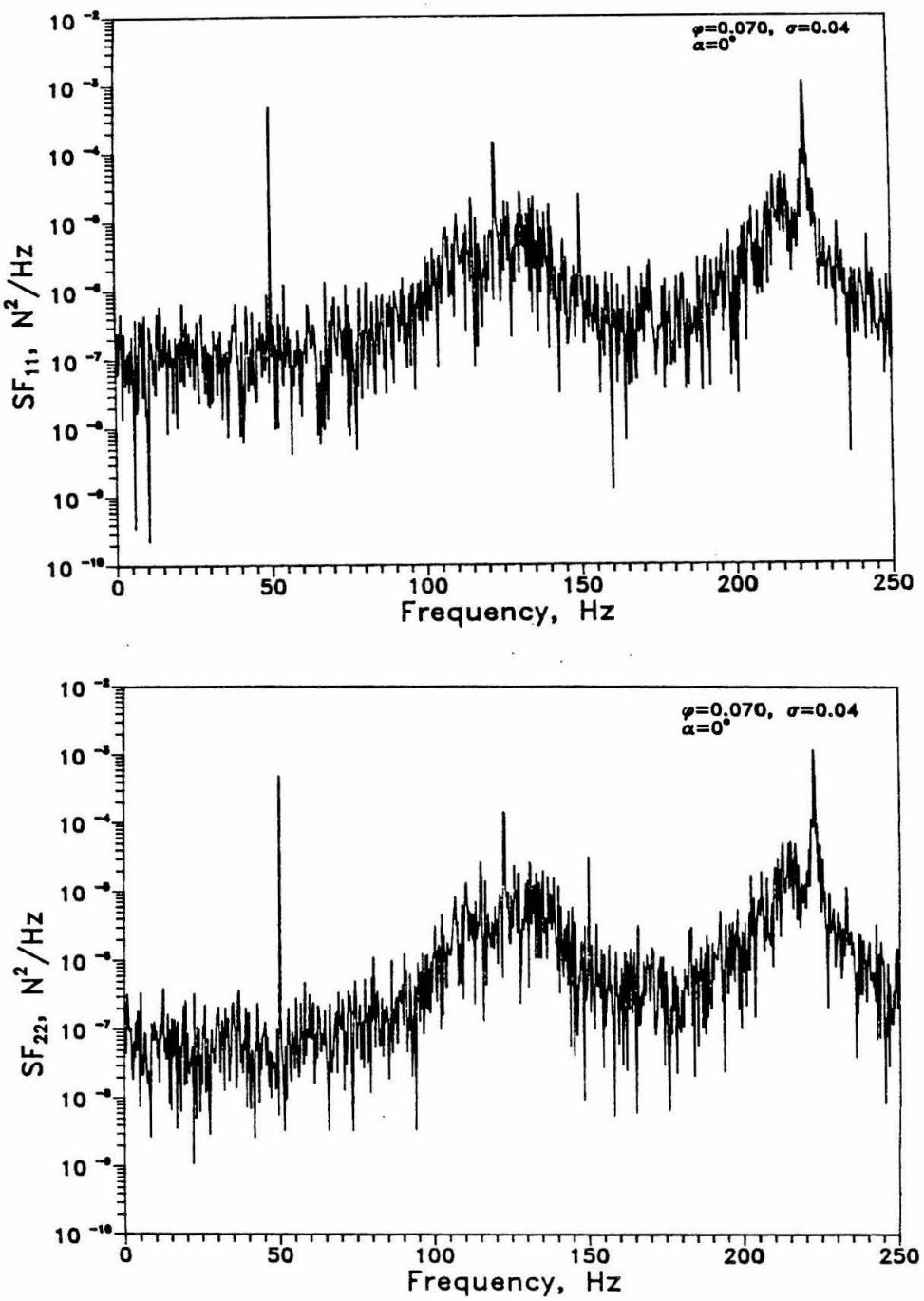

Figure 5.47: Spectral densities of the lateral force components measured in the rotating frame ($\alpha = 0°$), in cavitating flow ($\sigma = 0.04$, $\phi = 0.070$).

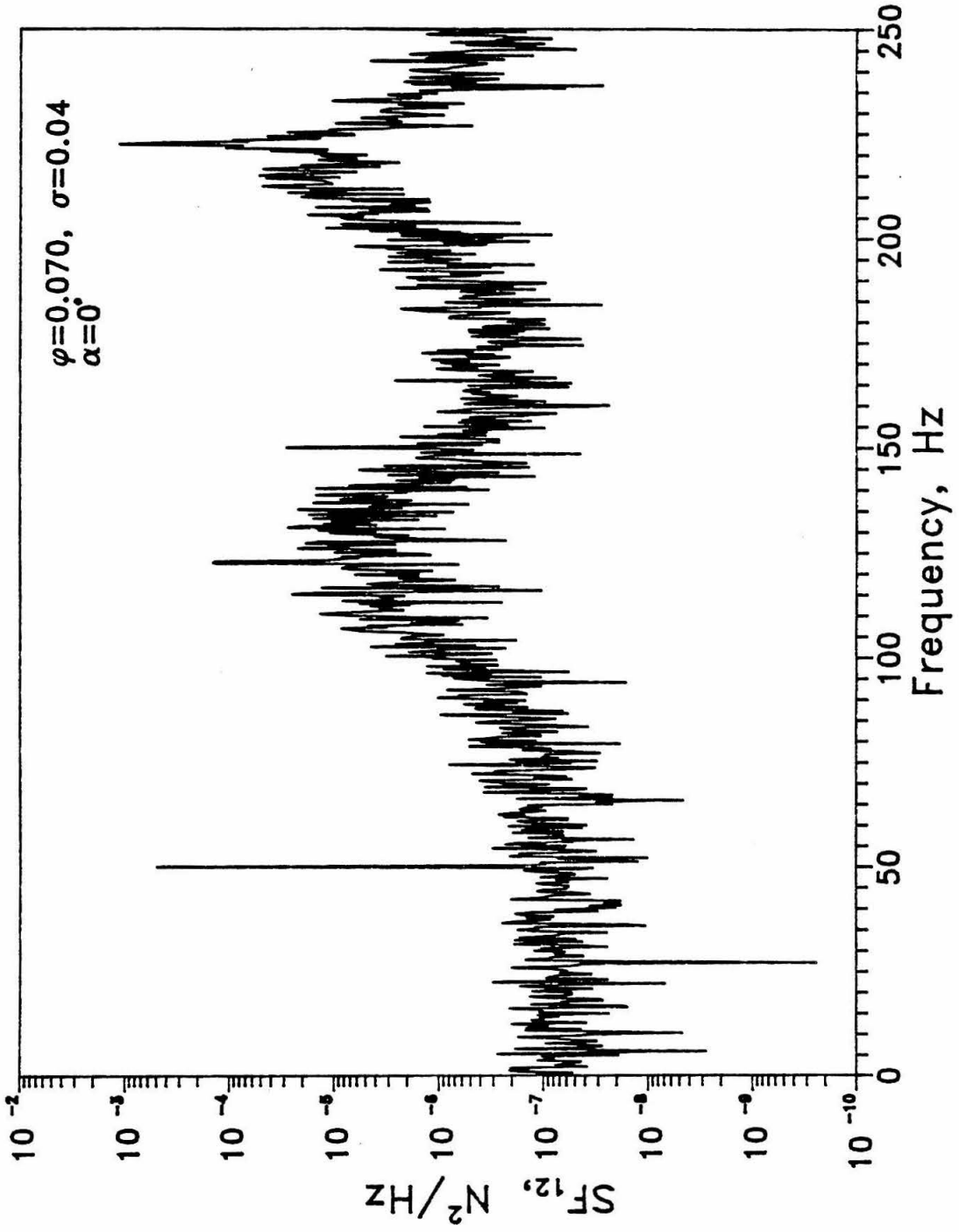

Figure 5.48: Cross-spectral density of the lateral force components measured in the rotating frame ($\alpha = 0°$), in cavitating flow ($\sigma = 0.04$, $\phi = 0.070$).

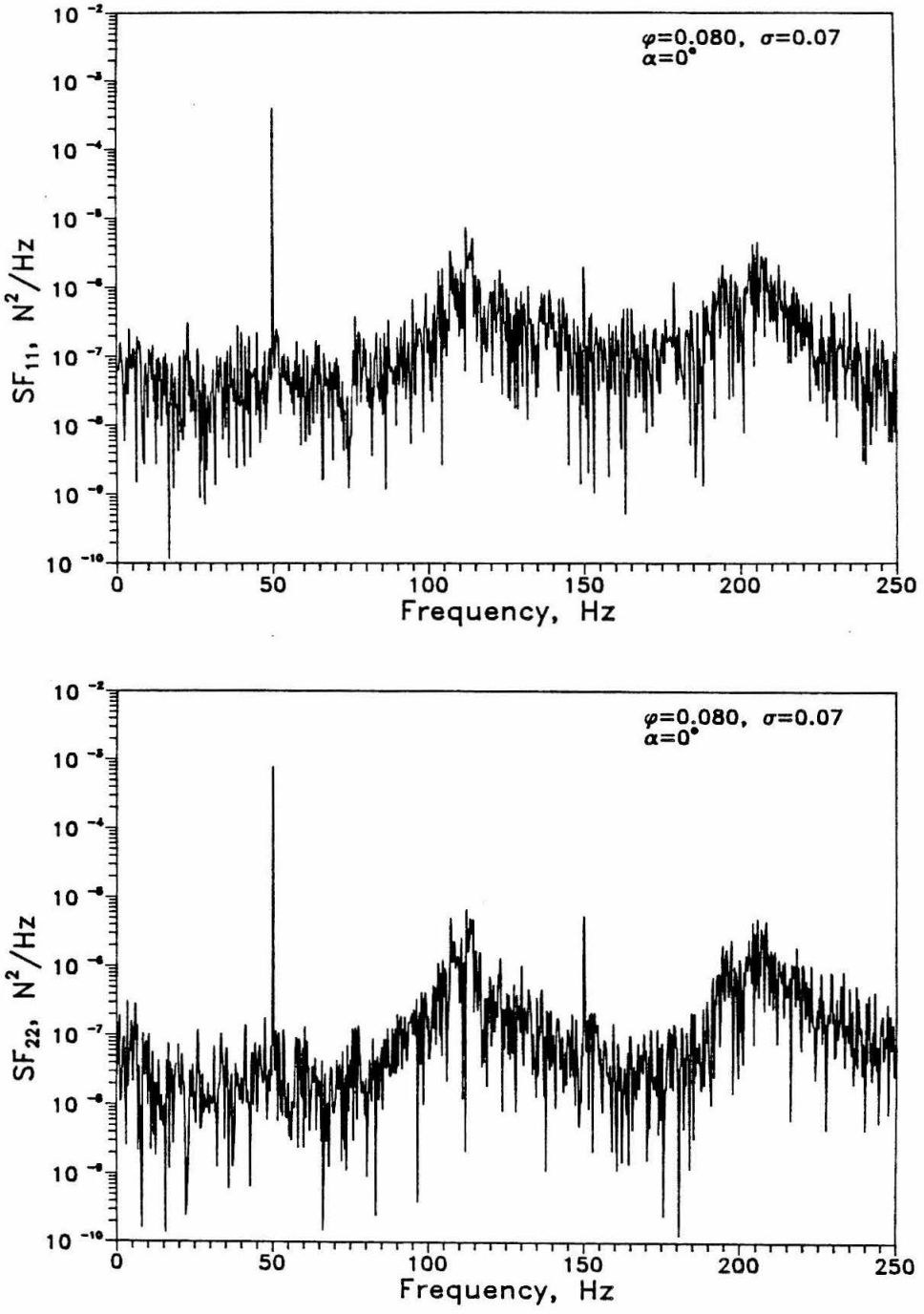

Figure 5.49: Spectral densities of the lateral force components measured in the rotating frame ($\alpha = 0°$), in cavitating flow ($\sigma = 0.07$, $\phi = 0.080$).

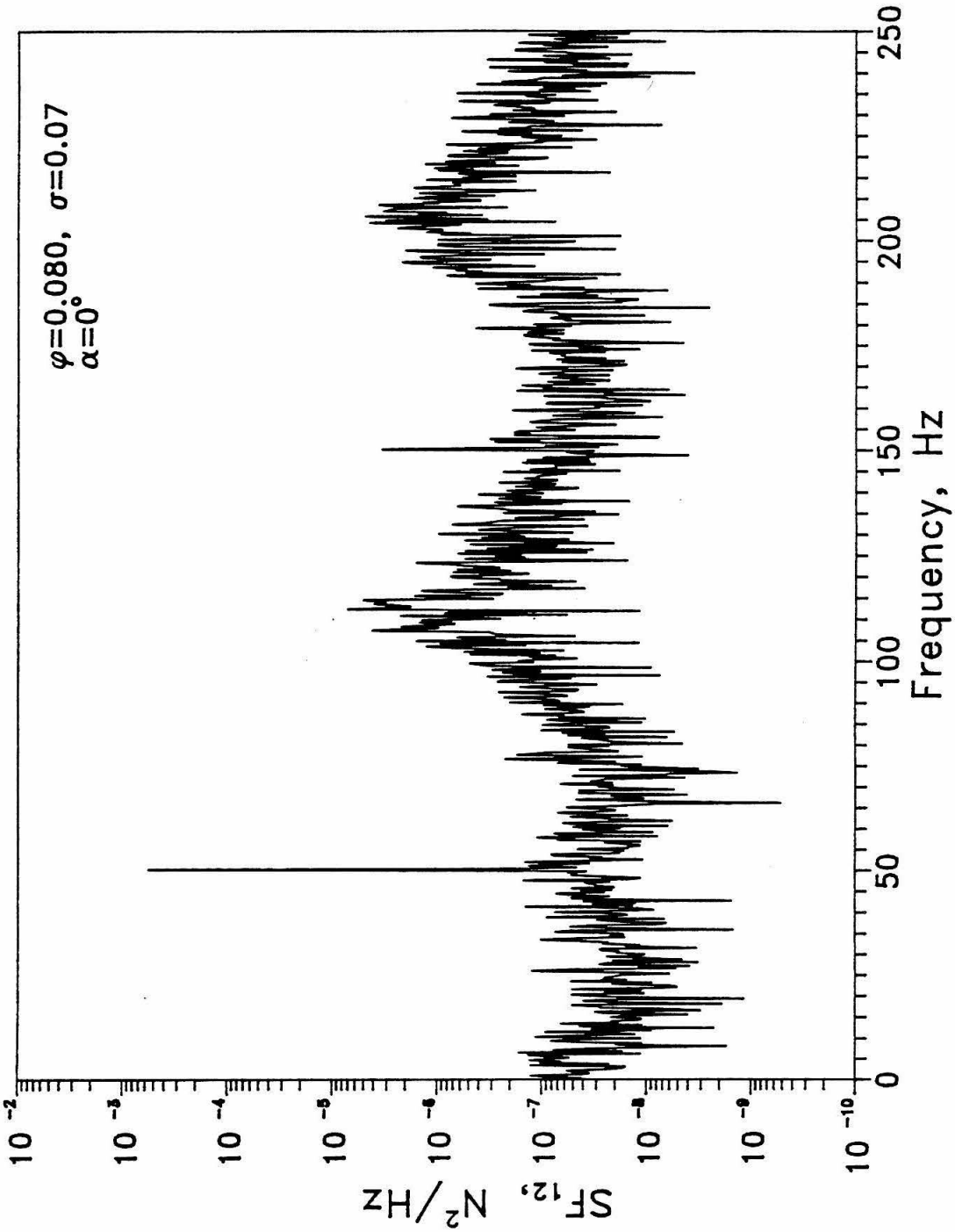

Figure 5.50: Cross-spectral density of the lateral force components measured in the rotating frame ($\alpha = 0°$), in cavitating flow ($\sigma = 0.07$, $\phi = 0.080$).

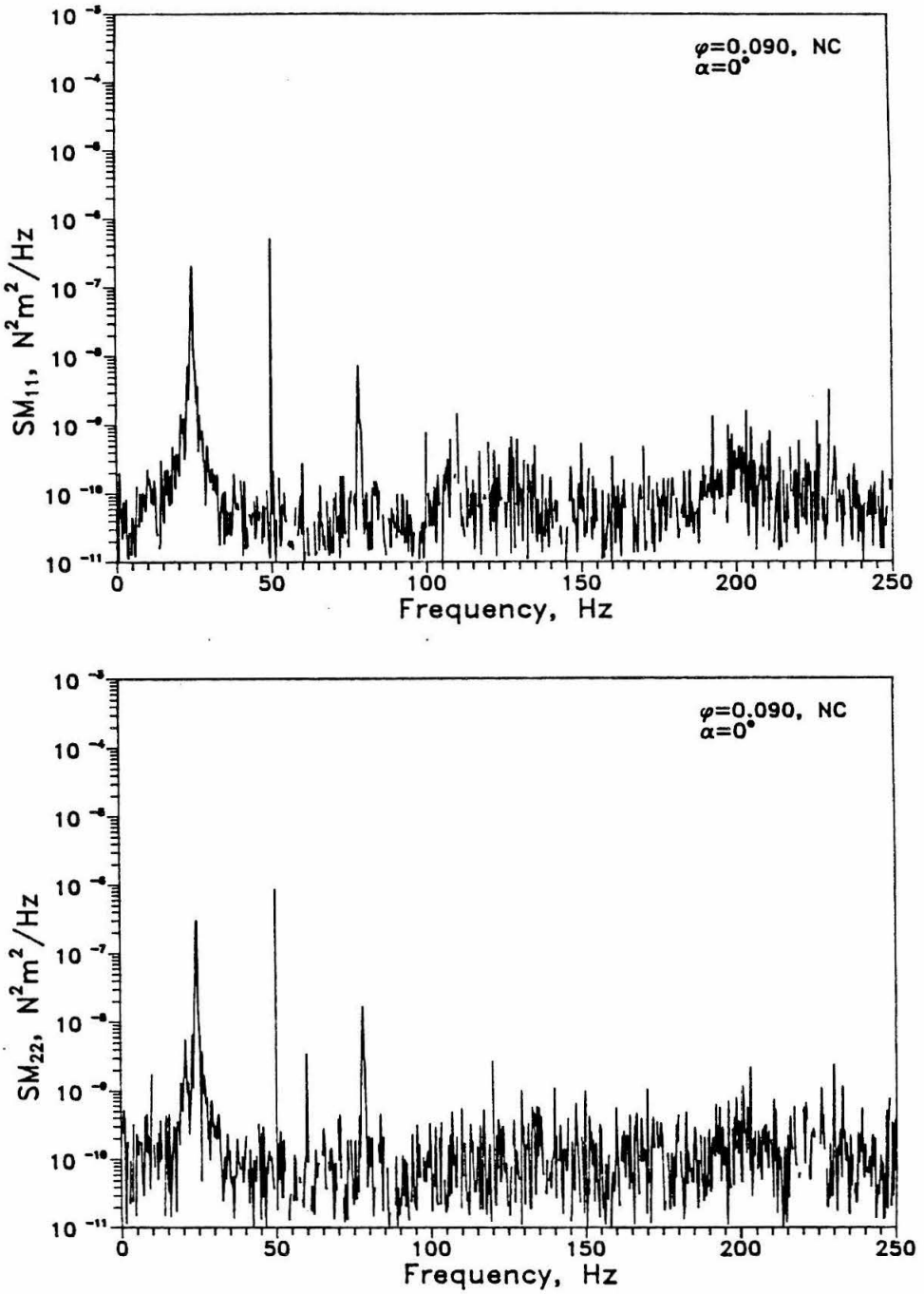

Figure 5.51: Spectral densities of the moment components measured in the rotating frame ($\alpha = 0°$), in noncavitating flow ($\phi = 0.090$).

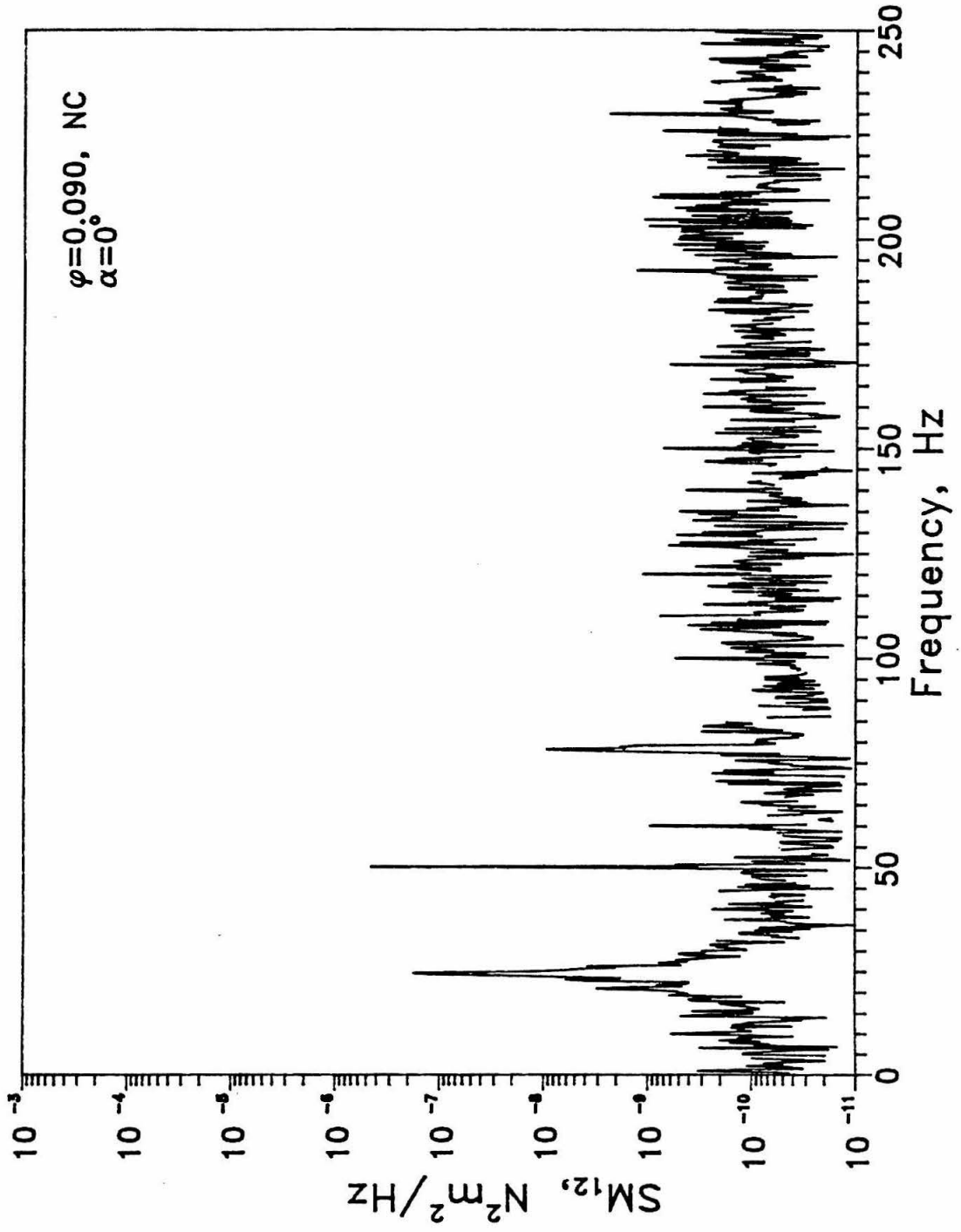

Figure 5.52: Cross-spectral density of the moment components measured in the rotating frame ($\alpha = 0°$), in noncavitating flow ($\phi = 0.090$).

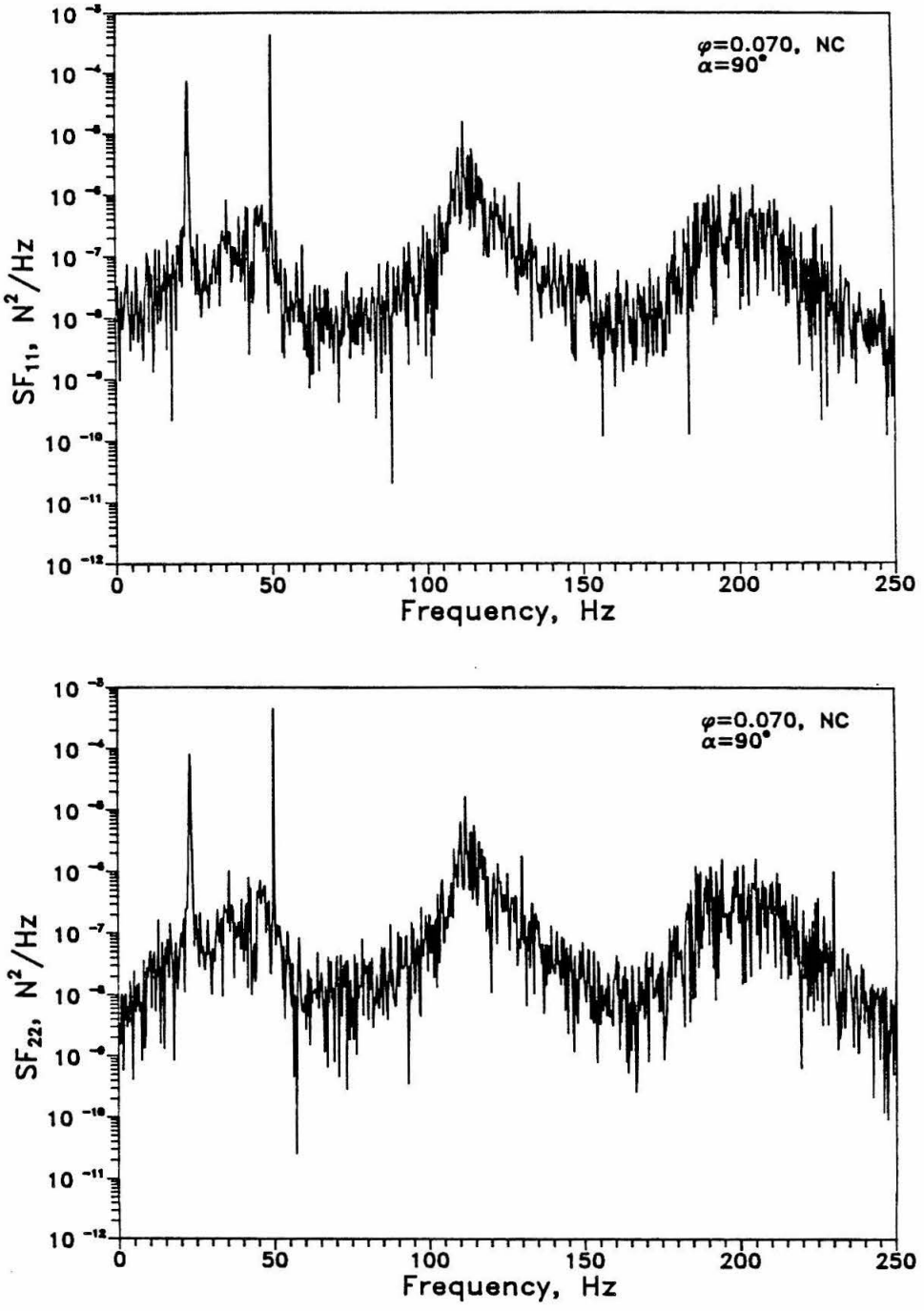

Figure 5.53: Spectral densities of the lateral force components in noncavitating flow ($\phi = 0.070$), measured in the rotating frame with the impeller at $\alpha = 90°$.

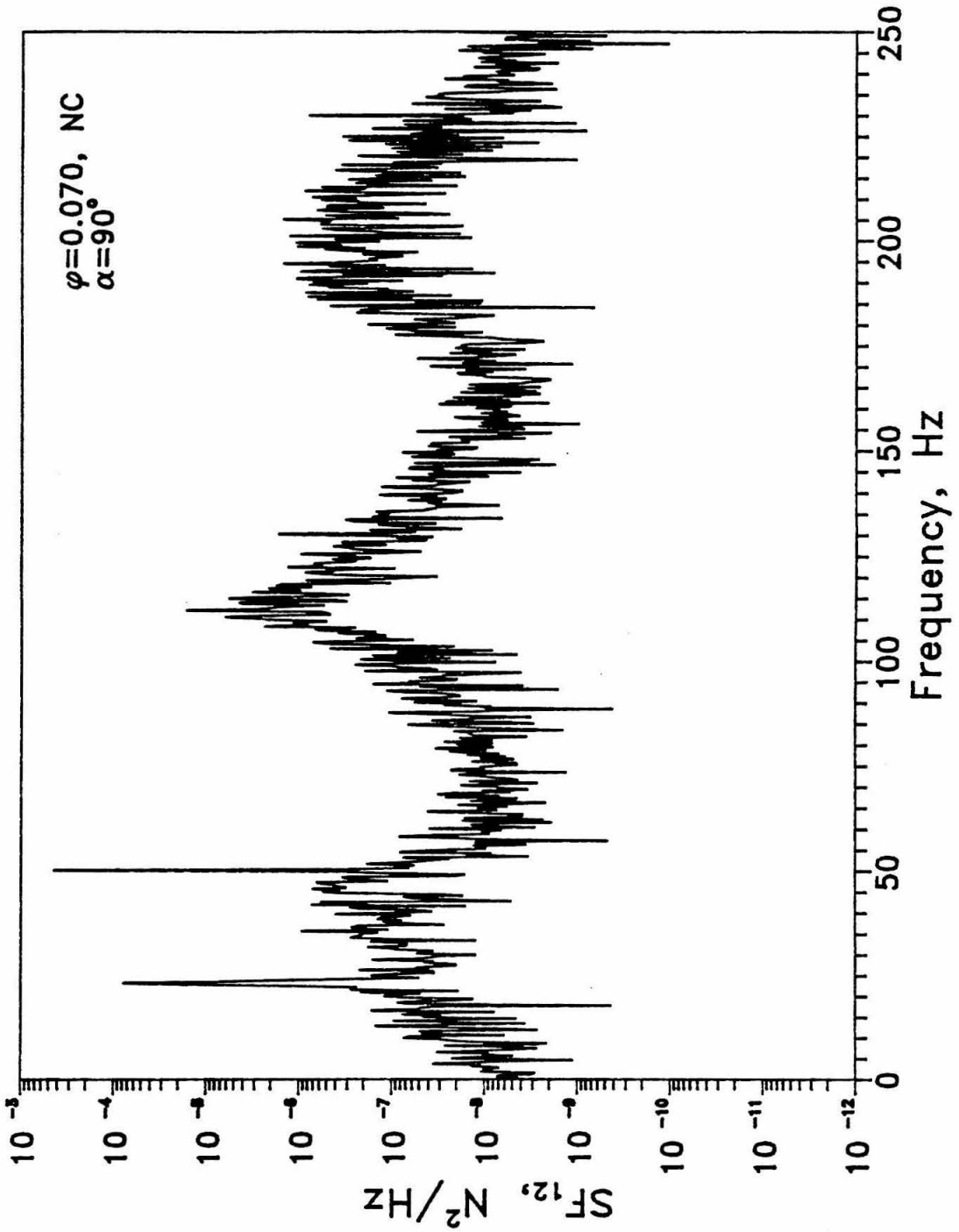

Figure 5.54: Cross-spectral density of the lateral force components in noncavitating flow ($\phi = 0.070$), measured in the rotating frame with the impeller at $\alpha = 90°$.

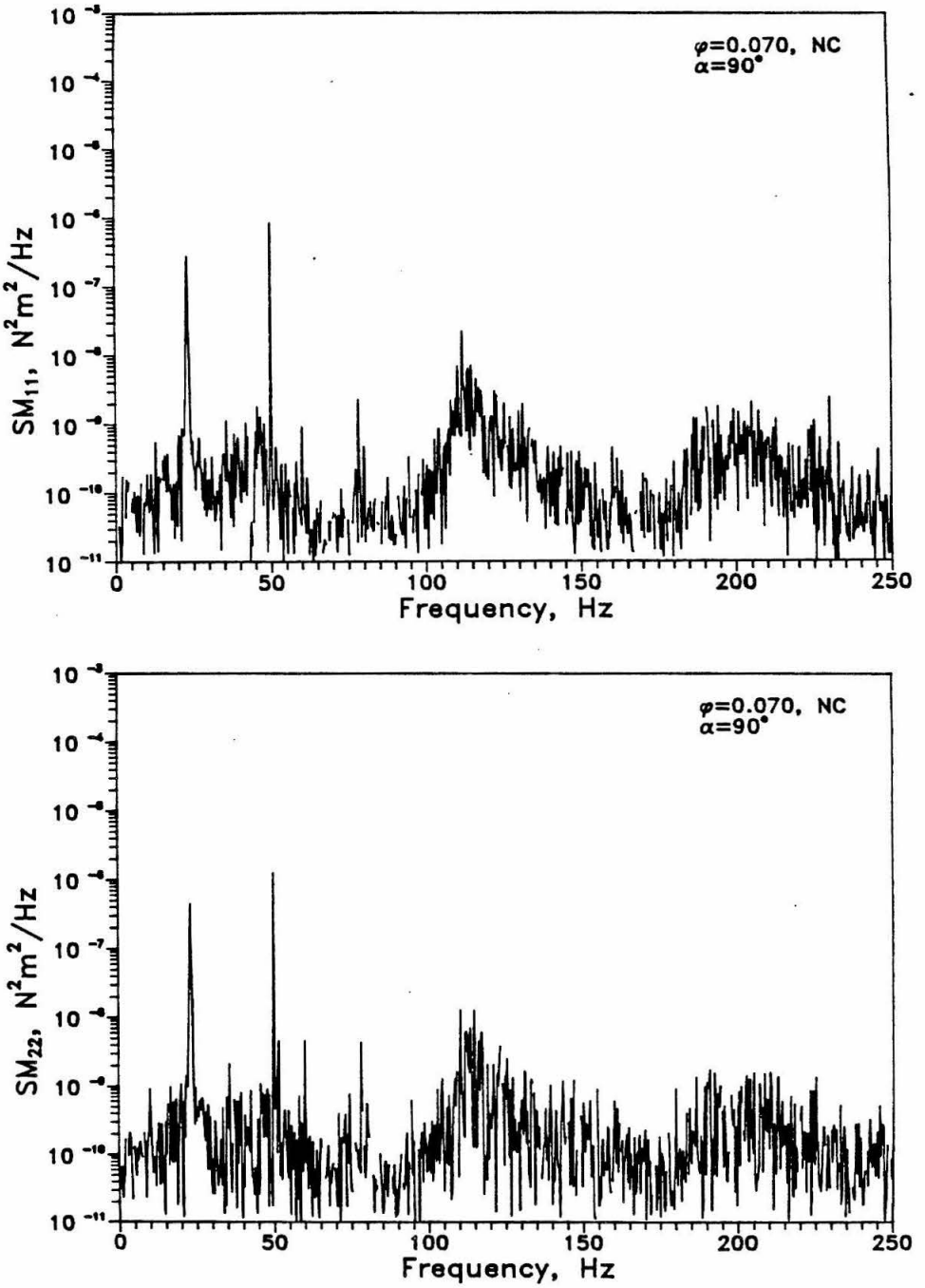

Figure 5.55: Spectral densities of the moment components in noncavitating flow ($\phi = 0.070$), measured in the rotating frame with the impeller at $\alpha = 90°$.

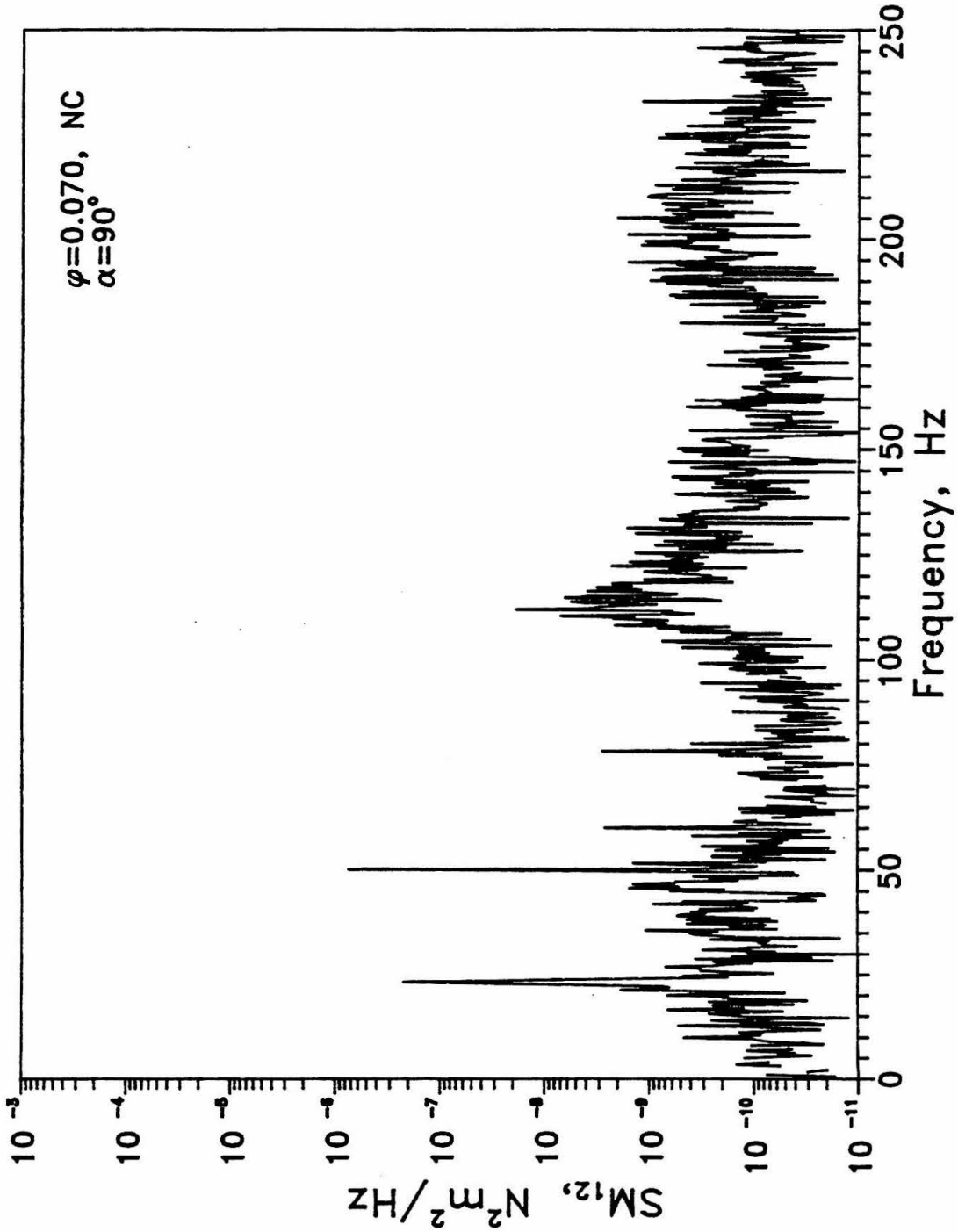

Figure 5.56: Cross-spectral density of the moment components in noncavitating flow ($\phi = 0.070$), measured in the rotating frame with the impeller at $\alpha = 90°$.

6

Summary and Conclusions

Rotordynamic instability is always a major design consideration in the developement of any rotating machinery. One of the least understood aspects of the problem is the effect of unsteady hydrodynamic forces on the stability of the rotor motion. The goal of this investigation was to test a specific inducer design developed by SEP in order to measure the hydrodynamic forces and moments and determine their effect on the stability of the rotor under cavitation.

Tests were performed at the Rotor Force Test Facility at Caltech, which has been constructed specifically for making such measurements. The following choices of fixed operating parameters were made as compromises between the range of desirable measurements and the inducer design features:

1. The inducer speed was set at 3000 RPM. This allowed a relatively high speed, desirable in cavitation experiments, yet it was low enough to permit whirling speeds from -0.6Ω to 0.6Ω.

2. The radius of whirl orbit was set at 0.254mm in order to achieve the smallest possible mean impeller tip clearance, consistent with the inducer design. This eccentricity was sufficiently large to provide meaningful results.

3. The smallest impeller tip clearance was set at 0.19mm (during phase 1), as small as possible, as required by the design characteristics, yet large enough to

avoid any possible contact between the rotor and the housing during the tests. This resulted in mean impeller tip clearance of 0.45mm. Phase 2 employed a second, larger mean impeller tip clearance measuring 0.71mm.

An auxiliary pump was also installed in order to increase the maximum possible flow rate.

Measurements of steady state noncavitating and cavitating performance data, radial forces and moments as well as rotordynamic coefficients for radial forces and moments for a range of flow conditions and whirl/shaft speed ratios were taken. Also, during phase 2, instantaneous force and moment data were stored and spectral analysis of these was performed. The main conclusions are as follows:

1. Hydraulic performance is consistent with expectations and similar to that of other pumps. Specifically, (a) the larger the impeller tip clearance is, the lower the head rise across the inducer, and (b) the higher the flow rate is, the higher the minimum cavitation number at which acceptable performance is obtained.

2. The design flow coefficient for this inducer was stated to be $\phi = 0.085$. Parenthetically, we should remark that this value seemed too high to us when compared with the design point for other similar inducers. At $\phi = 0.085$, this SEP inducer only produced a head coefficient of $\psi \approx 0.14$. We would have anticipated a lower design flow coefficient and a higher head rise. In fact, the low head rise at $\phi = 0.085$ caused severe test problems in the program since the low downstream pressure at the design flow would cause the boost pump to cavitate at rather high inducer cavitation numbers.

3. The steady hydrodynamic forces and moments are independent of the whirl speed ratio. They decrease slightly with larger impeller tip clearance. Cavitation, however, causes significant increases in their magnitude.

4. The presence of a sharp peak at $\frac{\omega}{\Omega} \approx 0.55$ in the plots of forces and moments is attributed to fluid motion in the cavity behind the inducer model. Its effect is confined to a very narrow neighborhood of $\frac{\omega}{\Omega} = 0.55$ and, therefore, does not affect the majority of the data outside this region.

5. The effect of the flow coefficient on the forces in noncavitating flow is significant in the region of small positive whirl/shaft speed ratios. Here, the effect of higher flow rate is such as to make the region where forces are destabilizing smaller. This is consistent with the observations made by Jery (1987) on centrifugal pumps. Judging from the limited data obtained for cavitating flows ($\phi = 0.070$ and $\phi = 0.080$),the effect of higher ϕ in cavitation is to increase the range of ω/Ω for which the forces are destabilizing.

6. In noncavitating flows, the effect of larger impeller tip clearance on the forces is insignificant near and above the design flow rate ($\phi = 0.085$), while for ϕ below design, the smaller the clearance is, the larger the region where forces are destabilizing. Data in cavitating flows for both clearances is available only for $\phi = 0.070$ and, therefore, no generalizations can be made. Nevertheless, for this flow coefficient only, the effect of the the clearance is the opposite of what it is in noncavitating flows, namely, the region of destabilization is larger for larger clearance.

7. Cavitation has the most pronounced effect on the hydrodynamic forces. Generally, the lower the cavitation number, the larger the region where forces are destabilizing. Moreover, not only does the magnitude of these forces increase dramatically with cavitation, but also, negative whirl/shaft speed ratios become destabilizing.

8. Spectral analysis of the forces indicates the presence of a peak at a frequency slightly less than half shaft speed, due to the characteristics of the test facility. The effect of cavitation is to increase the magnitude of the forces throughout

the frequency range. We do not currently have an explanation for the fact that the peak near half shaft speed disappears in cavitating flows.

9. The measurements made provide the net moments acting on the rotor. In addition to the moments associated with the lateral forces, these measurements include pure hydrodynamic moments as well as contributions from the thrust.

10. Measurements of the rotordynamic coefficients for the forces and moments confirm the assumption that the coefficient matrices satisfy $A_{xx} = A_{yy}$, $A_{xy} = -A_{yx}$, $B_{xx} = B_{yy}$ and $B_{xy} = -B_{yx}$. Thus, the rotordynamic coefficient matrices are independent of the axes orientation, and depend only on the flow conditions and the impeller characteristics.

11. The variation of the rotordynamic coefficients with whirl/shaft speed ratio is too complicated to permit a quadratic fit of the data. This is true for low whirl speed ratios in both directions, regardless of the flow conditions. The curves become even more complicated in the presence of cavitation. Thus, the representation of the forces in terms of generalized stiffness, damping and inertia matrices is not suitable for this inducer. This behavior is similar to that observed on other inducers by Arndt and Franz (1986). Therefore, it is clearly necessary to use the data given in this report in a rotordynamic analysis code which permits input of forces and moments as general functions of whirl speed rather than as stiffness, damping and inertia coefficients.

References

[1] Arndt, N. and Franz, R.J., "Observations of Hydrodynamic Forces on Several Inducers, Including the SSME LPOTP," Report E249.3, Division of Engineering and Applied Science, California Institute of Technology, Pasadena, Calif., 1986.

[2] Bendat, J.S. and Piersol, A.J., *Random Data: Analysis and Measurement Procedures,* John Wiley, 1971.

[3] Braisted, D.M., "Cavitation Induced Instabilities Associated with Turbomachines," *Ph.D. Thesis,* Division of Engineering and Applied Science, California Institute of Technology, Pasadena, Calif., 1979.

[4] Chamieh, D.S., "Forces on a Whirling Centrifugal Pump-Impeller," *Ph.D. Thesis,* Division of Engineering and Applied Science, California Institute of Technology, Pasadena, Calif., 1983.

[5] Chamieh, D.S., Acosta, A.J., Brennen, C.E., Caughey, T.K. and Franz, R.J., "Experimental Measurements of Hydrodynamic Stiffness Matrices for a Centrifugal Pump Impeller," 2nd Workshop on Rotordynamic Instability Problems in High Performance Turbomachinery, Texas A&M University, May 10–12, 1982.

[6] Franz, R.J., "Experimental Investigation of the Effect of Cavitation on the Rotordynamic Forces on a Whirling Centrifugal Pump Impeller," *Ph.D. Thesis,* Division of Engineering and Applied Science, California Institute of Technology, Pasadena, Calif., 1989.

[7] Hall, J.F., "An FFT Algorithm for Structural Dynamics," *Earthquake Engineering and Structural Dynamics,* Vol. 10 pp. 797–811, 1982.

[8] Jery, B., "Experimental Study of Unsteady Hydrodynamic Force Matrices on Whirling Centrifugal Pump Impellers," *Ph.D. Thesis,* Division of Engineering and Applied Science, California Institute of Technology, Pasadena, Calif., 1987.

[9] Jery, B., Brennen, C.E., Caughey, T.K. and Acosta, A.J., "Forces on Centrifugal Pump Impellers," 2nd International Pump Symposium, Houston, Texas, April 20–May 2, 1985.

[10] Miskovish, R.S. and Brennen, C.E., "Some Unsteady Fluid Forces Measured on Pump Impellers," Report E249.6, Division of Engineering and Applied Science, California Institute of Technology, Pasadena, California.

[11] Ng, S.L., "Dynamic Response of Cavitating Turbomachines," *Ph.D. Thesis,* Division of Engineering and Applied Science, California Institute of Technology, Pasadena, Calif., 1976.

Appendix

The plots used in the body of the report were chosen so as to show the effect of the various parameters on the hydrodynamic forces. The appendix contains separate plots of the measured forces for each individual flow condition. Also included are the coefficients of the rotordynamic force and moment matrices $[A]$ and $[B]$.

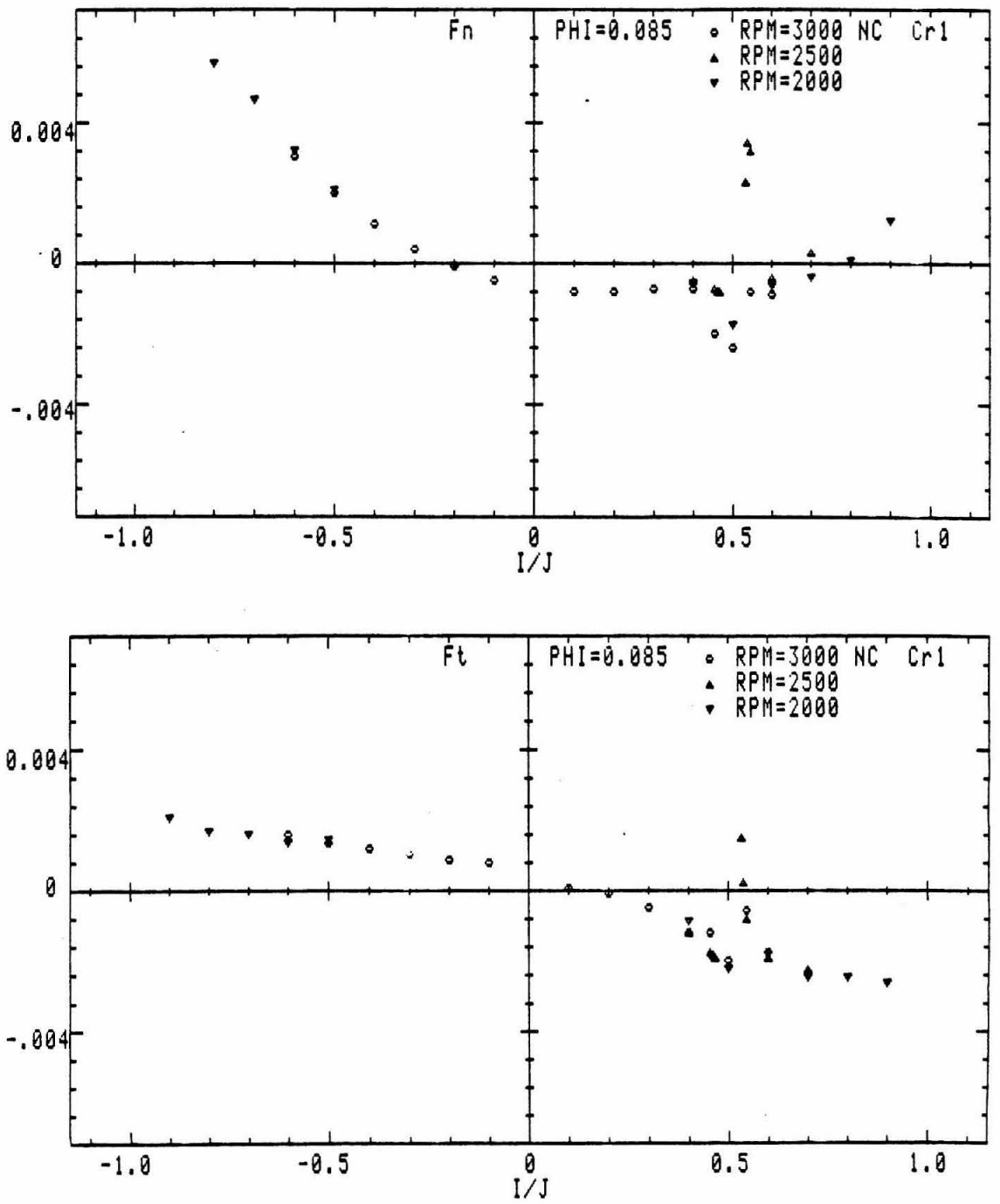

Figure A.1: Unsteady hydrodynamic forces for different shaft speeds, noncavitating flow ($\phi = 0.085$, Cr_1).

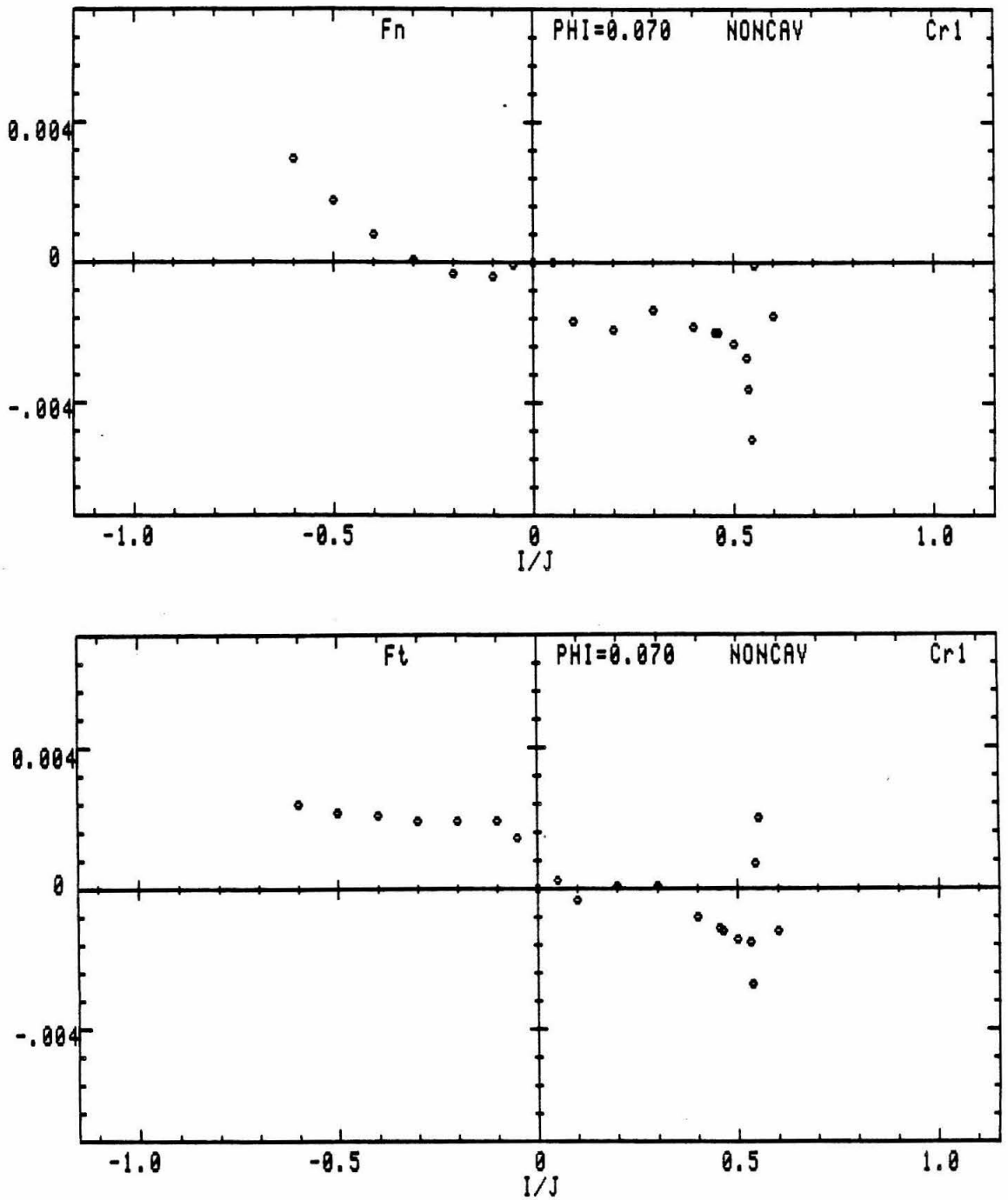

Figure A.2: Unsteady hydrodynamic forces ($\phi = 0.070$, noncavitating flow, Cr_1).

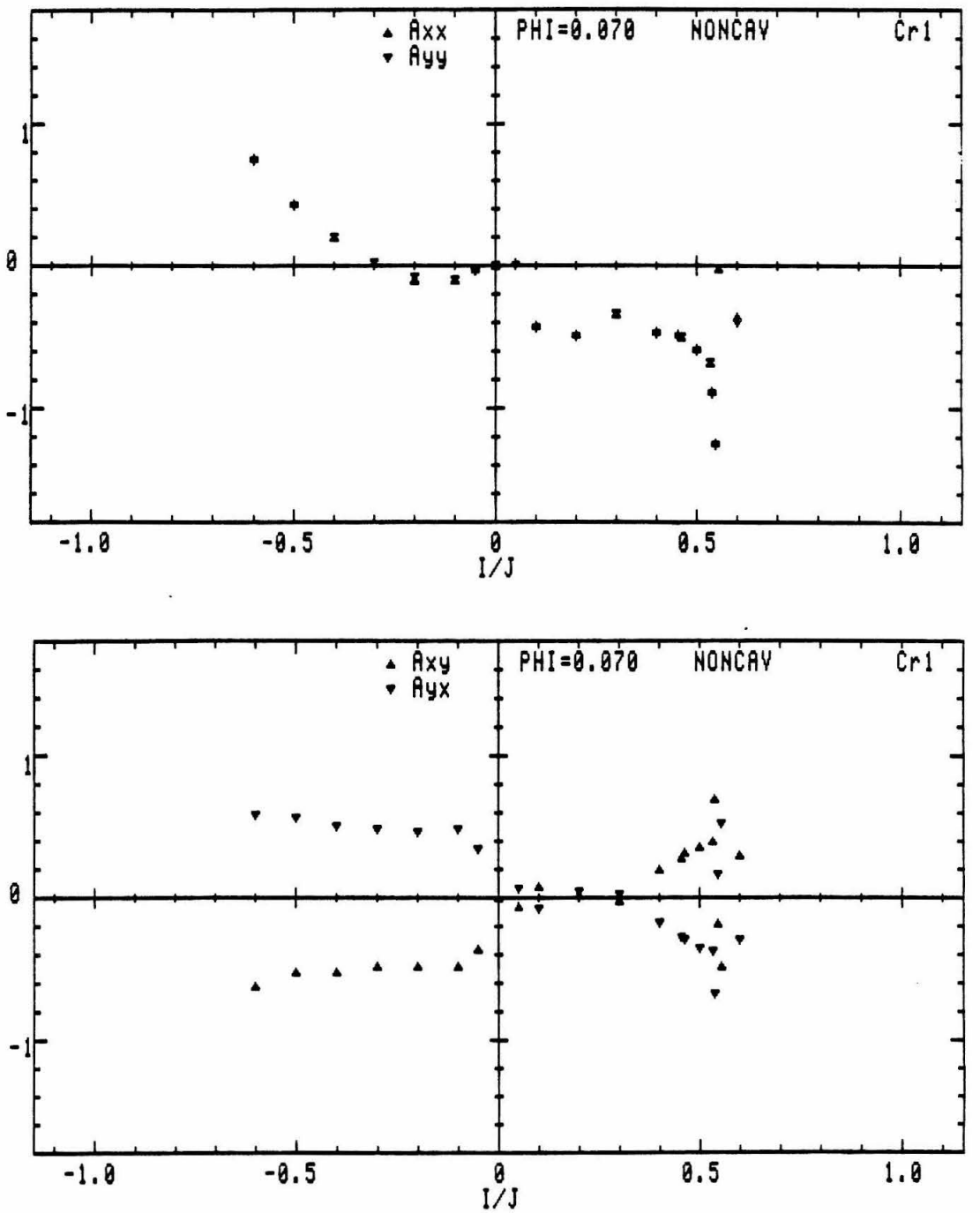

Figure A.3: Rotordynamic force coefficients ($\phi = 0.070$, noncavitating flow, Cr_1).

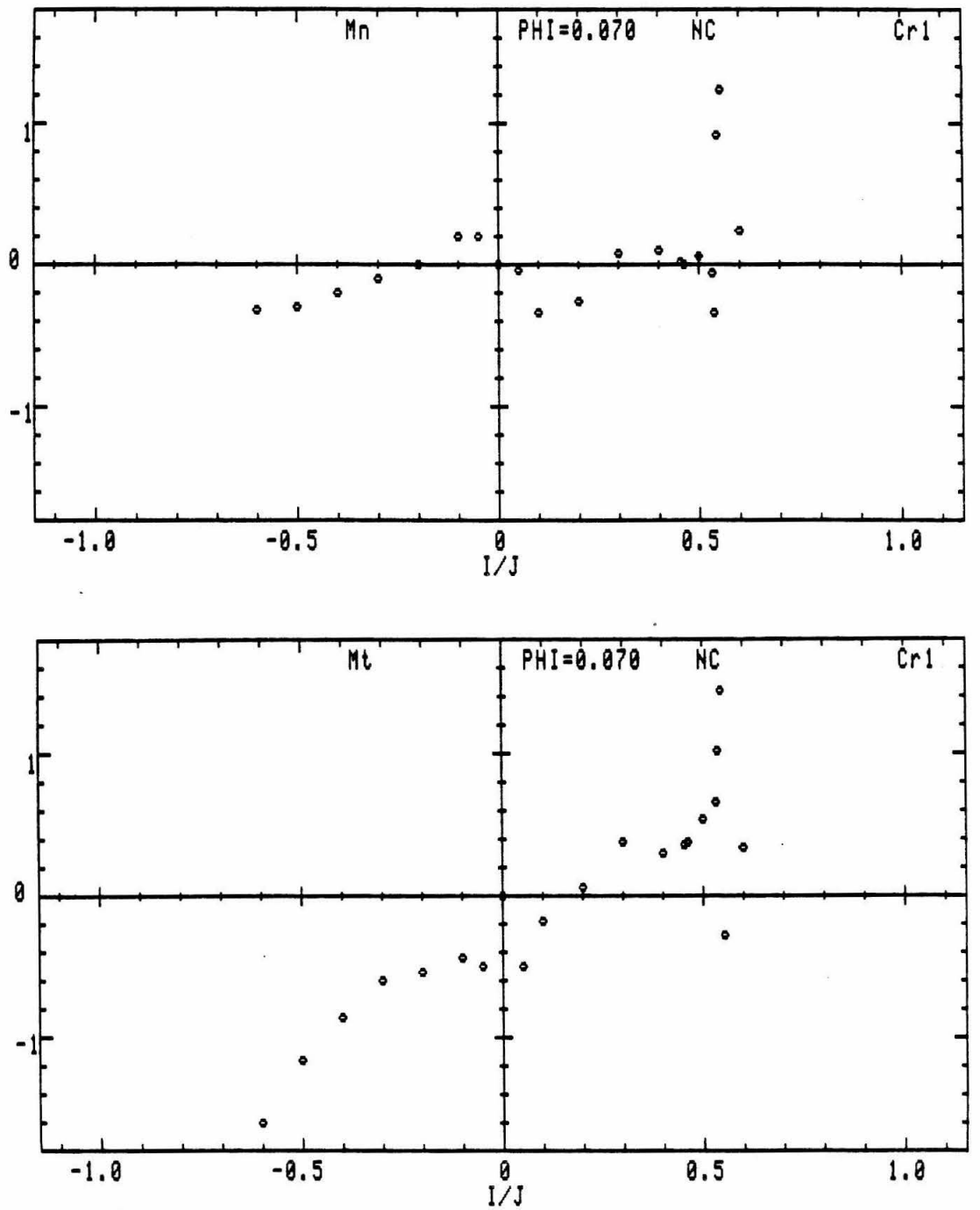

Figure A.4: Unsteady moments ($\phi = 0.070$, noncavitating flow, Cr_1).

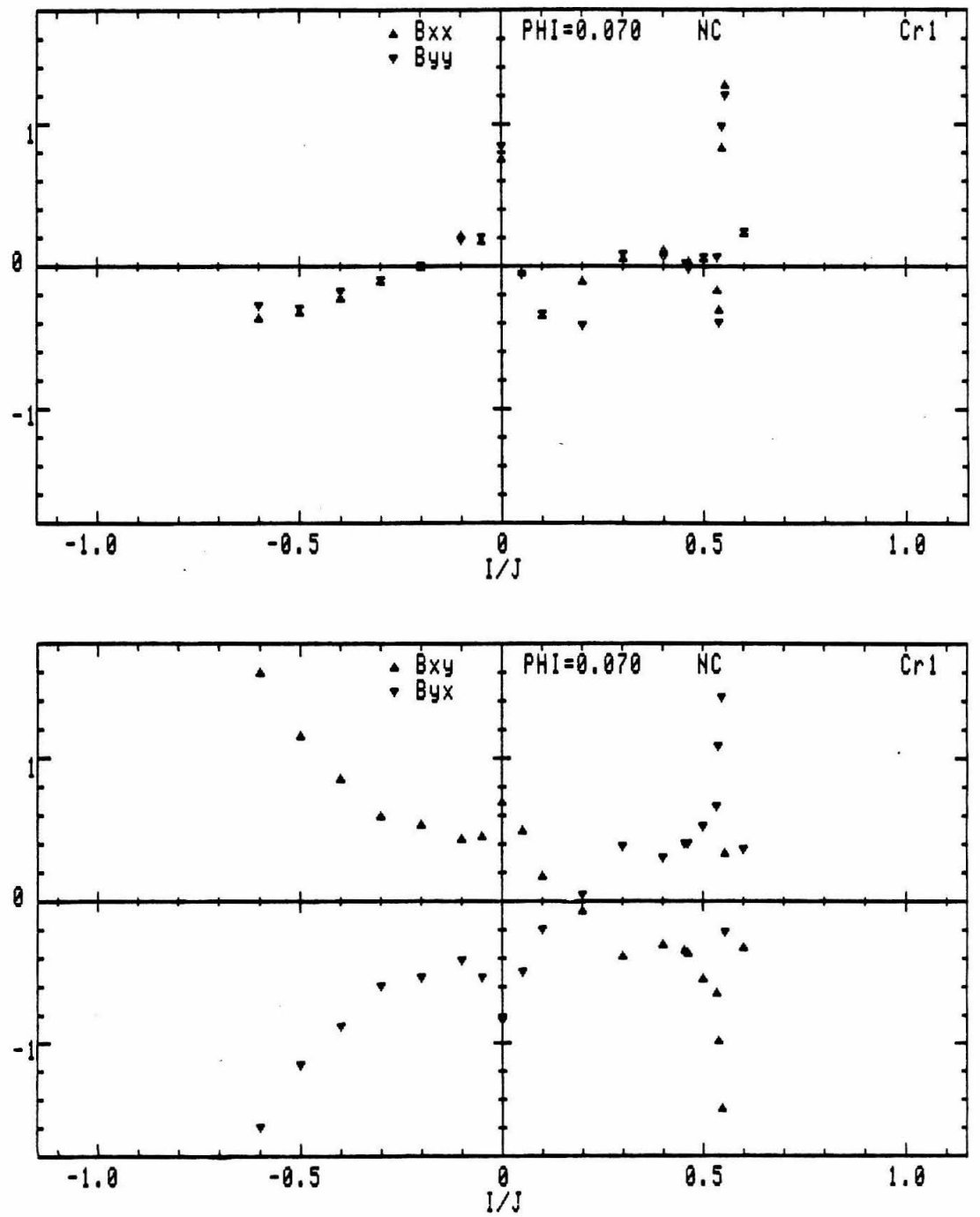

Figure A.5: Rotordynamic moment coefficients ($\phi = 0.070$, noncavitating flow, Cr_1).

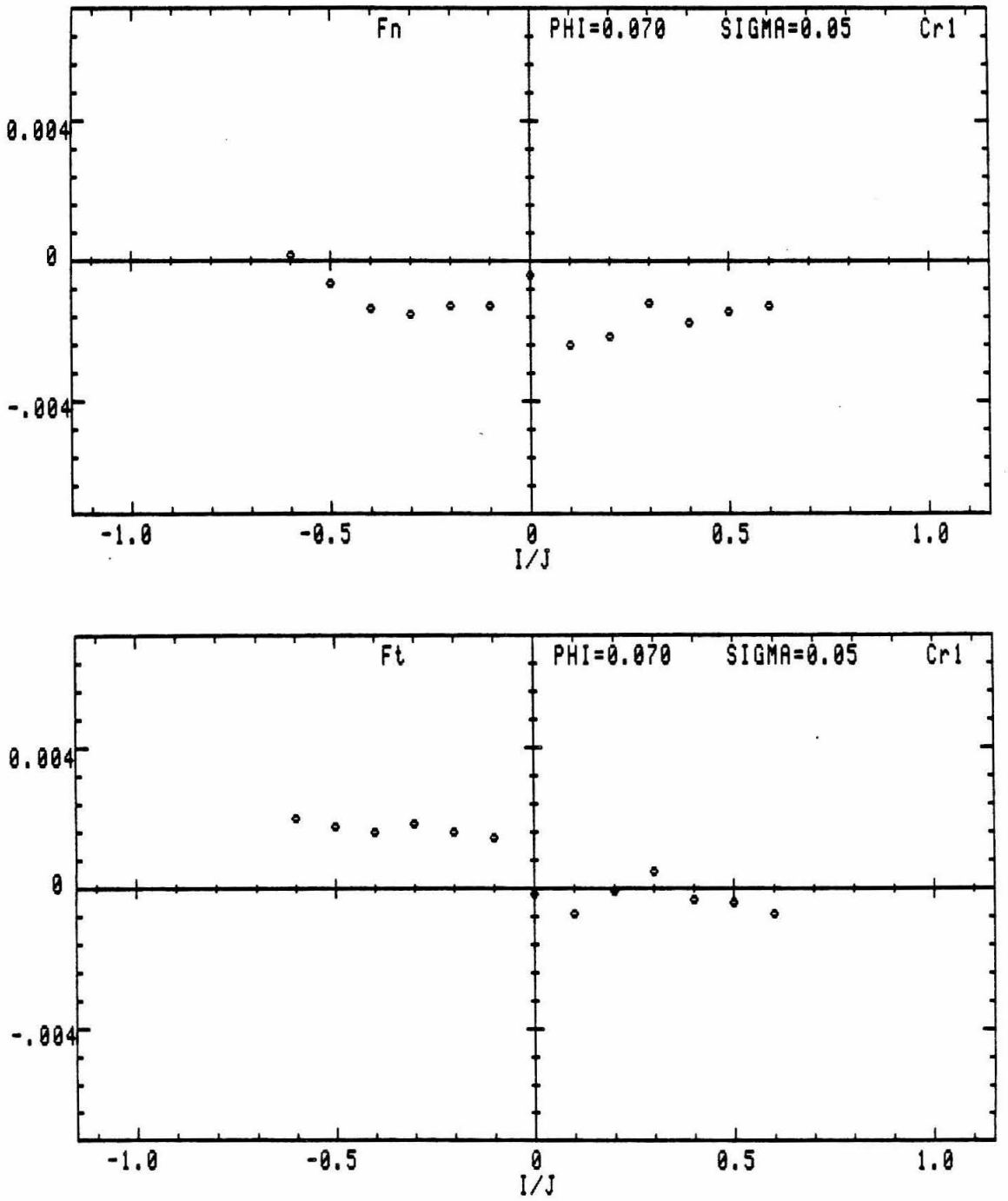

Figure A.6: Unsteady hydrodynamic forces ($\phi = 0.070$, $\sigma = 0.050$, Cr_1).

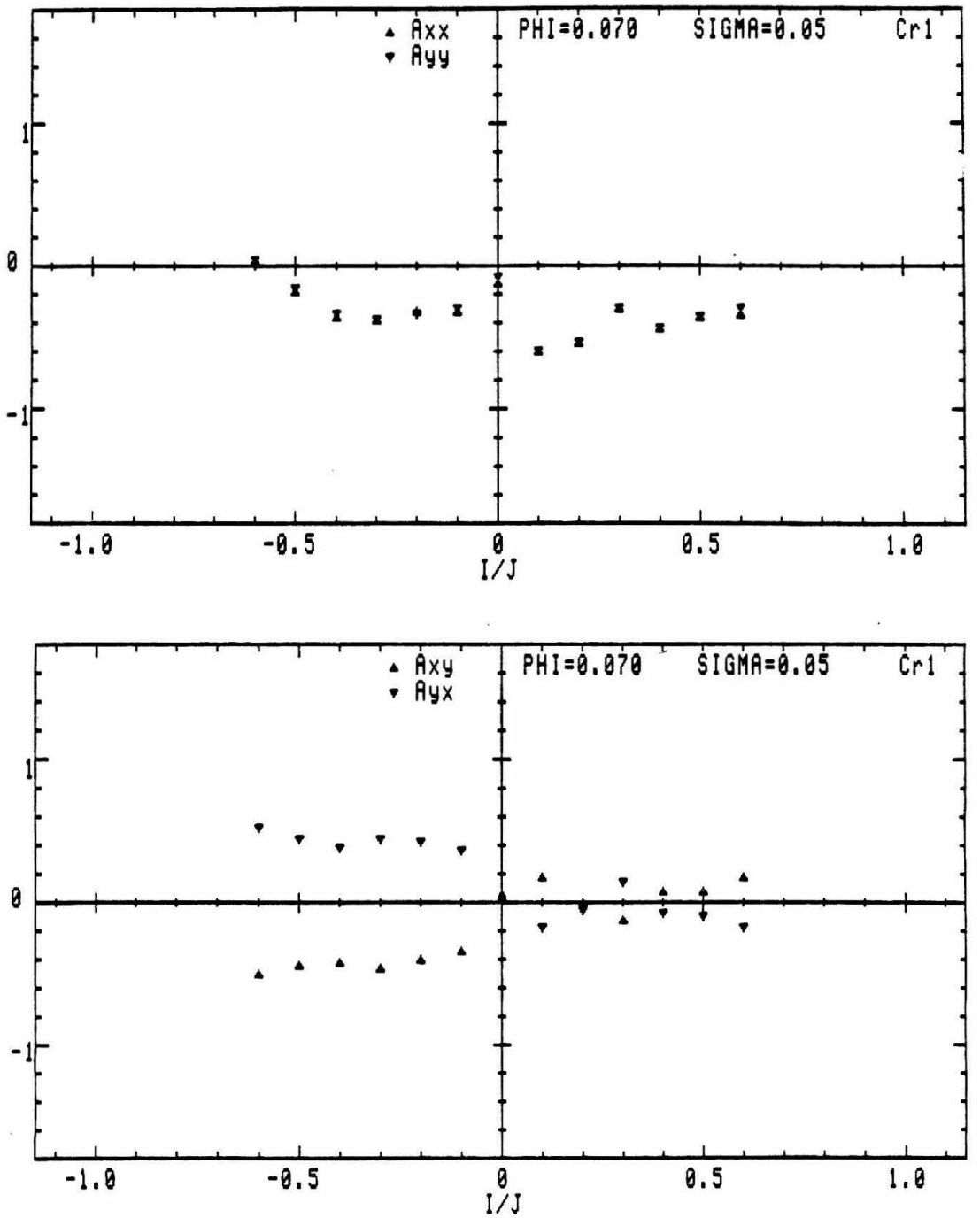

Figure A.7: Rotordynamic force coefficients ($\phi = 0.070$, $\sigma = 0.050$, Cr_1).

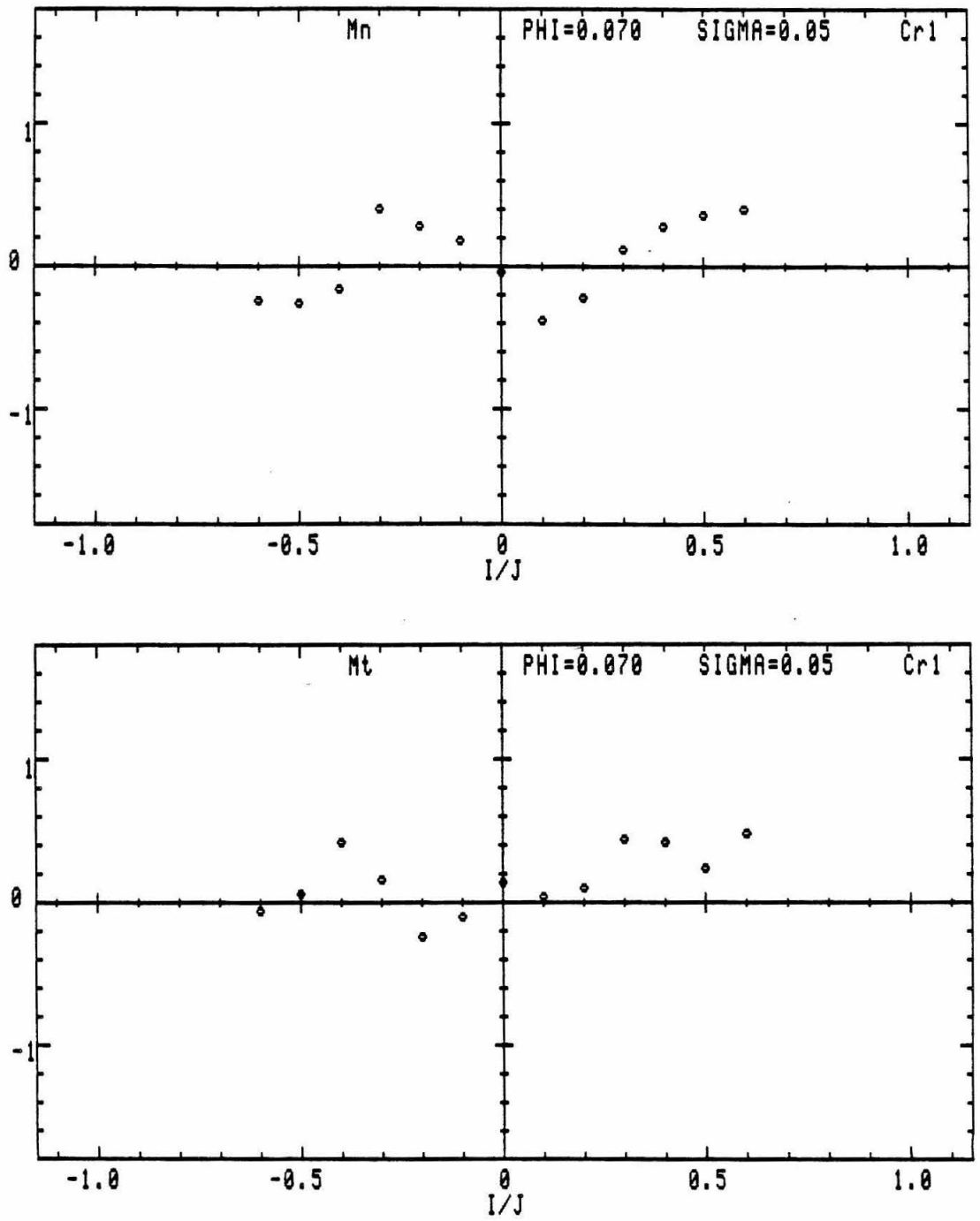

Figure A.8: Unsteady moments ($\phi = 0.070$, $\sigma = 0.050$, Cr_1).

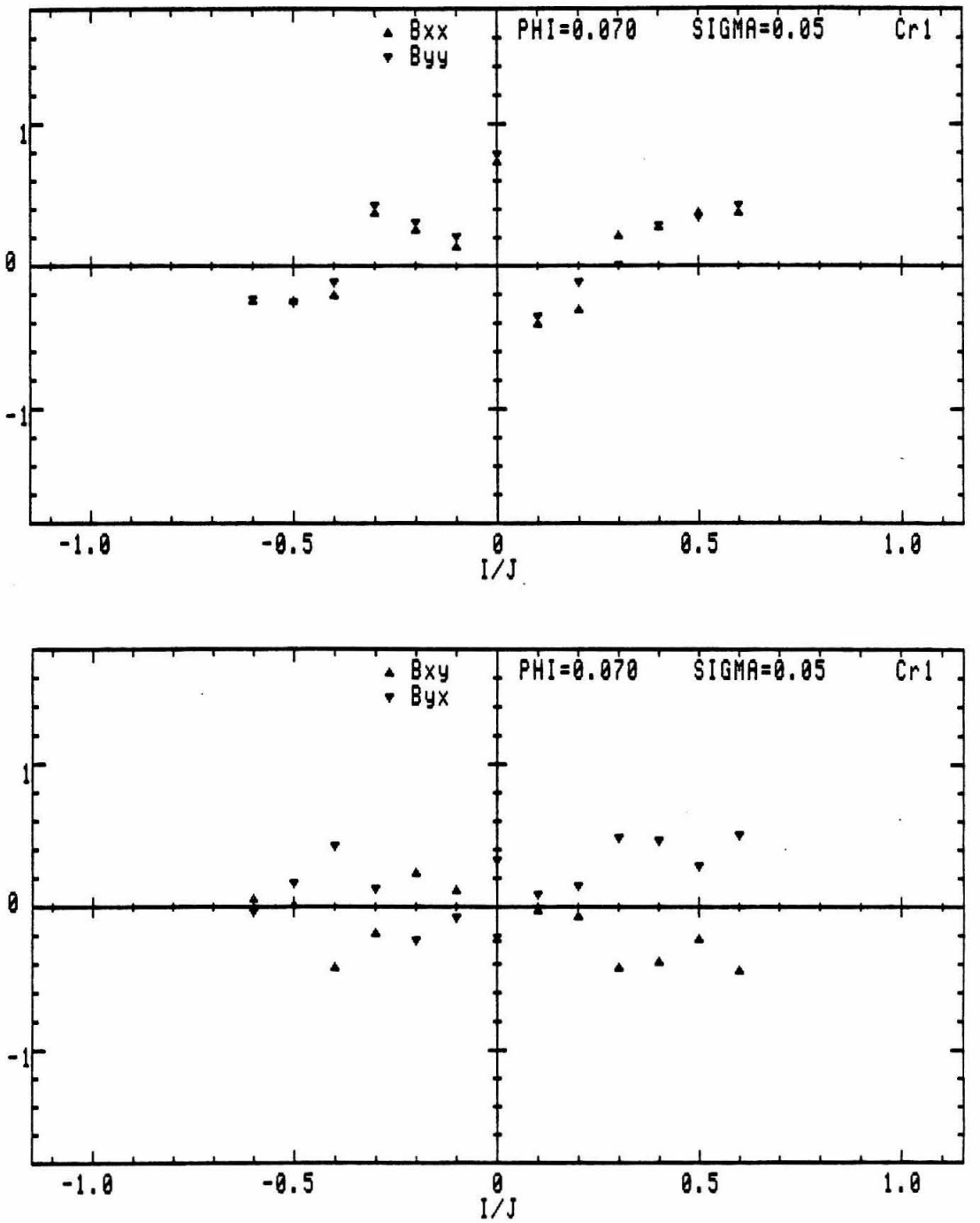

Figure A.9: Rotordynamic moment coefficients ($\phi = 0.070$, $\sigma = 0.050$, Cr_1).

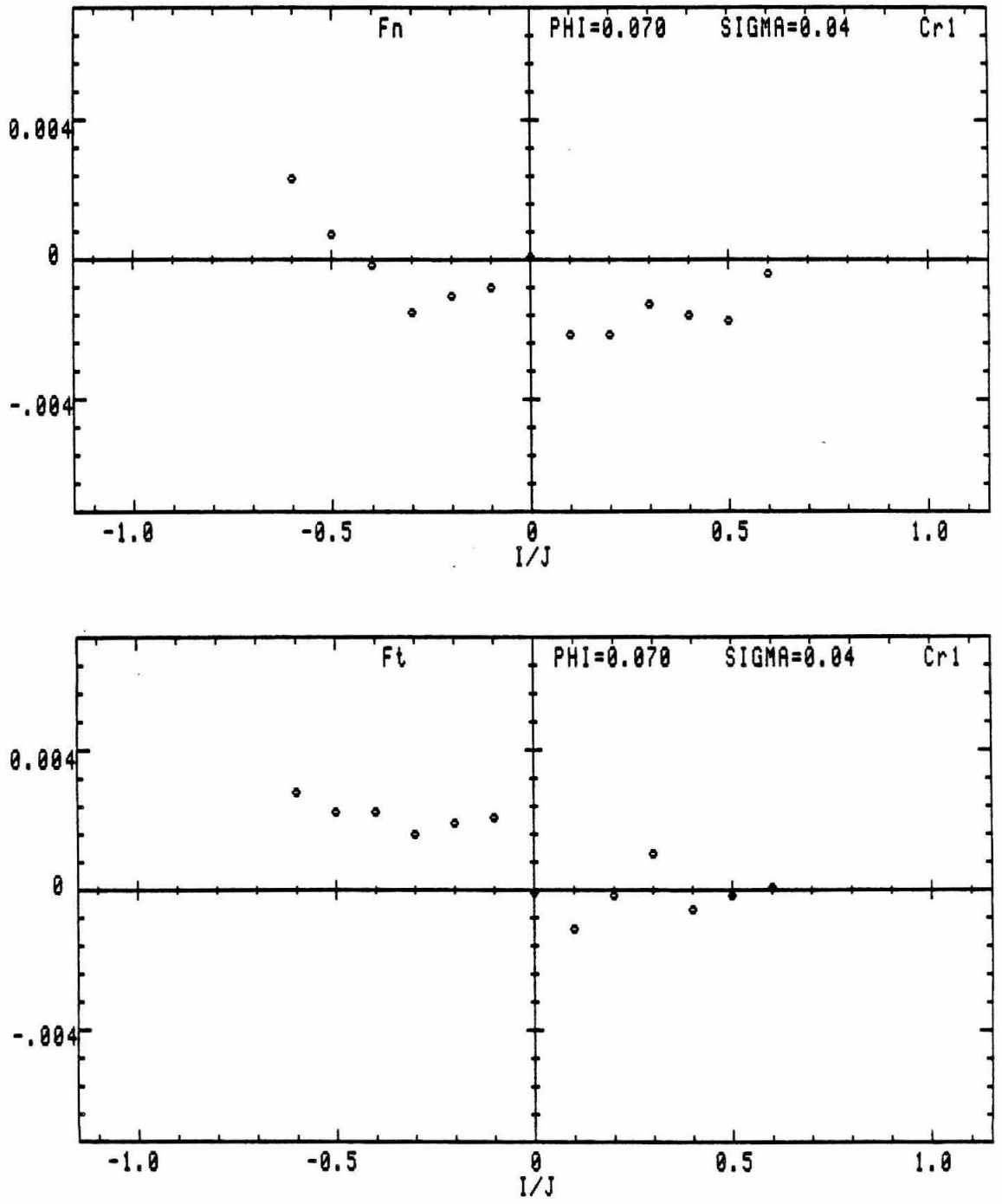

Figure A.10: Unsteady hydrodynamic forces ($\phi = 0.070$, $\sigma = 0.040$, Cr_1).

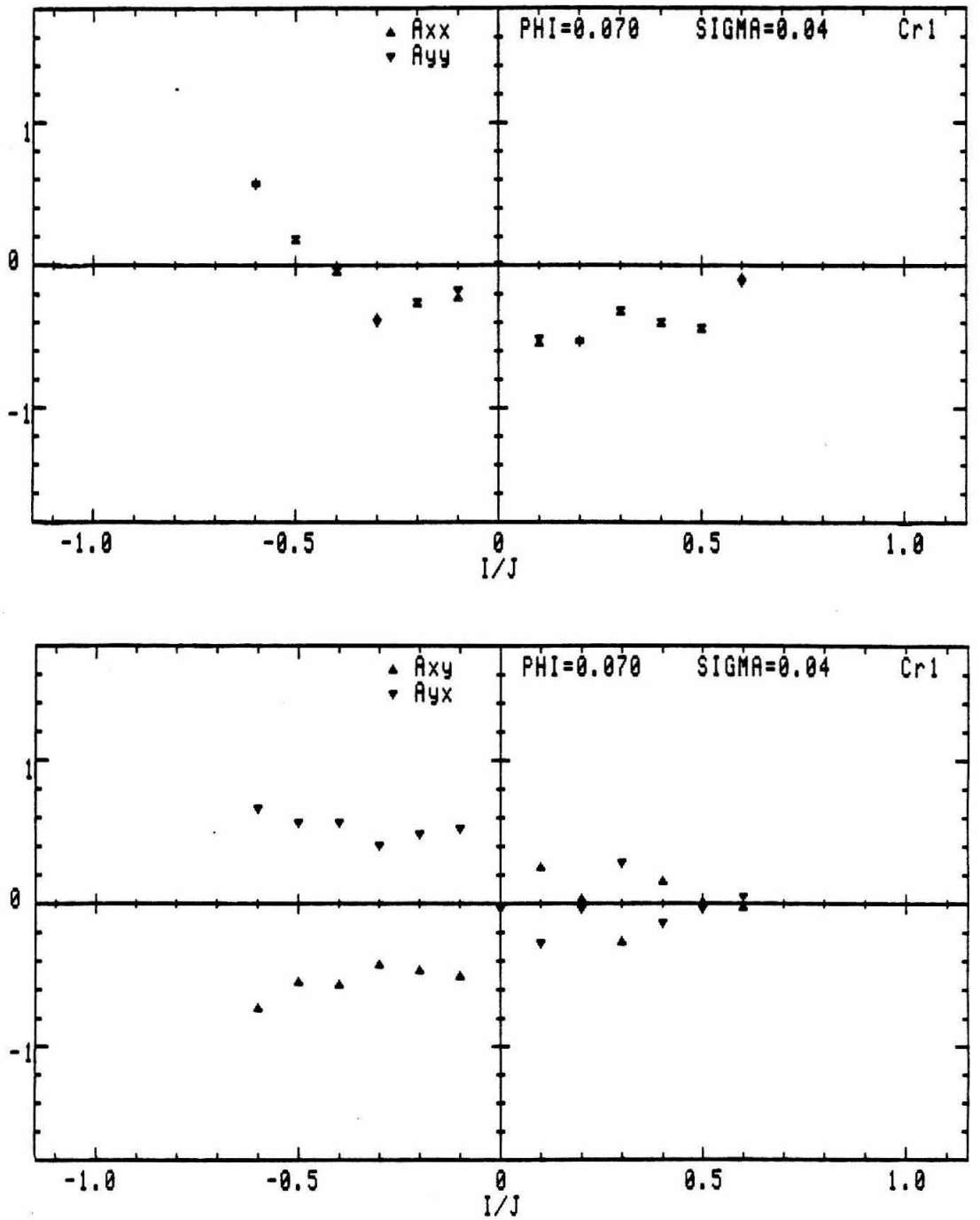

Figure A.11: Rotordynamic force coefficients ($\phi = 0.070$, $\sigma = 0.040$, Cr_1).

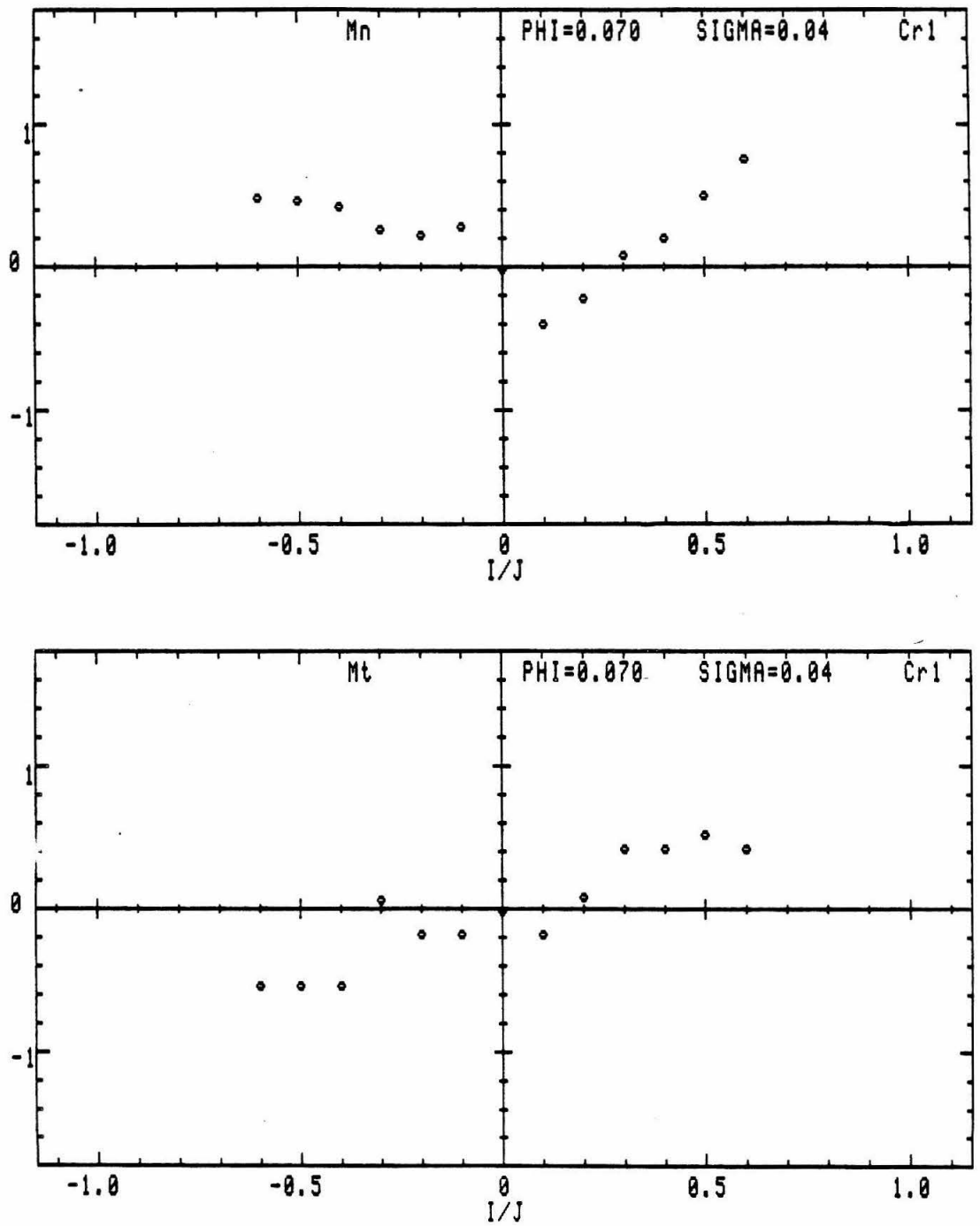

Figure A.12: Unsteady moments ($\phi = 0.070$, $\sigma = 0.040$, Cr_1).

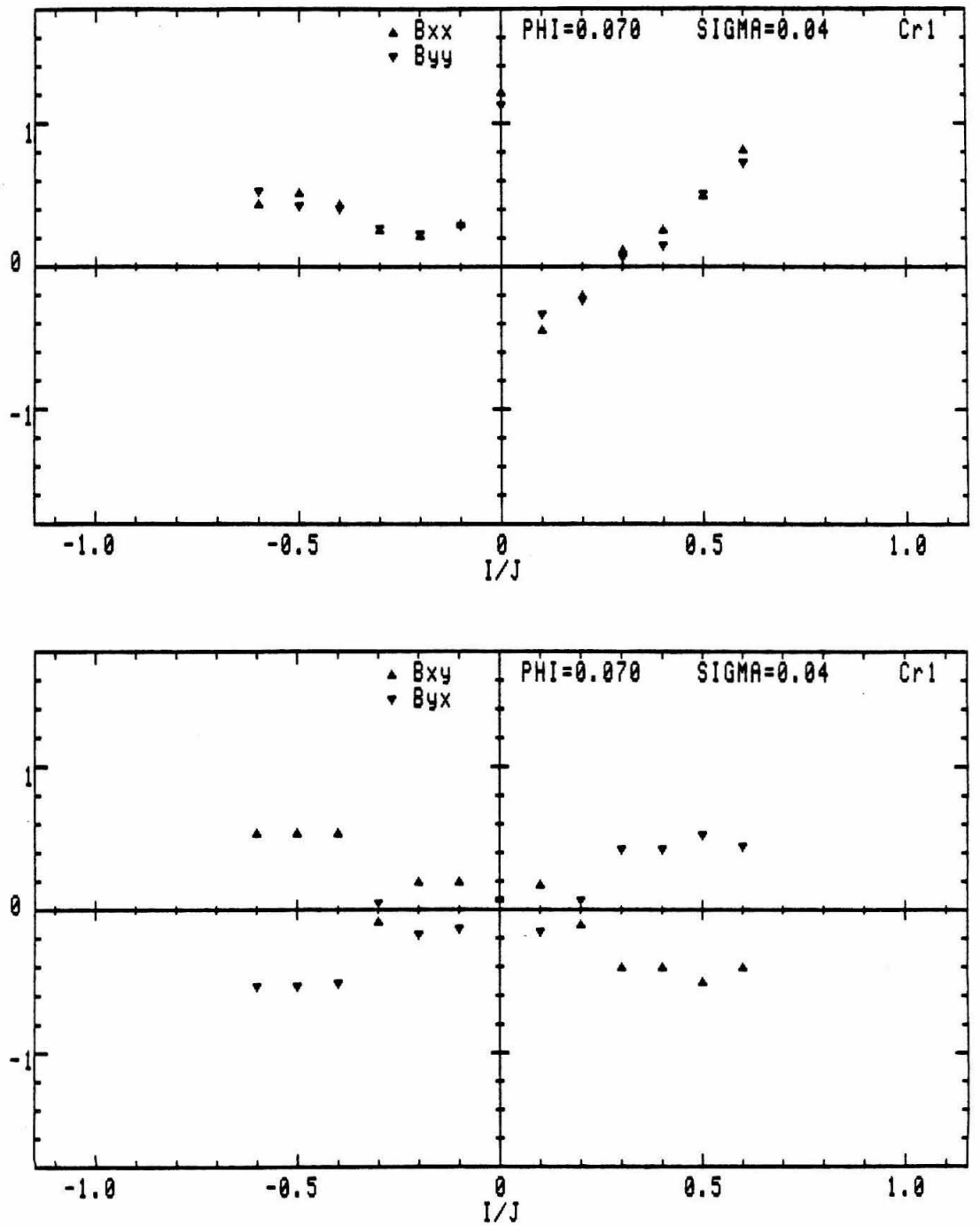

Figure A.13: Rotordynamic moment coefficients ($\phi = 0.070$, $\sigma = 0.040$, Cr_1).

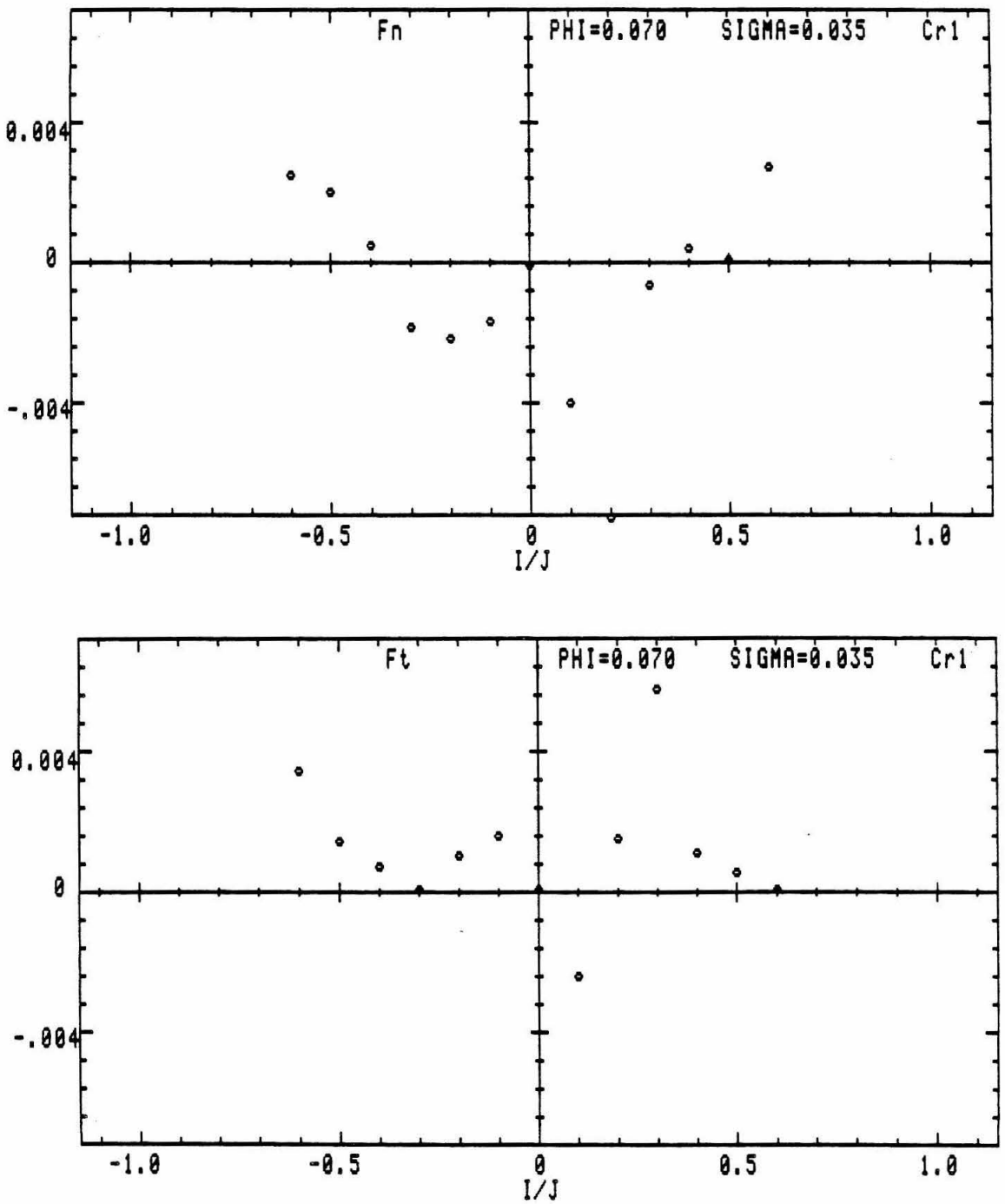

Figure A.14: Unsteady hydrodynamic forces ($\phi = 0.070$, $\sigma = 0.035$, Cr_1).

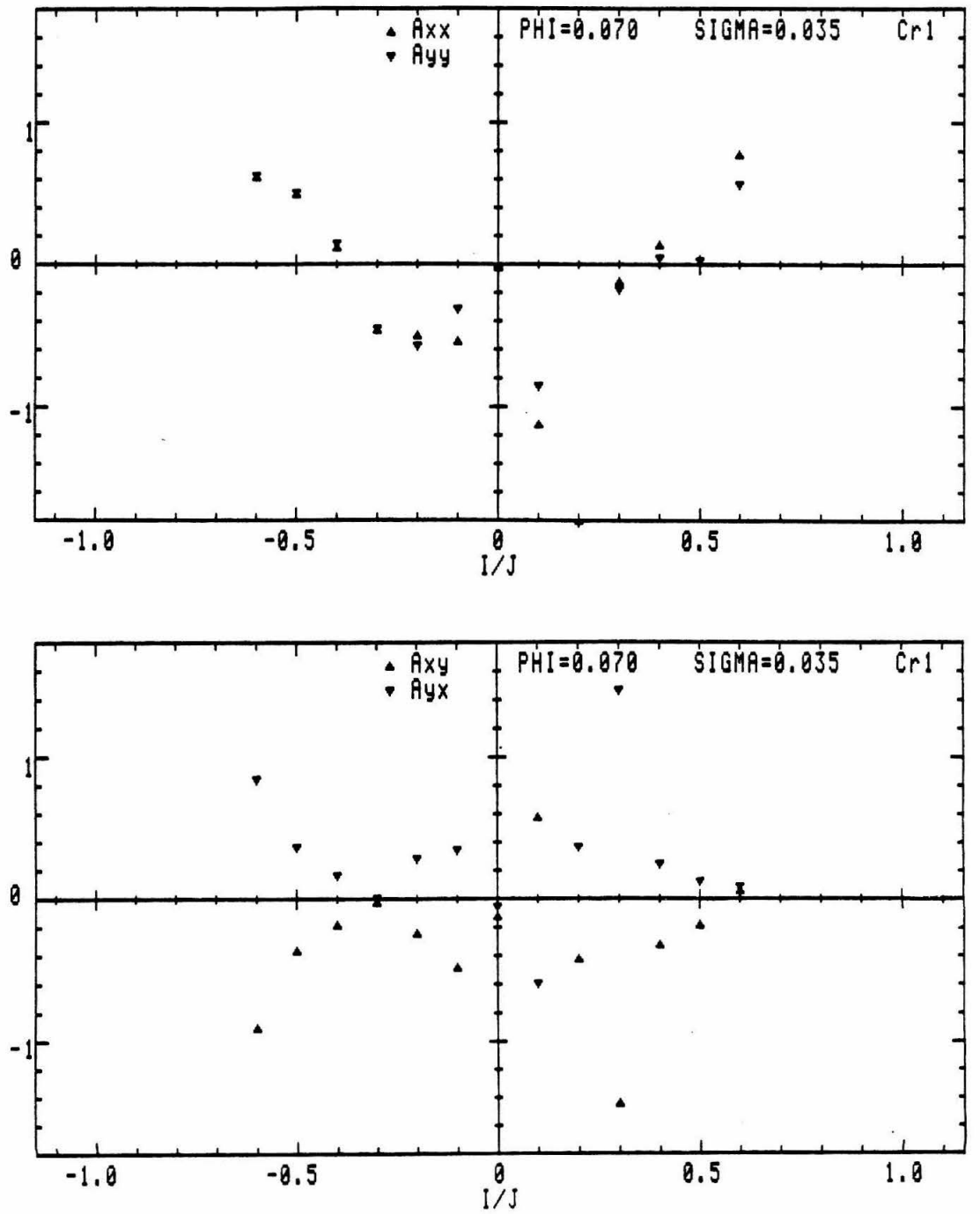

Figure A.15: Rotordynamic force coefficients ($\phi = 0.070$, $\sigma = 0.035$, Cr_1).

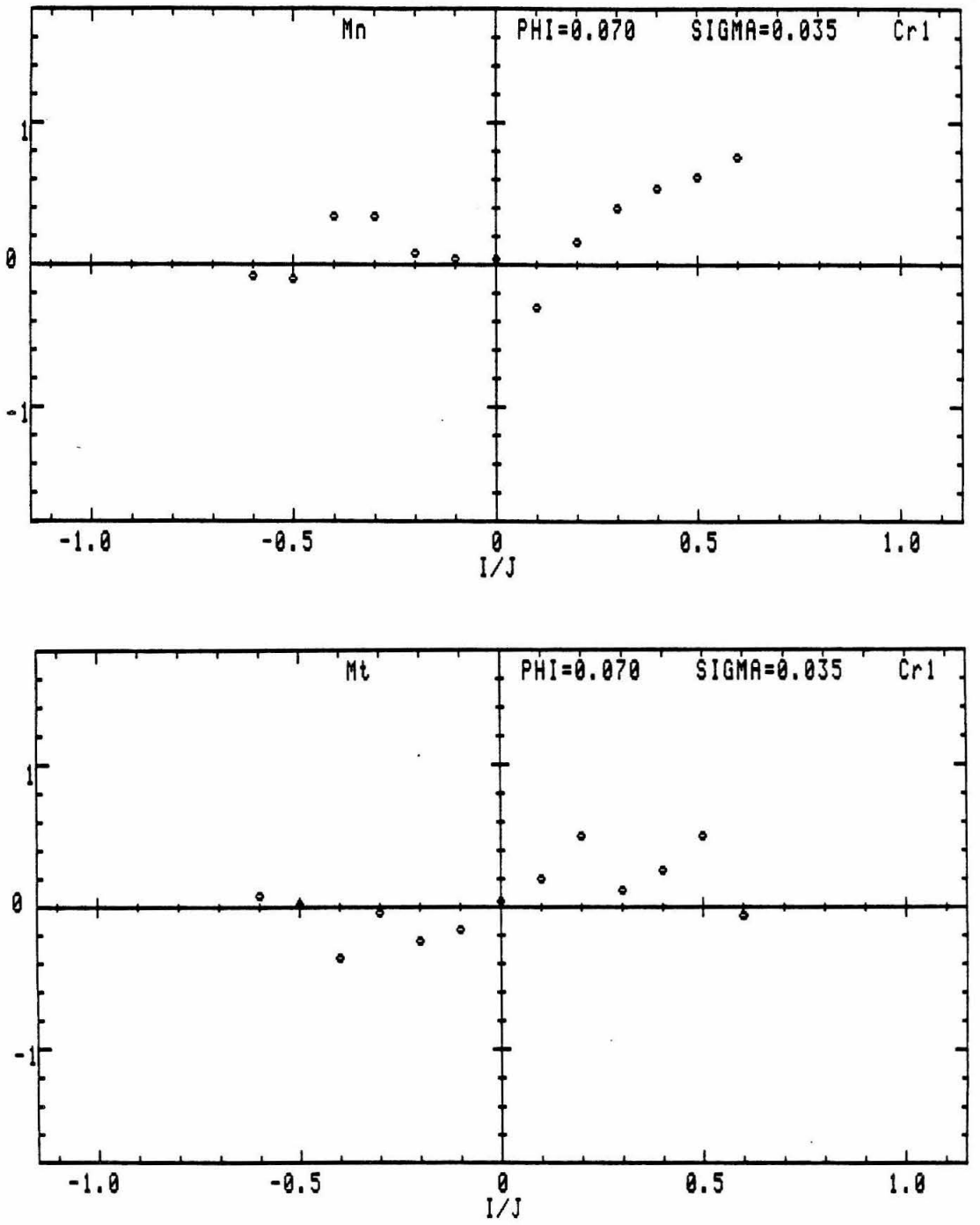

Figure A.16: Unsteady moments ($\phi = 0.070$, $\sigma = 0.035$, Cr_1).

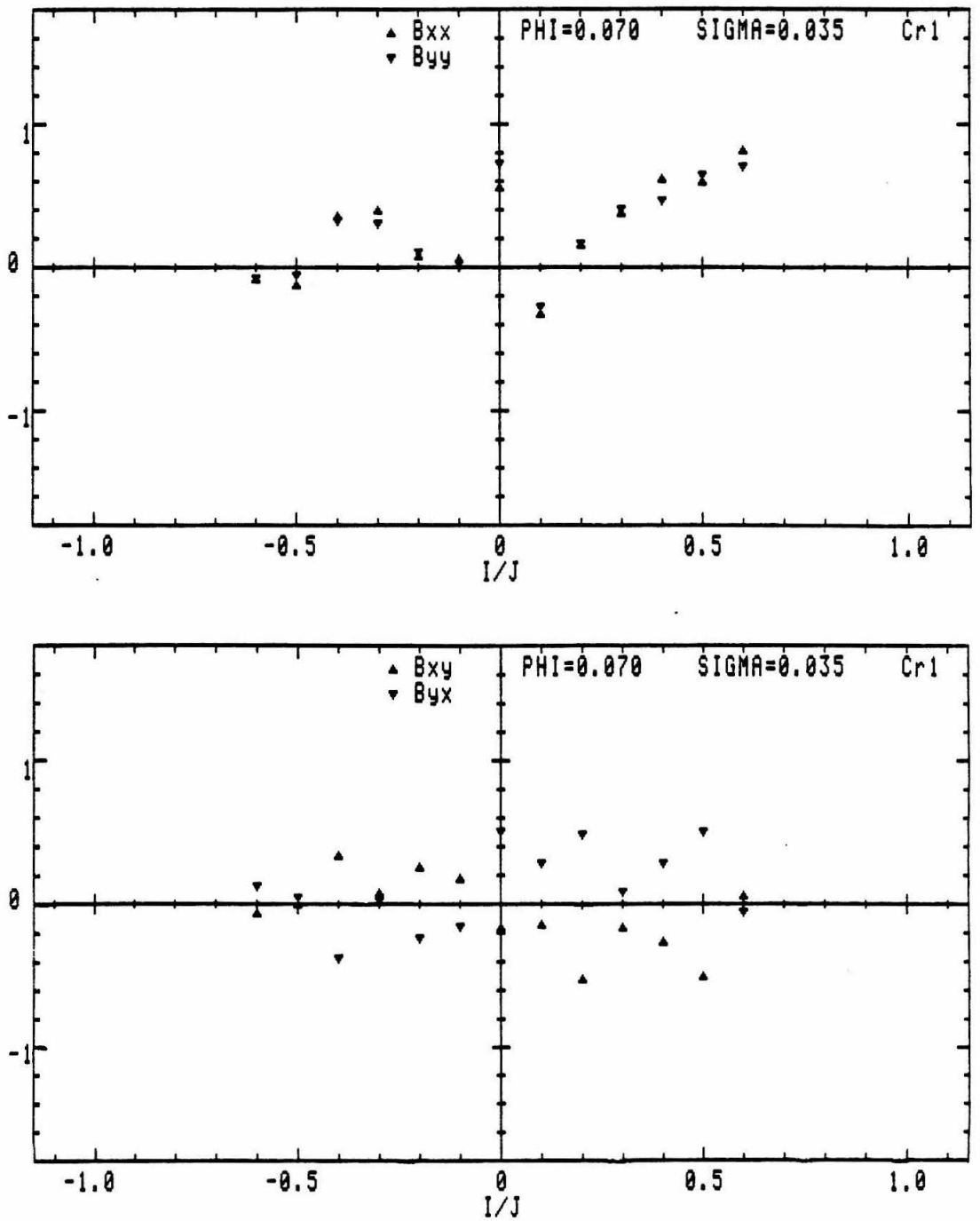

Figure A.17: Rotordynamic moment coefficients ($\phi = 0.070$, $\sigma = 0.035$, Cr_1).

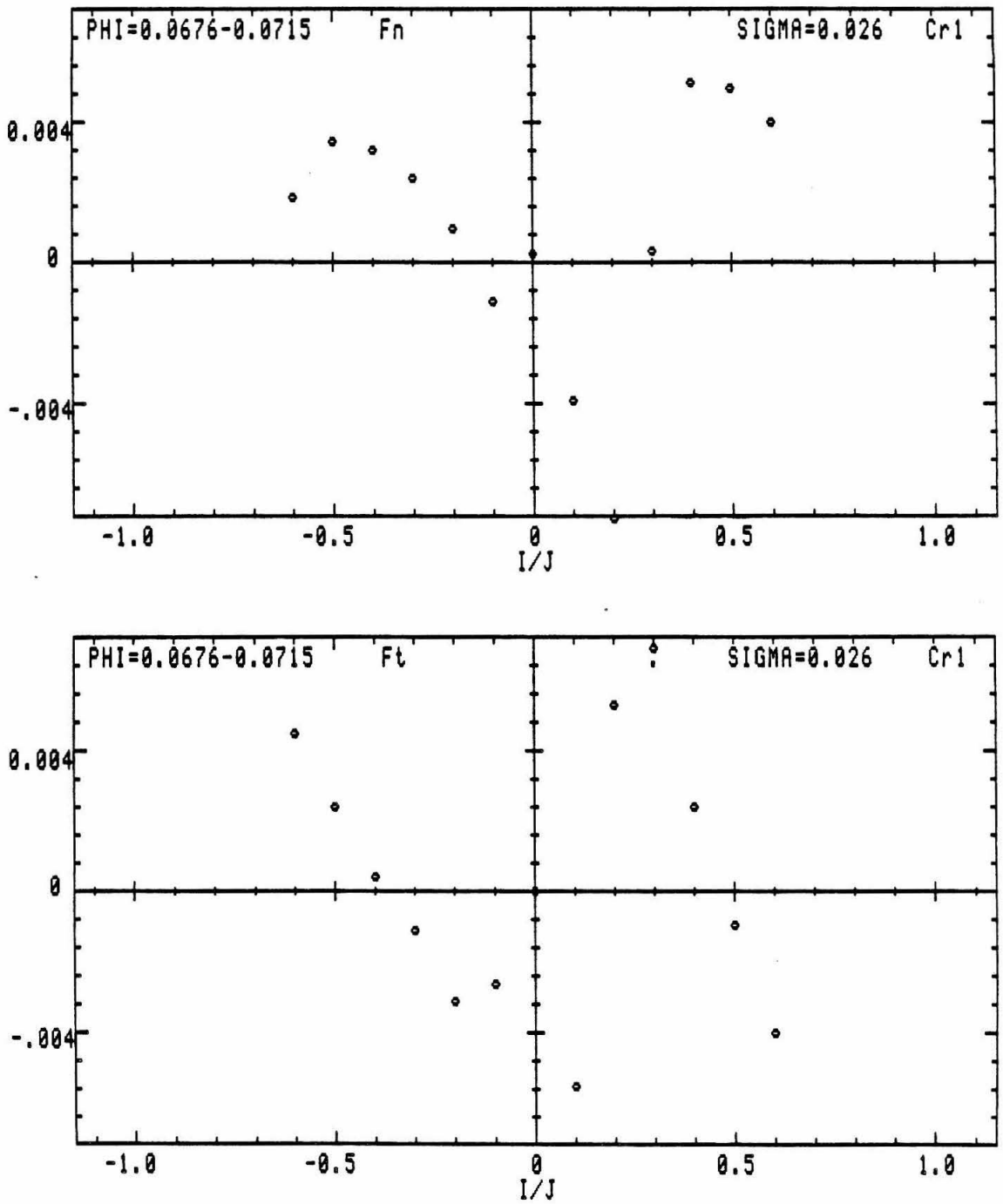

Figure A.18: Unsteady hydrodynamic forces ($\phi = 0.070$, $\sigma = 0.026$, Cr_1).

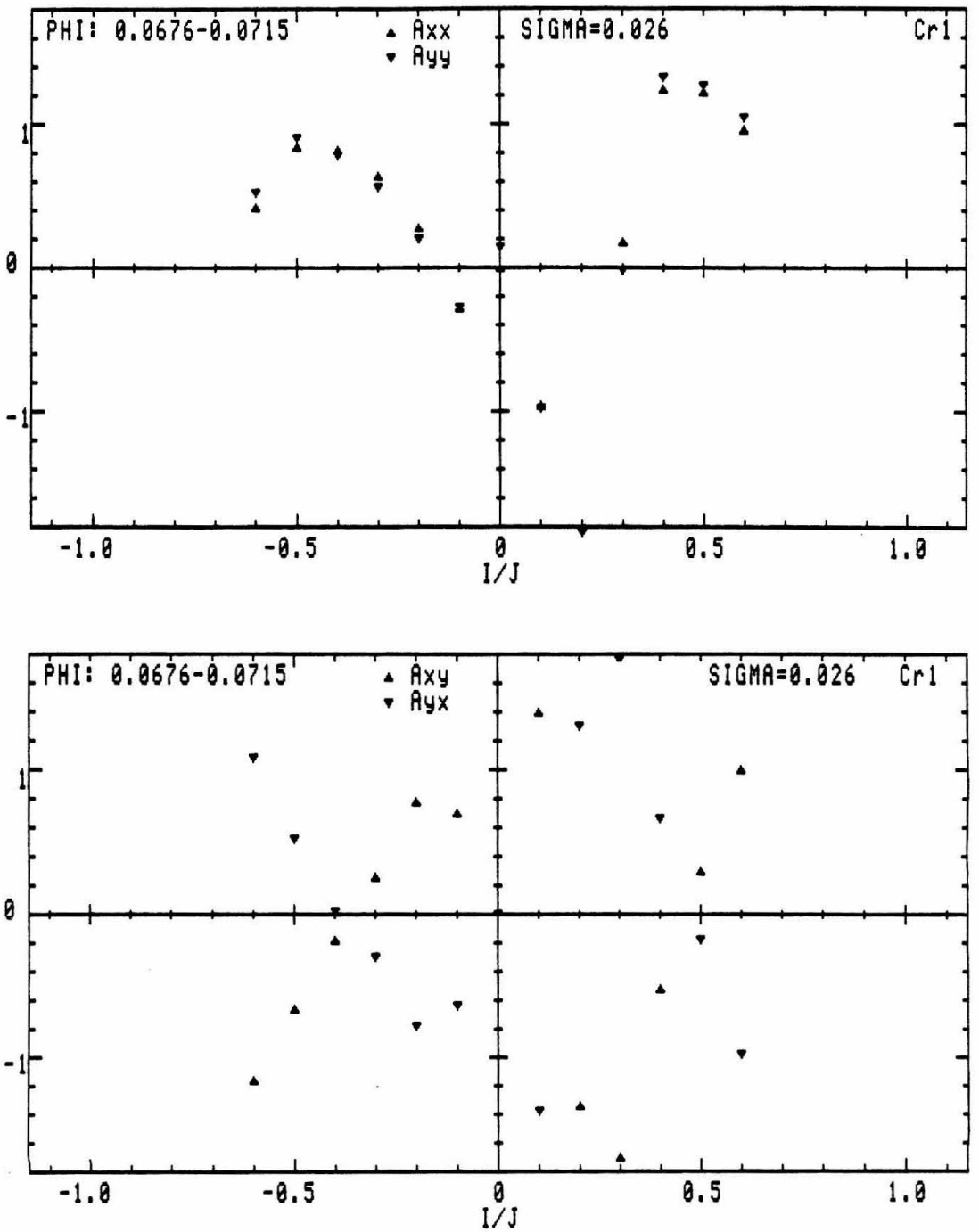

Figure A.19: Rotordynamic force coefficients ($\phi = 0.070$, $\sigma = 0.026$, Cr_1).

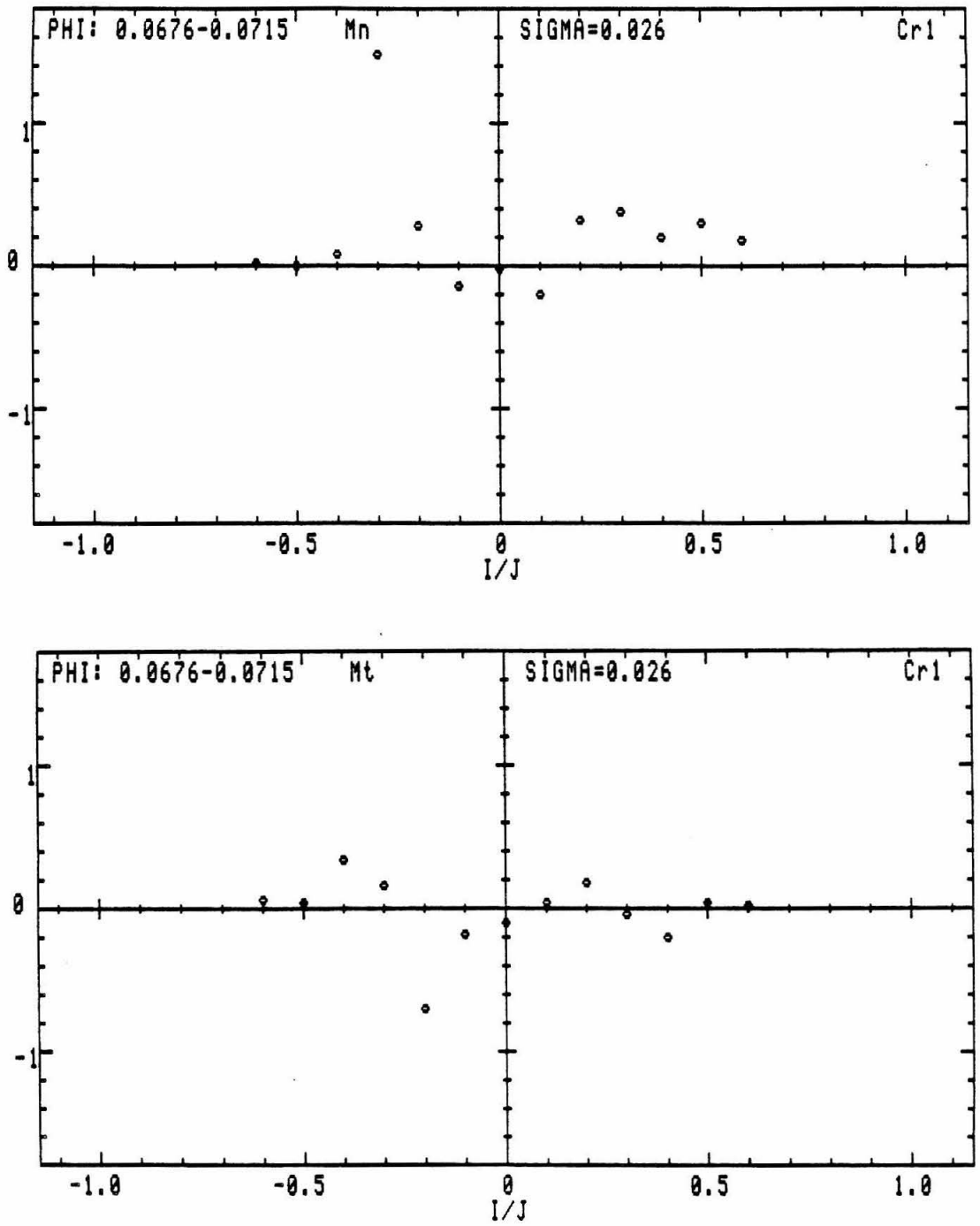

Figure A.20: Unsteady moments ($\phi = 0.070$, $\sigma = 0.026$, Cr_1).

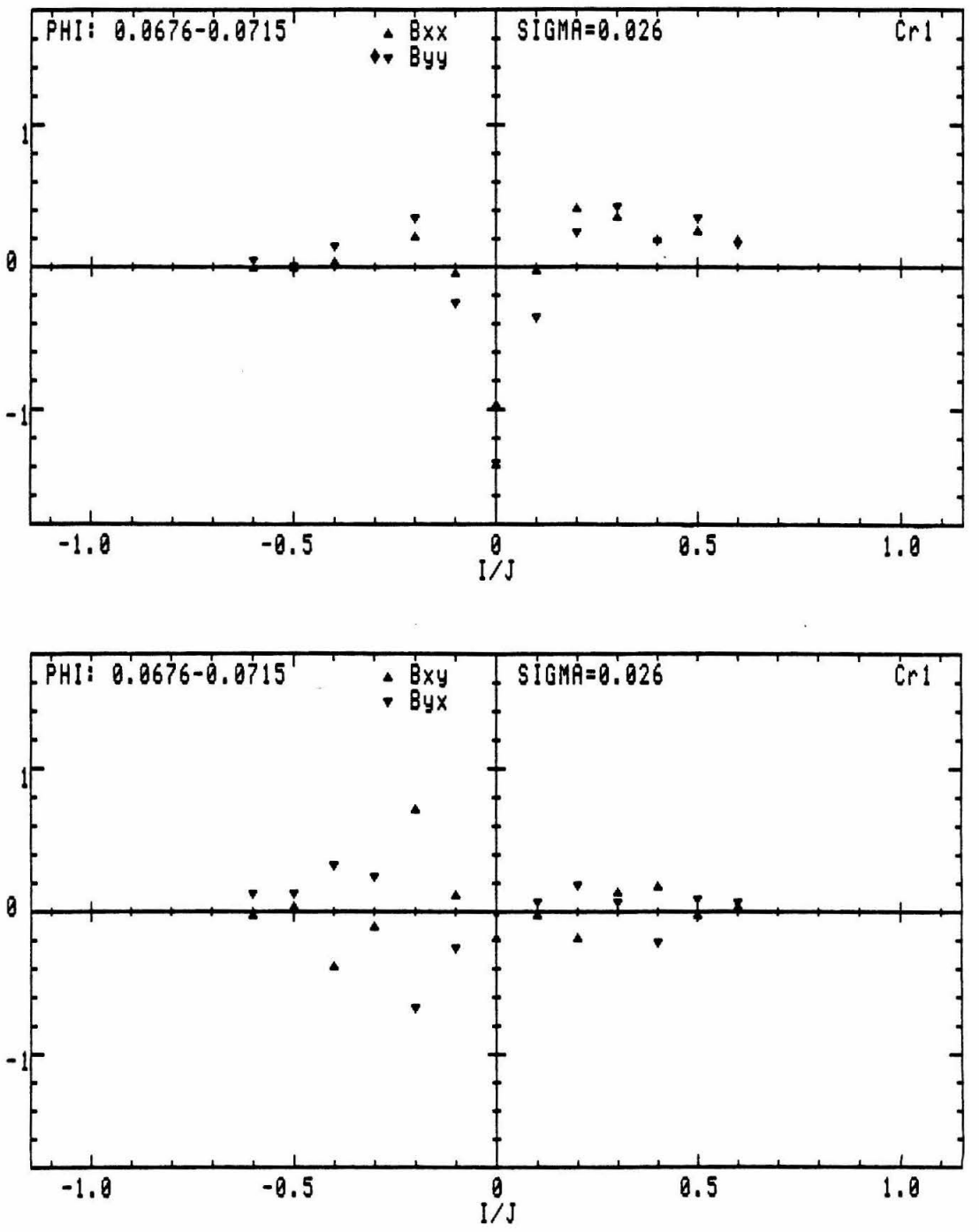

Figure A.21: Rotordynamic moment coefficients ($\phi = 0.070$, $\sigma = 0.026$, Cr_1).

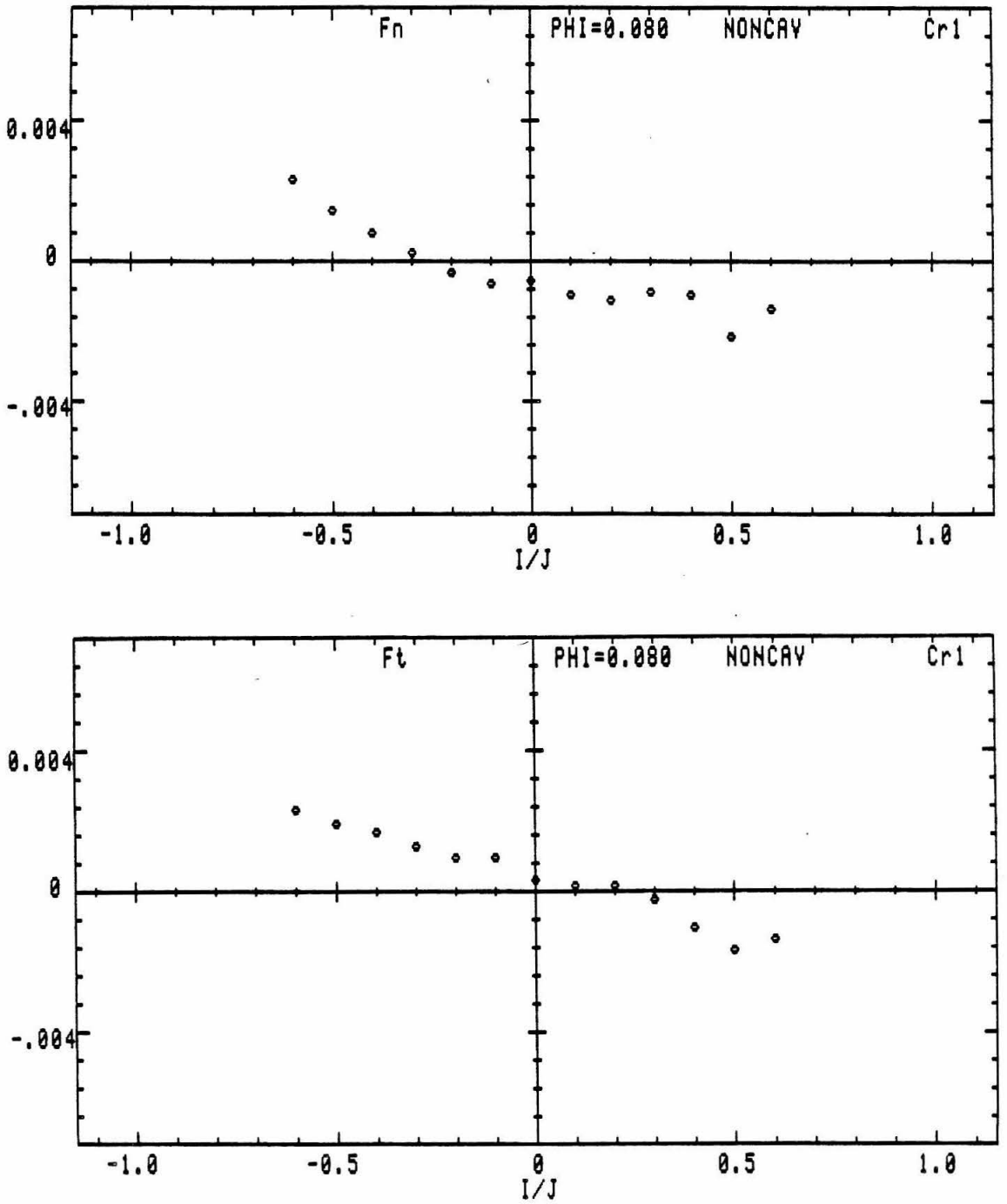

Figure A.22: Unsteady hydrodynamic forces ($\phi = 0.080$, noncavitating flow, Cr_1).

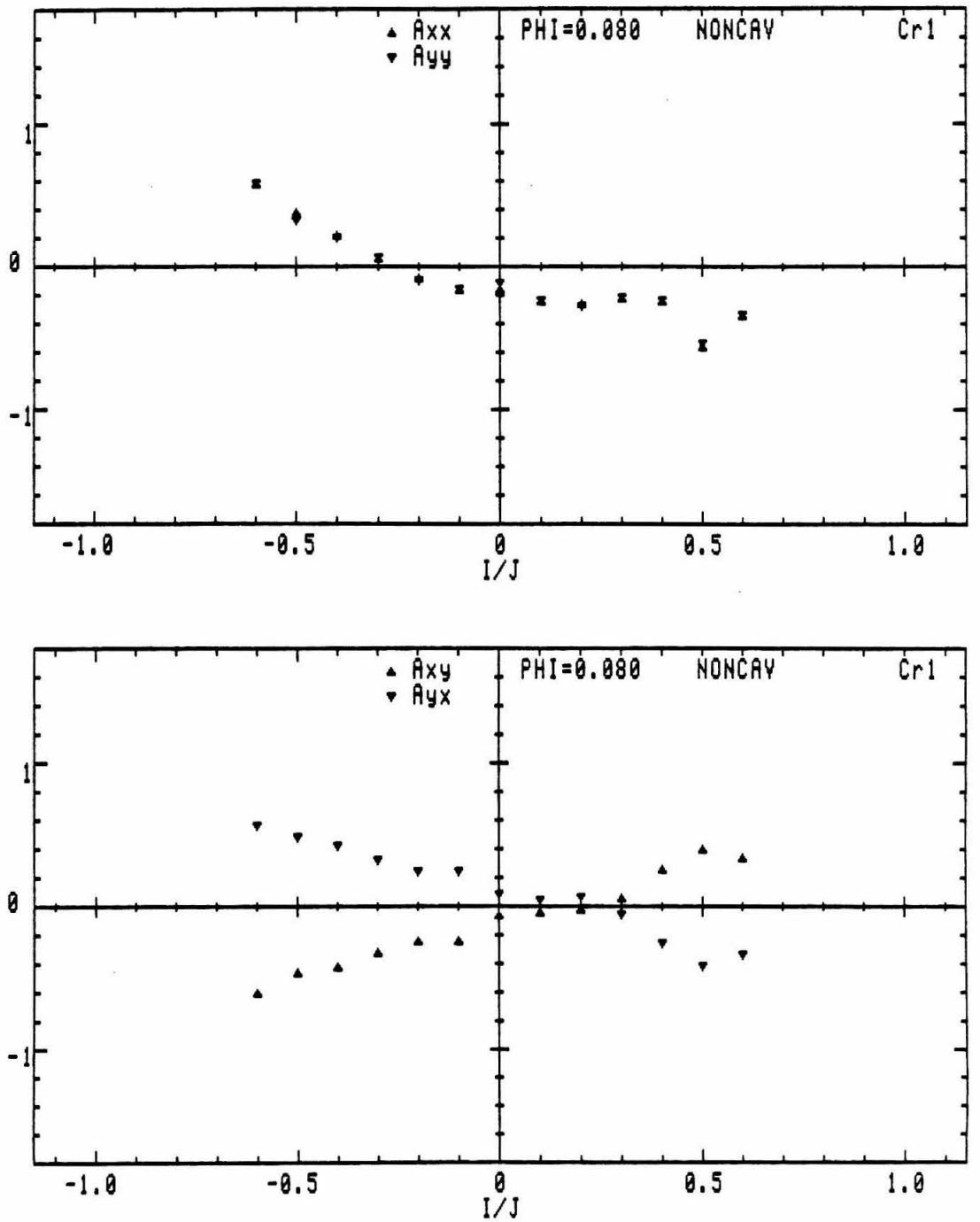

Figure A.23: Rotordynamic force coefficients ($\phi = 0.080$, noncavitating flow, Cr_1).

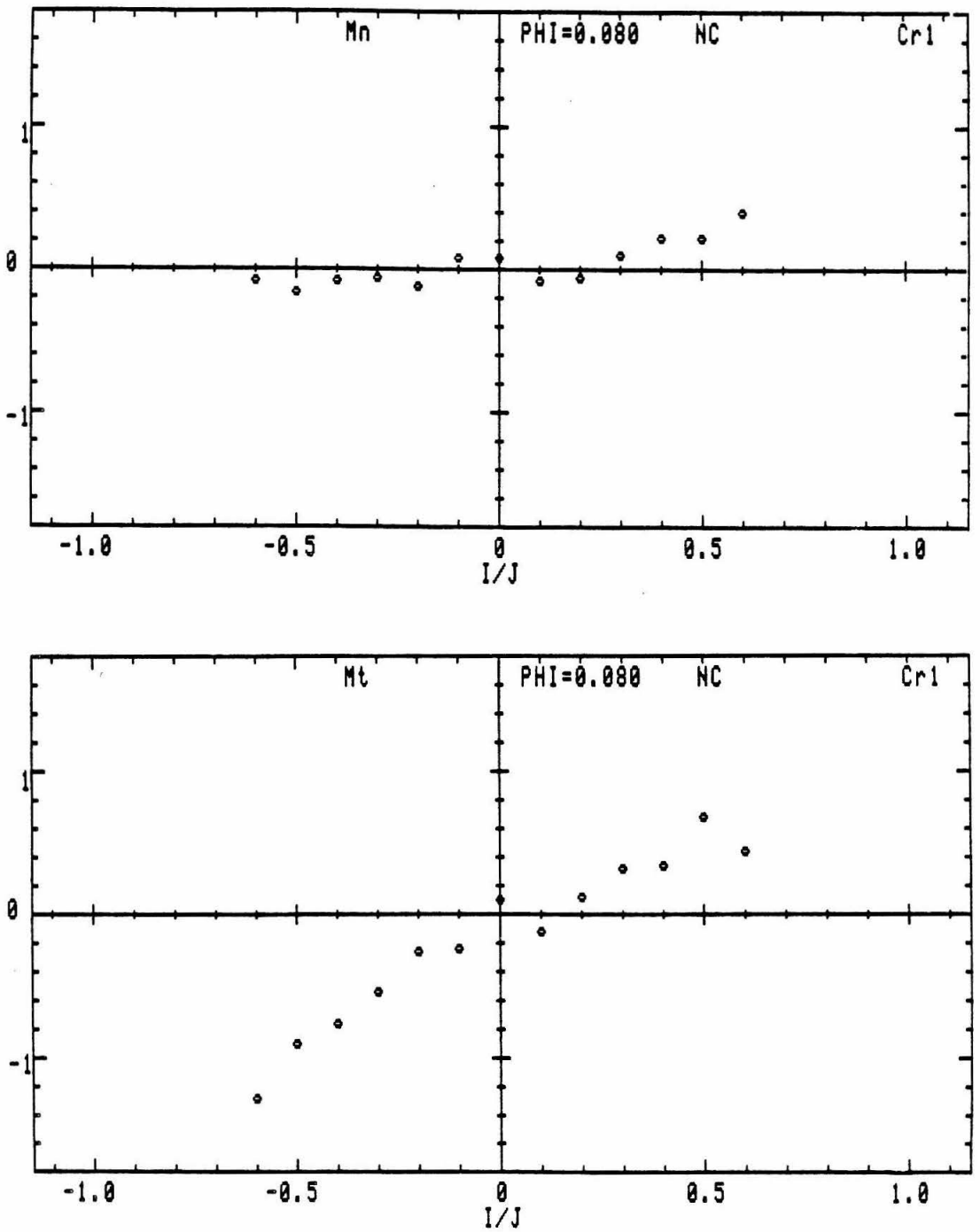

Figure A.24: Unsteady moments ($\phi = 0.080$, noncavitating flow, Cr_1).

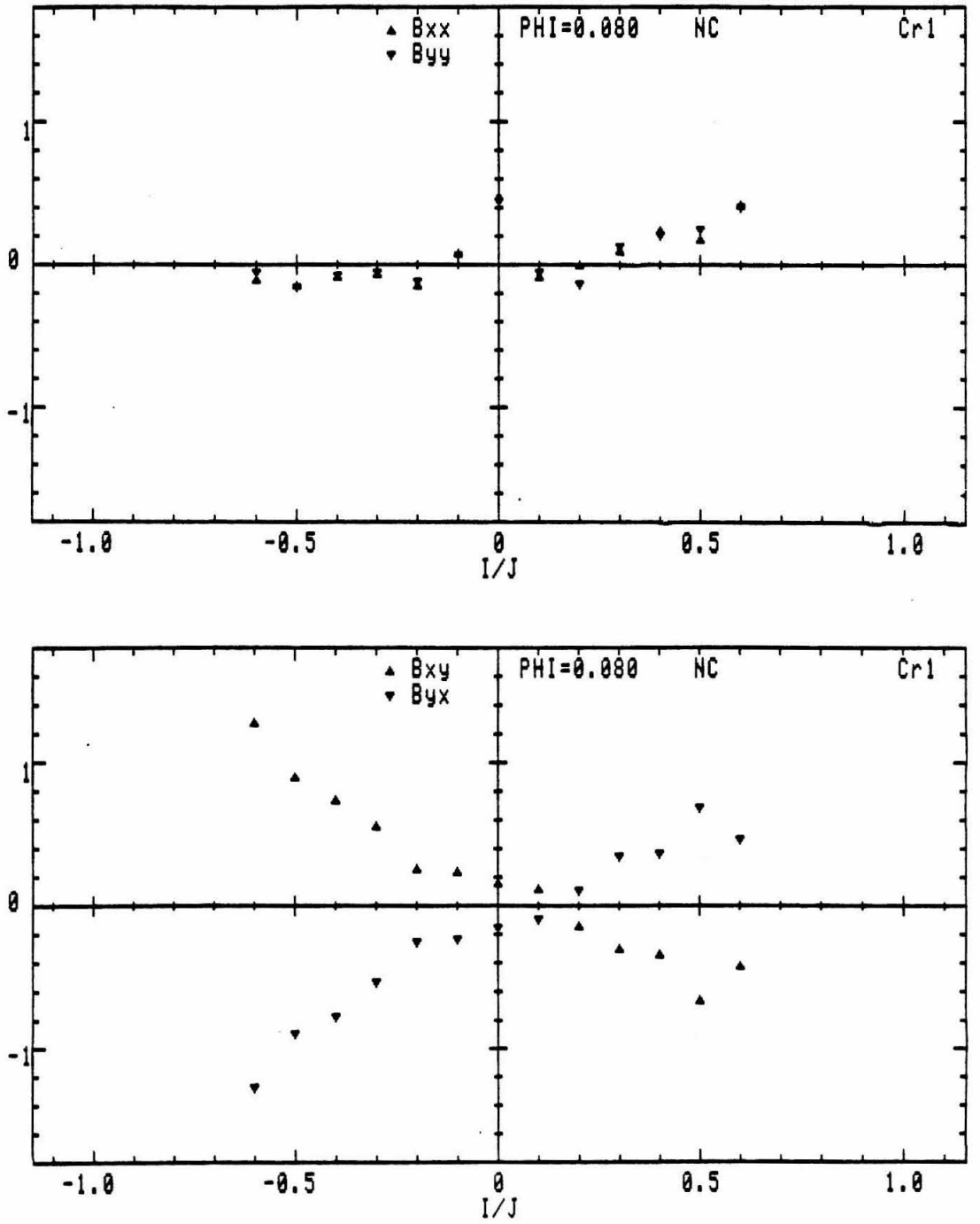

Figure A.25: Rotordynamic moment coefficients ($\phi = 0.080$, noncavitating flow, Cr_1).

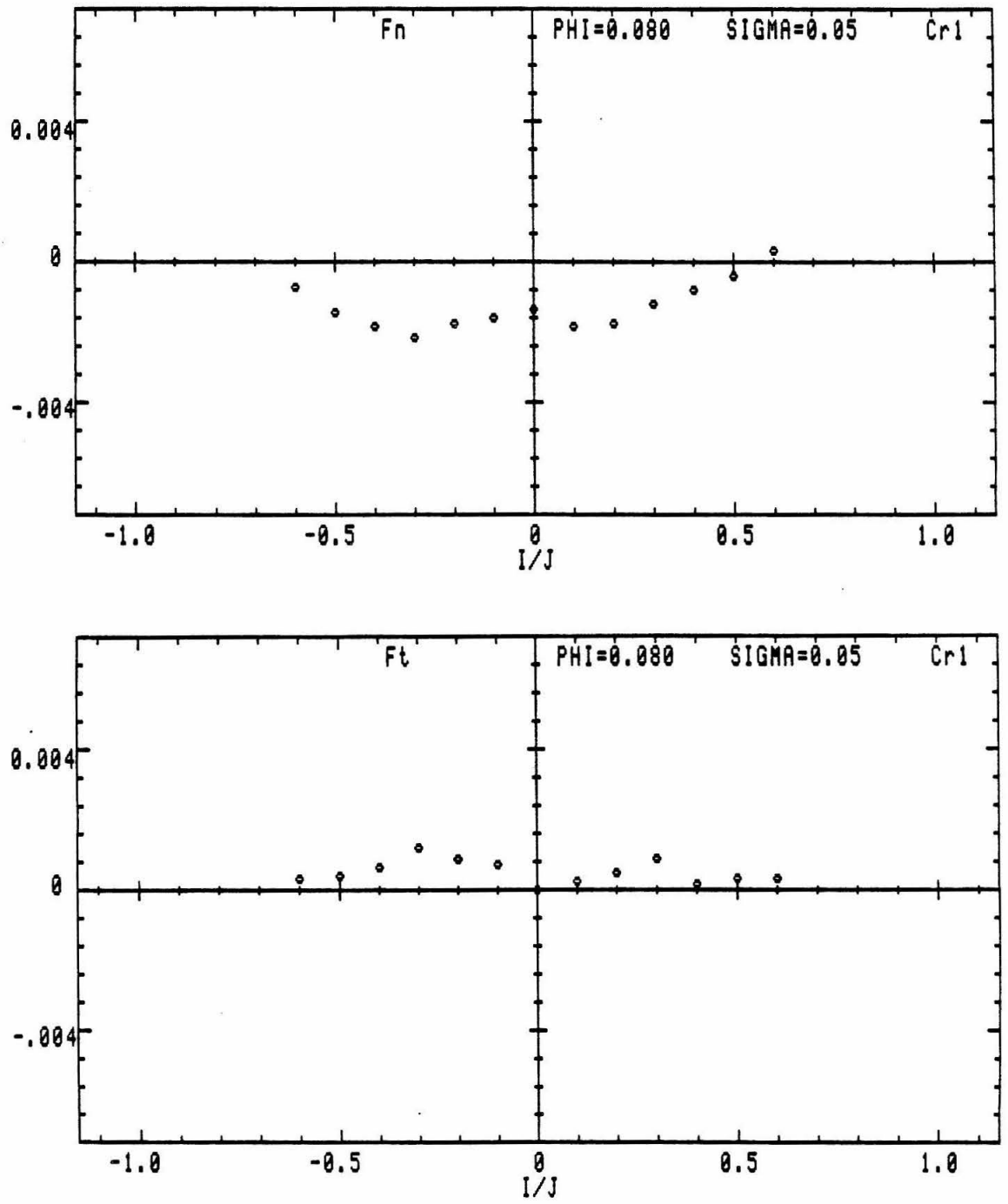

Figure A.26: Unsteady hydrodynamic forces ($\phi = 0.080$, $\sigma = 0.050$, Cr_1).

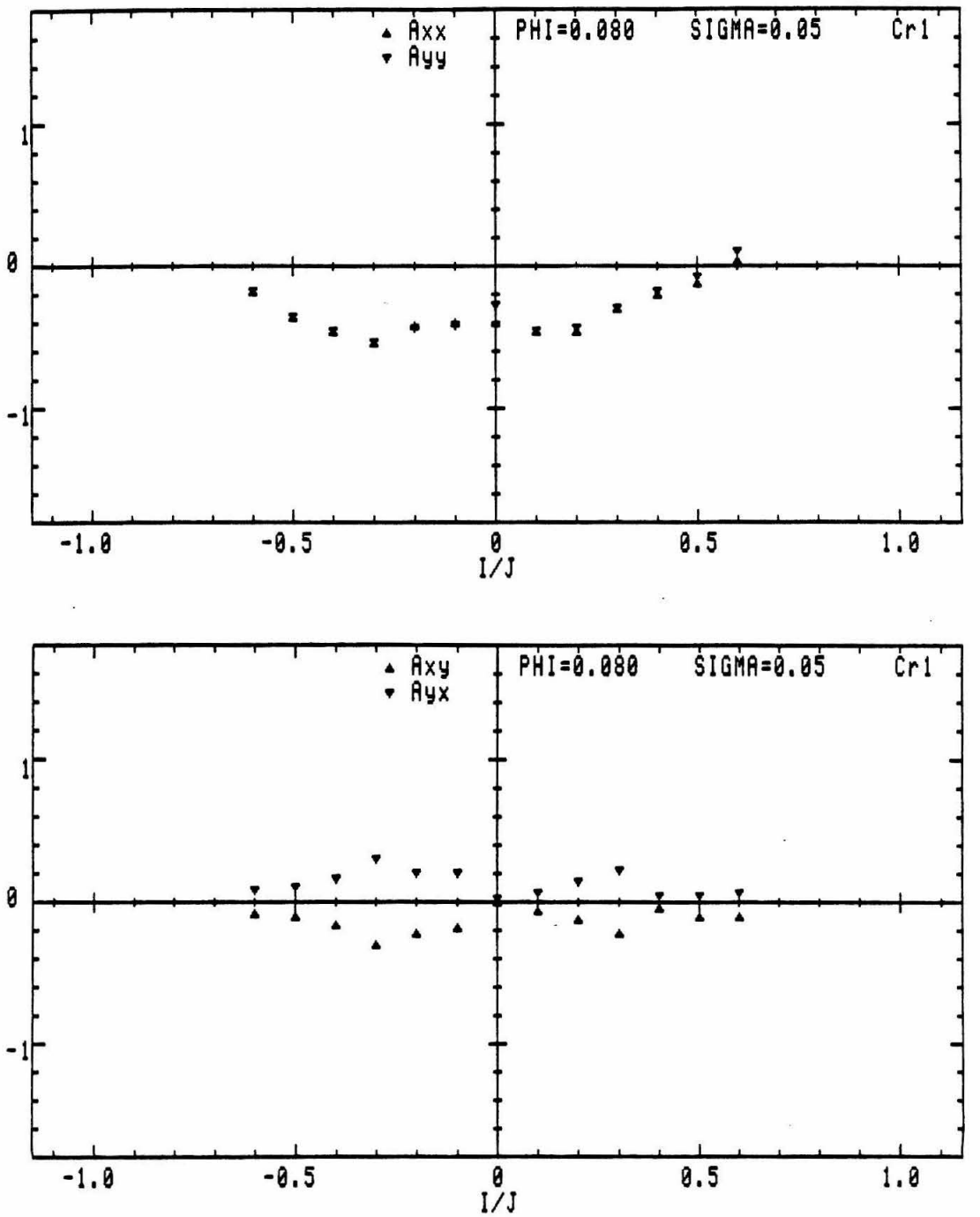

Figure A.27: Rotordynamic force coefficients ($\phi = 0.080$, $\sigma = 0.050$, Cr_1).

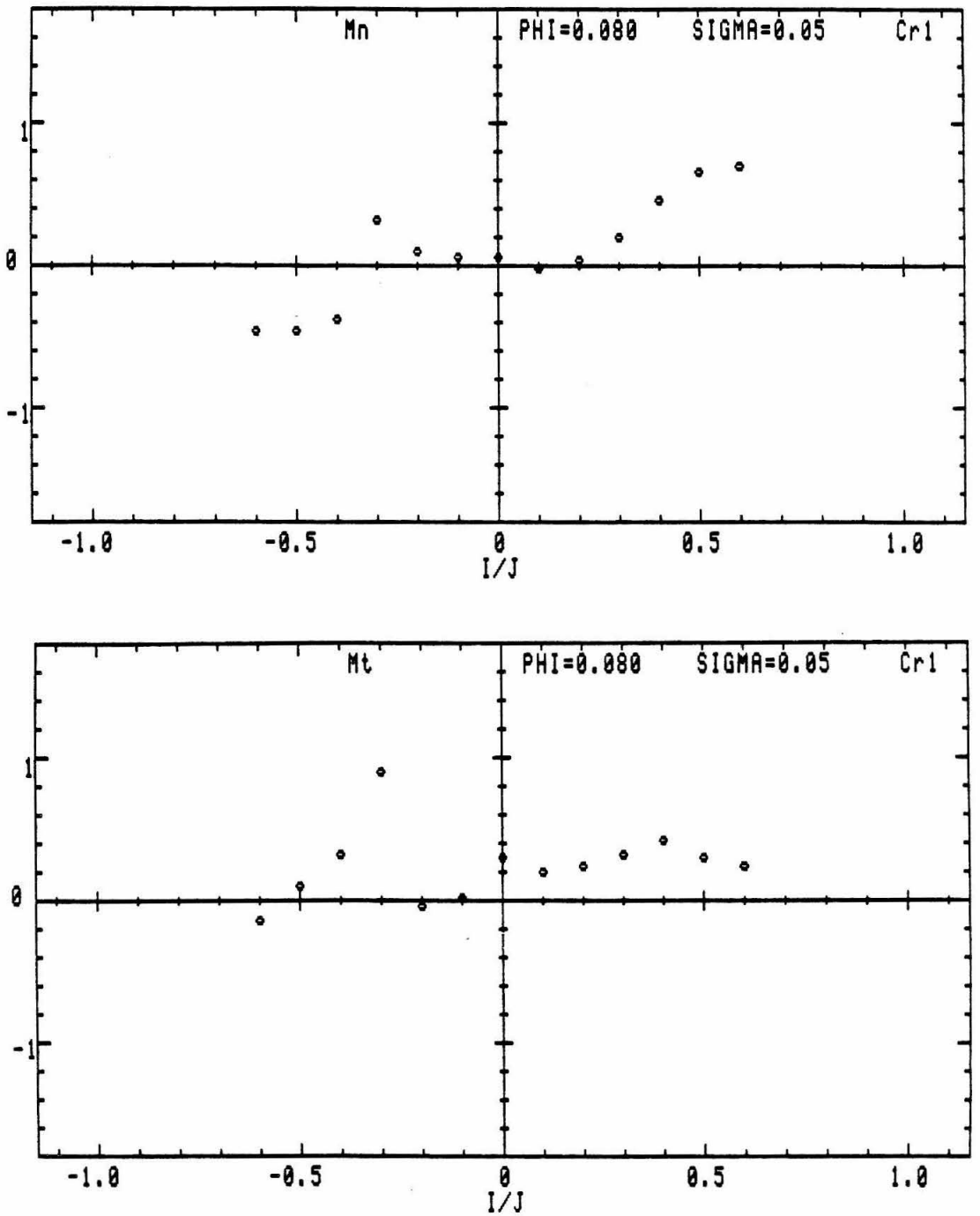

Figure A.28: Unsteady moments ($\phi = 0.080$, $\sigma = 0.050$, Cr_1).

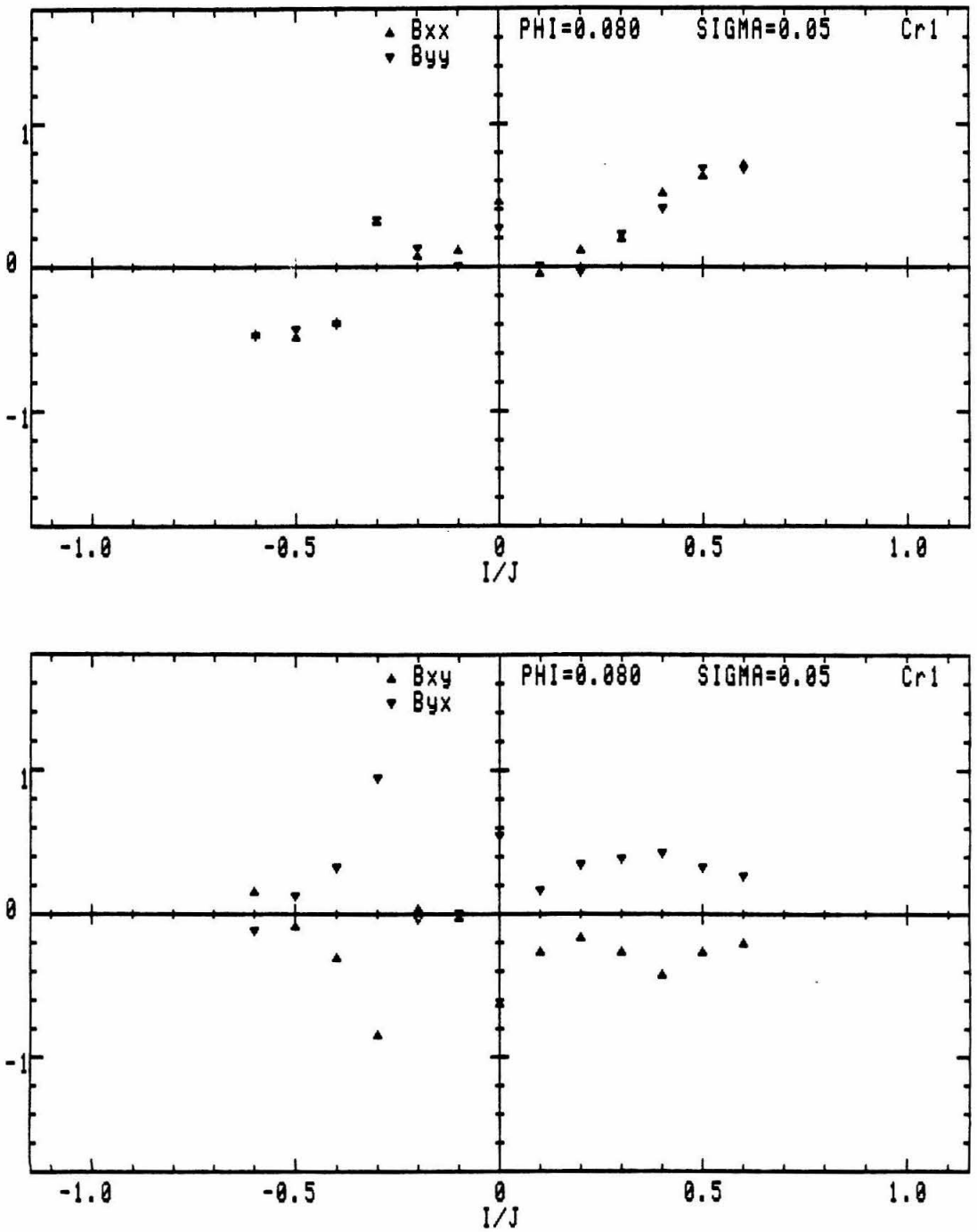

Figure A.29: Rotordynamic moment coefficients ($\phi = 0.080$, $\sigma = 0.050$, Cr_1).

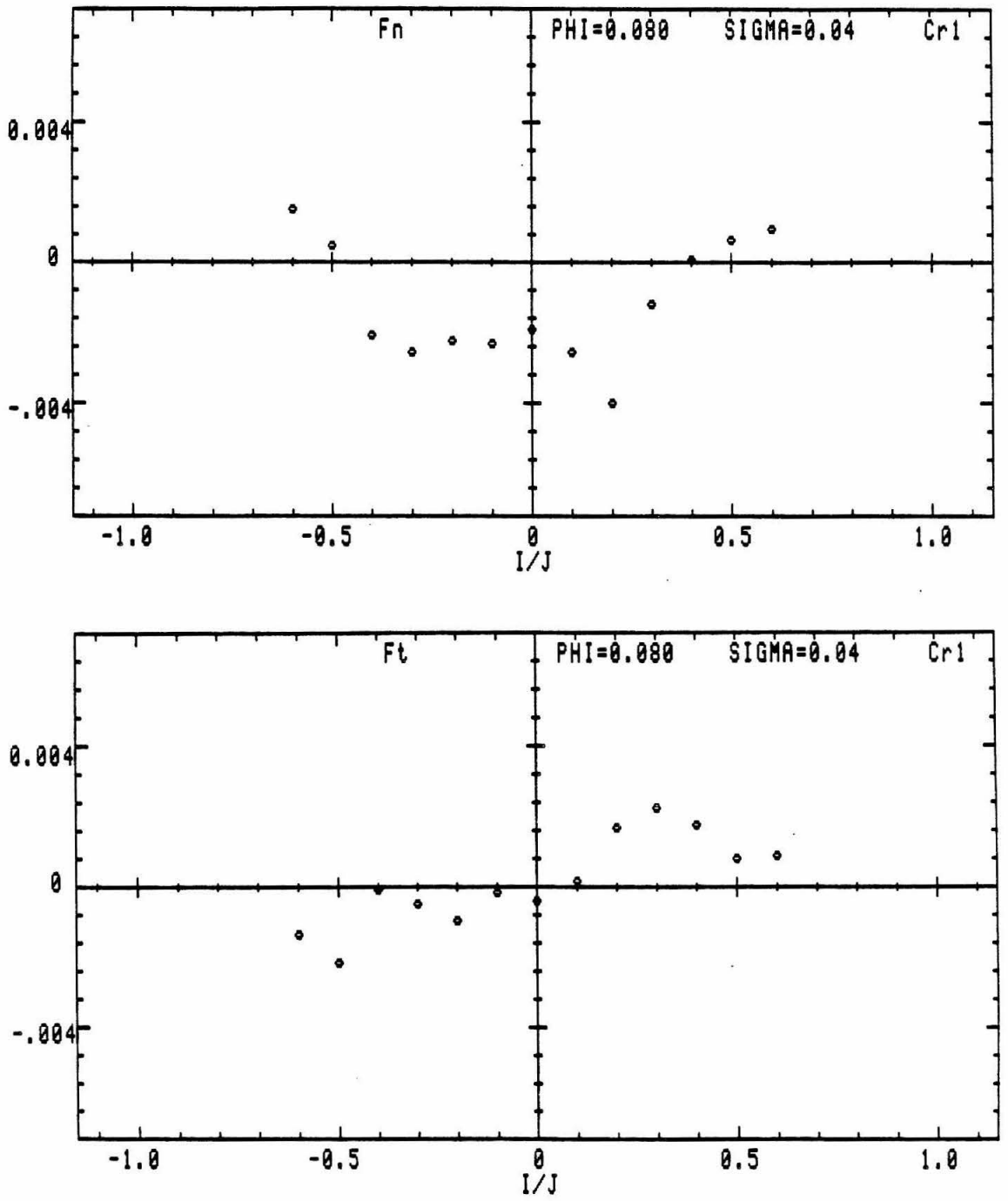

Figure A.30: Unsteady hydrodynamic forces ($\phi = 0.080$, $\sigma = 0.040$, Cr_1).

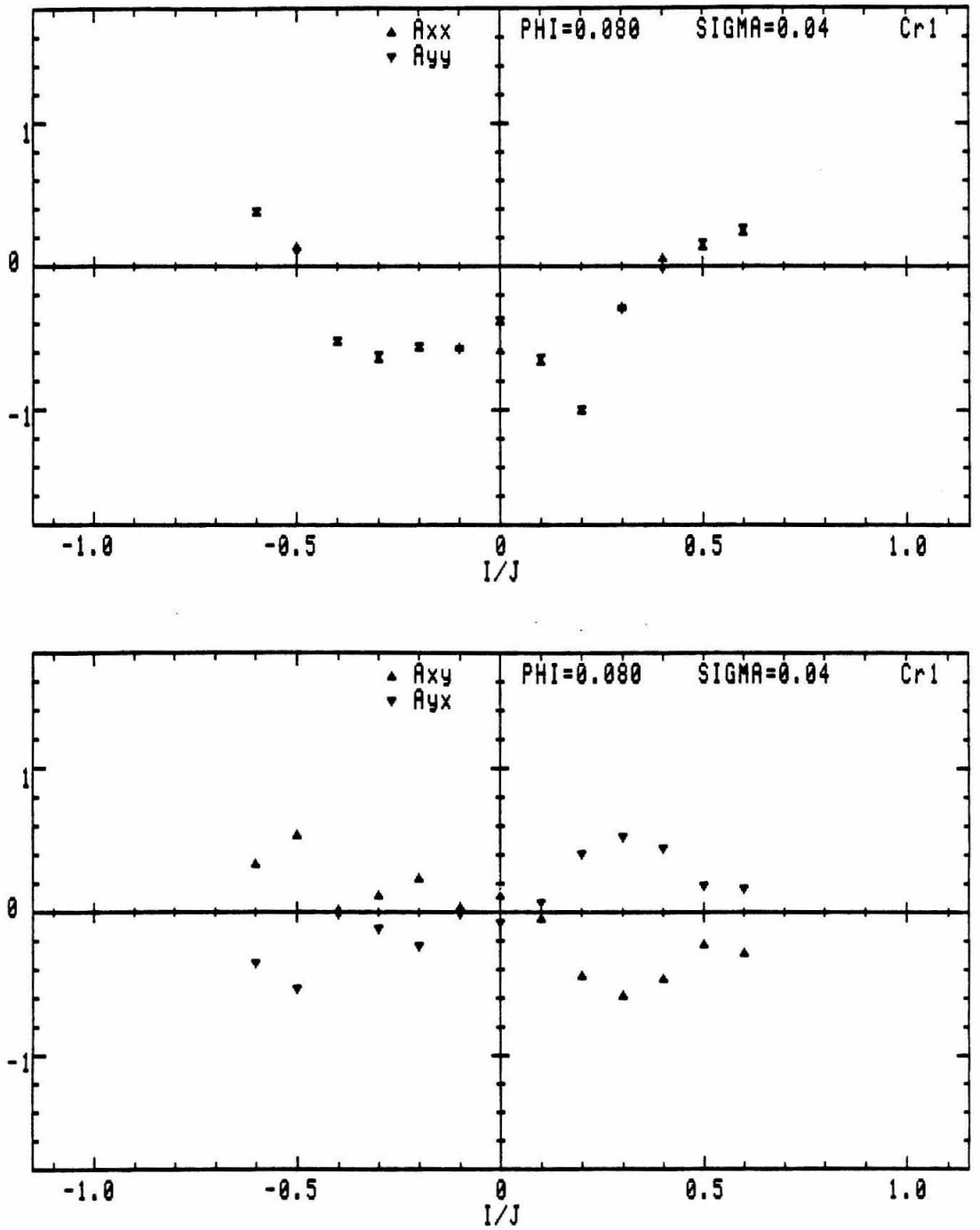

Figure A.31: Rotordynamic force coefficients ($\phi = 0.080$, $\sigma = 0.040$, Cr_1).

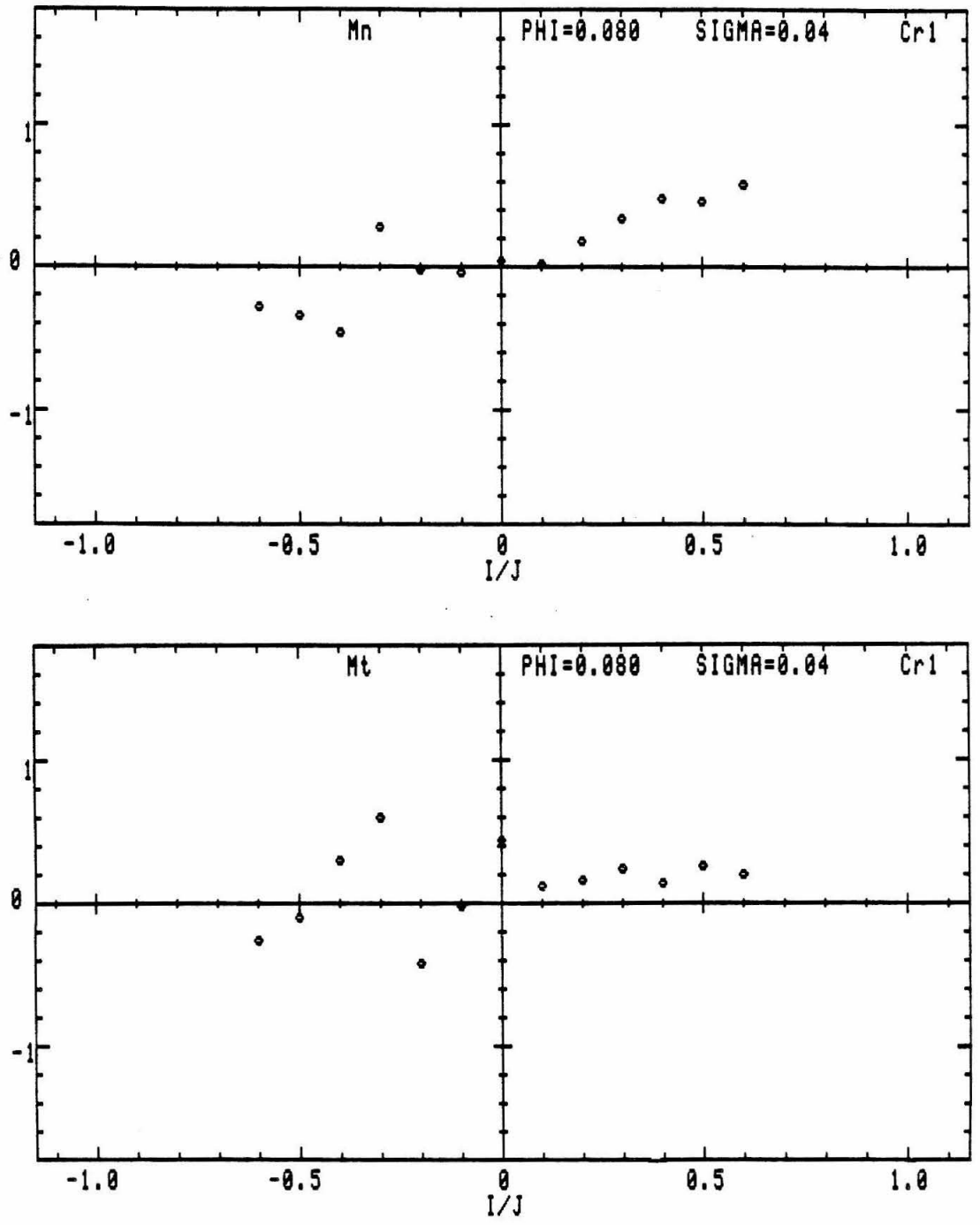

Figure A.32: Unsteady moments ($\phi = 0.080$, $\sigma = 0.040$, Cr_1).

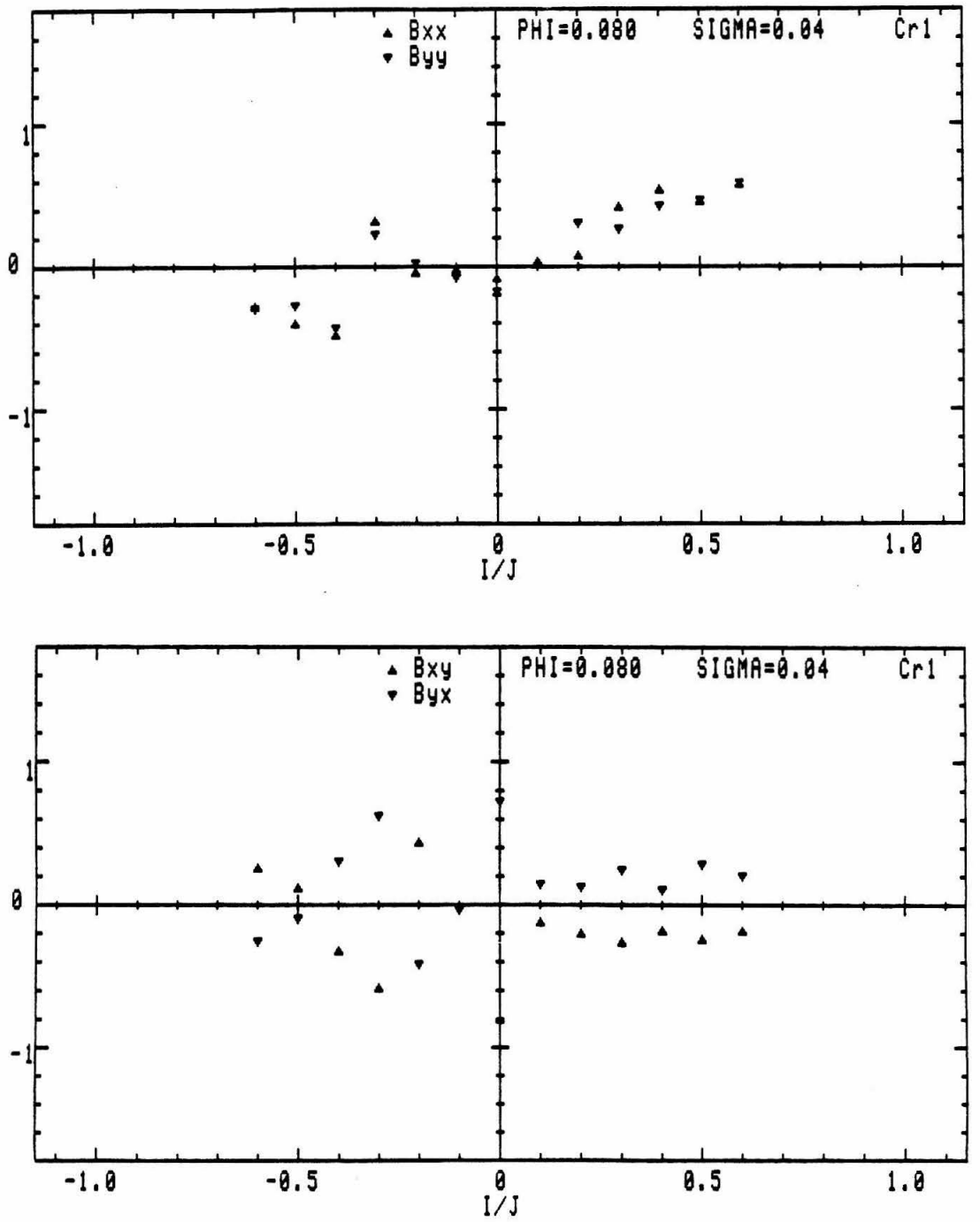

Figure A.33: Rotordynamic moment coefficients ($\phi = 0.080$, $\sigma = 0.040$, Cr_1).

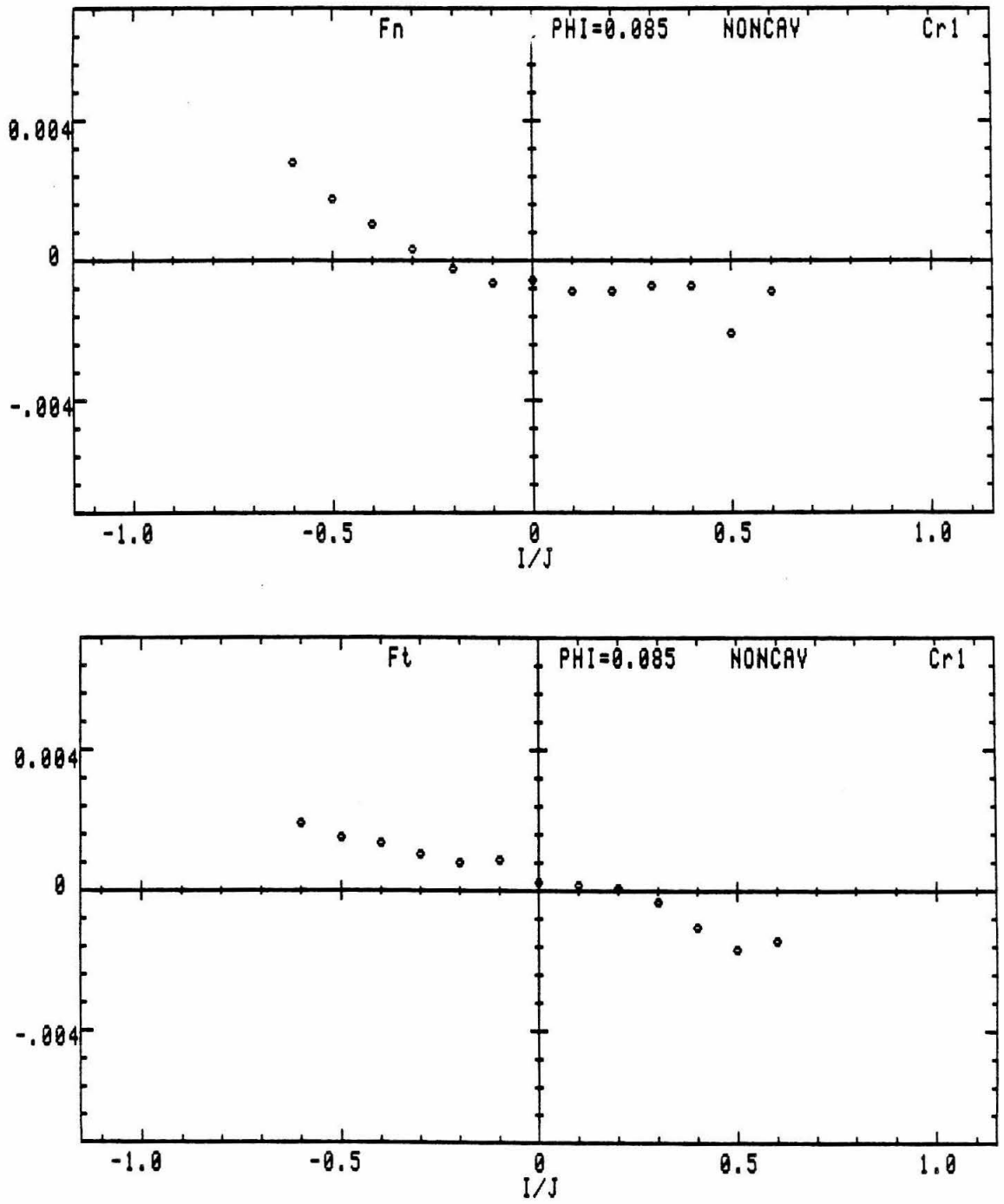

Figure A.34: Unsteady hydrodynamic forces ($\phi = 0.085$, noncavitating flow, Cr_1).

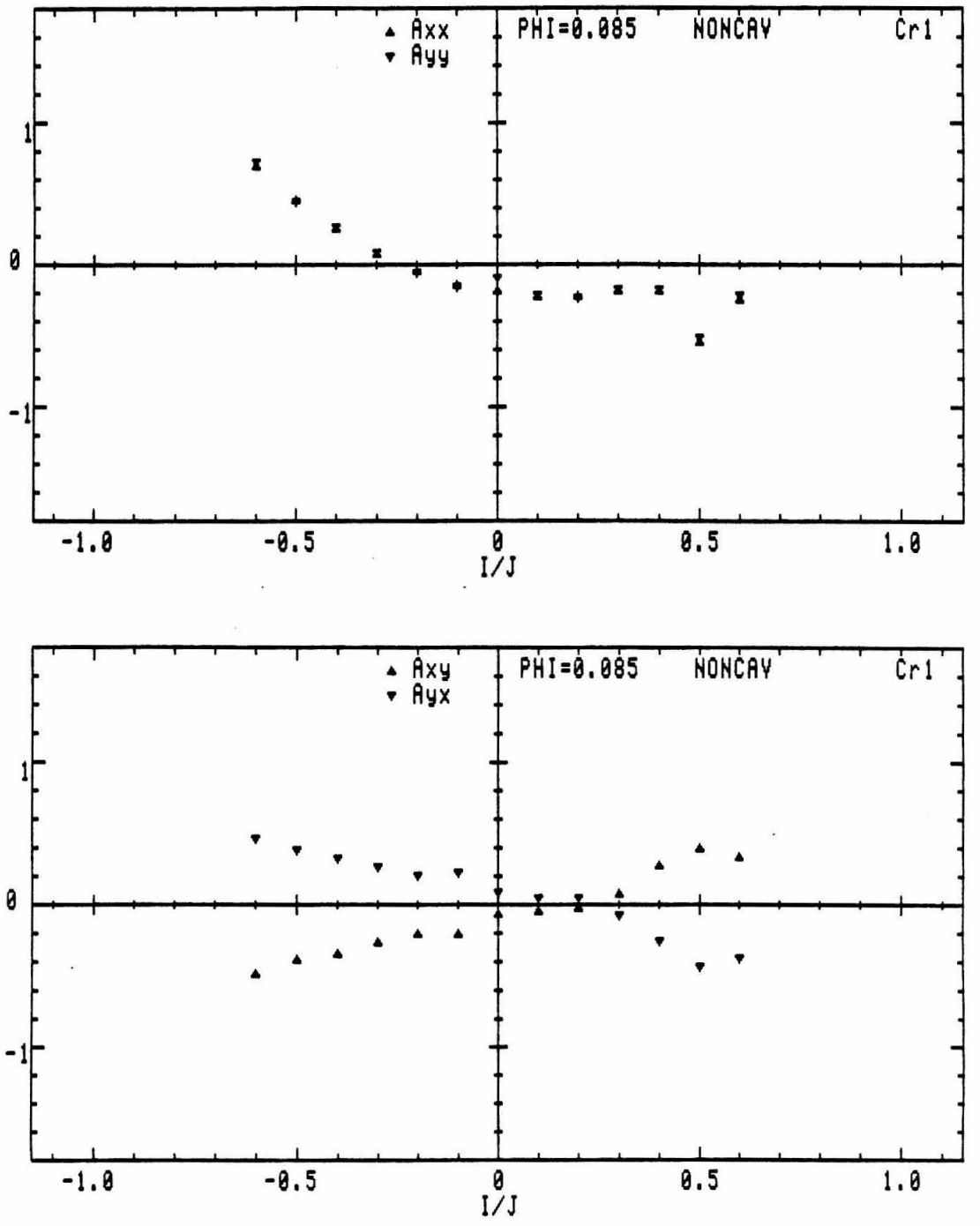

Figure A.35: Rotordynamic force coefficients ($\phi = 0.085$, noncavitating flow, Cr_1).

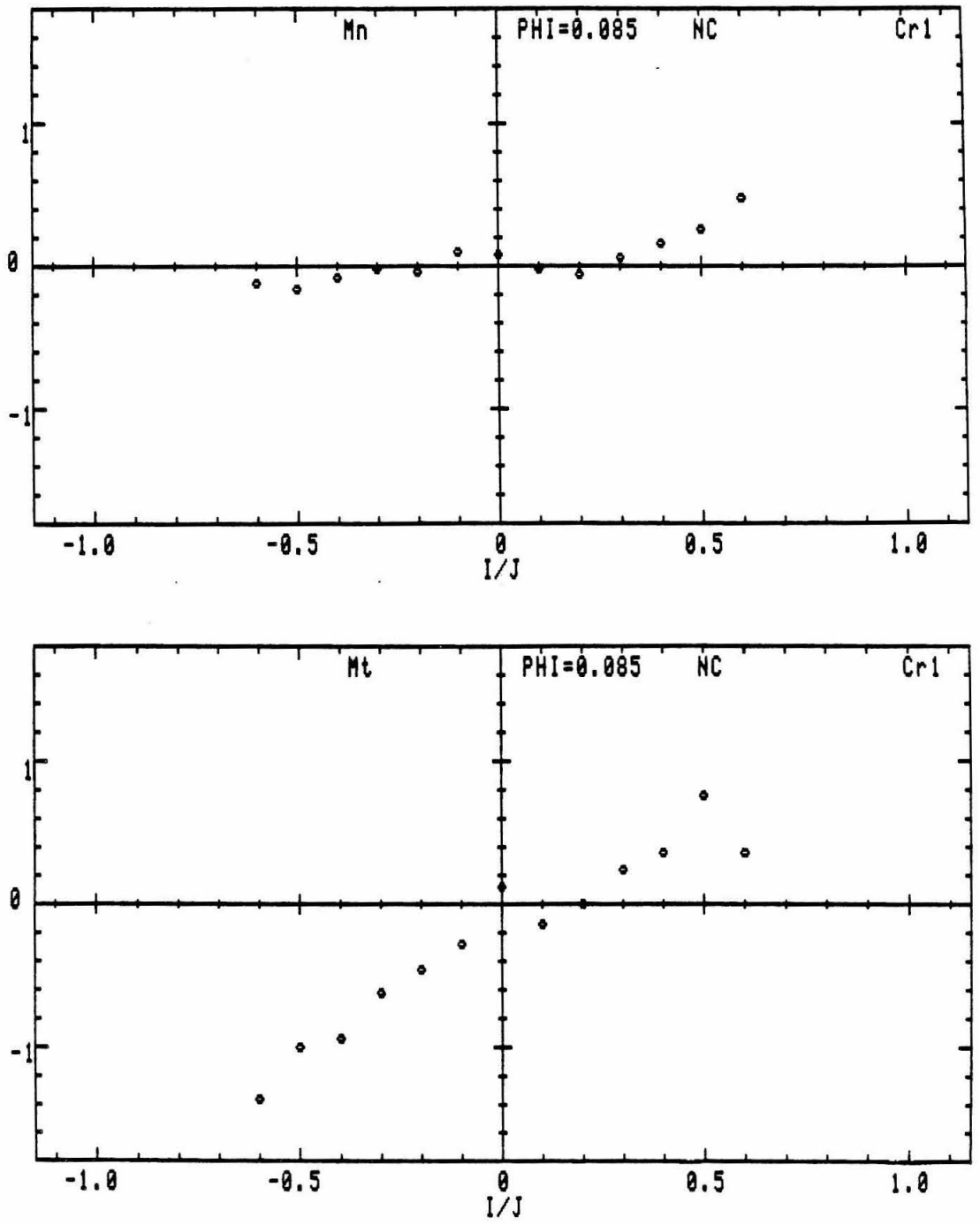

Figure A.36: Unsteady moments ($\phi = 0.085$, noncavitating flow, Cr_1).

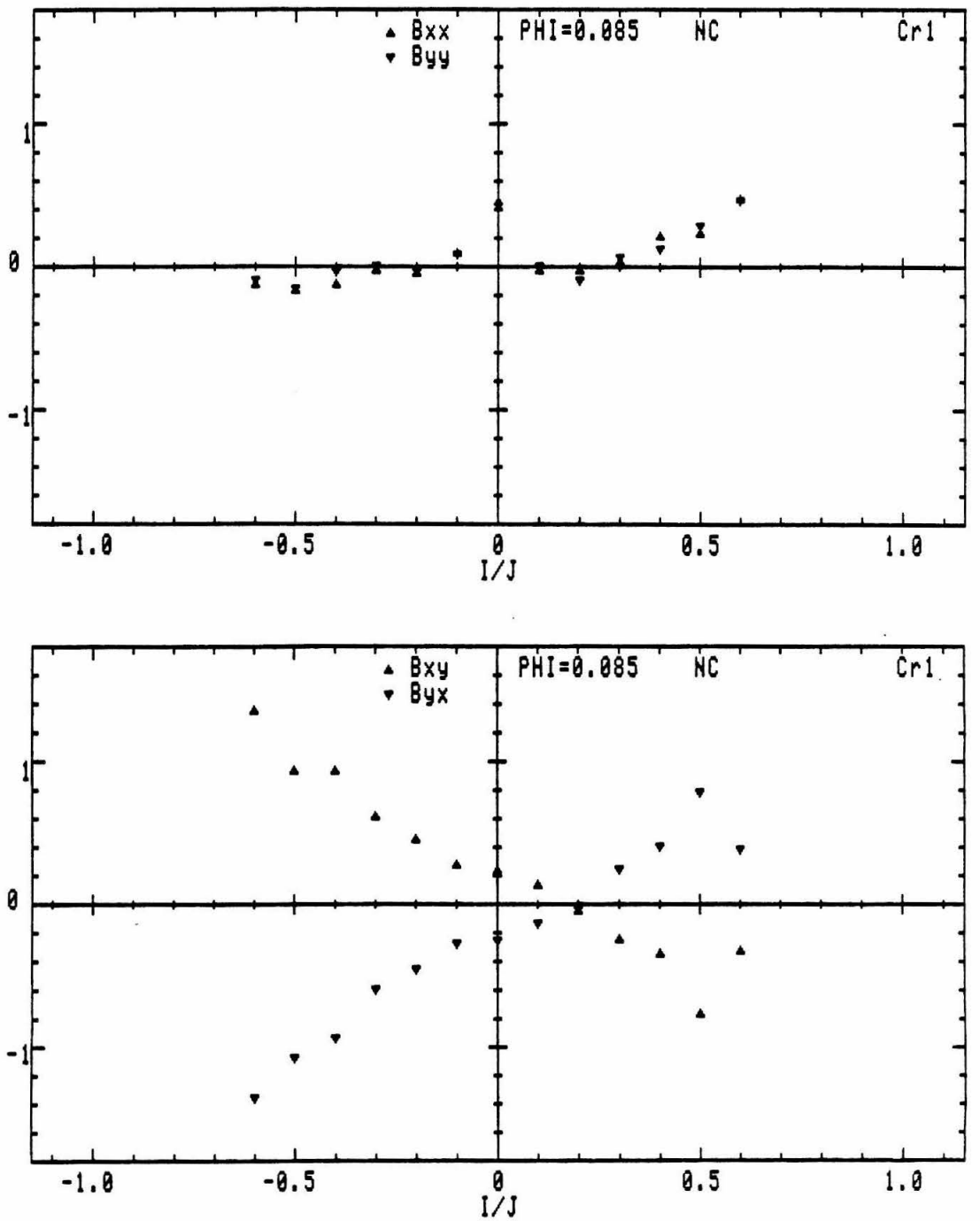

Figure A.37: Rotordynamic moment coefficients ($\phi = 0.085$, noncavitating flow, Cr_1).

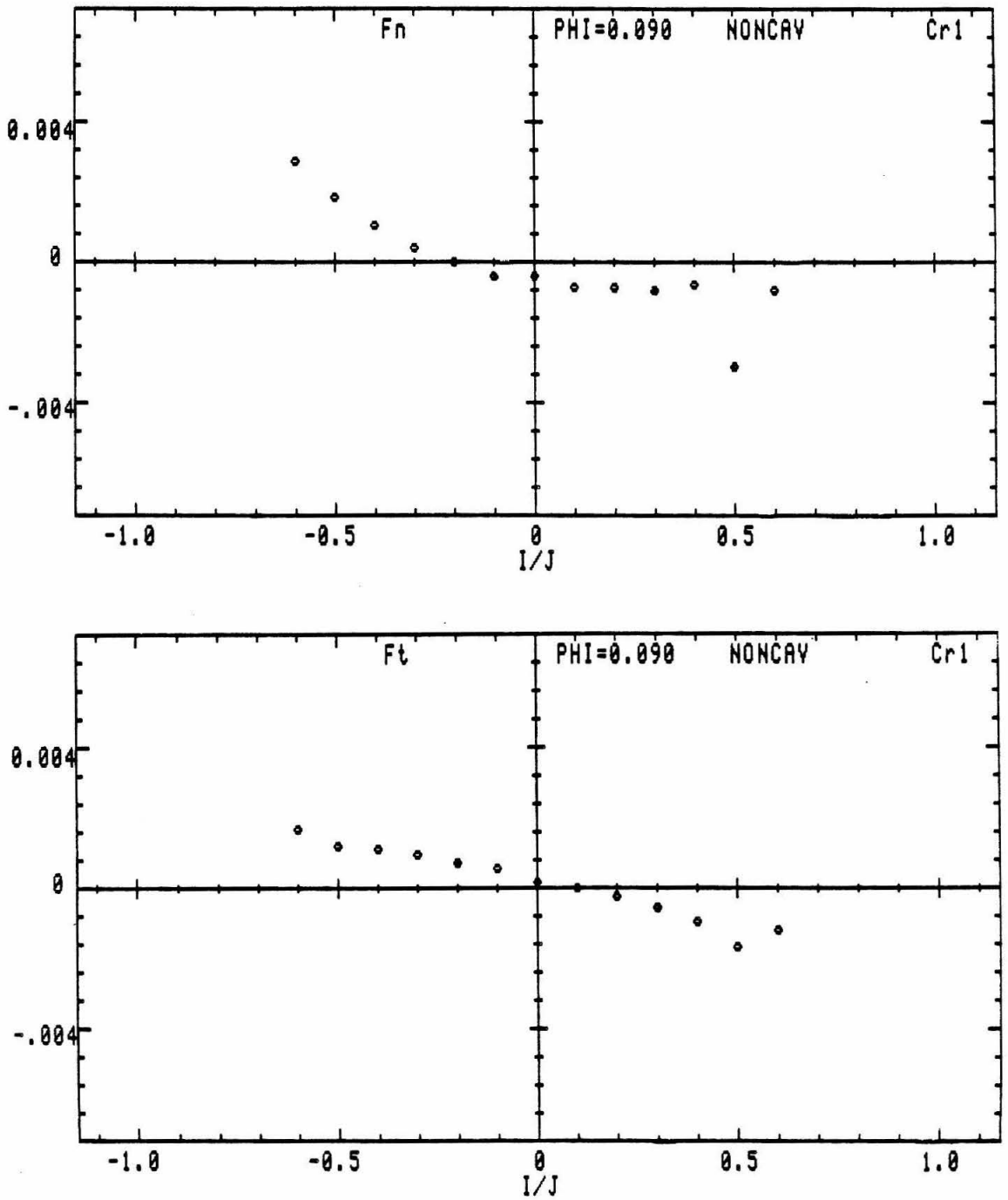

Figure A.38: Unsteady hydrodynamic forces ($\phi = 0.090$, noncavitating flow, Cr_1).

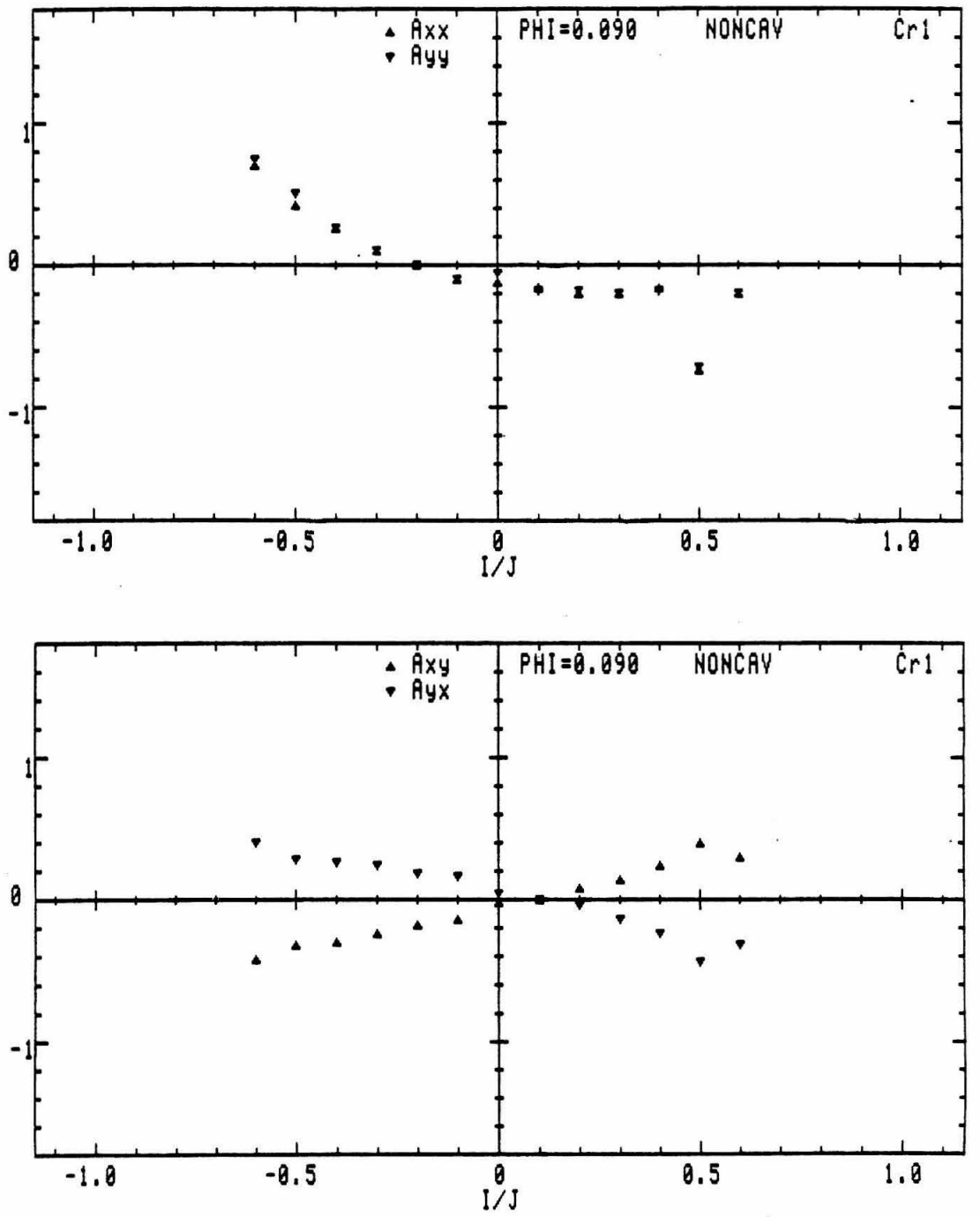

Figure A.39: Rotordynamic force coefficients ($\phi = 0.090$, noncavitating flow, Cr_1).

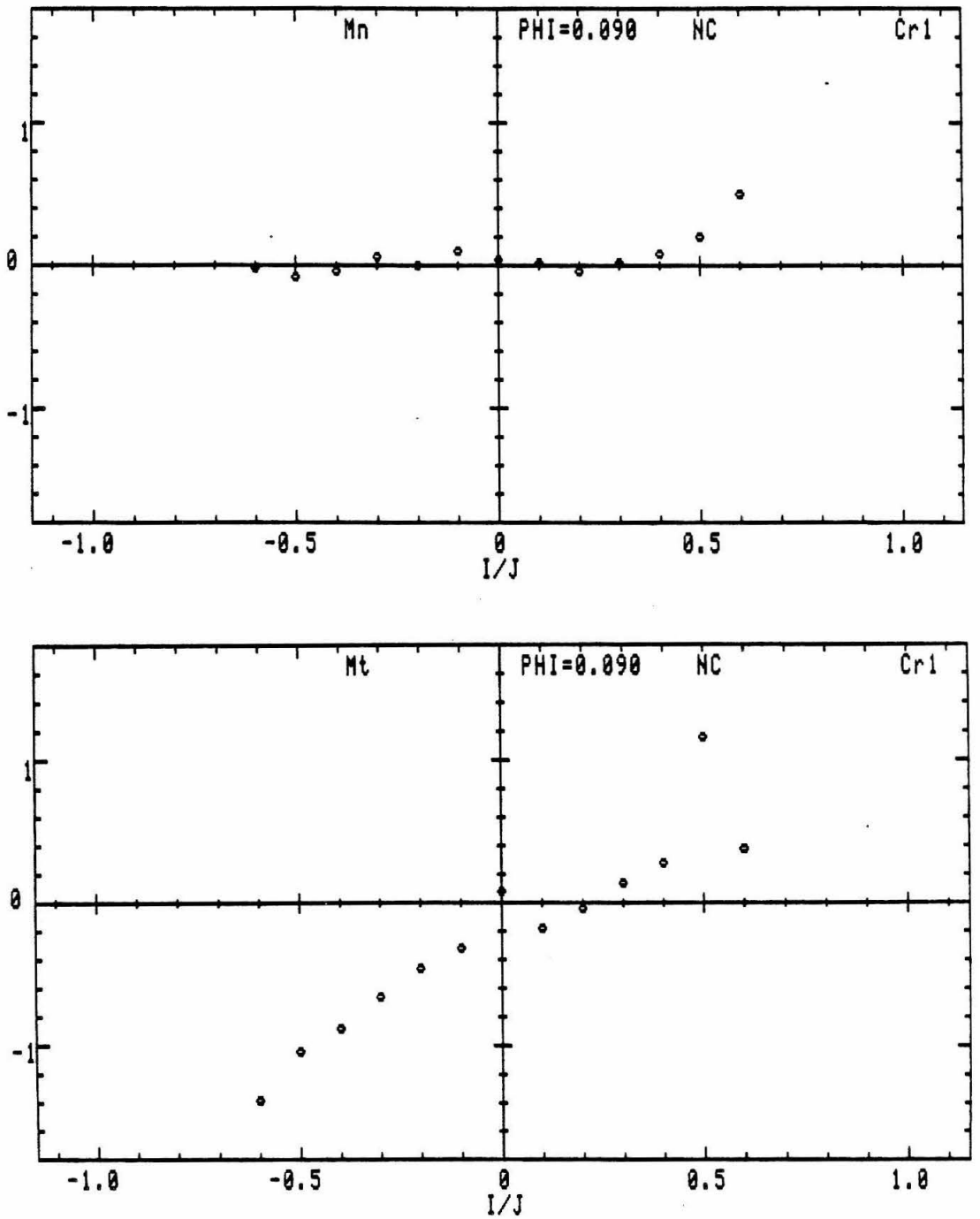

Figure A.40: Unsteady moments ($\phi = 0.090$, noncavitating flow, Cr_1).

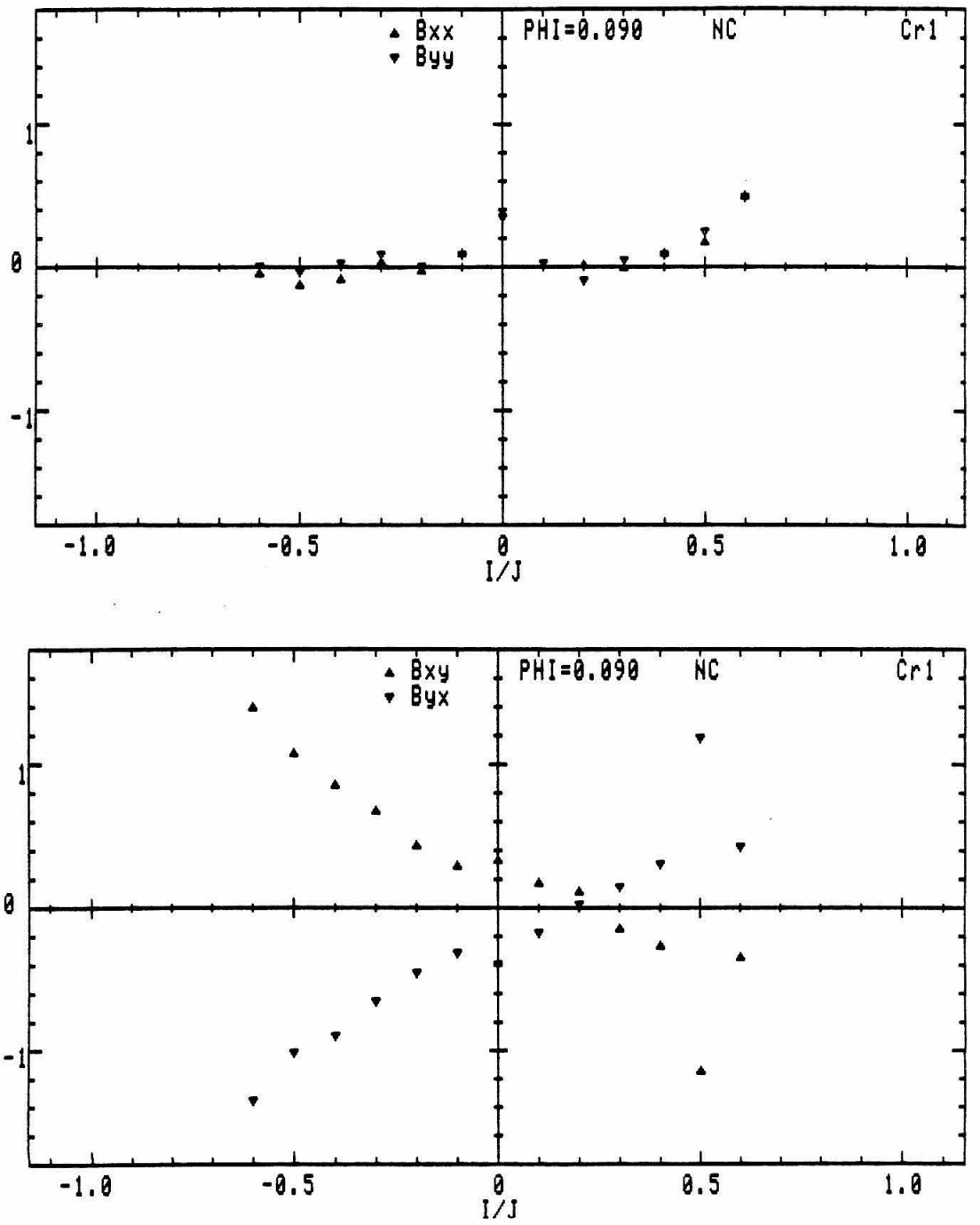

Figure A.41: Rotordynamic moment coefficients ($\phi = 0.090$, noncavitating flow, Cr_1).

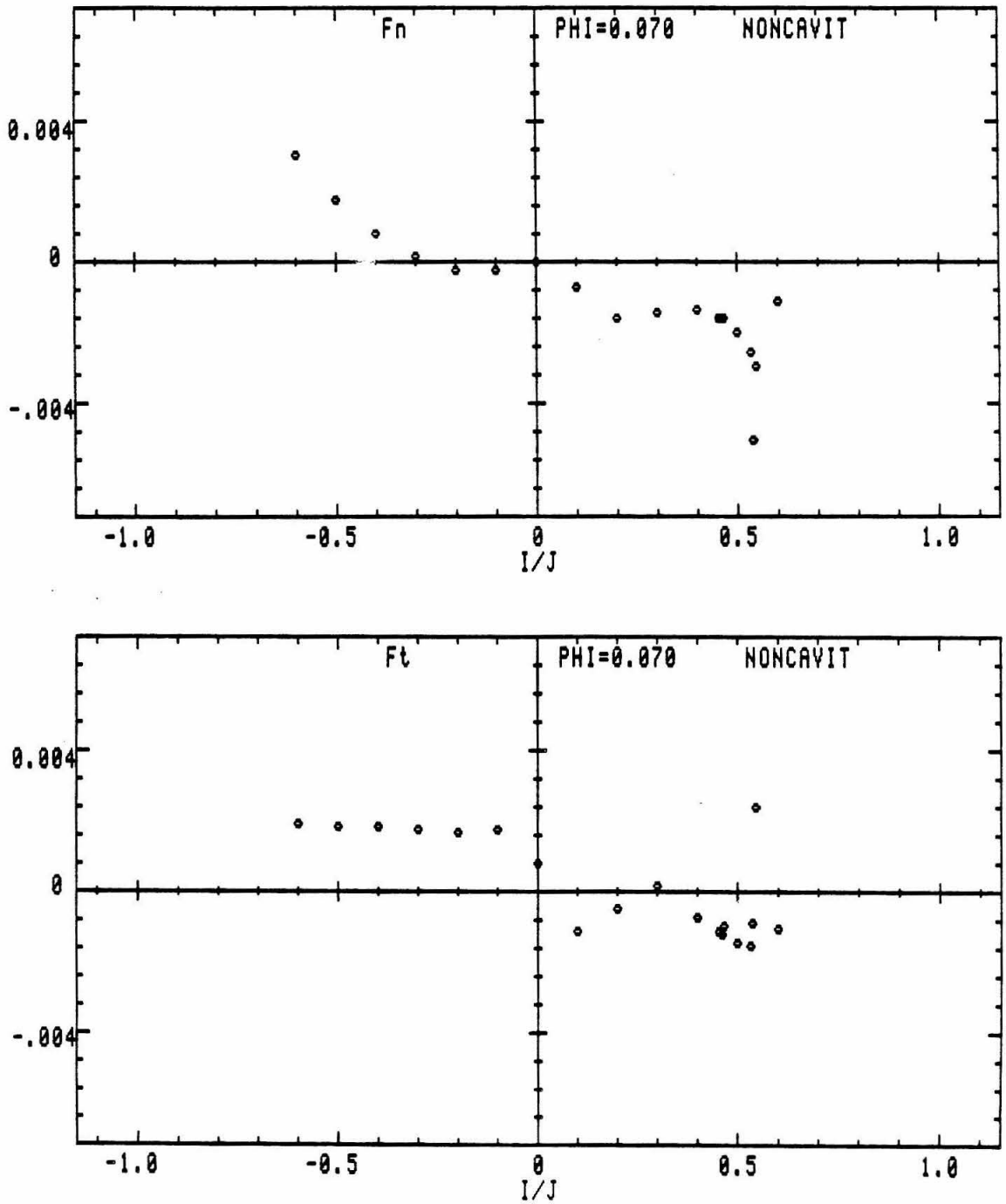

Figure A.42: Unsteady hydrodynamic forces ($\phi = 0.070$, noncavitating flow, Cr_2).

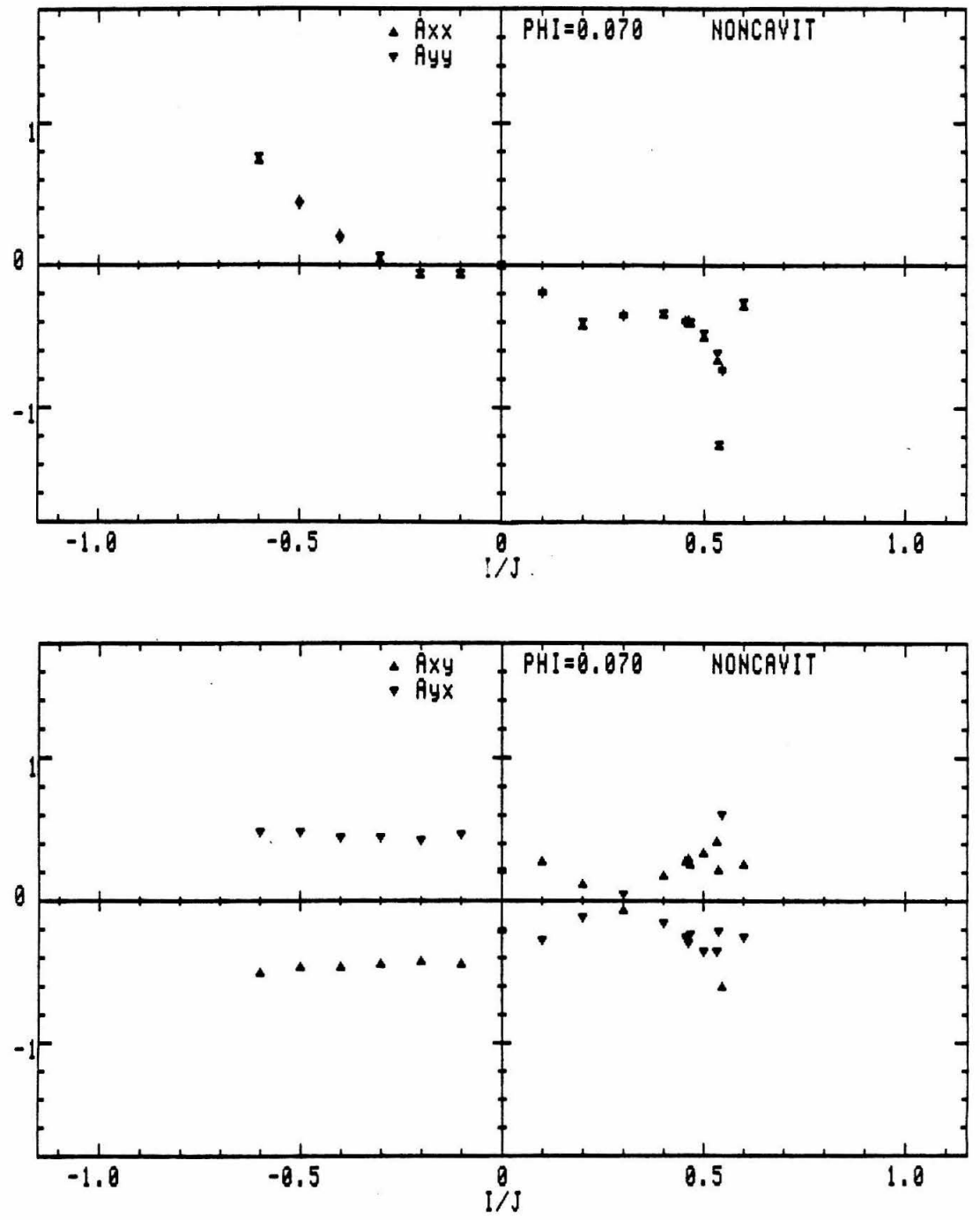

Figure A.43: Rotordynamic force coefficients ($\phi = 0.070$, noncavitating flow, Cr_2).

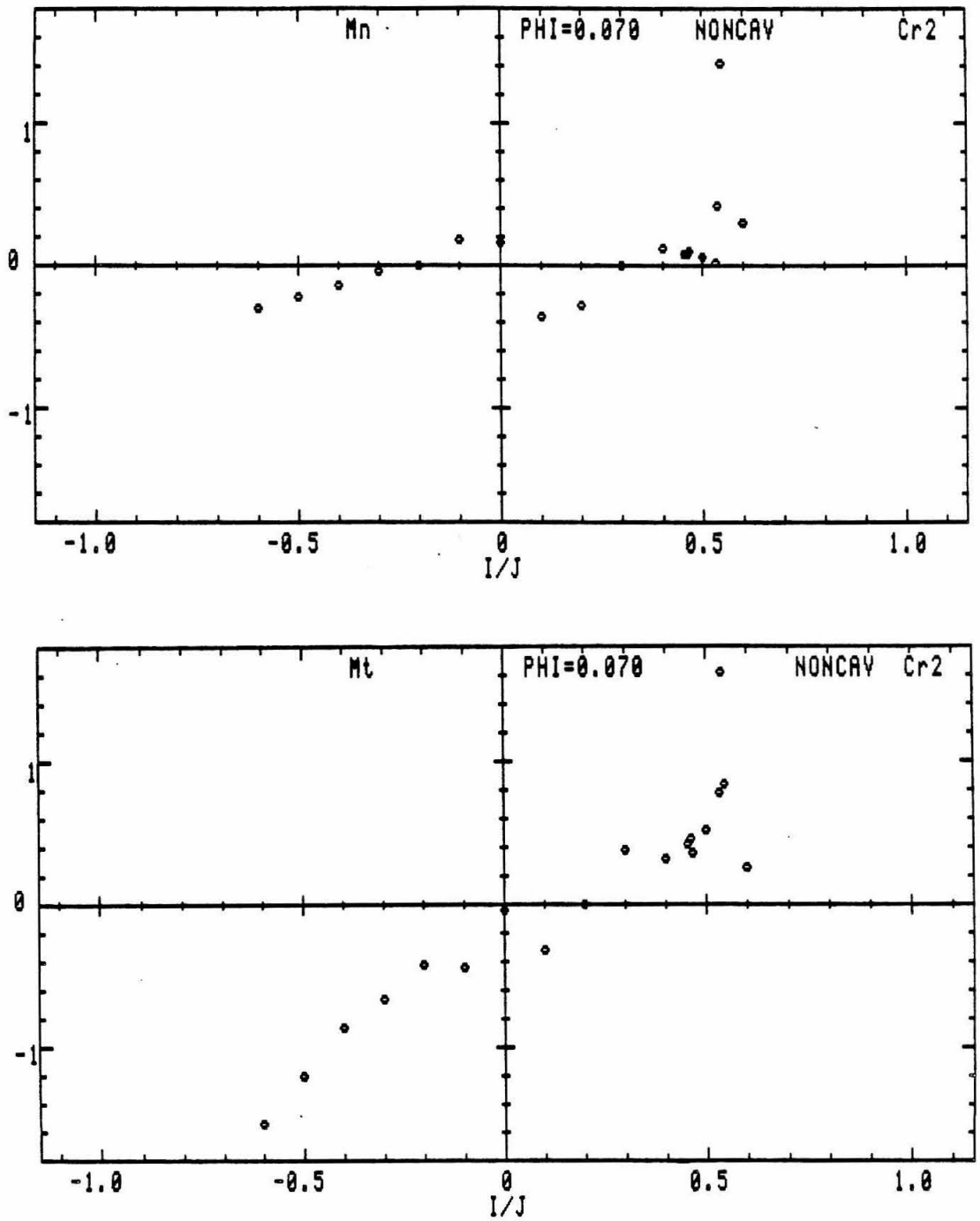

Figure A.44: Unsteady moments ($\phi = 0.070$, noncavitating flow, Cr_2).

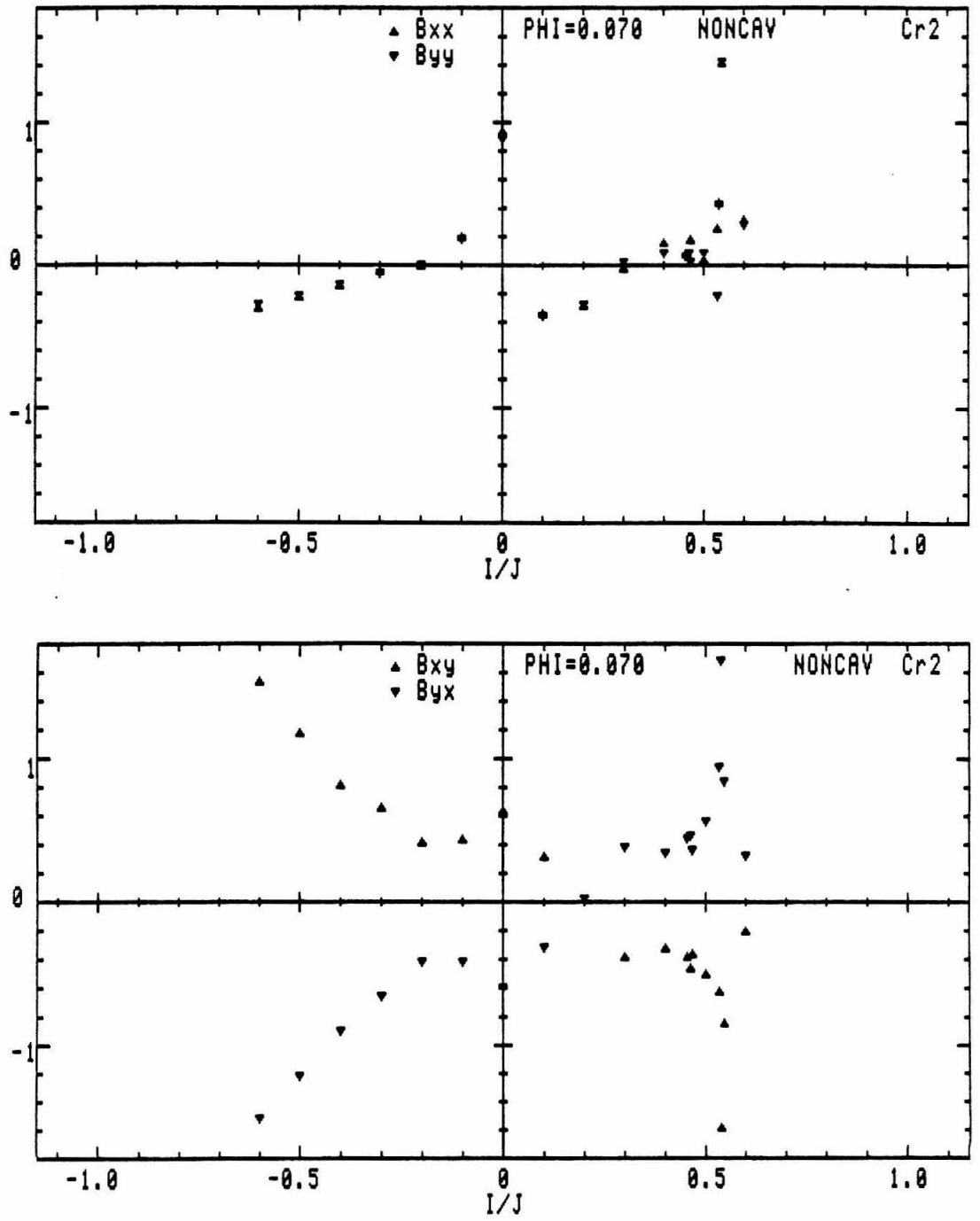

Figure A.45: Rotordynamic moment coefficients ($\phi = 0.070$, noncavitating flow, Cr_2).

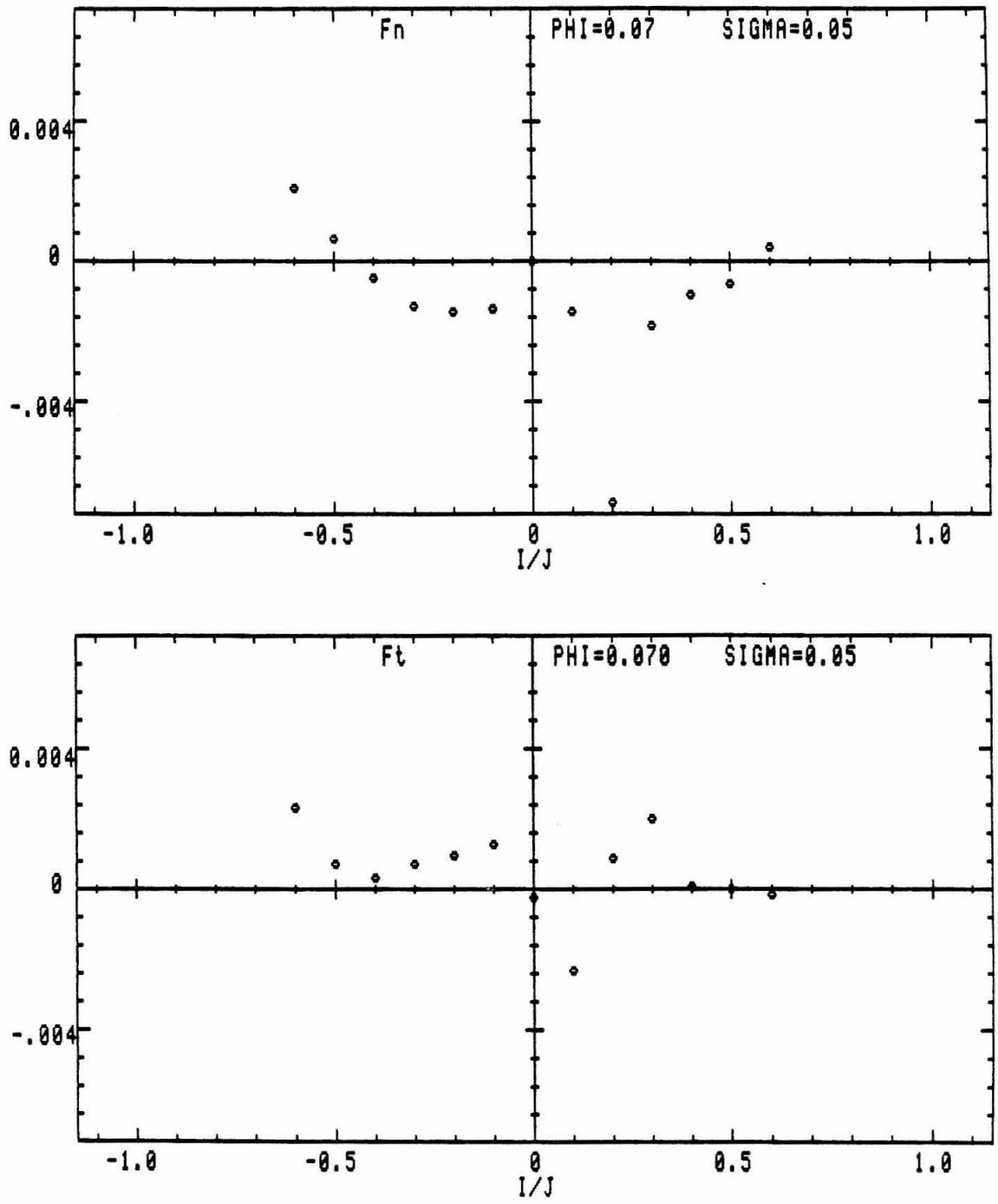

Figure A.46: Unsteady hydrodynamic forces ($\phi = 0.070$, $\sigma = 0.050$, Cr_2).

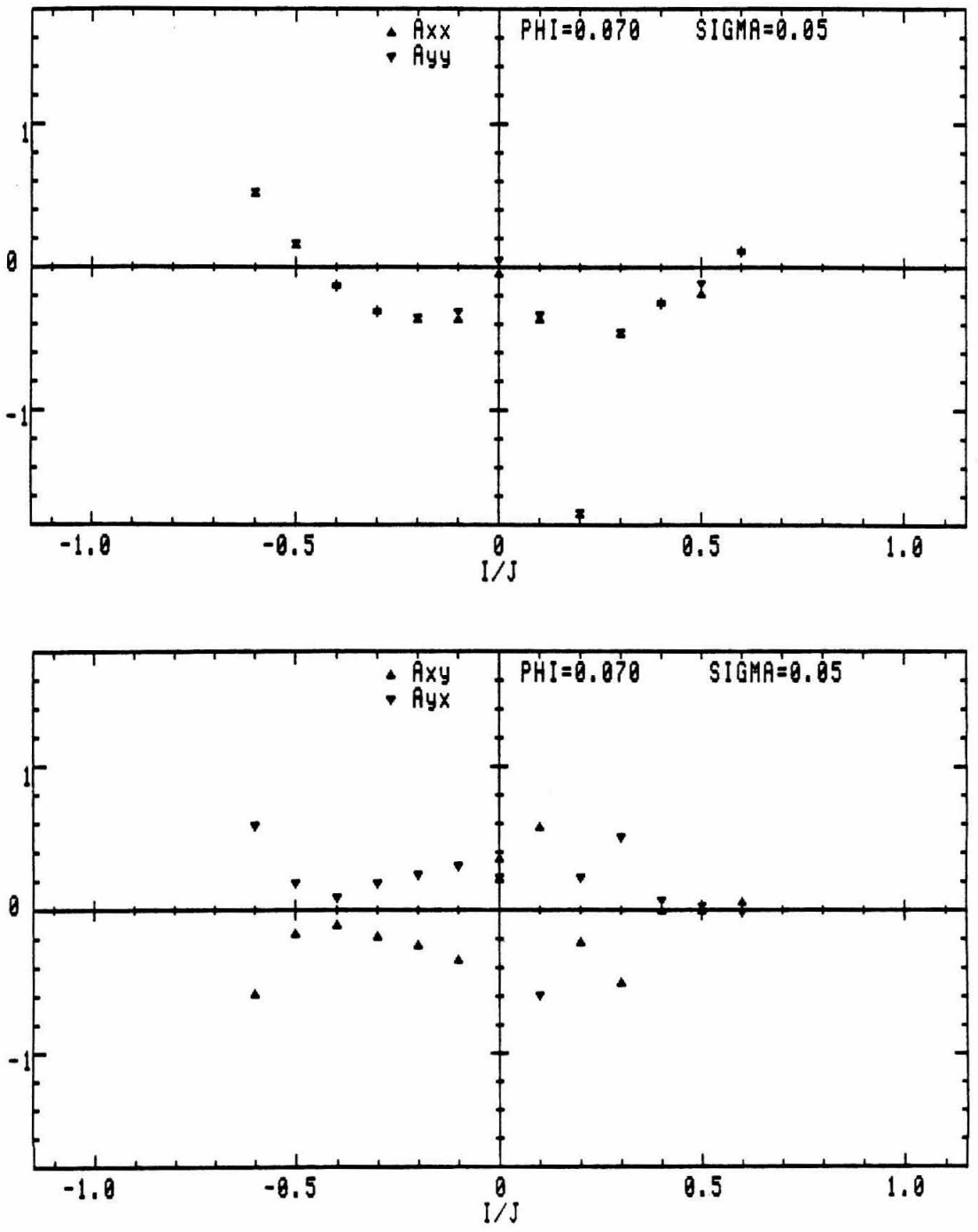

Figure A.47: Rotordynamic force coefficients ($\phi = 0.070$, $\sigma = 0.050$, Cr_2).

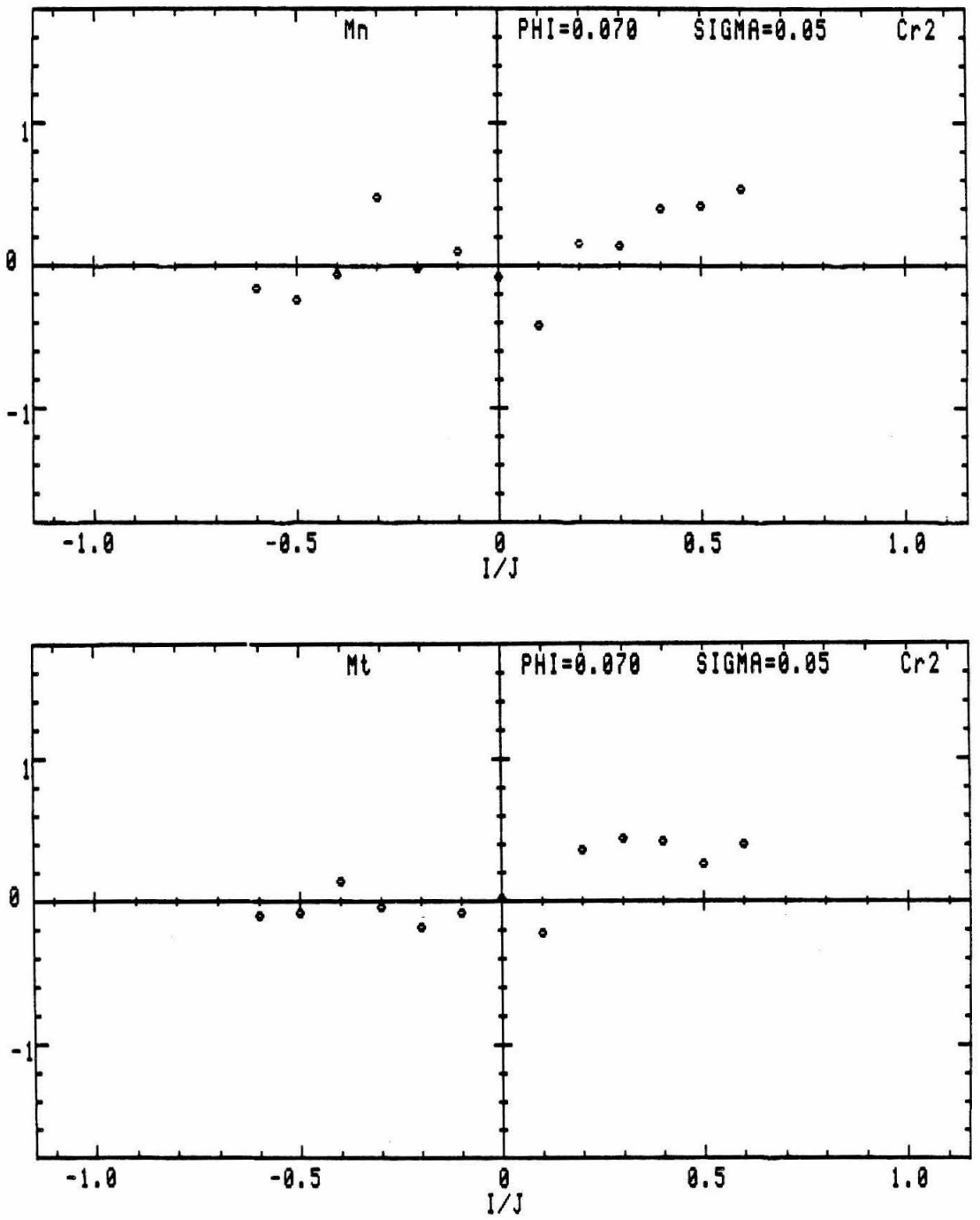

Figure A.48: Unsteady moments ($\phi = 0.070$, $\sigma = 0.050$, Cr_2).

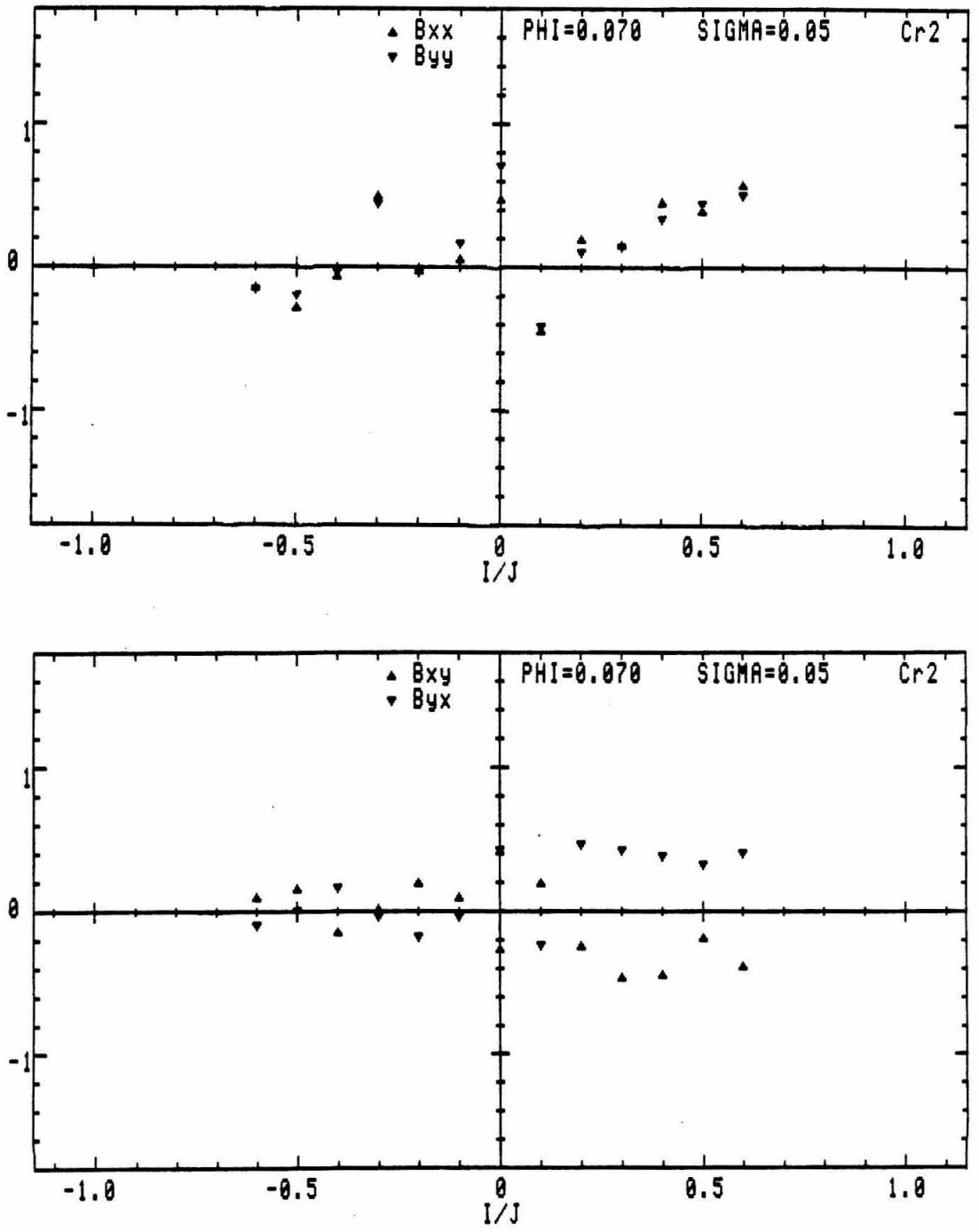

Figure A.49: Rotordynamic moment coefficients ($\phi = 0.070$, $\sigma = 0.050$, Cr_2).

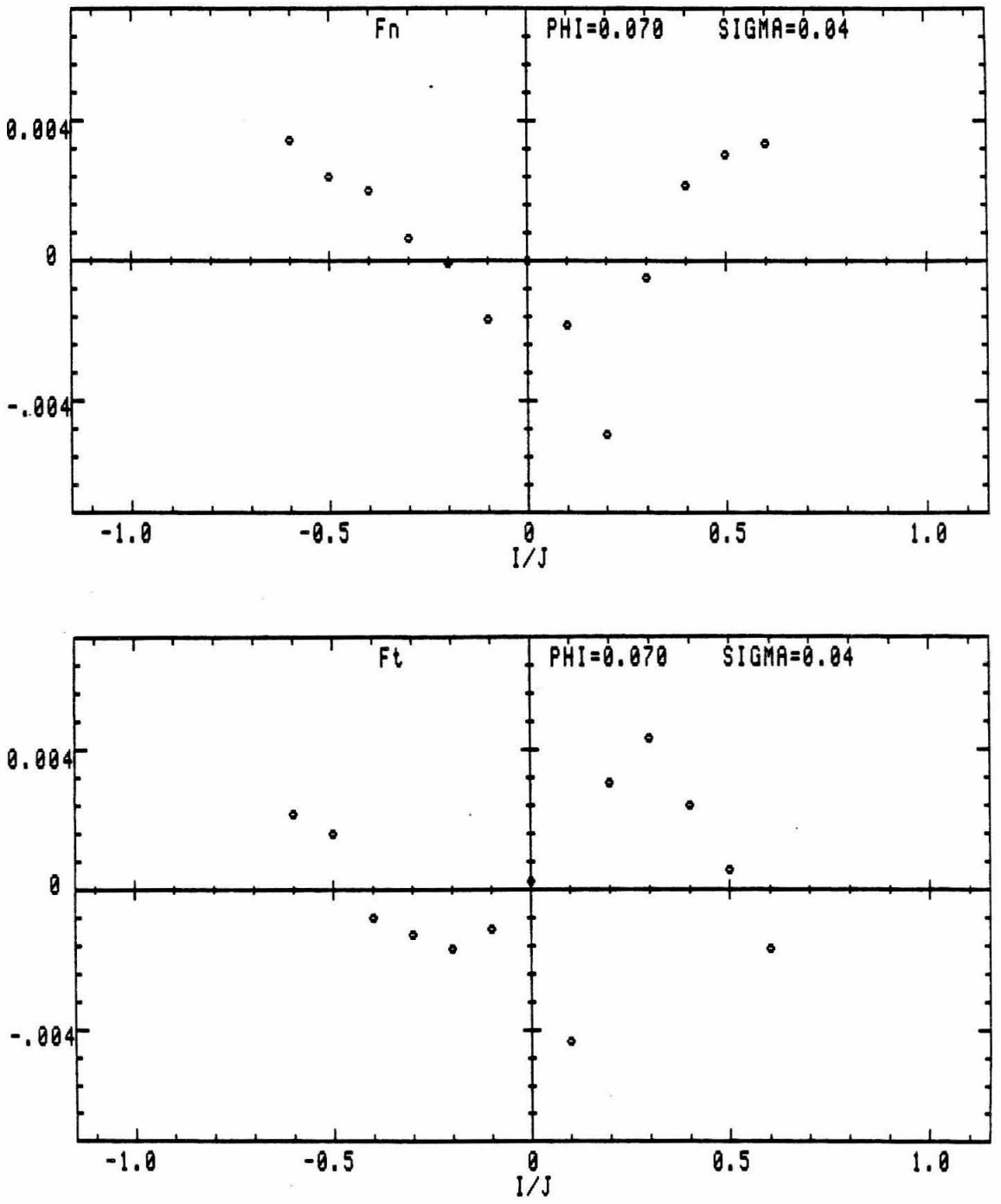

Figure A.50: Unsteady hydrodynamic forces ($\phi = 0.070$, $\sigma = 0.040$, Cr_2).

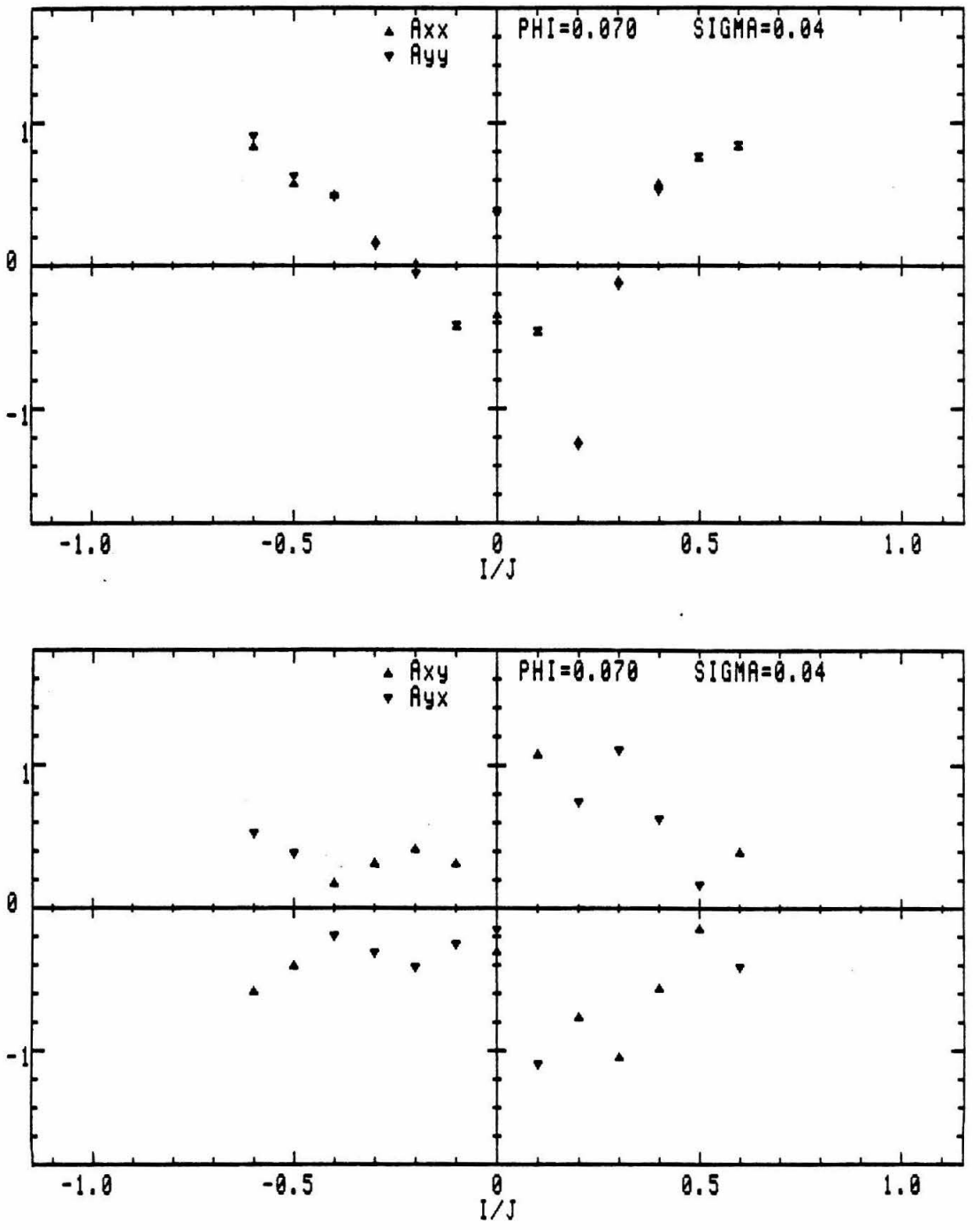

Figure A.51: Rotordynamic force coefficients ($\phi = 0.070$, $\sigma = 0.040$, Cr_2).

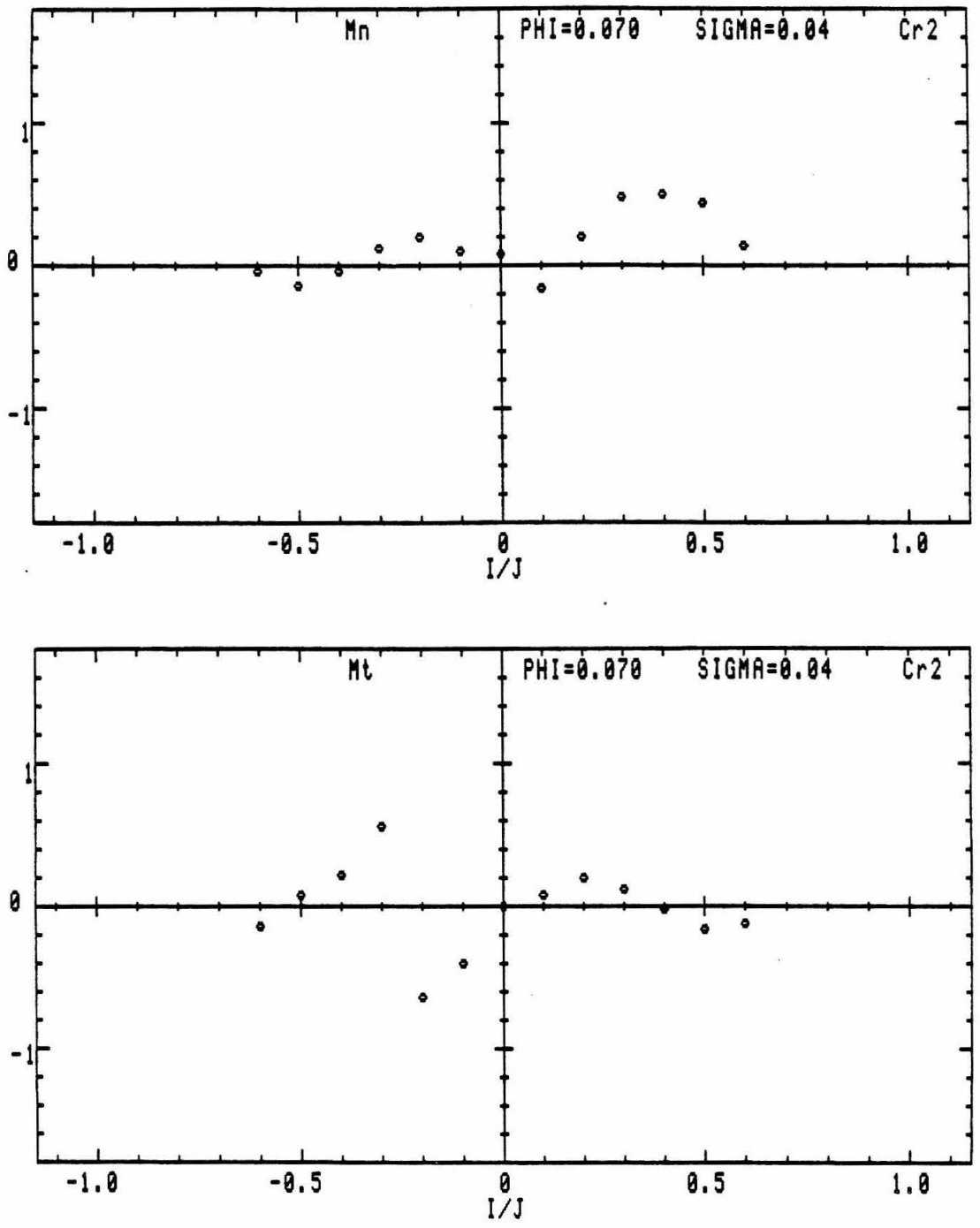

Figure A.52: Unsteady moments ($\phi = 0.070$, $\sigma = 0.040$, Cr_2).

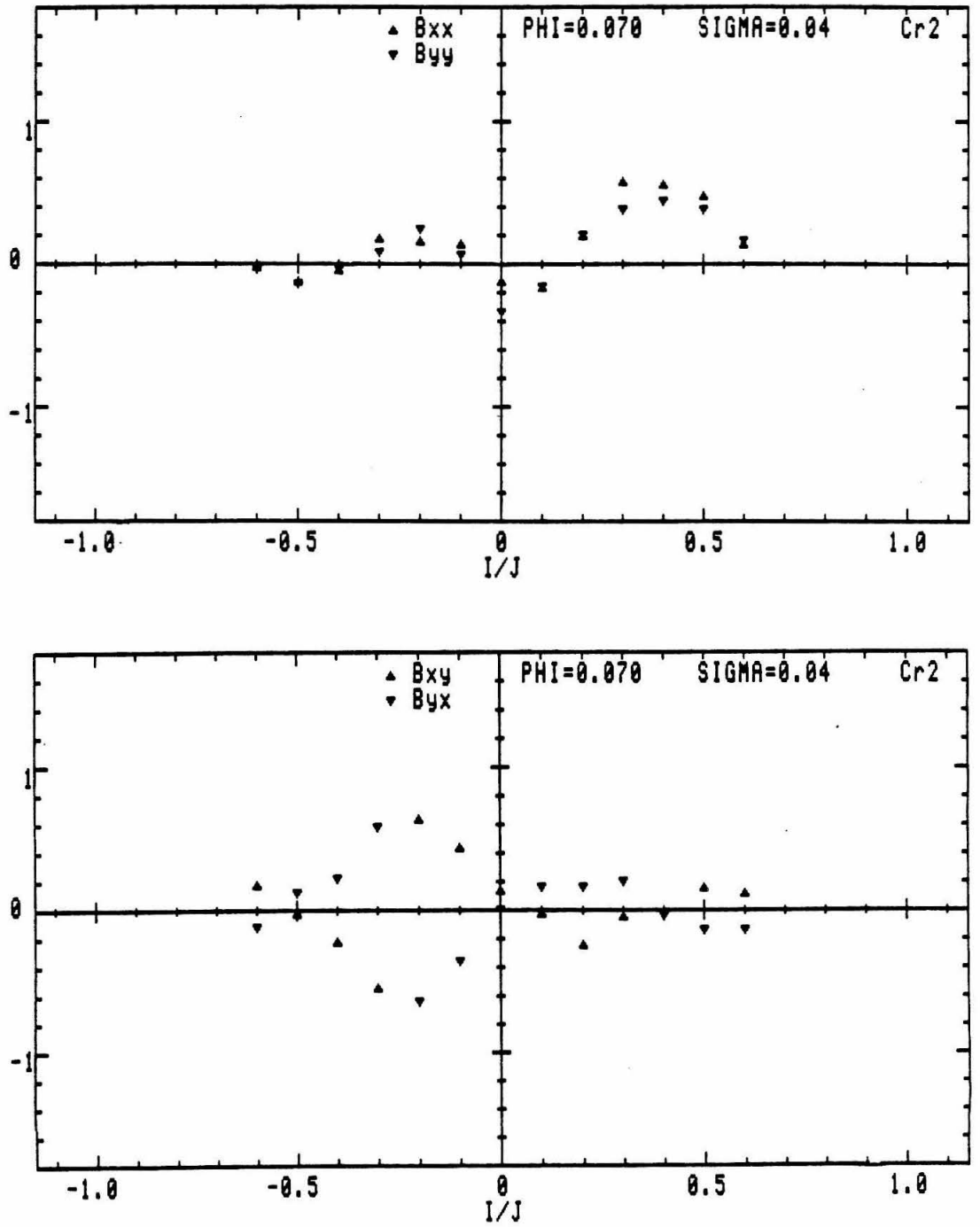

Figure A.53: Rotordynamic moment coefficients ($\phi = 0.070$, $\sigma = 0.040$, Cr_2).

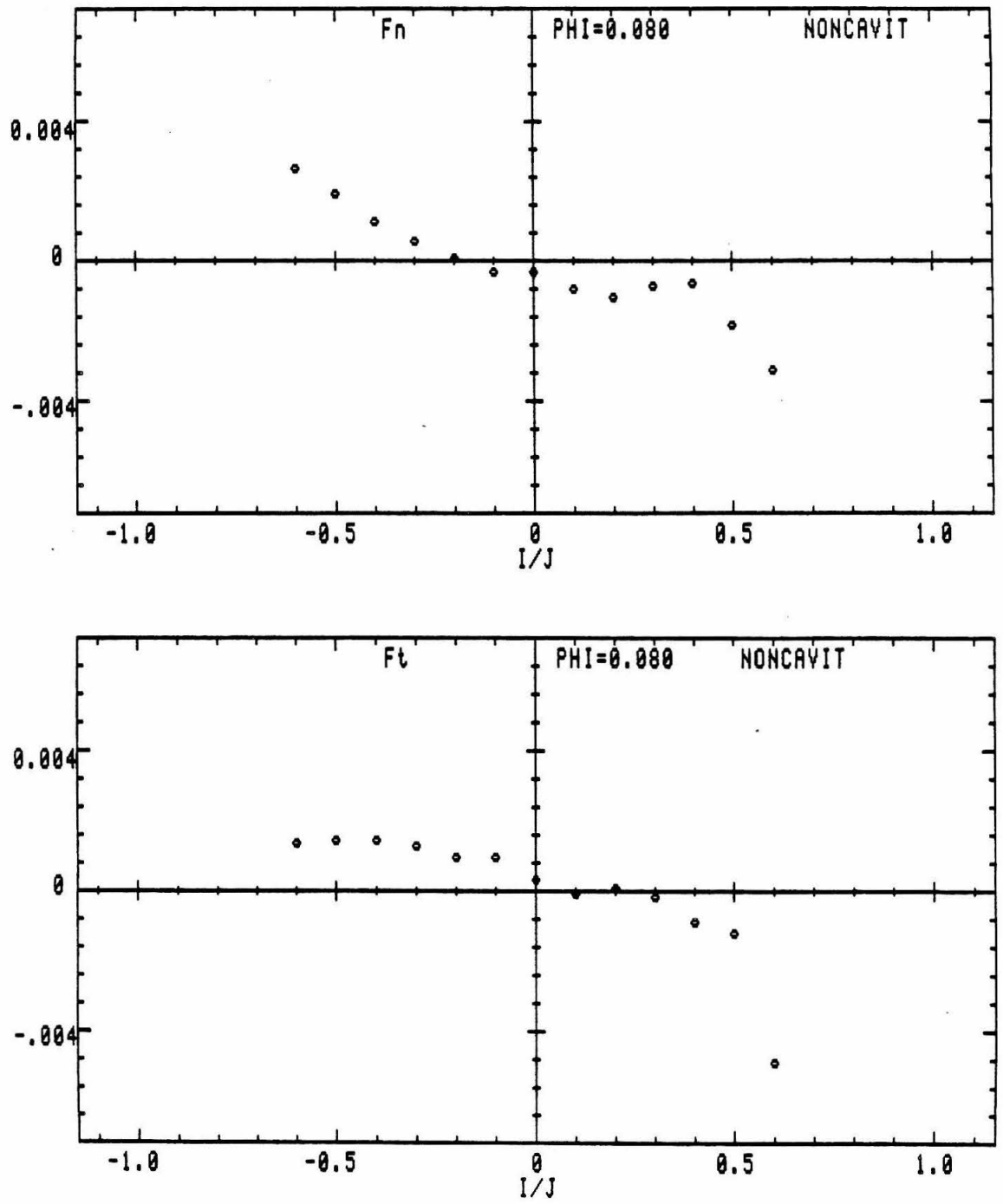

Figure A.54: Unsteady hydrodynamic forces ($\phi = 0.080$, noncavitating flow, Cr_2).

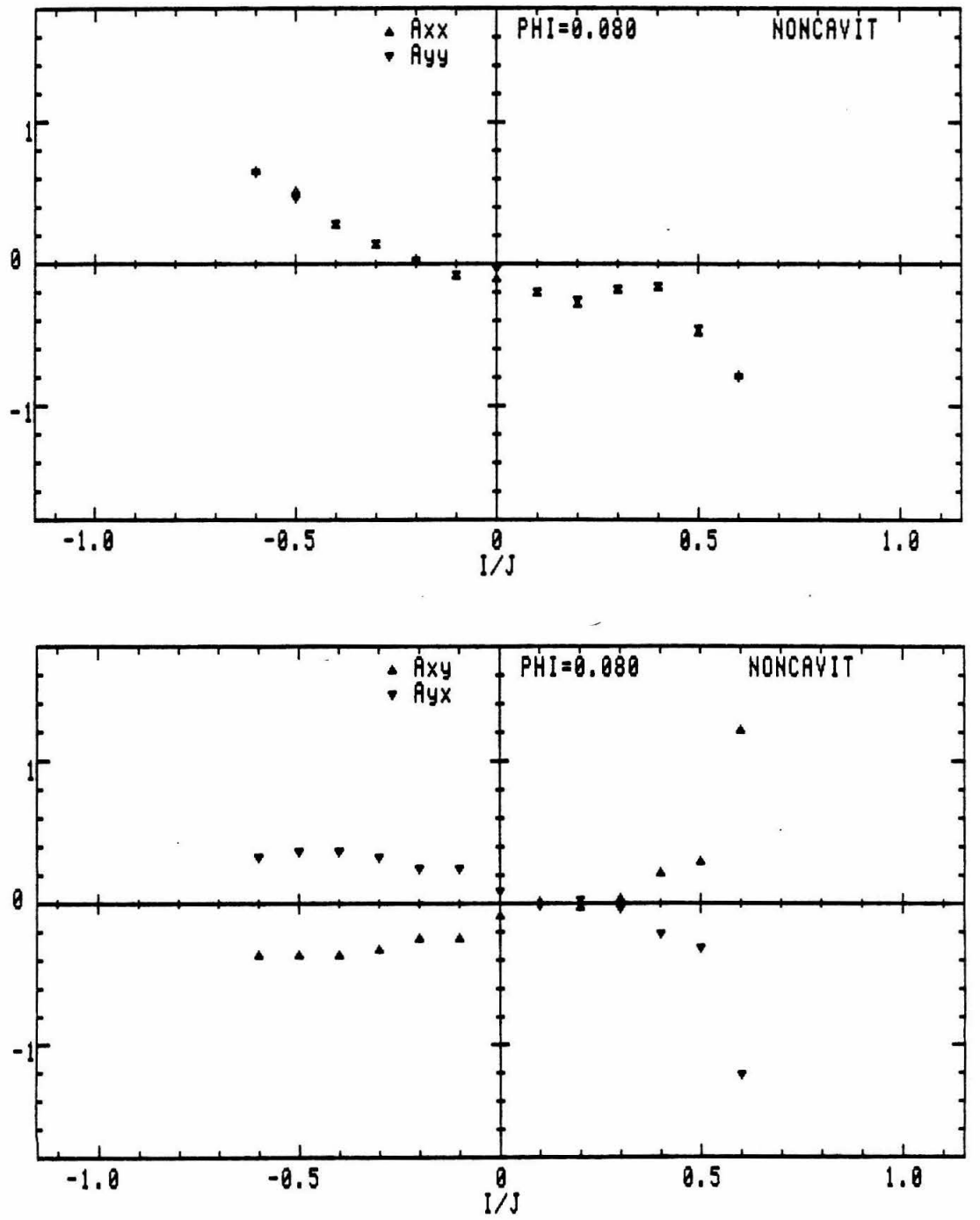

Figure A.55: Rotordynamic force coefficients ($\phi = 0.080$, noncavitating flow, Cr_2).

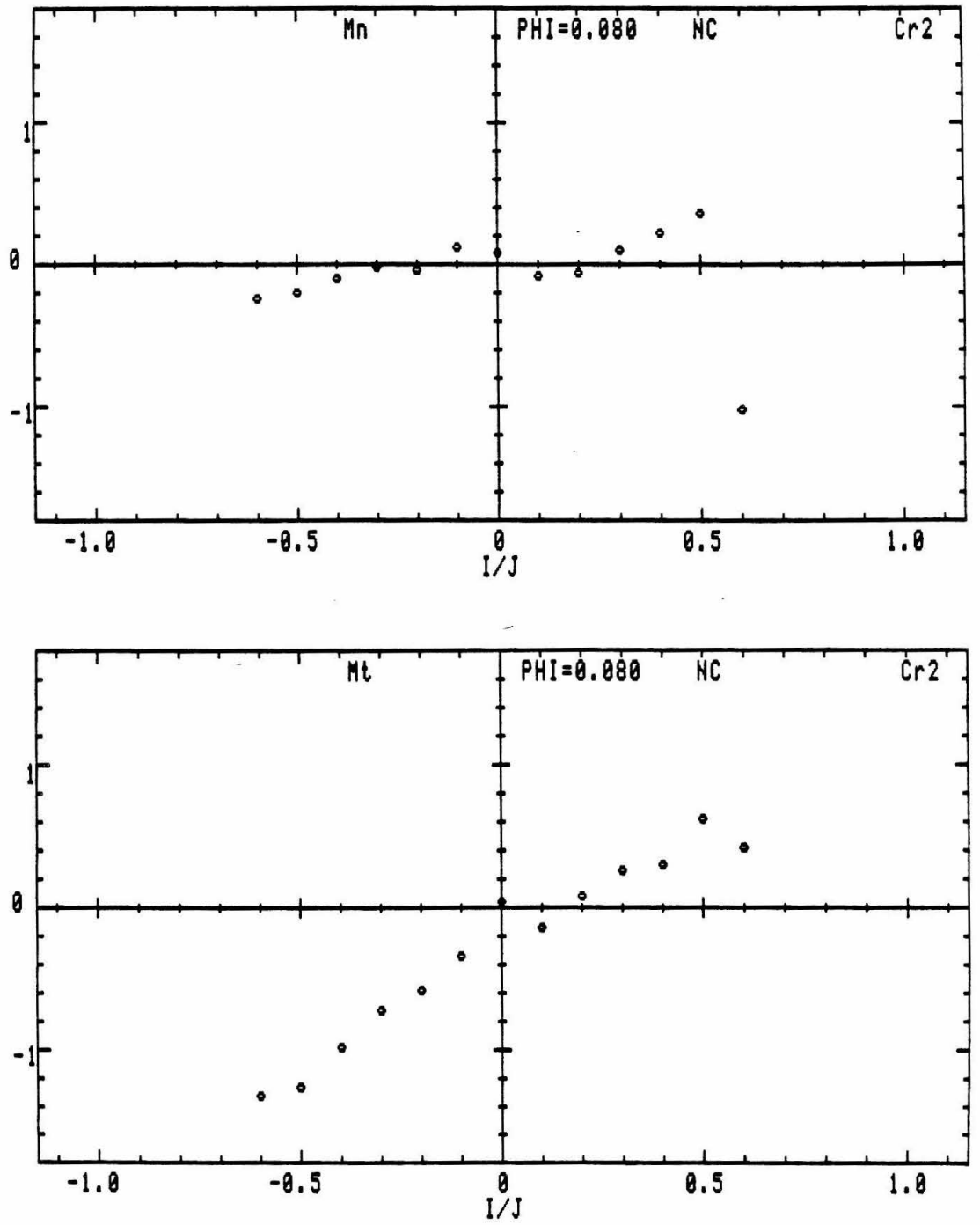

Figure A.56: Unsteady moments ($\phi = 0.080$, noncavitating flow, Cr_2).

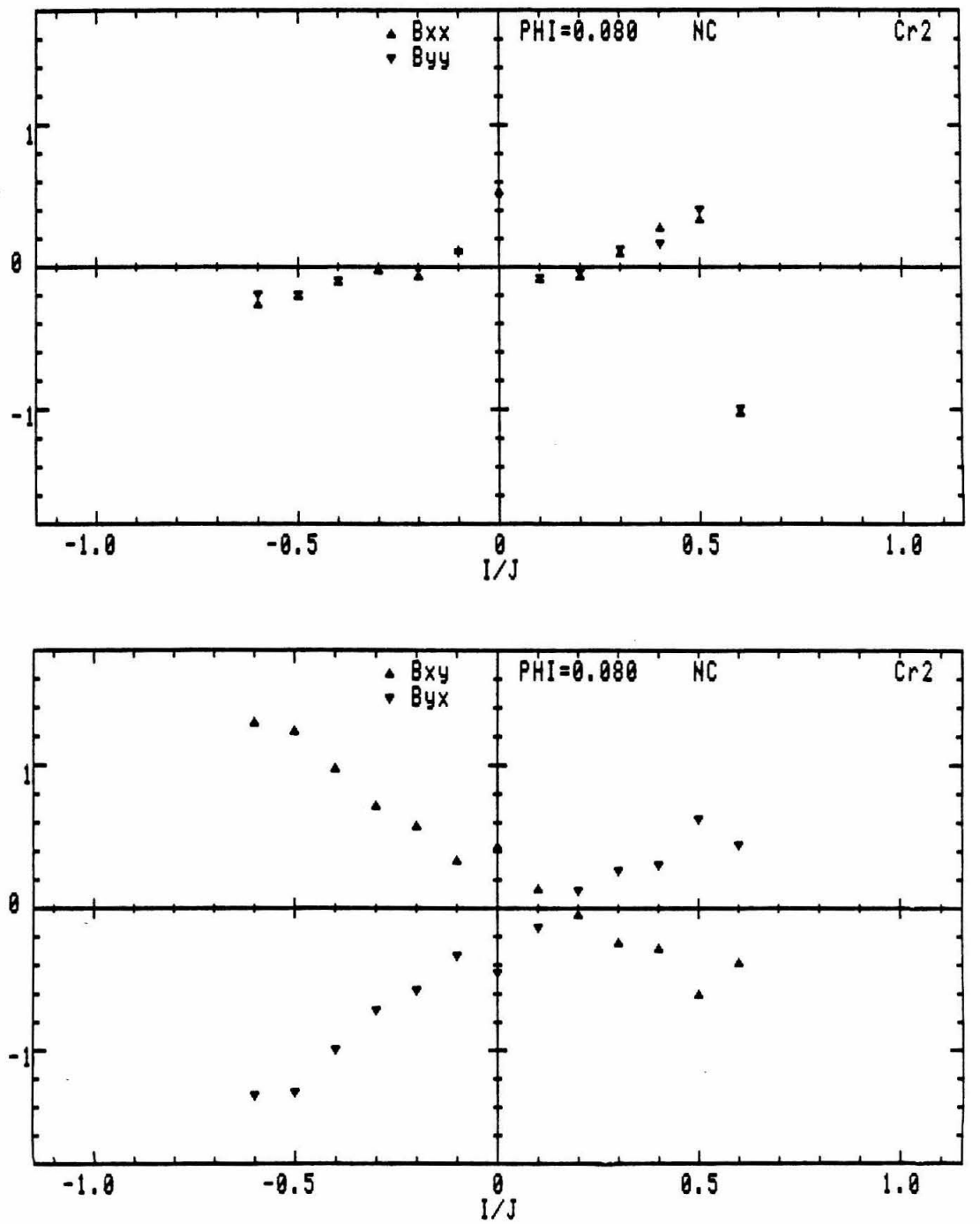

Figure A.57: Rotordynamic moment coefficients ($\phi = 0.080$, noncavitating flow, Cr_2).

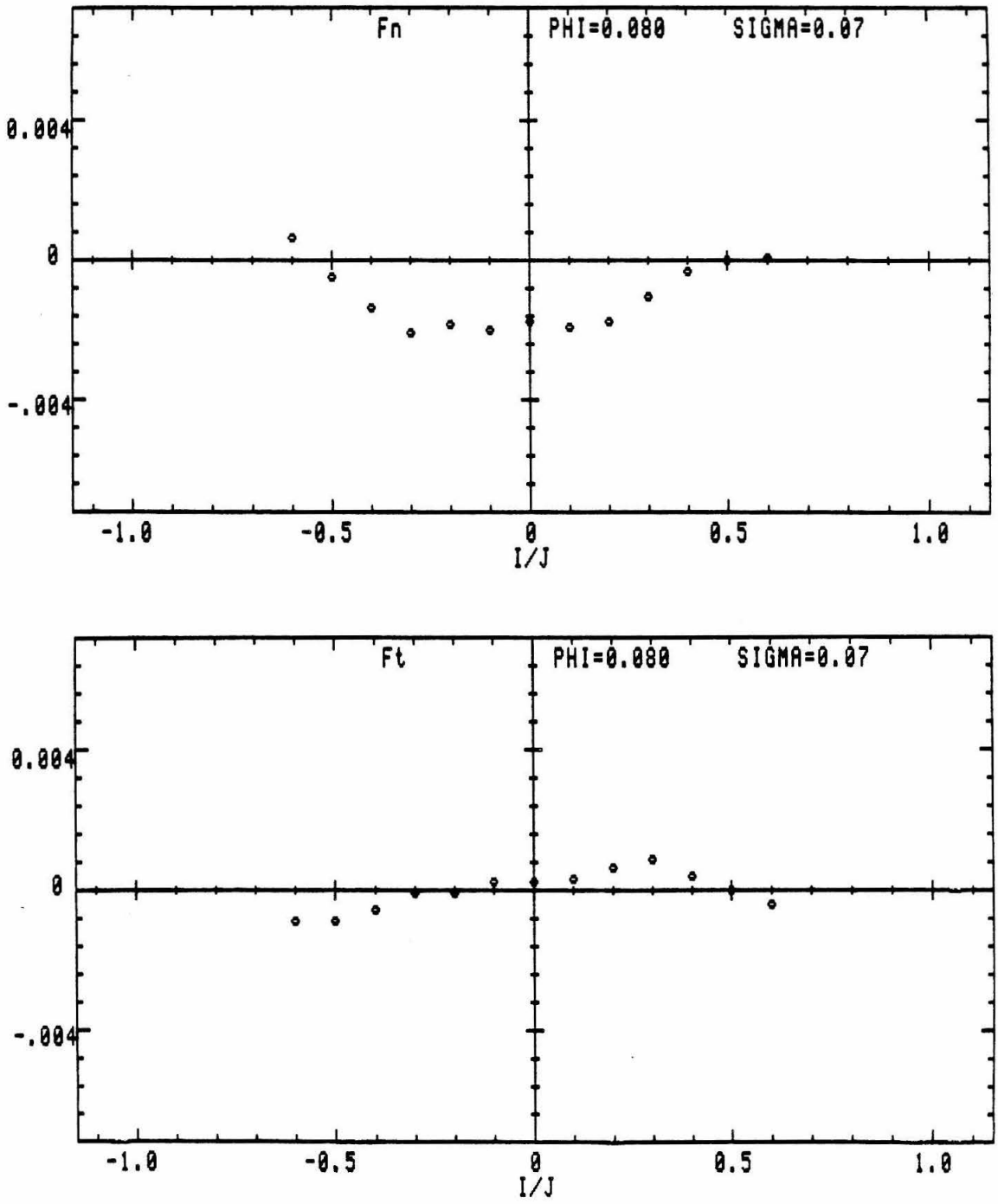

Figure A.58: Unsteady hydrodynamic forces ($\phi = 0.080$, $\sigma = 0.070$, Cr_2).

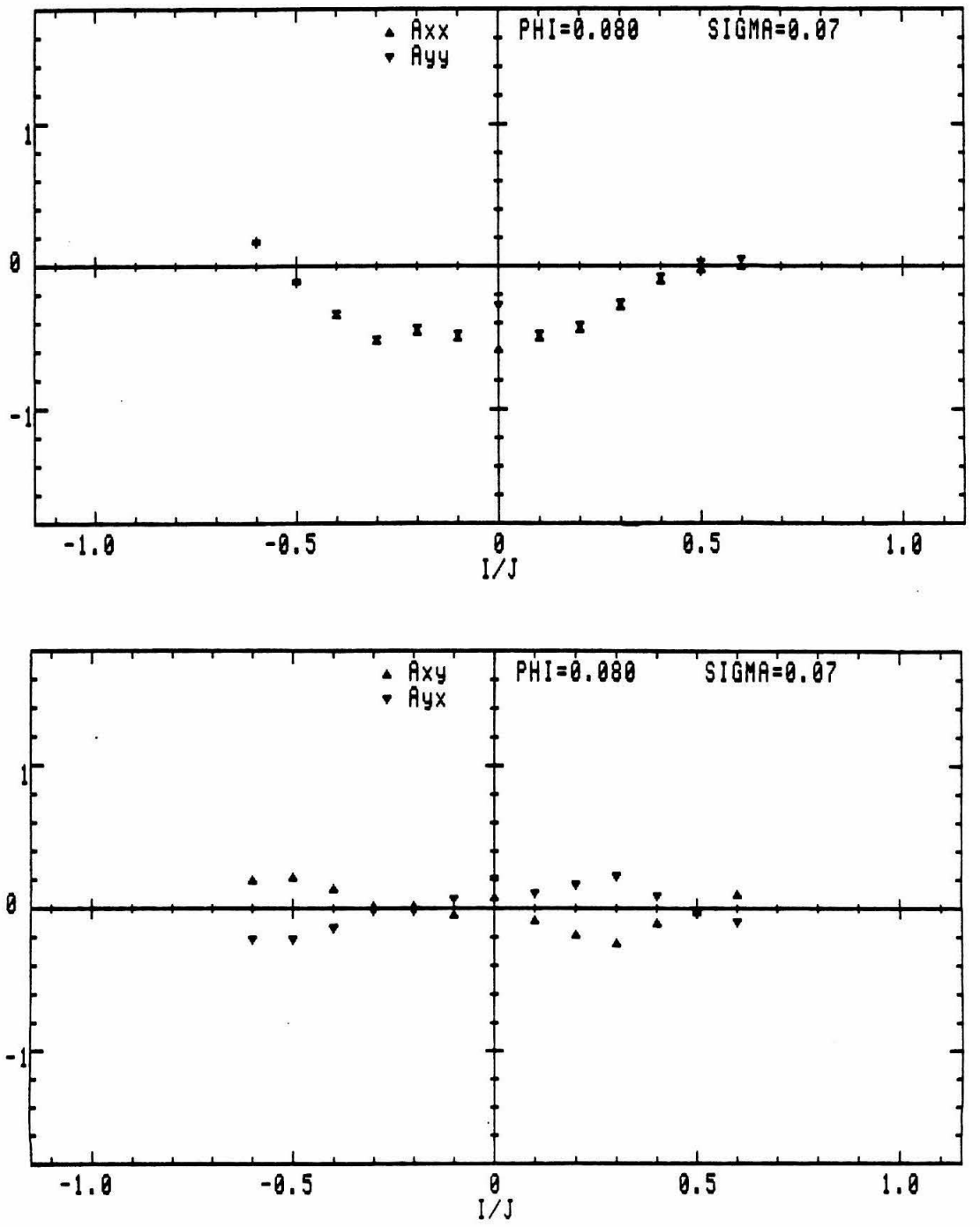

Figure A.59: Rotordynamic force coefficients ($\phi = 0.080$, $\sigma = 0.070$, Cr_2).

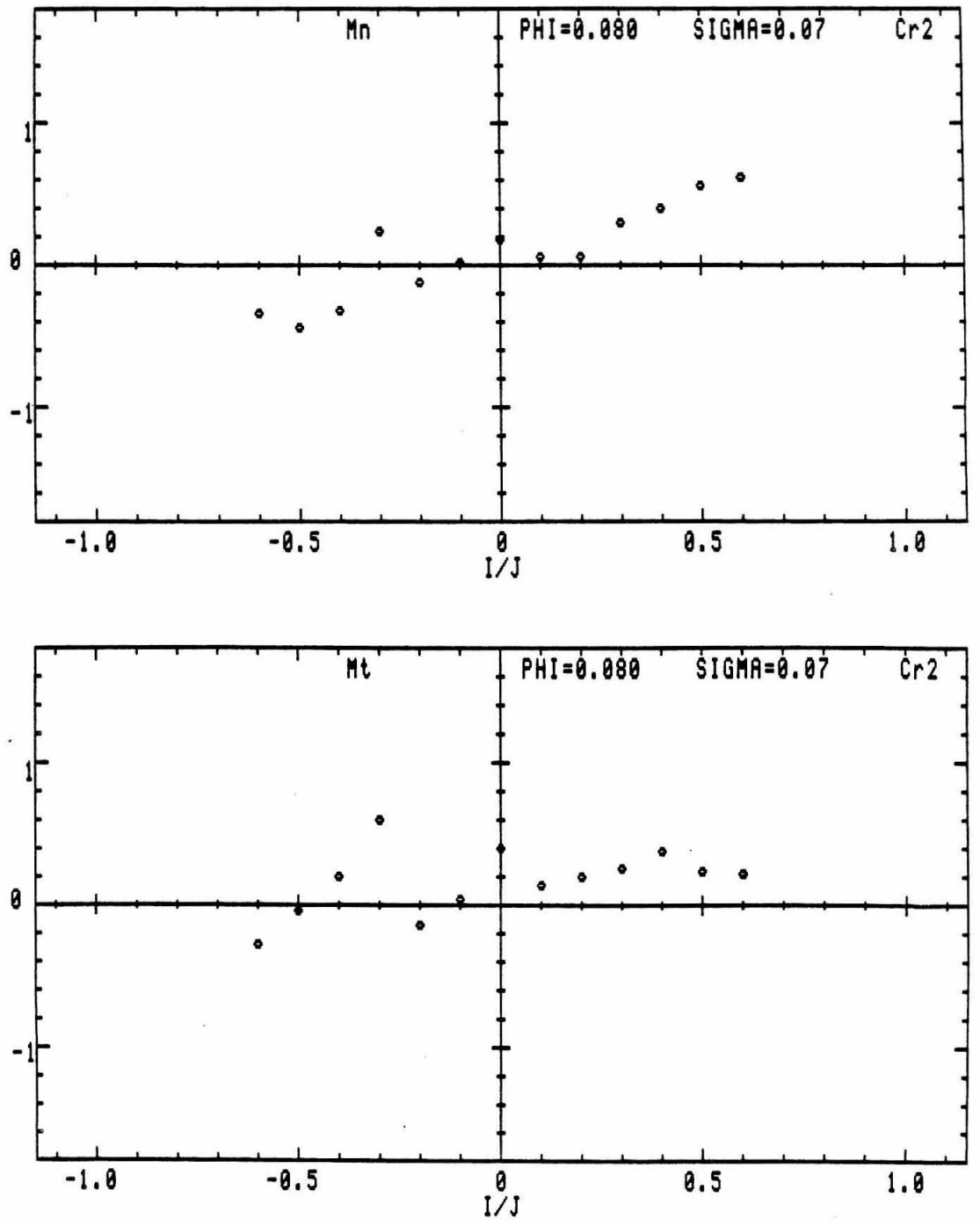

Figure A.60: Unsteady moments ($\phi = 0.080$, $\sigma = 0.070$, Cr_2).

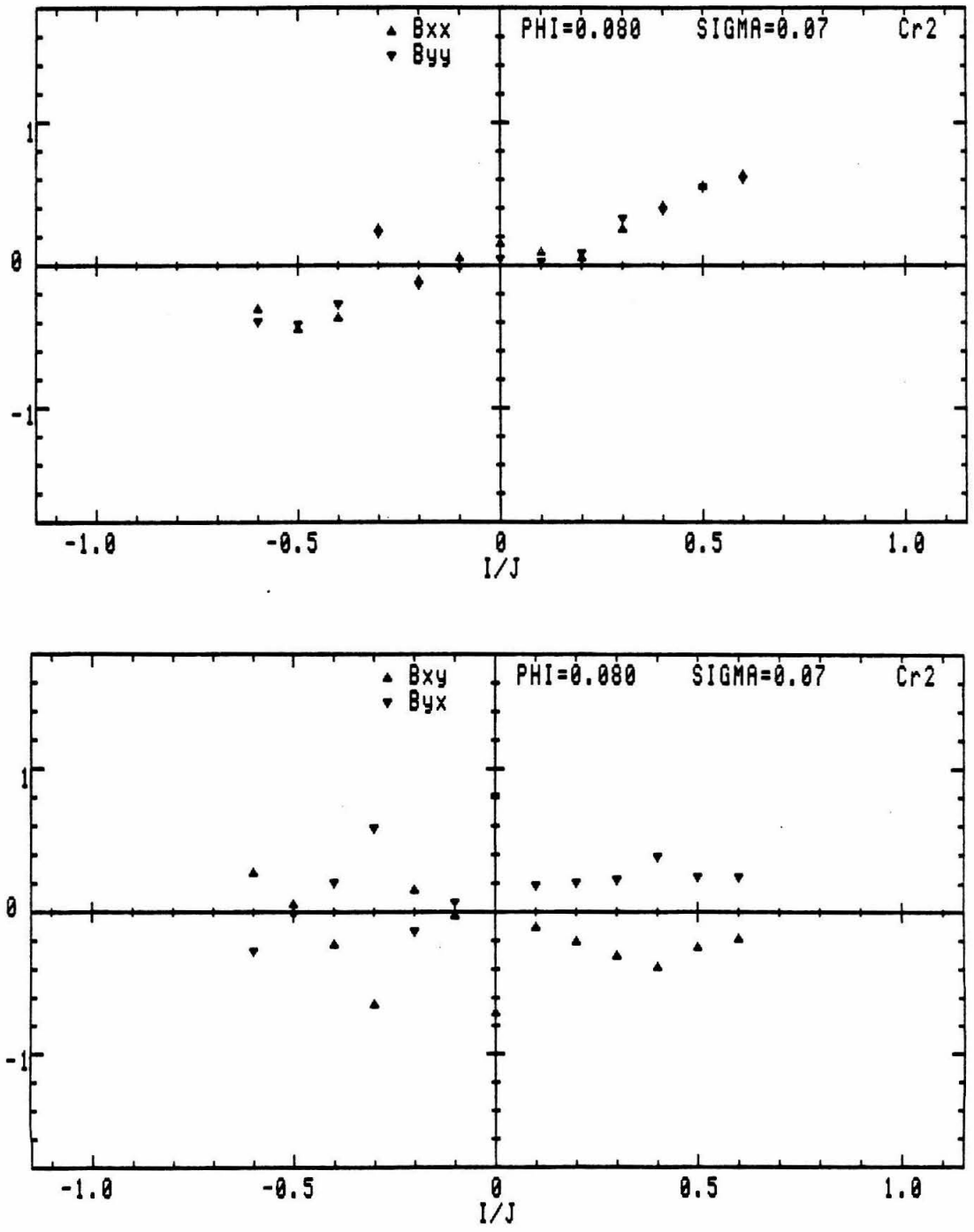

Figure A.61: Rotordynamic moment coefficients ($\phi = 0.080$, $\sigma = 0.070$, Cr_2).

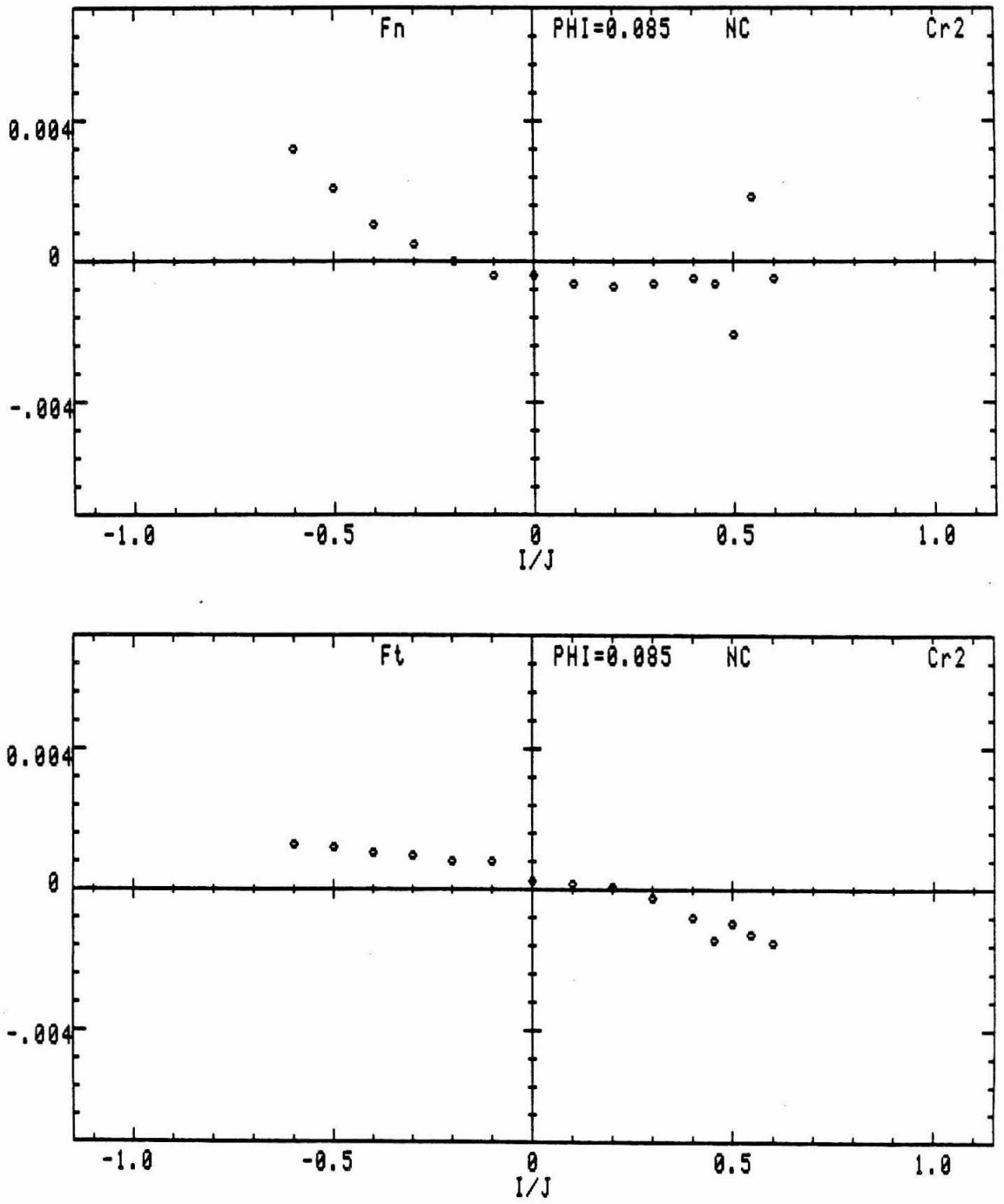

Figure A.62: Unsteady hydrodynamic forces ($\phi = 0.085$, noncavitating flow, Cr_2).

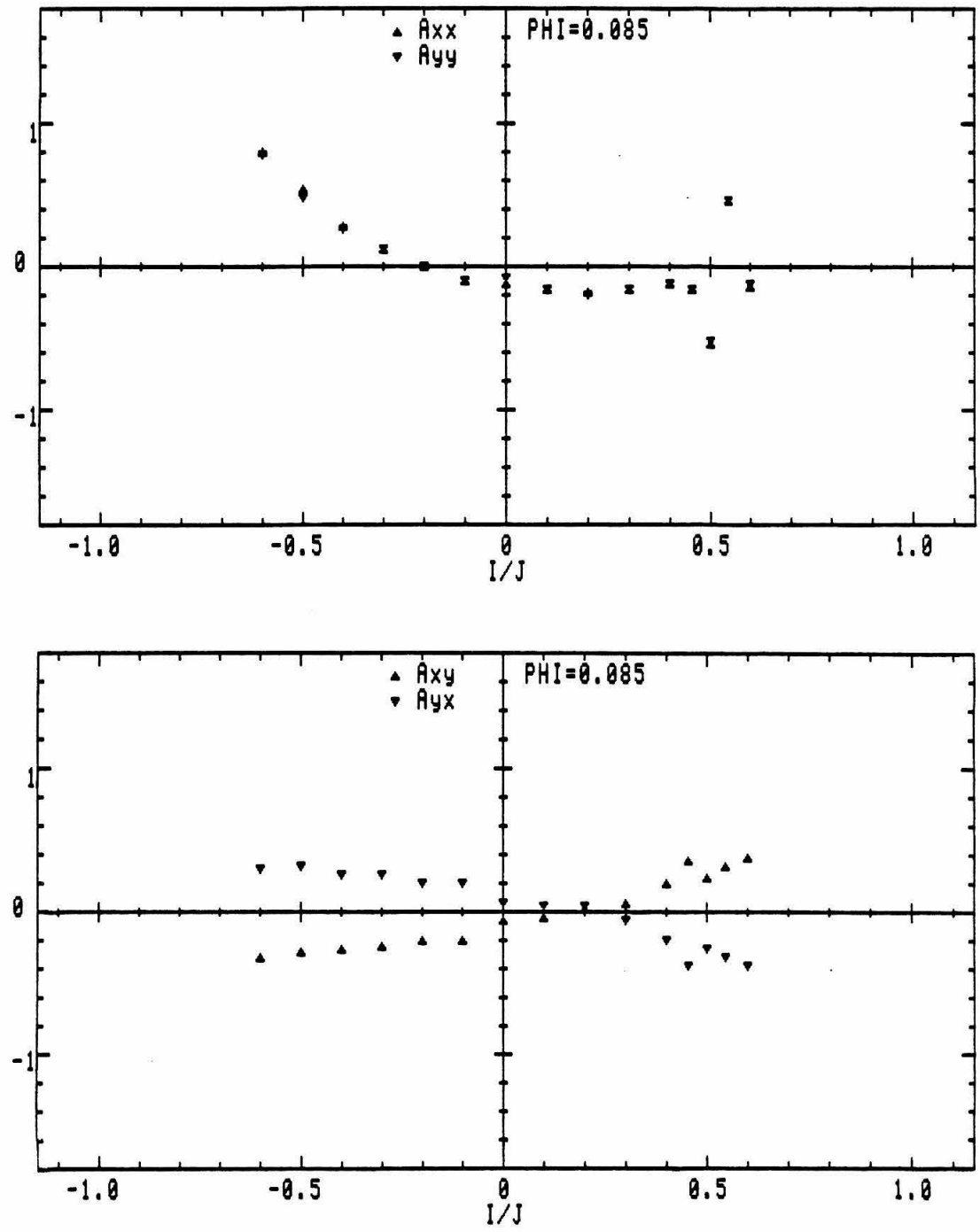

Figure A.63: Rotordynamic force coefficients ($\phi = 0.085$, noncavitating flow, Cr_2).

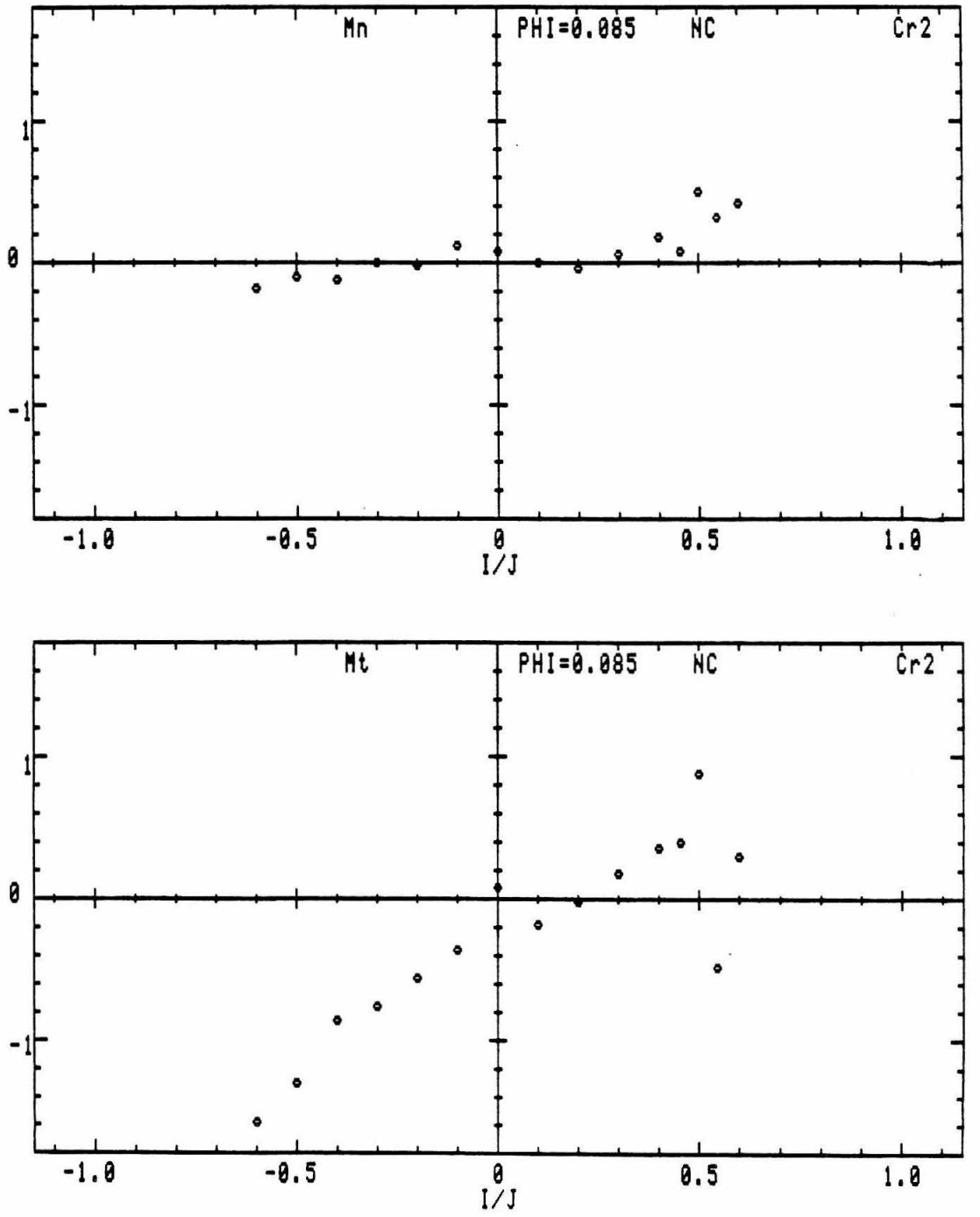

Figure A.64: Unsteady moments ($\phi = 0.085$, noncavitating flow, Cr_2).

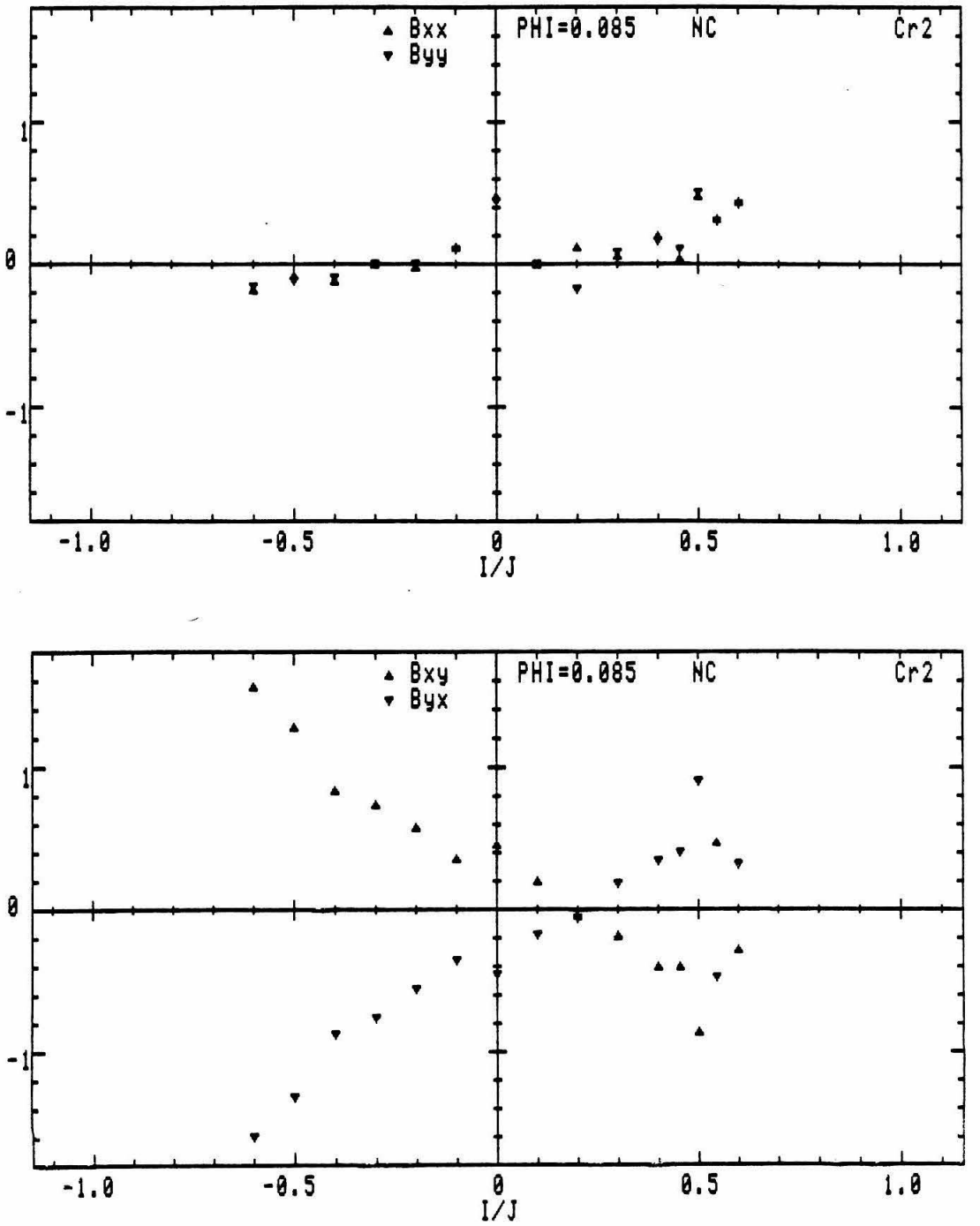

Figure A.65: Rotordynamic moment coefficients ($\phi = 0.085$, noncavitating flow, Cr_2).

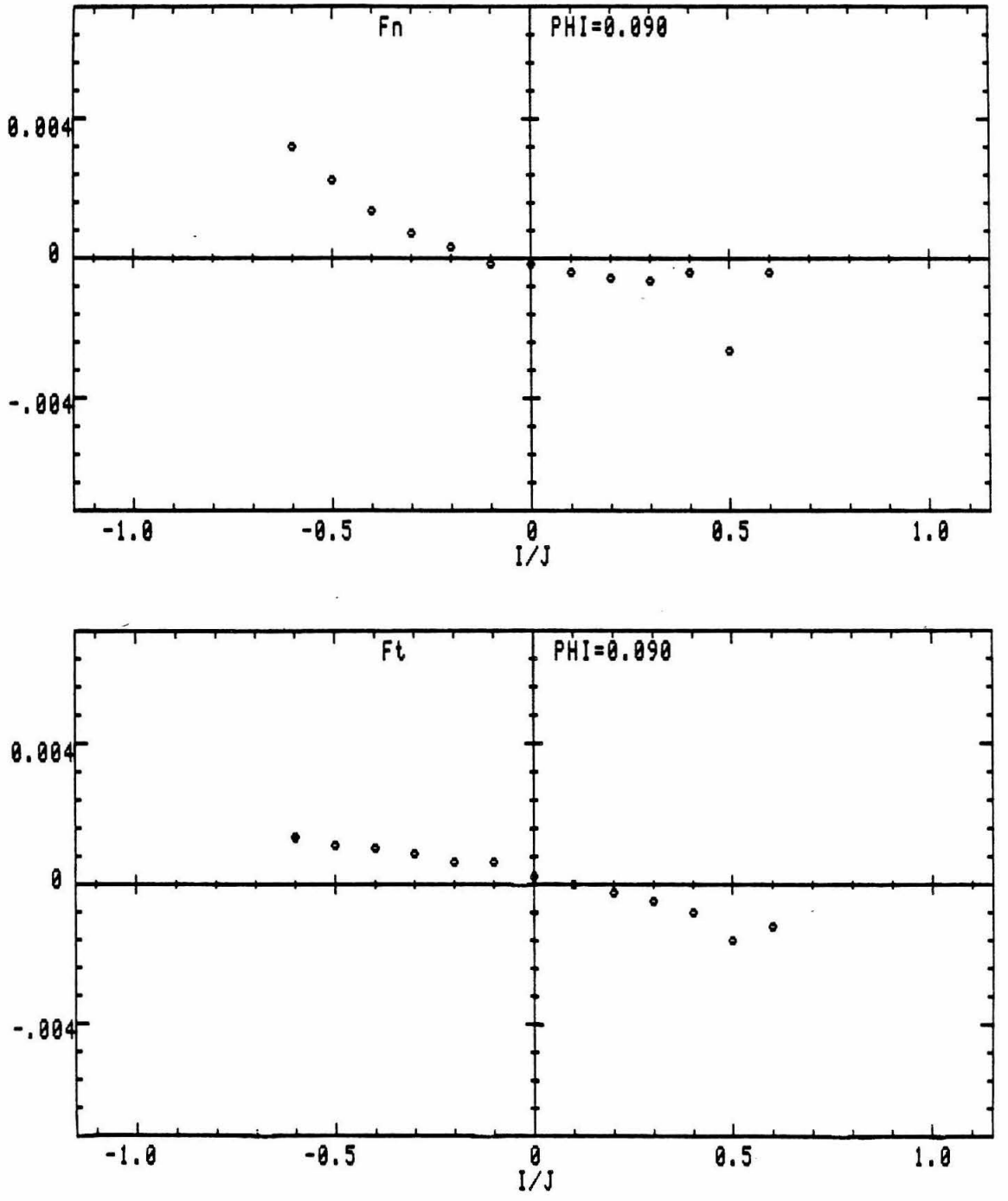

Figure A.66: Unsteady hydrodynamic forces ($\phi = 0.090$, noncavitating flow, Cr_2).

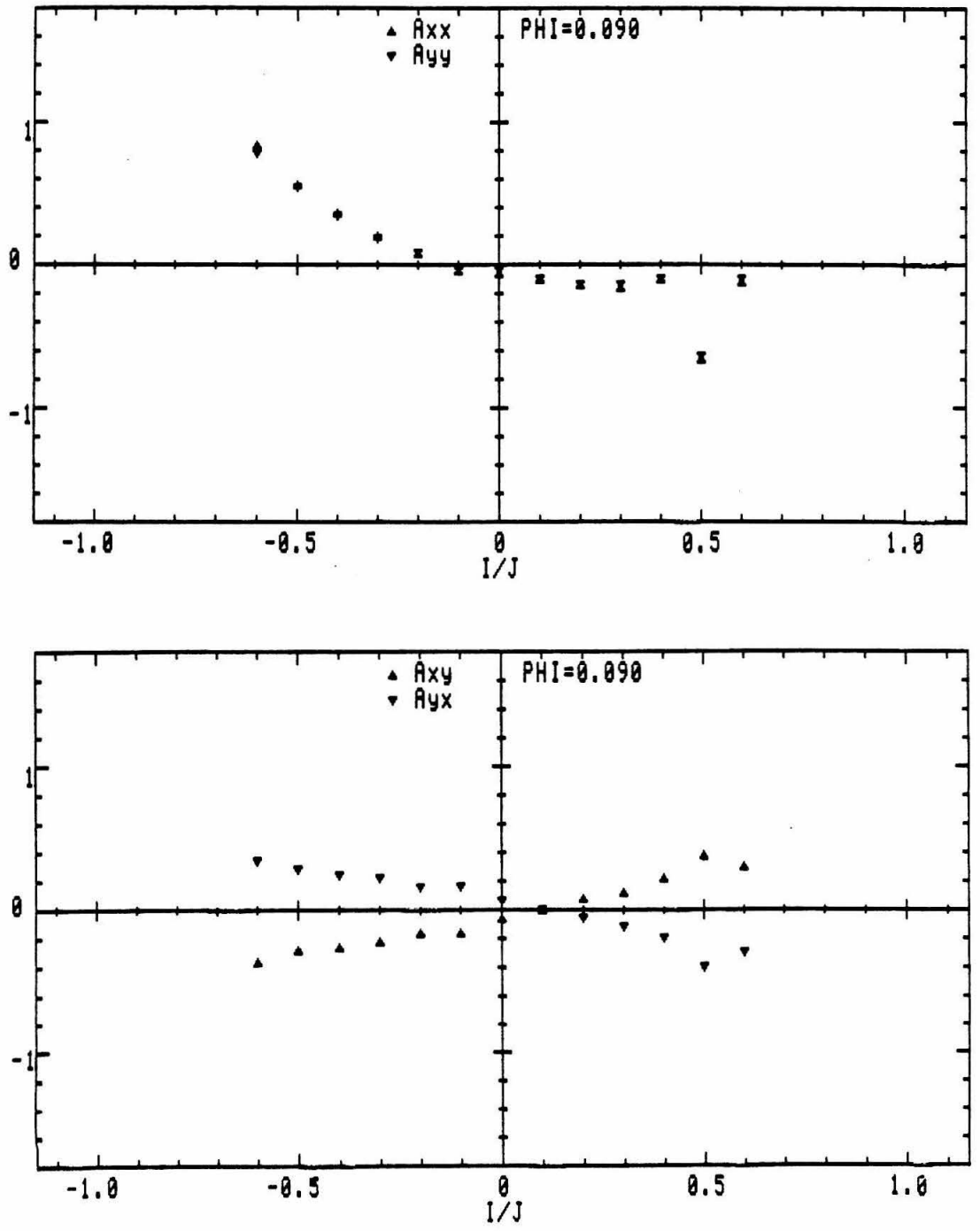

Figure A.67: Rotordynamic force coefficients ($\phi = 0.090$, noncavitating flow, Cr_2).

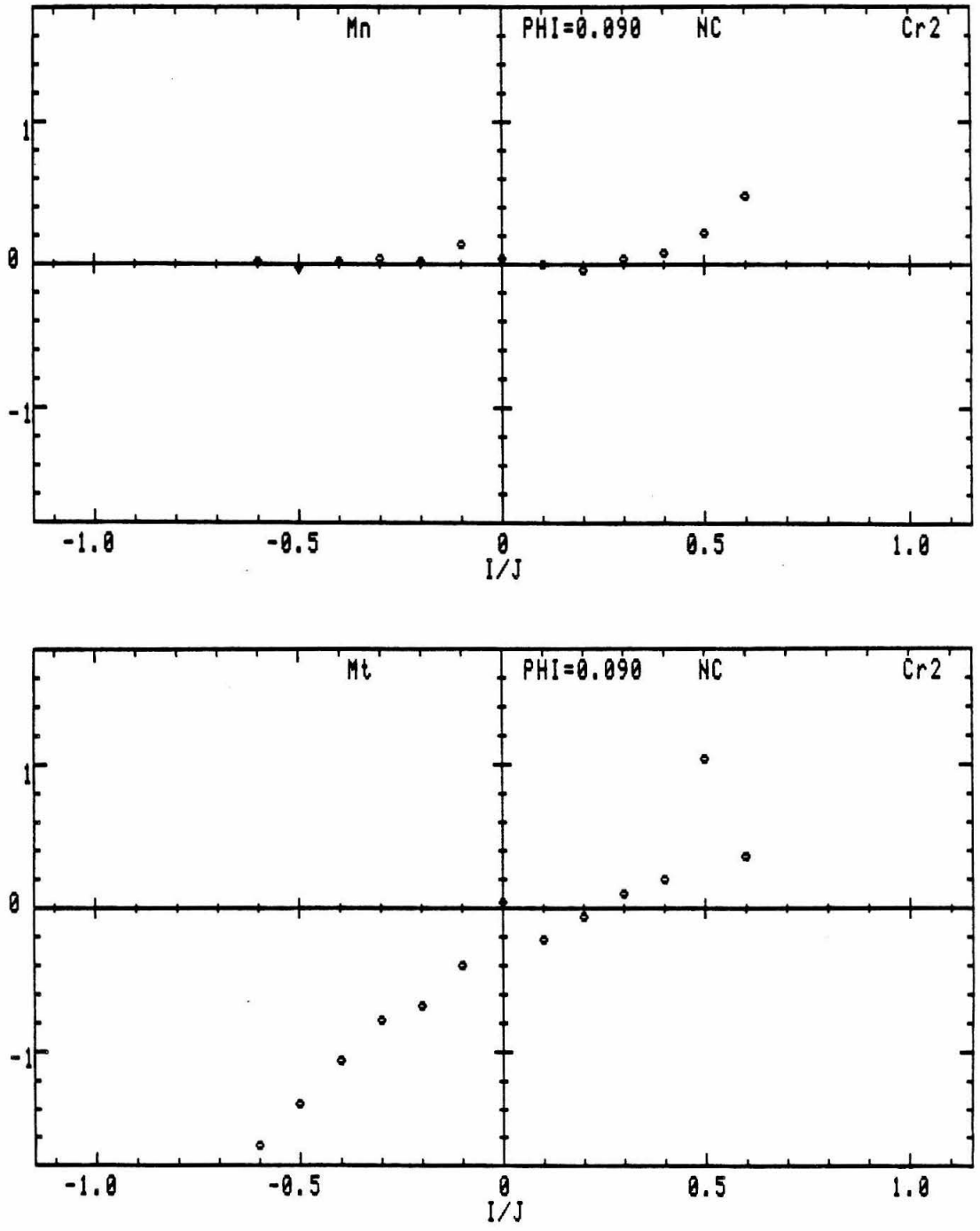

Figure A.68: Unsteady moments ($\phi = 0.090$, noncavitating flow, Cr_2).

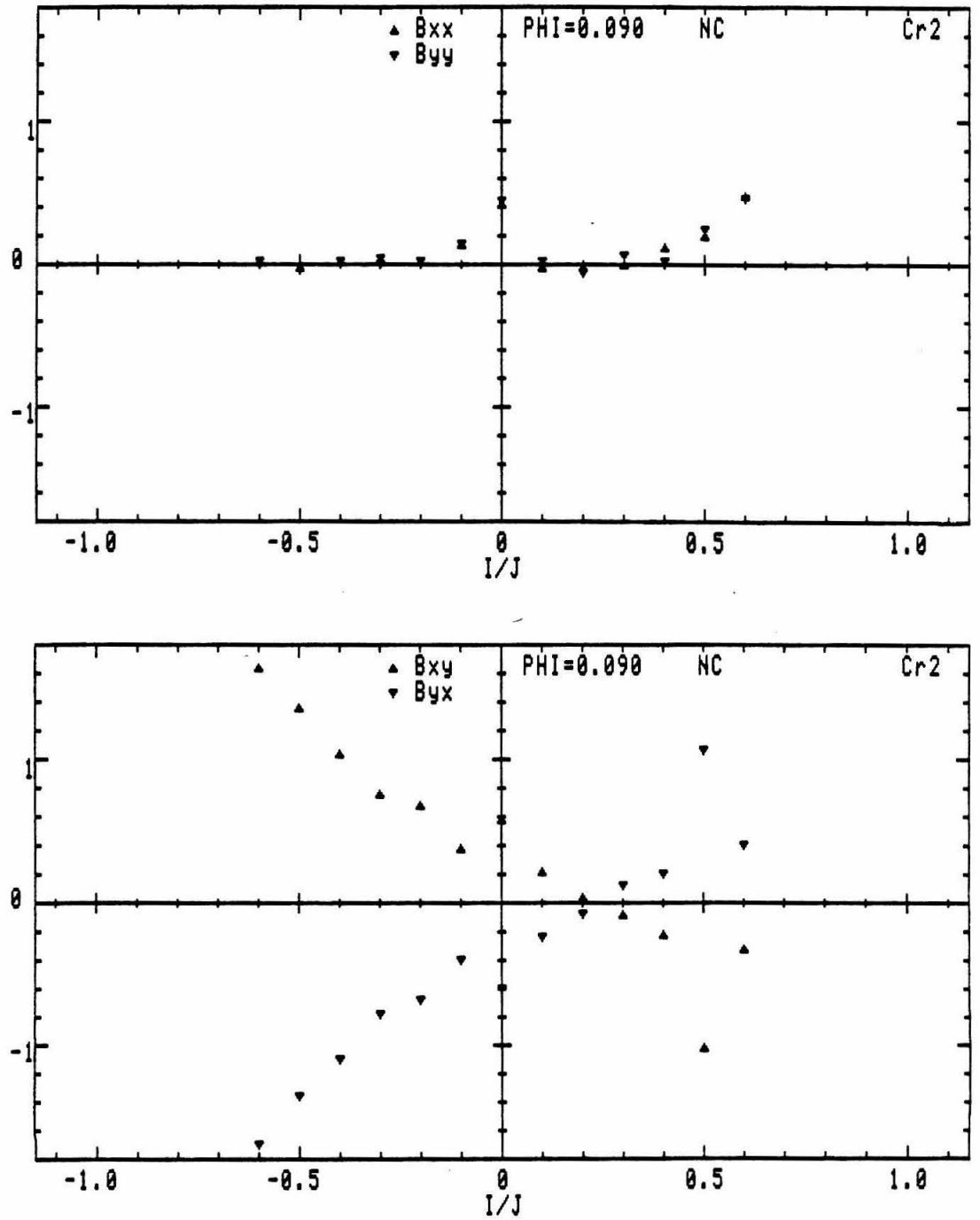

Figure A.69: Rotordynamic moment coefficients ($\phi = 0.090$, noncavitating flow, Cr_2).